Hydrodynamische modellering van golfenergieconvertorparken

Hydrodynamic Modelling of Wave Energy Converter Arrays

Brecht Devolder

Promotoren: prof. dr. ir. P. Troch, prof. dr. ir. P. Rauwoens
Proefschrift ingediend tot het behalen van de graden van
Doctor in de ingenieurswetenschappen: bouwkunde (Universiteit Gent)
en Doctor in de industriële ingenieurswetenschappen (KU Leuven)

UNIVERSITEIT
GENT

Vakgroep Civiele Techniek
Voorzitter: prof. dr. ir. P. Troch
Faculteit Ingenieurswetenschappen en Architectuur

KU LEUVEN

Departement Burgerlijke Bouwkunde
Voorzitter: prof. dr. ir. J. Monbaliu
Faculteit Industriële Ingenieurswetenschappen

Academiejaar 2017 - 2018

ISBN 978-94-6355-129-8
NUR 956, 928
Wettelijk depot: D/2018/10.500/47

Examination board

Supervisors:

prof. Peter Troch
Coastal Engineering Research Group
Department of Civil Engineering
Faculty of Engineering and Architecture
Ghent University
Technologiepark 904
B-9052 Ghent, Belgium

prof. Pieter Rauwoens
Construction Technology Cluster
Department of Civil Engineering
Faculty of Engineering Technology
KU Leuven - Campus Bruges
Spoorwegstraat 12
B-8200 Bruges, Belgium

Voting members:

prof. Patrick De Baets	Ghent University, Belgium	chairman
prof. Jaak Monbaliu	KU Leuven, Belgium	vice-chairman
prof. Marc Vantorre	Ghent University, Belgium	secretary
prof. Maarten Vanierschot	KU Leuven, Belgium	
Jonas Maertens	DEME, Belgium	
prof. Joris Degroote	Ghent University, Belgium	
prof. Javier López Lara	IH Cantabria, Spain	
dr. Pal Schmitt	QU Belfast, Northern Ireland (UK)	

Internal defence (KU Leuven - Campus Bruges): 15 May 2018
Public defence (Ghent University): 20 June 2018

Funding:

This research was funded by a PhD fellowship of the Research Foundation – Flanders (FWO)

Acknowledgements

After an intense but very interesting research period of three and a half years at Ghent University and KU Leuven, it is time to finish my PhD thesis. This thesis would not have been possible without some people whom I want to thank.

Firstly, I would like to thank my two supervisors for their support. My gratitude goes to prof. Peter Troch (Ghent University), for giving me the opportunity to join the coastal engineering research group. He introduced me to the topic of numerical wave tanks and wave energy converters. He provided me with ample of resources: specialised courses, fast computers, participating in conferences, etc. His international network gave me the opportunity to go on two short research stays at the Technische Universität Braunschweig and Queen's University Belfast. Thanks to dr. Hisham El Safti (TU Braunschweig) and dr. Pal Schmitt (QU Belfast) for guiding me during those periods. Also, a big thank you to my second supervisor prof. Pieter Rauwoens (KU Leuven), for introducing me to the numerical world and in particular CFD. Even after changing his job from Ghent University to KU Leuven, he was always available to guide me and to share his broad and specific knowledge. His insights in numerical schemes, mathematical operations and physical processes were a big help for me to bring my PhD research to a higher level. I'm also grateful to work in the construction technology cluster at KU Leuven (campus Bruges) during the final phase of my PhD period.

Secondly, I'm also thankful to all my colleagues both in Ghent and Bruges: my fellow PhD students, researchers, technicians and administrative staff. Not only for the interesting (scientific) discussions but also for the nice evenings in Ghent and Bruges to relax after working hours.

Apart from my professional contacts, there were always friends and family available for listening to me and for supporting me in everything you could imagine. Thank you so much for the relaxing weekends and holidays where we had a lot of fun. A special thanks goes to my parents who always supported me up till now. Last but definitely not least, there is one person who deserves the biggest thank you: my girlfriend Mieke. Thank you so much for living through the highs and the lows of the past years with me and for always being there for me. During the last month of writing this PhD thesis, I did not have much time for you but better times are coming up!

Brecht Devolder
March 2018

Contents

Nomenclature

Latin symbols (I)

A	area	m^2
D	diameter	m
E	root mean square error for the surface elevations	m
	root mean square error for the TKE profiles	m^2/s^2
	root mean square error for the velocity profiles	m/s
F	force	N
F_1	blending function for the $k-\omega$ SST model	
F_2	blending function for the $k-\omega$ SST model	
F_{LD}	linear damper force	N
F_b	external body force	N/m^3
$F_{bearings}$	force on the bearings of the WEC's sliding mechanism	N
F_{ext}	external force	N
$F_{\max}$	maximum force	N
F_{PTO}	force by the power take-off system	N
F_{surge}	horizontal wave-induced surge force	N
F_{sway}	horizontal wave-induced sway force	N
F_x	horizontal wave-induced surge force in X-direction	N
G	amplification factor	$-$
G_b	buoyancy term	$kg/m/s^3$
H	wave height	m
L	length	m
	wave length	m
N_z	number of cells in the vertical Z-direction	
P_k	production term of TKE	m^2/s^3
R_u	wave run-up	m
S	mean rate of strain of the flow	s^{-1}
T	wave period	s
T_d	damped natural period	s
U	horizontal particle velocity at the wave crest	m/s
V	volume	m^3
W	width	m

Latin symbols (II)

X	horizontal space direction	
Y	second horizontal space direction	
Z	vertical space direction	
a	acceleration	m/s^2
$\tilde{a}$	intermediate value of the acceleration	m/s^2
a_1	constant value in the $k-\omega$ SST model	$-$
b	hydrodynamic damping coefficient	kg/s
c	damping coefficient for the linear damper	kg/s
c_α	compression constant	
d	draft	m
	water depth	m
dx	spring compression increment	mm
f_σ	surface tension tensor term	N/m^3
g	gravitational constant	m/s^2
$\vec{g}$	gravitational acceleration vector	m/s^2
k	restoring spring coefficient	kg/s^2
	turbulent kinetic energy	m^2/s^2
$\overline{k}$	time averaged turbulent kinetic energy	m^2/s^2
k_{spring}	spring stiffness coefficient	N/mm
k_{sup}	supplementary turbulent kinetic energy	m^2/s^2
m	bottom slope	$-$
	mass	kg
m_a	added mass	kg
$\vec{n}$	unit vector	$-$
p	pressure	N/m^2
p^*	pressure in excess of the hydrostatic	N/m^2
q_0	initial position during a free decay test	m
r	residual	$-$
s	wave steepness	$-$
t	time	s
u	fluid velocity	m/s
$\overline{u}$	time averaged horizontal velocity	m/s
u_c	compression velocity	m/s
v	kinematic velocity	m/s
x	horizontal space coordinate	m
$\vec{x}$	Cartesian coordinate vector	m
y	second horizontal space coordinate	m
y^+	dimensionless wall distance	$-$
z	vertical space coordinate	m
	vertical position	m

Greek symbols

Δ	difference	
ΔT	time step	s
Δt	time step	s
Δx	grid spacing in X-direction	m
Δy	grid spacing in Y-direction	m
Δz	grid spacing in Z-direction	m
Σ	sum	
α	relaxation factor	$-$
	volume fraction	$-$
β	constant value in the $k-\omega$ and $k-\omega$ SST model	$-$
β^*	constant value in the $k-\omega$ and $k-\omega$ SST model	$-$
γ	constant value in the $k-\omega$ and $k-\omega$ SST model	$-$
δ	small constant value for the acceleration	m/s^2
δ_{ij}	Kronecker delta	$-$
ε	turbulent dissipation	m^2/s^3
ζ_d	damping ratio	$-$
η	surface elevation	m
$\eta_{\max}$	maximum surface elevation	m
θ	blending parameter	$-$
κ	mean curvature of the interface	m^{-1}
μ	coefficient of friction	$-$
	dynamic viscosity	$kg/m/s$
μ_{air}	dynamic viscosity of air	$kg/m/s$
μ_{eff}	effective dynamic viscosity	$kg/m/s$
μ_{water}	dynamic viscosity of water	$kg/m/s$
ν	kinematic viscosity	m^2/s
ν_t	turbulent kinematic viscosity	m^2/s
ξ	breaker parameter	$-$
ρ	density	kg/m^3
ρ_{air}	density of air	kg/m^3
ρ_{water}	density of water	kg/m^3
σ	surface tension coefficient	kg/s^2
σ_k	constant value in the $k-\omega$ and $k-\omega$ SST model	$-$
σ_t	constant value in the buoyancy term G_b	$-$
σ_ω	constant value in the $k-\omega$ and $k-\omega$ SST model	$-$
$\vec{\tau}$	shear stress tensor	$kg/m/s^2$
τ_{ij}	Reynolds stress tensor	m^2/s^2
ϕ	variable	
	wave phase	$-$
ω	specific dissipation rate	s^{-1}
ω_d	damped frequency	rad/s
ω_n	natural frequency	rad/s

Symbols

$^\circ$	angle	degrees
∂	partial derivative	
d	total derivative	

Dimensionless groups

KC	Keulegan-Carpenter number
Re	Reynolds number

Subscripts

0	deep water conditions
av	average value
exp	experimental
$extra.$	extrapolated
f	focussing
i	Cartesian index
	sub iteration
	wave component
j	boundary face
max	maximum value
min	minimum value
num	numerical
w	water
	water-plane
wet	underwater

Superscripts

$-$	time average
$\sim$	phase average
$'$	Reynolds fluctuation
0	initial state
eq	equilibrium
n	time level

Abbreviations

2D	two-dimensional
2DV	two-dimensional in a vertical plane
3D	three-dimensional
AMI	Arbitrary Mesh Interface
CFD	Computational Fluid Dynamics
CFL	Courant-Friedrich-Lewy
CoM	Centre of Mass
CPU	Central Processing Unit
DHI	Danish Hydraulic Institute
DNS	Direct Numerical Simulation
EMEC	European Marine Energy Centre
FNPF	Fully Non-linear Potential Flow
FPA	Floating Point Absorber
FSI	Fluid-Structure Interaction
FWO	Research Foundation – Flanders
GGDH	Generalized Gradient Diffusion Hypothesis
IPCC	International Panel on Climate Change
LD	Linear Damper
LES	Large Eddy Simulation
LSM	Level Set Method
NS	Navier-Stokes
NWT	Numerical Wave Tank
PTFE	Polytetrafluoroethylene
PTO	Power Take-Off
RANS	Reynolds-Averaged Navier-Stokes
RMSE	Root Mean Square Error
SGDH	Standard Gradient Diffusion Hypothesis
SGS	Sub-Grid Scale
SST	Shear Stress Transport
SWL	Still Water Level
TKE	Turbulent Kinetic Energy
TVD	Total Variation Diminishing
VoF	Volume of Fluid
WEC	Wave Energy Converter
WG	Wave Gauge

Samenvatting

Dutch summary

Golfenergie uit windgolven in de oceaan of in de zee wordt geabsorbeerd door middel van golfenergieconvertoren (GECs). In dit onderzoek worden drijvende "point absorber" GECs, ofwel boeien die drijven op het wateroppervlak, bestudeerd. Deze drijvende "point absorber" GECs die zich in de oceaan of in de zee bevinden, reageren op invallende golven en beginnen te bewegen in zes vrijheidsgraden. De GECs absorberen energie uit de golven door middel van een PTO ("power take-off") systeem dat de GEC-beweging omzet in elektriciteit. Om een aanzienlijke hoeveelheid golfenergie te absorberen op een kostenefficiënte manier, worden een aantal GECs bij elkaar geplaatst op een bepaalde locatie. De individuele GECs worden gerangschikt in een array lay-out (of een matrix of park) met een welbepaalde geometrische configuratie. Als de individuele GECs dicht bij elkaar geplaatst worden, zullen ze niet enkel elkaar maar ook de totale elektriciteitsproductie van de GEC array beïnvloeden ("near-field" effecten). Ten eerste verstoort de aanwezigheid van een GEC het invallende golfveld door zowel golfreflectie als golfdiffractie. Ten tweede leidt de beweging van een GEC tot het genereren van golven, die geradieerde golven worden genoemd. Het golfveld rond een GEC wordt dus verstoord door een combinatie van invallende, gereflecteerde, gediffracteerde en geradieerde golven. Dit leidt tot zones met hogere of lagere golfhoogtes in vergelijking met het inkomende golfveld. Het geval waarin één GEC wordt gepositioneerd in het zoggebied van een andere GEC waar lagere golfhoogtes worden waargenomen, moet vermeden worden. Door de individuele GECs in de zones met hogere golfhoogtes te plaatsen, neemt de totale energie absorptie en elektriciteitsproductie van de GEC array aanzienlijk toe. Naast deze "near-field" effecten heeft een GEC array ook een invloed op het golfklimaat over een grotere afstand ("far-field" effecten). De afname in golfhoogtes achter een GEC array heeft gevolgen voor andere gebruikers in de zee, het milieu of zelfs de kustlijn.

In dit onderzoek worden enkel de "near-field" effecten behandeld. De GECs worden getest in een driedimensionale (3D) niet-lineaire viskeuze numerieke golftank (NGT). De NGT is geïmplementeerd in een model gebaseerd op numerieke stromingsmechanica (CFD), OpenFOAM, en bestaat uit twee fluïdumfasen: water met lucht erbovenop. De 3D onsamendrukbare Navier-Stokes vergelijkingen, die de fysica met een zeer hoge nauwkeurigheid beschrijven, worden opgelost op een rooster in een numeriek domein. De positie van het vrij water oppervlak wordt bepaald door het oplossen van een advectie vergelijking voor de volumefractie van

water, geformuleerd volgens de "volume of fluid" (VoF) methode. Traditioneel wordt voor GEC modellering gebruik gemaakt van lineaire modellen gebaseerd op de randelementenmethode ("boundary element method", BEM) voor het oplossen van de potentiaalstroming. Maar toch is CFD noodzakelijk om simulaties te kunnen uitvoeren betreffende de overlevingskansen van GECs die onderworpen worden aan brekende golven. CFD is ook vereist wanneer regelmethoden worden toegepast. Hierbij gaan de GEC bewegingen in resonantie waarbij significante niet-lineaire en viskeuze effecten in combinatie met grote GEC bewegingen zich voordoen. Dit onderzoek richt zich op het verkleinen van twee kennishiaten betreffende een NGT. Het eerste heeft te maken met verbeterde turbulentiemodellering voor NGTs die gebruik maken van een tweefasig stromingsmodel. Dit is bovendien toepasbaar voor een breed gamma van kustwaterbouwkundige en offshore processen zoals golf-structuur interactie, golf-stroming interactie, golfbreking, sedimenttransport, enz. Het tweede hiaat vindt men terug bij fluïdum-structuur interactie simulaties van een drijvend object. Hierbij kunnen zich instabiliteiten voordoen tussen het stromingsmodel en het bewegingsmodel ten gevolge van "added mass" effecten. Tijdens dit onderzoek zijn verbeterde voorspellingsmethoden ontwikkeld voor turbulentiemodellering en efficiënte fluïdum-structuur interactie simulaties in een NGT. Al deze ontwikkelde methoden worden gekoppeld en gevalideerd door gebruik te maken van experimentele gegevens die verkregen zijn door metingen in een fysieke golfgoot of golfbassin.

Het eerste deel van het proefschrift behandelt een verbeterde turbulentiemodellering tijdens golfvoortplanting, golf-structuur interactie en golfbreking. De simulaties gebeuren in een NGT met behulp van het tweefasig stromingsmodel *interFoam* beschikbaar in OpenFOAM. Heel wat auteurs van wetenschappelijke publicaties geven aanbevelingen voor het modelleren van turbulentie. Maar in het algemeen leiden deze turbulentiemodellen tot golfdemping over de lengte van de NGT. Bovendien voorspellen deze een overschatting van de turbulente kinetische energie (TKE) in het hydrodynamische stromingsveld. Deze twee specifieke problemen worden aangepakt door gebruik te maken van RANS turbulentiemodellen, aangepast voor een variabele dichtheid. Deze aanpassing betreft niet alleen het expliciet opnemen van de dichtheid in de turbulentie transportvergelijkingen maar ook het impliciet toevoegen van een densiteitsbronterm in de TKE-vergelijking. Ten eerste is een laminaire oplossing voldoende nauwkeurig in het stromingsveld tijdens propagatie van de golven voorafgaand aan golfbreking. In dat geval dwingt de densiteitsbronterm de oplossing van het stromingsveld nabij het vrij wateroppervlak naar een laminaire oplossing. Ten tweede, in de branding waar golven breken, worden significante turbulentieniveaus verwacht. In deze zone wordt de densiteitsbronterm gelijk aan nul en wordt een volledig turbulent stromingsveld opgelost door het numerieke model. Twee RANS-modellen aangepast voor een variabele dichtheid, $k-\omega$ en $k-\omega\ SST$, zijn getest en gevalideerd met behulp van experimentele gegevens die beschikbaar zijn in de literatuur. De invloed van de densiteitsbronterm in het $k-\omega\ SST$ model wordt aangetoond door regelmatige golven te laten propageren. Dit levert als resultaat dat overmatige golfdemping voor niet-brekende golven met een hoge steilheid wordt vermeden. Verder zijn de numerieke resultaten van golfoploop rond een offshore paalfundering onder regelmatige golven in goede

overeenstemming met experimentele metingen in een fysieke golfgoot. Tijdens simulaties van brekende golven en in vergelijking met traditionele turbulentiemodellen, voorspellen de turbulentiemodellen aangepast voor een variabele dichtheid, $k-\omega$ en $k-\omega\ SST$, resultaten die het best overeenstemmen met de experimentele metingen voor de golfverheffingen, snelheidsprofielen en TKE-niveaus. In het algemeen resulteert een turbulentiemodel aangepast voor een variabele dichtheid niet alleen in een stabiel golfvoortplantingsmodel zonder golfdemping ten gevolge van RANS turbulentiemodellering. Maar het voorspelt ook nauwkeuriger het turbulentieniveau in het stromingsveld van de branding waar golven breken. In het bijzonder verminderen de turbulentiemodellen aangepast voor een variabele dichtheid aanzienlijk de overschatting van TKE in het tweefasig stromingsgebied, dat gewoonlijk in de literatuur wordt beschreven.

In het tweede deel van het proefschrift wordt het tweefasig stromingsmodel met beweegbare roosterpunten, *interDyMFoam*, gekoppeld aan een bewegingsmodel om de beweging van starre objecten te simuleren. Enkel de dominante beweging van de dompende "point absorber" GEC, de op- en neerwaartse beweging, wordt beschouwd. Deze veronderstelling maakt een vermindering mogelijk van zes vrijheidsgraden naar één vrijheidsgraad voor het bewegingsmodel. Een tweede orde nauwkeurig Crank-Nicolson tijdsintegratieschema wordt aangewend om de snelheid en de positie van de GEC uit te rekenen, gebaseerd op zijn versnelling. Een koppelingsalgoritme is nodig om een geconvergeerde oplossing te bereiken tussen het hydrodynamische stromingsveld rond het drijvende object en de kinematische beweging van het drijvende object tijdens elke tijdstap in de tijdsafhankelijke simulatie. Het koppelingsalgoritme wordt gestabiliseerd door middel van een impliciete koppeling in de sub iteraties tijdens elke tijdstap. Een snelle convergentie van het gekoppelde stromings–bewegingsmodel wordt bereikt wanneer de "added mass" met een goede nauwkeurigheid gekend is. In dit werk wordt de waarde van de "added mass" geschat door een Jacobiaan te berekenen. Dit is gebaseerd op beschikbare oplossingen van de versnelling van het drijvende object en de daarop werkende kracht uit vorige sub iteraties. Dit resulteert in efficiënte numerieke simulaties met een minimale CPU-tijd. Het gekoppelde stromings–bewegingsmodel wordt eerst gevalideerd met experimentele data voor één enkele GEC tijdens een vrije responstest en testen waarbij de GEC onderworpen wordt aan regelmatige golven. De experimentele metingen zijn uitgevoerd in de grote golfgoot van de afdeling civiele techniek aan de Universiteit Gent. Een goede overeenkomst wordt gevonden tussen de numerieke en de experimentele metingen, niet alleen voor de dompbeweging van de GEC, maar ook voor het verstoorde golfveld rond de GEC. Vervolgens wordt een meer uitdagende simulatie van een impact test van een vrij vallende wig op het wateroppervlak uitgevoerd en gevalideerd met experimentele metingen van de dompbeweging en de verticale snelheid die beschikbaar zijn in de literatuur. De noodzaak voor een niet-lineair viskeus stromingsmodel, zoals een CFD NGT, wordt aangetoond door middel van een "proof of concept" studie dat de overlevingskansen van een GEC inschat en zo het ontwerp van een GEC bepaalt. Brekende golven worden gegenereerd en deze slaan in op de GEC om zo de GEC beweging en de krachten op de GEC te begroten. Tot slot worden de numerieke simulaties van één enkele dompende GEC uitgebreid tot een aantal dompende GECs

die in een array configuratie zijn geplaatst. Hiervoor worden er in het numerieke model glijdende roosterpunten rond de individuele GECs geïmplementeerd om onafhankelijke bewegingen van dicht bij elkaar geplaatste GECs mogelijk te maken. Deze methodologie verhindert ongewenste roostervervormingen aan het vrij water oppervlak om de nauwkeurigheid van de numerieke oplossing te verbeteren. Als een wereldwijd baanbrekend resultaat worden numerieke simulaties getoond van een array bestaande uit twee, vijf en negen GECs geïnstalleerd in een CFD NGT. De numerieke resultaten worden gevalideerd met experimentele gegevens uit de database van WECwakes, gegenereerd in het golfbassin van DHI (Denemarken). Als resultaat worden er goede overeenkomsten gevonden voor de dompbewegingen van de GECs, de horizontale krachten op de GECs en het verstoorde golfveld rond de GECs. Dit onderzoek betreffende fluïdum-structuur interactie simulaties met behulp van het ontwikkelde gekoppelde stromings–bewegingsmodel in een NGT, opent de mogelijkheden voor numerieke simulaties in een NGT van een willekeurige drijvende structuur of structuren geïnstalleerd in een willekeurig golfklimaat.

In dit werk is fundamenteel onderzoek verricht om meer nauwkeurige voorspellingsmethoden in NGTs te ontwikkelen en op die manier de huidige kennishiaten te verkleinen. Bovendien worden complexe fysische processen, zoals golfbreking, turbulente effecten en resonante niet-lineaire GEC bewegingen gedempt door viskeuze krachten, nauwkeurig berekent in een CFD NGT. Dit in tegenstelling tot traditionele BEM modellen waarin deze processen niet, of sterk vereenvoudigd, in rekening worden gebracht. Al deze bijdragen versterken de haalbaarheid om simulaties van kustwaterbouwkundige en offshore processen of toepassingen in een CFD NGT uit te voeren als aanvulling op experimentele kleinschalige modelproeven in een fysieke golfgoot of golfbassin.

Summary

Wave energy from wind-generated waves in the ocean or sea is absorbed by wave energy converters (WECs). In this research, floating point absorber (FPA) WECs are studied which are floating devices on the water surface. FPA WECs installed in the ocean or sea respond to the incoming waves and start moving in six degrees of freedom. The WECs extract energy from the waves by using a power take-off (PTO) system which converts the WEC's motion into electricity. In order to absorb a considerable amount of wave energy at a location in a cost-effective way, a number of WECs are arranged in an array layout using a particular geometrical configuration. If the individual WECs are installed close to each other, they will interact with each other, affecting the overall electricity production of the array (near-field effects). Firstly, the presence of a WEC unit disturbs the incoming wave field by both wave reflection and wave diffraction. Secondly, the WEC's motion leads to the generation of waves, called radiated waves. The wave field around a WEC is thus perturbed by a combination of incoming, reflected, diffracted and radiated waves. This results in zones with higher or lower wave heights compared to the incident wave field. The case where one WEC is positioned in the wake region of another WEC where lower wave heights are observed must be avoided. By positioning the individual WECs in the zones with higher wave heights, the total energy extraction of the WEC array is significantly improved, increasing the electricity production. In addition to these near-field effects, a WEC array also influences the wave climate further away (far-field effects). The wave height reduction behind an entire WEC array affects other users in the sea, the environment or even the coastline.

In this research, only the near-field effects are considered. The WECs are tested in a three-dimensional (3D) non-linear viscous numerical wave tank (NWT). The NWT is implemented in the computational fluid dynamics (CFD) toolbox OpenFOAM and consists of two fluid phases: water with air on top. The 3D incompressible Navier-Stokes equations, which represent the physics with a very high accuracy, are solved on a mesh in a computational domain. The interface between water and air is resolved by a conservation equation formulated by the volume of fluid (VoF) method. Compared to traditional linear potential flow solvers based on a boundary element method (BEM), CFD is necessary to resolve complex physical processes. Examples are survivability simulations of WECs subjected to breaking waves and WECs operating in resonance mode by applying control methods resulting in significant non-linear and viscous effects combined with large WEC mo-

tions. The present research focusses on filling two knowledge gaps for a NWT. The first one is related to enhanced turbulence modelling for NWTs using a two-phase fluid solver and therefore applicable for a wide range of coastal and offshore processes such as wave-structure interaction, wave-current interaction, wave breaking, sediment transport, etc. The second gap is related to fluid-structure interaction simulations of a floating body. Instabilities between the fluid solver and the motion solver might happen due to added mass effects. During this research, enhanced prediction tools for turbulence modelling and efficient fluid-structure interaction simulations in a NWT have been developed. All these developed methods are coupled and validated by using experimental data obtained in a physical wave flume or basin.

The first part of the thesis deals with enhanced turbulence modelling for wave propagation, wave-structure interaction and wave breaking. The simulations are performed in a NWT using the two-phase fluid solver *interFoam* available in OpenFOAM. Many authors give recommendations for turbulence modelling, but in general, these suffer from wave damping along the length of the NWT and these overpredict the turbulent kinetic energy (TKE) in the hydrodynamic flow field. These two specific problems are addressed by applying buoyancy-modified RANS turbulence models in which the density is included explicitly in the turbulence transport equations and a buoyancy source term is added implicitly to the TKE-equation. Firstly, in the flow field prior to wave breaking (i.e. during wave propagation), a laminar solution is sufficiently accurate. In that case, the buoyancy term forces the solution of the flow field near the free water surface to a laminar solution. Secondly, in the surf zone where waves break, significant turbulence levels are expected. For this zone, the buoyancy term goes to zero and a fully turbulent flow field is resolved by the numerical model. Two buoyancy-modified RANS models, $k-\omega$ and $k-\omega\ SST$, are tested and validated using experimental data available in literature. The influence of the buoyancy source term in the $k-\omega\ SST$ model is demonstrated for the simulation of propagating regular waves. As a result, excessive wave damping for non-breaking high-steepness waves is prevented. Furthermore, the simulation results of wave run-up around a monopile under regular waves are in a good agreement with experimentally obtained data in a physical wave flume. For wave breaking simulations, the results predicted by the buoyancy-modified turbulence models, $k-\omega$ and $k-\omega\ SST$, have the best agreement with the experimental measurements for the surface elevations, undertow profiles and TKE levels compared to traditional turbulence models. In general, a buoyancy-modified turbulence model not only results in a stable wave propagation model without wave damping due to RANS turbulence modelling but it also predicts the turbulence level inside the flow field more accurately in the surf zone where waves break. In particular, the buoyancy-modified turbulence models significantly reduce the overestimation of TKE in the two-phase flow field, commonly presented in literature.

In the second part of the thesis, the two-phase fluid solver with dynamic mesh handling, *interDyMFoam*, is coupled with a motion solver in order to simulate rigid body motions. Only the governing motion of the FPA WEC's behaviour is considered, the heave motion (i.e. up- and downward motion). This assumption allows a

reduction from a six to a one degree of freedom motion. A second order accurate Crank-Nicolson time integration scheme is used to derive the velocity and the position of the WEC from its acceleration. A coupling algorithm is needed to have a converged solution between the hydrodynamic flow field around the floating body and the kinematic motion of the floating body during every time step in the transient simulation. The coupling algorithm is stabilised by using implicit coupling in the sub iterations during every time step. Rapid convergence of the coupled fluid–motion solver is achieved if the added mass is known to a good accuracy. In this work, the added mass is estimated by calculating a Jacobian, based on the available solutions of previous sub iterations for the acceleration of the floating body and the force acting on it. This results in computationally efficient simulations with a minimal CPU time. Firstly, the coupled fluid–motion solver is validated for a single WEC unit during a free decay test and tests where the WEC is subjected to regular waves. The experimental data is obtained in the large wave flume of the department of civil engineering at Ghent University. A good agreement is found between the numerical and the experimental measurements, not only for the WEC's heave motion but also for the perturbed wave field around the WEC. Subsequently, a more challenging simulation of a free falling wedge impacting on the water surface is performed and validated with experimental measurements for the heave motion and vertical velocity available in literature. In order to demonstrate the need for a non-linear viscous fluid solver, such as a CFD NWT, a proof of concept study is presented for the design of a WEC unit under survivability conditions. Breaking waves are generated which are impacting on the WEC in order to quantify the WEC's motion and the forces acting on the WEC. Finally, the numerical simulations of a single floating WEC are extended to a number of heaving WECs installed in an array configuration. Therefore, sliding meshes are implemented around the individual WECs to allow for independent motion of closely-spaced WECs. This methodology prevents undesirable mesh deformation around the air-water interface to enhance the accuracy of the numerical solution. As a worldwide pioneering result, numerical simulations of an array consisting of two, five and nine WECs installed in a CFD NWT are presented. The numerical results are validated with experimental data from the WECwakes database conducted in the wave basin at DHI (Denmark). As a result, good agreements are found for the WECs' heave motions, horizontal surge forces on the WECs and the perturbed wave field around the WECs. This research on fluid-structure interaction simulations using the developed coupled fluid–motion solver in a NWT opens up the possibilities for numerical simulations of any kind of floating structure(s) installed in any sea state using a NWT.

In this work, fundamental research has been carried out to develop enhanced prediction tools for NWTs in order to reduce the present knowledge gaps. Furthermore, complex physical processes are accurately simulated in a CFD NWT, such as breaking waves, turbulent effects and resonant non-linear WEC motions damped by viscous forces. These effects are however not captured, or strongly simplified, by the widely used BEM models. All these achievements increase the feasibility to perform simulations of coastal and offshore processes or applications in a CFD NWT, complementary to experimental small-scale model tests in a physical wave flume or wave basin.

Chapter 1

Introduction

1.1 Background and motivation

Historically, climate has been changing slowly but now it is accelerating leading to warmer summers and colder winters as reported by the Intergovernmental Panel on Climate Change (IPCC, 2014). Also sea level rise and super storms are consequences we are facing more often during the last decades. Governments are changing policies on an international level to address the origins of climate change such as the Paris Agreement made in 2015 (UNFCCC, 2015). One measure is to invest in renewable energy resources of which solar and wind energy are widely known (IPCC, 2012). Wind energy has moved from onshore to offshore up to innovative floating wind turbines such as the DeepCwind floating semi-submersible wind system for example (Robertson et al., 2017). Over the last years, coastal and offshore structures became more complex to withstand the increasing wave loading due to climate change, as reported in Mori et al. (2014) and Bitner-Gregersen and Gramstad (2016). The fact that waves exert a large load on structures triggered the question: can we extract energy from waves in the ocean or sea to produce electricity? This question strengthened the research into wave energy as a part of marine renewable energy production.

Wind waves in the ocean and sea are generated by the wind blowing over the water surface. These waves have a unique feature: they are able to transport energy without significant losses over large distances. The energy from waves can be absorbed by wave energy converters (WECs) to generate electricity, as already described in the 1970s by Salter (1974). There are numerous device types available and the choice is based on the location, geometry, mooring type and operating method. An overview of different WEC types, along with other marine renewable energy devices such as tidal and wind turbines, is presented in Day et al. (2015). In this research, floating point absorber (FPA) WECs are selected. These FPA WECs are floating devices on the water surface producing energy by their motion under wave loading. An artist impression of a FPA WEC type is visualised in Figure 1.1. The WEC body is floating, connected to the seabed by a mooring line and a power take-off (PTO) system is required to convert the WEC's motion under wave loading

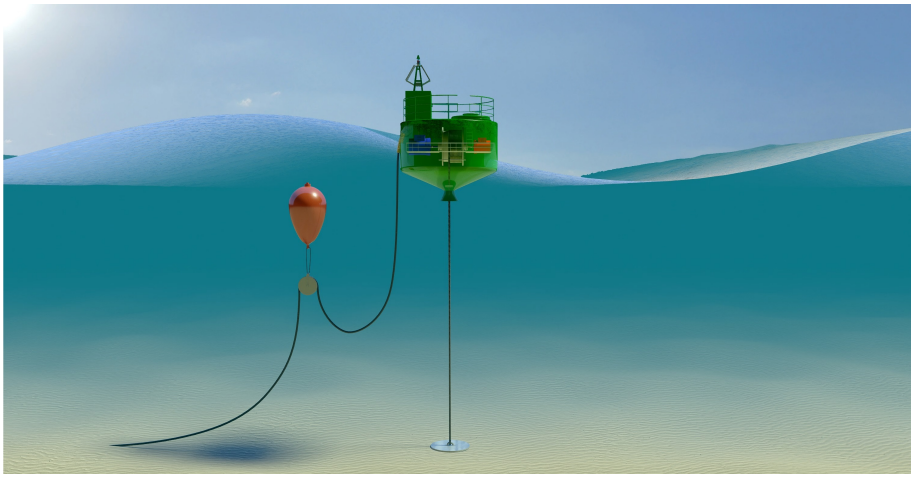

Figure 1.1: Artist impression of the FlanSea WEC (FlanSea, 2013)

into electricity (e.g. electrical generator or hydraulic cylinder). In addition, FPA WECs have some advantages over other WEC types. Firstly, the direction of the incoming waves is not important with respect to the energy extraction. Secondly, due to the antenna effect, wave energy can be captured over a width larger than the physical width of a FPA WEC, resulting in a theoretical maximum absorption efficiency larger than $100\ \%$ (Babarit, 2017). Lastly and most importantly for this research, FPA WECs have a simple operating principle and device geometry which facilitates the design and the experimental or numerical testing.

In order to absorb a considerable amount of wave energy at a location in a cost-effective way, multiple WECs are arranged in arrays using a particular geometrical configuration. Interactions between the individual WECs affect the overall electricity production of the array (near-field effects). A WEC responds to incident waves and starts moving in six degrees of freedom. The WEC's motion leads to the generation of waves, called radiated waves. Furthermore, the presence of a WEC disturbs the incoming waves by wave reflection and wave diffraction. The perturbed wave field around a WEC is thus a combination of incoming, radiated, reflected and diffracted waves. This results in zones with higher or lower wave heights compared to the incident wave field. The situation where one WEC is positioned in the wake region of another WEC, where lower wave heights are observed, must be avoided. By arranging the individual WECs positioned in zones with higher wave heights, the total energy extraction of the WEC array is significantly improved. In addition to these near-field effects, a WEC array also influences the wave field further away (far-field effects). The wave height reduction behind an entire WEC array affects other users in the sea, the environment or even the coastline. If such a WEC array is installed close to the shoreline, it could act as a coastal defence system by reducing the wave loading on beaches for example (Mendoza et al., 2014; Abanades et al., 2015).

In general, the installation of a WEC array changes the incident wave field significantly and affects both the hydrodynamic response and the energy absorption of the individual WECs based on the local, perturbed, wave field. Therefore, WEC array design is key to maximise the total electricity production of the complete WEC array. Detailed methods are required to quantify the complex wave field modifications and to find the optimal layout to position the individual WEC units. In order to answer those fundamental questions on WEC array design, various approaches are followed: physical modelling, numerical modelling or a combination of both. The first approach is performing traditional physical model tests. A WEC on a smaller scale is constructed and installed in an artificial environment representing the sea or ocean: a wave flume or a wave basin. Experimental model tests are performed under controllable circumstances and therefore the hydrodynamic parameters of the flow field and the WEC's kinematic motions are easier to measure compared to field tests in open sea such as the EMEC (European Marine Energy Centre) test facility in Orkney (Scotland, UK). During physical model tests, the effect of the smaller scale requires attention because the properties of water and air cannot be downscaled. Scale effects are mainly important for wave impact forces on structures (Bullock et al., 2001) such as during a survivability simulation of a WEC for example. A general outline of physical modelling of WECs is included in Pecher and Kofoed (2017). A number of model tests for single WEC units and WEC arrays are available in scientific literature, however the most extensive dataset for WEC arrays was generated in 2013 during the WECwakes project funded by the EU FP7 Hydralab IV program (Stratigaki et al., 2014, 2015). Model tests were conducted in the shallow water wave basin of the Danish Hydraulic Institute (DHI; Hørsholm, Denmark). Up to 25 WECs units have been installed in the wave basin using different geometrical configurations and subjected to all kind of wave conditions. A photograph made during a test with 25 WECs is shown in Figure 1.2. This large and unique database is publicly available for researchers under the Hydralab rules. In this research, the experimental WECwakes dataset is used to validate the developed numerical model. Complementary to physical modelling, numerical modelling is often applied for WEC array design. Computers are used to solve a set of equations inside a computational domain with suitable boundary conditions on the borders in order to replicate the sea or ocean. The obtained numerical results are only as good as the physics involved in the equations being solved. Therefore, physical wave flumes or wave basins are always needed to generate experimental data for the validation of these numerical models. Numerical models are deployed on both small and large scale set-ups and do not suffer from scale effects. Depending on the complexity of the model, the CPU time needed to obtain results might be long.

Nowadays, the use of numerical methods for WEC modelling is growing due to the increasing available computational power. However, the complex flow features around WECs and WEC arrays, require a continuous development and optimisation of these numerical models. The aim of the research presented in this thesis is the development of enhanced numerical tools for the simulation of water waves and wave-structure interaction problems, in particular for WEC arrays. Therefore, in the next section 1.2, an overview of the available state of the art numerical models

Figure 1.2: A 5×5 WEC array subjected to irregular long-crested waves in the DHI wave basin during the WECwakes project. Adopted from Stratigaki et al. (2014).

for WECs is reported and the knowledge gaps are defined.

1.2 State of the art

This section frames the research conducted within the thesis by presenting a concise overview of state of the art techniques for numerical modelling of WECs and WEC arrays. As described later in the outline, section 1.4, an in-depth literature review is included in every chapter focussing on one particular research topic.

1.2.1 Numerical modelling of WECs

There exist a large variety of numerical models to study the interaction between waves and WECs. These models have one aspect in common: they all calculate the hydrodynamic flow field around a WEC and the WEC's response under wave action. The choice for a particular model is based on a trade off between the accuracy of the results and the computing time needed. The higher the complexity of a model, the higher the accuracy but the longer the simulation takes in terms of CPU time. Furthermore, the choice for a model also depends on the physics which need to be resolved. For example, there are models specialised in calculating the hydrodynamic flow field around and the response of the WECs (near-field zone) while other models are better suited for studying the impact of WEC arrays at a larger distance (far-field zone) (Folley et al., 2012). Most recently, different numerical models are combined to perform numerical simulations of both the near-field and far-field

zone. Those coupled models use the advantage of each individual model to perform efficient simulations in terms of CPU time depending on the physics to be resolved. Examples are presented in Troch and Stratigaki (2016), Verbrugghe et al. (2017b) and Verbrugghe et al. (2018) where a wave propagation model is coupled with a wave-structure interaction solver. The wave propagation solver is able to calculate the wave field in a large domain (far-field zone) with minimal CPU effort. The wave-structure interaction solver resolves the hydrodynamic flow field around a WEC and its response in a relatively small domain (near-field zone) to minimise the overall CPU time.

An overview of all the available state of the art numerical models for single WECs and WEC arrays is extensively reported in the book: *Numerical modelling of wave energy converters: state-of-the-art techniques for single devices and arrays* edited by Folley (2016a). Specifically for point absorber WECs, a review of various numerical methods is presented in Li and Yu (2012). In this thesis, only near-field effects are studied in a limited area around the WECs. The following paragraphs give an overview of possible numerical tools to study these effects.

At first, numerical models based on semi-analytical techniques were used for modelling simple WEC geometries. Pioneering research on point absorber WEC arrays was carried out by Budal (1977), Evans (1980) and Falnes (1980), which resulted in analytical expressions for the maximum power absorption of the array, often referred to as the point absorber method. This method assumes that the WEC's diameter is small compared to the wave length and to the WEC-WEC spacing (no interactions between the WECs). A detailed overview of all the available semi-analytical techniques is reported in Child (2016). Due to the limited computational power at that time, the derivations were restricted to a linear theory. The computational power has been increased significantly over the past decades, enabling the use of complex methods for WEC modelling, reducing the model assumptions. Nowadays, semi-analytical models are still used to perform preliminary simulations of large WEC arrays or to optimise the array layout because they have a minimised computational cost.

Still assuming potential flow theory, more advanced techniques based on linear hydrodynamic theory were developed to model complex WEC geometries. The most frequently used models are based on the boundary element method (BEM) which is a panel method to estimate the hydrodynamic coefficients which describe added mass, damping, wave diffraction and wave excitation forces. Examples of software packages are Aquaplus (Delhommeau, 1987), ANSYS Aqwa (2018), WAMIT (2016) and Nemoh (Babarit and Delhommeau, 2015). They all calculate the hydrodynamic response of WECs to an incident wave field in frequency domain. In Alves (2016), an overview of frequency domain models for WECs is published. Next to semi-analytical techniques, frequency domains are also used to perform simulations of large WEC arrays or to optimise an array layout because the computational power has been increased significantly over the past years. An alternative to frequency domain modelling is time domain modelling, as presented in Ricci (2016). These models are necessary to take into account realistic PTO systems and mooring forces which are often non-linear. This makes time-domain modelling extremely powerful (Folley et al., 2012), but compared to frequency do-

main models, they require more computational effort. Apart from deterministic models (frequency domain and time domain), probabilistic models are also used for WECs, such as spectral domain models. These spectral domain models use a statistical representation of the sea state and predict the WEC's response by a transformation function, more information is available in Folley (2016b). All these frequency, time and spectral domain models are however restricted to linear problems and thus limited to small amplitude waves and small motions of the WECs. Note that time domain models allow the implementation of non-linear terms such as hydrodynamic forces (non-linear buoyancy forces) and external forces (non-linear PTO forces).

Over the past years, the available computational power has been increased significantly and more advanced, non-linear, models became also suitable for WEC modelling. A review of all non-linear methods for WEC modelling is reported in Penalba et al. (2017). Examples are fully non-linear potential flow (FNPF) models and computational fluid dynamics (CFD) models. FNPF models are computational more efficient in terms of CPU time than CFD models. FNPF models are assuming an inviscid flow and they are able to model steep waves and large device motions for non-breaking wave conditions, as summarised by Fitzgerald (2016). FNPF models cannot capture overturning and breaking waves, wave slamming, green water events, air entrainment, water exit or entry problems and turbulence. Furthermore, for point absorber WECs, viscous damping forces are important to predict realistic WEC motions and accurate energy absorption, especially near resonance (Li and Yu, 2012). In addition, it is yet unclear how important non-linear potential flow effects are relative to viscous flow effects, particularly at full scale (Fitzgerald, 2016; Penalba et al., 2017). The most complete WEC models are using a non-linear viscous fluid solver developed within a computational fluid dynamics (CFD) toolbox. CFD solves the Navier-Stokes equations, representing the physics with a very high accuracy. Compared to the widely used BEM solvers based on potential flow theory, CFD is necessary to model complex physical processes for WEC modelling. For example, wave breaking events need to be resolved accurately to perform survivability simulations of WECs subjected to extreme wave conditions. By applying intelligent and precise control strategies to maximise the WEC's power output (Davidson et al., 2018), the WEC's motion goes into resonance for which viscosity and non-linear effects play a major role. Moreover, if non-linear viscous effects cause flow separation and vortex shedding, turbulent effects need to be incorporated. These processes are only resolved within a CFD model by performing a direct numerical simulation (DNS, turbulence is resolved), large eddy simulation (LES, turbulence is partially resolved by the mesh and partially modelled) or a Reynolds-averaged Navier-Stokes (RANS, turbulence is modelled) simulation. In Wolgamot and Fitzgerald (2015), the use of CFD for WECs is reviewed and a good agreement between CFD and experimental results has been reported for various studies, demonstrating the feasibility of CFD simulations for wave energy applications. As mentioned in Mingham et al. (2016), CFD models are categorised in two classes: Eulerian and Lagrangian methods. The first class discretises the computational domain in a finite set of points, a mesh, on which the numerical equations are solved by using a finite difference method or a finite volume method. Most of

the CFD methods used for WEC modelling are based on a two-phase fluid solver which resolves the water as well as the air phase to cope with air entrainment during wave breaking for example. Both incompressible and compressible models are available but for WEC modelling, incompressible models are mostly used. However, compressibility might become important during survivability simulations with breaking waves due to air entrainment and pressure fluctuations. The second class, Lagrangian methods, are all mesh-less methods and uses particles which are moving inside the computational domain. For WEC modelling, smoothed particle hydrodynamics (SPH) methods are popular of which a feasibility study is reported in Verbrugghe et al. (2017a). The advantages as well as the drawbacks of CFD models for WEC applications are briefly outlined in Schmitt et al. (2012). Note that all CFD models are still suffering from long computing times, even for small domains. They also involve numerical errors by approximating algorithms and discretisation schemes (both spatial and temporal). Validation of CFD models, both on small and full scale, is required to check whether all the physics involved in the hydrodynamic flow field are included and captured correctly within the CFD model. In general, CFD models are very similar to experimental model tests in a wave flume or basin. CFD has the advantage that the WEC's geometry can be changed easily, a higher resolution of data can be extracted and scale effects are absent. A study of scale effects is reported in Schmitt and Elsäßer (2017) for an oscillating wave surge converter. By performing RANS simulations, they investigated whether Froude scaling is adequate to extrapolate small scale physical model tests to full scale. They demonstrated that some differences in flow patterns are observed between small and full scale simulations. Another advantage of CFD is the repeatability of the generated wave field compared to experimental model tests. For example, in O'Boyle et al. (2011, 2017) and Lamont-Kane et al. (2013), it is reported that there is a strong dependency of the wave tank homogeneity and wave making quality on the assessment of WEC array interactions for example. Therefore over the last years, numerical wave tanks (NWTs) have been developed within CFD software. A NWT is the equivalent of a physical wave basin and they share the same objective: reproducing the physics as observed in the ocean or in the sea in a controllable environment to study physical processes in detail or to check design criteria. A review of wave makers for CFD NWTs is presented in Schmitt and Elsaesser (2015a) and two main categories are defined: direct simulation of a wave maker by a moving mesh (Higuera et al., 2015; Vanneste and Troch, 2015) or using numerical methods to generate the desired hydrodynamic wave-induced flow field. The latter category is mostly used and is further divided into four subcategories (Schmitt and Elsaesser, 2015a):

1. Relaxation method: relaxation of theoretical results to the variables in the NWT by a smooth blending function. This method requires additional relaxation zones increasing the size of the computational domain (Mayer et al., 1998; Jacobsen et al., 2012);

2. Mass source function: adding a source term to the continuity equation which adds or removes water in the NWT (Lin and Liu, 1999);

3. Impulse source function: adding a source term to the momentum equation which generates velocities at the boundaries (Choi and Yoon, 2009);

4. Boundary method: customised boundary conditions to generate and absorb the waves. This method only acts on the boundaries of the computational domain. Applications of boundary wave generation are found in (Troch and De Rouck, 1999; del Jesus et al., 2012; Higuera et al., 2013a,b) for example.

1.2.2 A numerical wave tank in OpenFOAM

In this research, the NWT is implemented in the open source CFD software OpenFOAM (Weller et al., 1998). Over the past years, three main branches are developed and made available by respectively the OpenFOAM Foundation (2018), OpenCFD (2018) and the foam-extend community (Foam-extend, 2016). In this work, OpenFOAM-2.2.2 (2013) and OpenFOAM-3.0.1 (2015a) provided by the OpenFOAM Foundation (2018) are deployed.

The NWT used in this research is a two-phase fluid solver with suitable boundary conditions to generate and absorb waves. The fluid solver uses the three-dimensional (3D) incompressible Navier-Stokes equations to calculate the hydrodynamics (i.e. pressure and velocity) in the water as well as in the air phase. The volume of fluid (VoF) method is applied by solving a conservation equation for the volume fraction to determine the position of the free water surface in the NWT. A good description of the VoF method implemented in the OpenFOAM versions used in this thesis is provided in Berberović et al. (2009). OpenFOAM uses the finite volume method to solve the governing equations, see Versteeg and Malalasekera (2007) for example. Boundary conditions for wave generation and absorption are mostly adopted from external toolboxes such as waves2foam (Jacobsen et al., 2012), IHFOAM (Higuera et al., 2013a,b) or olaFlow (OlaFlow CFD, 2018). The former toolbox is based on the relaxation technique while the two latter toolboxes are a set of customised boundary conditions (see previous section 1.2.1). In addition, these wave generation and absorption toolboxes are able to simulate the flow through porous media such as breakwaters for example. Also currents, with or without waves, are generated in NWTs in order to enhance the reproduction of the physics observed in reality. For the research presented in this thesis, the IHFOAM toolbox (Higuera et al., 2013a,b) is used to generate and absorb waves by customised boundary conditions since no additional space is required for relaxation zones in the computational domain. Different wave theories are implemented for both regular and irregular wave generation, as well as uni-directional and multi-directional wave generation are available. The wave absorption methodology in IHFOAM is assuming shallow water conditions, which is however not always the case. As mentioned in Higuera et al. (2013a), the absorption function works relatively well outside its range of applicability.

1.2.3 Knowledge gaps

At this moment, the wave energy sector has not demonstrated economic viability (Penalba et al., 2017). For example, maximising the power output over the com-

plete range of possible sea states for operational conditions has not been achieved yet. Another bottleneck is the survivability of WECs during storm conditions to avoid structural and mechanical failure (Ransley et al., 2017a). Therefore, accurate and detailed numerical methods, such as a CFD NWT, are necessary to reproduce and understand the behaviour of WECs to all possible environmental loads under both operational and survivability conditions. NWTs implemented in a CFD toolbox are only recently used for traditional offshore applications for which, in general, large motions are not desired (e.g. offshore oil and gas platforms or ships). On the contrary, for wave energy applications, large WEC motions are one of the key objectives in order to maximise the energy extraction. All this makes a CFD NWT a promising tool for WEC testing but more research is required before applying it for practical problems.

In the present state of the art techniques for wave modelling and wave-structure interaction simulations of WECs using a CFD NWT, the following knowledge gaps exist. Note that only the relevant gaps are presented related to the research carried out within this PhD thesis. Firstly, it is clear that no standard RANS turbulence model exists for simulating propagating waves and breaking waves in a NWT using CFD. Moreover, it is generally known that none of the traditional turbulence models (e.g. $k-\varepsilon$, $k-\omega$ and $k-\omega\ SST$) are developed for two-phase flow simulations but for an incompressible single phase flow. For example, the $k-\omega$ model is originally developed for aerodynamic and aerospace applications (Wilcox, 1998) while the $k-\varepsilon$ by Launder and Spalding (1974) is still the most widely used turbulence model for industrial applications. Secondly, fluid-structure interaction simulations require a stable coupling algorithm between a fluid solver and a motion solver. In particular for a two-phase fluid solver, Devolder et al. (2015) discovered stability issues due to added mass effects for rigid body simulations using the *interDyMFoam* solver implemented in OpenFOAM. Thirdly, mesh motion for rigid body simulations requires attention by using a two-phase fluid solver using VoF. Different methodologies are available such as mesh distortion or re-meshing of the computational domain, see Schmitt and Elsaesser (2015b). A robust and efficient approach for the unstructured finite volume method is to solve a diffusive Laplace equation in order to determine the mesh deformation, as developed by Jasak and Tuković (2006). This method might become unstable for large motions of independently heaving FPA WECs closely installed in an array configuration. Lastly, all developed numerical tools need thorough verification and validation by using reliable experimental measurements. For example, CFD simulations of a WEC array are scarce and have only been reported by a few researchers, e.g. Agamloh et al. (2008) and Mccallum (2017).

1.3 Objectives and methodology

In this work, fundamental research is performed to fill the knowledge gaps defined in section 1.2.3. Therefore, the following objectives are tackled within this thesis:

1. Enhanced turbulence modelling in a NWT;
   Significant wave damping over the length of a NWT based on traditional

RANS turbulence modelling during wave propagation must be avoided for NWTs using a two-phase fluid solver. In addition, more accurate predictions for the turbulent quantities in the flow field are required.

2. Accelerated coupling between a CFD fluid solver and a motion solver;
   For transient simulations of floating bodies, stabilisation of the coupling algorithm between the two-phase fluid solver and the motion solver during every time step must be achieved. In addition, the coupling algorithm needs to be accelerated in order to reduce the number of sub iterations during every time step and to achieve efficient simulations of the hydrodynamic flow field around a floating body along with its kinematic motion.

3. Mesh motion in a NWT for fluid-structure interaction (FSI) simulations;
   For simulations of a WEC, and specifically for closely-spaced WECs in an array layout, modelled in a CFD NWT, mesh motion is extremely important in obtaining good accuracy of the numerical results. The influence of mesh motion on the free water surface must be limited for two-phase fluid solvers using a VoF method.

4. Validation of the NWT using experimental data.
   Numerical methods need validation by using experimental data to check whether the governing physical processes are included and resolved correctly with a certain degree of accuracy. Experimental data is obtained by performing model tests in a physical wave flume or wave basin.

To achieve the objectives, a methodology is followed in which a NWT implemented in OpenFOAM is deployed. The first part of the thesis focusses on enhanced turbulence modelling for wave propagation and wave breaking simulations in a NWT using the two-phase fluid solver *interFoam* available in OpenFOAM. In general most of the RANS turbulence models are overpredicting the turbulent kinetic energy (TKE) in the hydrodynamic flow field. In this thesis, that specific problem is addressed by applying buoyancy-modified RANS turbulence models in which the density is included explicitly in the turbulence transport equations and a buoyancy source term is added implicitly to the TKE-equation. Two buoyancy-modified RANS models, $k-\omega$ and $k-\omega\ SST$, are tested and validated for wave propagation, wave run-up around a monopile structure and wave breaking on a sloping beach. In the second part of the thesis, the two-phase fluid solver with dynamic mesh handling, *interDyMFoam*, is coupled with a motion solver in order to simulate rigid body motions. A coupling algorithm is needed to have a converged solution between the hydrodynamic flow field around and the kinematic motion of the floating body during every time step in the transient simulation. The coupling algorithm derived in this thesis is stabilised and accelerated so that only few sub iterations during every time step are needed to have a converged fluid–motion coupling. Validation studies are presented for a free decay test of a single WEC unit, an impact test of a free falling wedge on the water surface and the response of a single WEC unit and WEC arrays under incident regular waves. Finally, a proof of concept study is performed to outline the application of a CFD NWT for survivability simulations of a WEC subjected to breaking waves.

1.4 Outline

This thesis is organised in seven chapters, each highlighting one research topic which has been published in or is under review for publication in a journal or conference proceedings.

Part I of this thesis focusses on enhanced RANS turbulence modelling for simulating waves using a two-phase fluid solver as a NWT. Chapter 2 investigates turbulence modelling with respect to wave propagation and wave-structure interaction of a fixed monopile. Subsequently in Chapter 3, the performance of various turbulence models is analysed for wave breaking simulations.

Fluid-structure interaction (FSI) simulations are the main topic in Part II of this thesis. In Chapter 4, the coupling between a motion solver and a fluid solver is investigated, optimised and validated by using experimental data. Subsequently, the coupled fluid–motion solver is applied to study WECs in a NWT. Chapter 5 reports the validation study for a single WEC unit in operational conditions by using experimental data followed by a survivability simulation of a single WEC unit subjected to breaking waves. In the next Chapter 6, a number of WECs are arranged in an array configuration to study the interactions between the individual WECs and the wave field modification around the WECs. The numerically obtained results are validated by using the experimental WECwakes database.

In Chapter 7, a summary of the key findings is presented and some recommendations for future research are made.

Appendix A presents an in-depth analysis of the turbulent kinetic energy in the flow field during wave breaking events, as an extension to Chapter 3.

Part I

Turbulence modelling for a numerical wave tank implemented in OpenFOAM

Chapter 2

Wave propagation and wave-structure interaction simulations

In this chapter, wave propagation and wave interaction with a fixed monopile structure in a numerical wave tank are studied for the case of non-breaking waves. RANS turbulence modelling is applied by using a $k-\omega\ SST$ model and wave damping over the length of the computational domain is observed for high steepness waves. This specific issue is addressed by using a buoyancy-modified $k-\omega\ SST$ model which avoids wave damping and enhances significantly the predictive skills of a numerical wave tank in terms of surface elevations. Finally, the buoyancy-modified $k-\omega\ SST$ model is validated by using experimental data of wave run-up measurements around a monopile subjected to regular waves (De Vos et al., 2007).

This chapter is originally published as:
Devolder, B., Rauwoens, P., and Troch, P. (2017). Application of a buoyancy-modified $k-\omega\ SST$ turbulence model to simulate wave run-up around a monopile subjected to regular waves using OpenFOAM®. *Coastal Engineering*, 125:81–94. doi:10.1016/j.coastaleng.2017.04.004.

Application of a buoyancy-modified $k-\omega\ SST$ turbulence model to simulate wave run-up around a monopile subjected to regular waves using OpenFOAM®

Brecht Devolder, Pieter Rauwoens, Peter Troch

Abstract
The objective of the present work is to investigate wave run-up around a monopile subjected to regular waves inside a numerical wave flume using the Computational Fluid Dynamics (CFD) toolbox OpenFOAM®. Reynolds-Averaged Navier-Stokes (RANS) turbulence modelling is performed by applying the $k-\omega\ SST$ model. Boundary conditions for wave generation and absorption are adopted from the IH-FOAM toolbox. Simulations of propagating water waves show sometimes excessive wave damping (i.e. a significant decrease in wave height over the length of the numerical wave flume) based on RANS turbulence modelling. This anomaly is prevented by implementing a buoyancy term in the turbulent kinetic energy equation. The additional term suppresses the turbulence level at the interface between water and air. The proposed buoyancy-modified $k-\omega\ SST$ turbulence model results in an overall stable wave propagation model without significant wave damping over the length of the flume. Firstly, the necessity of a buoyancy-modified $k-\omega\ SST$ turbulence model is demonstrated for the case of propagating water waves in an empty wave flume. Secondly, numerical results of wave run-up around a monopile under regular waves using the buoyancy-modified $k-\omega\ SST$ turbulence model are validated by using experimental data measured in a wave flume by De Vos et al. (2007). Furthermore, time-dependent high spatial resolutions of the numerically obtained wave run-up around the monopile are presented. These results are in line with the experimental data and available analytical formulations.

Keywords: CFD; OpenFOAM®/IHFOAM; Buoyancy-modified turbulence model; Monopile; Wave run-up

2.1 Introduction

Numerous offshore wind farms have already been installed or are under construction. Wind turbines are mounted on large foundations in the seabed, such as vertical cylinders, called monopiles. The design of such a monopile is mainly dependent on the total force acting on it. However, some smaller pieces are attached to that monopile (e.g. boat landing facility, J-tube, ladder, platform and door). In order to design these smaller parts, wave run-up around the monopile caused by incident waves should be assessed accurately. Therefore, both experimental and numerical research have already been conducted.

Experimental research has been performed in order to define the wave run-up pattern around a monopile. For example, De Vos et al. (2007) described small scale model tests in which wave run-up was measured around a monopile placed in relatively deep water conditions using different regular and irregular wave trains. Moreover, analytical formulations are proposed to determine the maximum wave run-up for both regular and irregular waves. Kazeminezhad and Etemad-Shahidi (2015) have recently re-analysed several datasets and presented alternative formulations in which pre-calculation of the wave kinematics is not necessary to assess the maximum wave run-up.

Numerical modelling of wave run-up around a monopile is also reported in literature. Christensen et al. (2005) described a study of the forces acting on a monopile caused by extreme waves propagating over a sloping bed. Numerical results were compared with analytical solutions and experiments and a good agreement was found. A numerical study with a 3-D ComFLOW model performed by Peng et al. (2012) reproduced experimental data measured by De Vos et al. (2007). A grid sensitivity study showed that a minimum grid size of $D/10$ was needed in the zones of interest (i.e. around the still water level and near the monopile with diameter D) to obtain a grid independent solution. The Courant-Friedrichs-Lewy (CFL) condition controlled the time step which may not exceed $T/100$ for accuracy purposes (where T is the wave period). The paper presented only absolute values of wave run-up and no comparisons with regard to time series were provided. The authors also mentioned that for large wave run-up, the numerical model slightly underestimates the measured run-up. Lara et al. (2013) presented a numerical simulation of a pile group subjected to waves using the IHFOAM toolbox. Only numerical results were presented which indicated that IHFOAM is a capable toolbox for analysing wave run-up around and wave-induced forces on offshore piles. Ransley et al. (2013) compared numerical results with experimental data for extreme wave impacts on a fixed truncated circular cylinder. The numerical solution was obtained without turbulence modelling but the authors expect that it plays an important role in (extreme) wave-structure interaction. El Safti et al. (2014) presented a hybrid 2D-3D CFD model to investigate wave forces on piled structures. In this study, turbulent effects were incorporated by using a one-equation eddy-viscosity Sub-Grid Scale (SGS) Large Eddy Simulation (LES) model. The authors' motivation to use LES was to include the effects of air compressibility during breaking wave impact on structures. Paulsen et al. (2014) analysed strong nonlinear forces caused by steep or breaking waves and ringing loads due to steep

nonlinear waves. Turbulence modelling was excluded because the forces acting on the monopile were mainly inertia dominated. A fair agreement was found between numerical and experimental data. Chen et al. (2014) investigated nonlinear wave interactions with offshore structures for different wave conditions. They concluded that OpenFOAM is suitable for accurate modelling of nonlinear wave interactions with monopiles. The time step was initially $0.01\ s$ and changed automatically to satisfy a maximum Courant number of 0.5. Grid convergence was reached for a horizontal and vertical resolution of respectively $L/70$ and $H/8$ (with a refinement factor of 2 around the still water level and the monopile; where L is the wave length and H is the wave height).

More recently, Kamath et al. (2015a,b) reported CFD results of wave interaction with multiple vertical cylinders. They performed simulations using a $k-\omega$ turbulence model and observed unphysical wave damping based on RANS turbulence modelling. Therefore, both eddy viscosity limiters and free surface turbulence damping at the interface were applied. This unphysical wave damping caused by RANS turbulence modelling is not only observed during CFD simulations of monopiles. Several other authors also reported wave damping when using CFD for wave modelling: Mayer and Madsen (2000), Jacobsen et al. (2012), Vanneste and Troch (2015) and Elhanafi et al. (2017).

In general, the majority of literature presents wave-induced forces acting on a monopile rather than wave run-up phenomena. Therefore, turbulence modelling was omitted and no indication of the influence of turbulence on wave run-up was given. However, some authors reported the necessity of using a turbulence model. For example Higuera et al. (2013a,b) applied both $k-\varepsilon$ and $k-\omega\ SST$ turbulence models since they are widely used. Furthermore, turbulence modelling is needed in the case of significant vortex shedding or when wave breaking occurs around the monopile due to even steeper waves. This can happen when irregular waves are generated, then energy is transferred between the different frequencies increasing the wave height at a particular time instant and at a certain location. If that location is close to the monopile, waves can break and prominent vortex shedding can occur. This paper will tackle the implementation of a suitable turbulence model in order to simulate properly wave propagation in a numerical wave flume and wave run-up around a monopile. In general, non-breaking waves induce a very low level of turbulence. However, when the wave-induced flow encounters an object, a monopile in this case, the flow is disturbed and becomes turbulent. For the waves studied in this research, the Reynolds (Re) number and Keulegan-Carpenter (KC) number vary from 4.65×10^4 to 5.84×10^4 and from 4.26 to 5.17 respectively. According to Sumer and Fredsøe (1997), a pair of asymmetric vortices will develop resulting in a turbulent flow around the monopile. Moreover, even if the KC numbers are small for the waves studied, the boundary layer around the monopile may be turbulent.

We present a study of wave run-up around a monopile subjected to regular waves using the Computational Fluid Dynamics (CFD) toolbox OpenFOAM® (2013). Reynolds-Averaged Navier-Stokes (RANS) turbulence modelling is performed by applying the $k-\omega\ SST$ model. Sometimes, this RANS approach causes excessive wave damping (i.e. a significant decrease in wave height over the length of the

numerical wave flume). Therefore, a buoyancy term is implemented in the turbulent kinetic energy (TKE) equation of the $k-\omega\ SST$ model. The idea of adding a buoyancy term is taken from Van Maele and Merci (2006a) who modify the $k-\varepsilon$ model to simulate buoyant plumes. These fire-induced flows are characterised by continuous density variations. For water waves, the density is discontinuous at the free water surface resulting in an infinite density gradient. However, when a Volume of Fluid (VoF) method is applied for wave modelling, the density gradient is smeared out over several cells leading to a continuous change in density around the air-water interface. Consequently, the change in density around the interface between water and air is similar to the change in density observed in fire flows. As a result of implementing a buoyancy term, an overall stable wave propagation model without significant wave damping over the length of the flume is obtained. Numerical simulations are performed and compared with two different sets of wave parameters described in the laboratory study of De Vos et al. (2007).

The remainder of this paper is organised as follows. Firstly, in section 2.2, the previous experimental study by De Vos et al. (2007) is introduced. In section 2.3, the governing equations for the numerical model are presented, followed by a description of the computational domain, the boundary conditions applied and the solver settings. Subsequently in sections 2.4 and 2.5, the numerical model is used to perform several simulations while in section 2.6 the obtained results are discussed in detail. Finally, the conclusions and future work are drawn in section 2.7.

2.2 Previous experimental study

In this research, data is reused from a laboratory study by De Vos et al. (2007) conducted in a wave flume at Aalborg University, Denmark. The flume has a length of $30\ m$, a width of $1.5\ m$ and a height of $1\ m$. The pile diameter was $0.12\ m$ whereas a constant water depth of $0.50\ m$ was maintained during regular wave tests. The offshore slope was held constant at $1:100$ and will be neglected in the present numerical study because shoaling effects are negligible.

A definition sketch of the wave gauges' position to measure wave run-up around the monopile is given in Figure 2.1. Herein, nine wave gauges are installed $2\ mm$ away from the monopile's surface. The position of the wave gauges is an important parameter to determine wave run-up. Therefore, the position of the numerical wave gauges is the same as the ones installed in the experimental flume. The nine wave gauges are characterised by their angle with respect to the incoming waves of respectively $0°$, $22.5°$, $45°$, $67.5°$, $90°$, $112.5°$, $135°$, $157.5°$ and $180°$, as depicted in Figure 2.1.

2.3 Numerical model

The numerical simulations presented are achieved using OpenFOAM® (2013), version 2.2.2. Firstly, the flow equations are introduced with emphasis on the turbulence model. Subsequently, the computational domain is presented together with

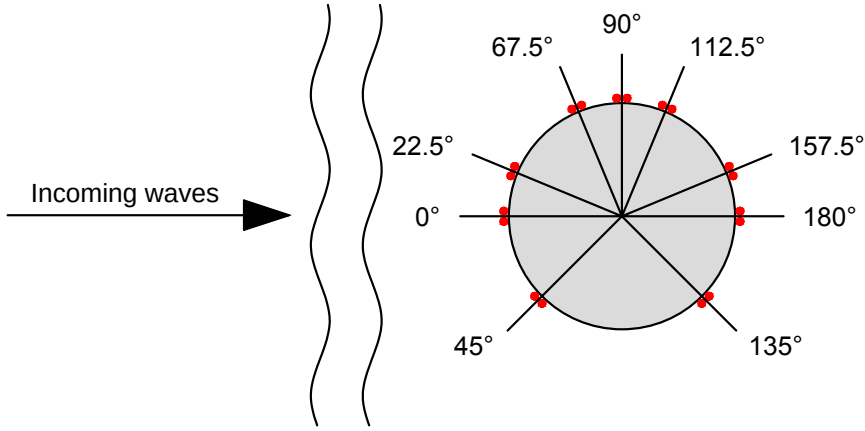

Figure 2.1: Position of the nine wave gauges (two dots per gauge) around the monopile where each wave gauge is characterised by its angle with respect to the direction of the incoming waves. The wave gauges are installed $2\ mm$ away from the monopile's surface (adapted from De Vos et al. (2007)).

the grid characteristics. The last two parts of this section are dedicated to explain the different boundary conditions and solver settings.

2.3.1 Flow equations

The numerical model uses the incompressible RANS equations to express the motion of a fluid consisting of a mass conservation equation (2.1) and a momentum conservation equation (2.2) written in Einstein summation notation as:

$$\frac{\partial u_i}{\partial x_i} = 0 \tag{2.1}$$

$$\frac{\partial \rho u_i}{\partial t} + \frac{\partial \rho u_j u_i}{\partial x_j} - \frac{\partial}{\partial x_j}\left[\mu_{eff}\frac{\partial u_i}{\partial x_j}\right] = -\frac{\partial p^*}{\partial x_i} + F_{b,i} + f_{\sigma,i} \tag{2.2}$$

in which u_i $(i = x, y, z)$ are the Cartesian components of the fluid velocity, ρ is the fluid density, μ_{eff} is the effective dynamic viscosity, p^* is the pressure in excess of the hydrostatic, F_b is an external body force (including gravity) and f_σ is the surface tension tensor term which will be neglected. Note that the mean values for the variables considered are written in terms of Favre-averaging (density weighted) due to the varying density.

The interface between water and air is obtained by the Volume of Fluid (VoF) method (Hirt and Nichols, 1981). The method is based on a volume fraction α which is 0 for a completely dry cell and 1 for a completely wet cell and in between

0 and 1 for an interface cell containing both water and air. The volume fraction is solved by an advection equation (2.3):

$$\frac{\partial \alpha}{\partial t} + \frac{\partial u_i \alpha}{\partial x_i} + \frac{\partial u_{c,i} \alpha \left(1-\alpha\right)}{\partial x_i} = 0 \tag{2.3}$$

The last term on the left-hand side is an artificial compression term where $u_{c,i} = \min[c_\alpha |u_i|, \max(|u_i|)]$. In the present study, the default value of c_α equal to 1 is applied. If a larger value is used, the compression of the interface increases, leading to larger detrimental velocity gradients around that interface.

The density of the fluid ρ within a computational cell is calculated by a weighted value based on the volume fraction α. The effective dynamic viscosity μ_{eff} is obtained by the sum of a weighted value based on the volume faction α and an additional turbulent dynamic viscosity $\rho\nu_t$:

$$\rho = \alpha\rho_{water} + (1-\alpha)\rho_{air} \tag{2.4}$$

$$\mu_{eff} = \alpha\mu_{water} + (1-\alpha)\mu_{air} + \rho\nu_t \tag{2.5}$$

In a post processing step, the position of the free water surface is determined by a discrete integration of the volume fraction α over a vertical line (Z-direction) divided in n equal parts:

$$z_{water\ level} = \sum_{i=0}^{n-1} \alpha_i (z_{i+1} - z_i) \tag{2.6}$$

2.3.2 Turbulence modelling

Turbulent effects are incorporated in the RANS equations (2.1) and (2.2) by solving one or more additional transport equations to yield a value for the turbulent kinematic viscosity ν_t. The $k-\omega\ SST$ turbulence model is applied in all the simulations presented. $k-\omega\ SST$ has shown good results in literature to simulate the flow around circular cylinders and two-phase flows. For example, Rahman et al. (2008) mentioned that the $k-\omega\ SST$ turbulence model is much more recommendable for high Reynolds numbers in a uniform free stream flow passing a 2D cylinder. Moreover, it has an adequate boundary layer treatment. Brown et al. (2014) evaluated different RANS turbulence models for spilling breakers and concluded that the $k-\omega\ SST$ model performs best for wave elevation predictions.

The incompressible $k-\omega\ SST$ model for a single fluid is a two-equation model (Menter et al., 2003) and is formulated in OpenFOAM as:

$$\frac{\partial k}{\partial t} + \frac{\partial u_j k}{\partial x_j} - \frac{\partial}{\partial x_j}\left[\left(\nu + \sigma_k \nu_t\right)\frac{\partial k}{\partial x_j}\right] = P_k - \beta^* \omega k \tag{2.7}$$

Table 2.1: Default values for ϕ_1 and ϕ_2 used in equation (2.10) to calculate σ_k, σ_ω, β and γ for the $k-\omega\ SST$ turbulence model.

ϕ	σ_k	σ_ω	β	γ
ϕ_1	0.85034	0.5	0.075	0.5532
ϕ_2	1.0	0.85616	0.0828	0.4403

$$\begin{aligned}\frac{\partial \omega}{\partial t}+\frac{\partial u_j \omega}{\partial x_j}-\frac{\partial}{\partial x_j}\left[\left(\nu+\sigma_\omega \nu_t\right)\frac{\partial \omega}{\partial x_j}\right]\\ =\frac{\gamma}{\nu_t}G-\beta\omega^2+2\left(1-F_1\right)\frac{\sigma_{\omega 2}}{\omega}\frac{\partial k}{\partial x_j}\frac{\partial \omega}{\partial x_j}\end{aligned} \tag{2.8}$$

$$\begin{aligned}P_k &= \min(G,\ 10\beta^* k\omega)\\ G &= \nu_t \frac{\partial u_i}{\partial x_j}\left(\frac{\partial u_i}{\partial x_j}+\frac{\partial u_j}{\partial x_i}\right)\\ \nu_t &= \frac{a_1 k}{\max(a_1\omega,\ SF_2)}\end{aligned} \tag{2.9}$$

where k is the turbulent kinetic energy, P_k is the production term of k, ν is the kinematic viscosity, ν_t is the turbulent kinematic viscosity, ω is the specific dissipation rate, S is the mean rate of strain of the flow, $\beta^*=0.09$, $a_1=0.31$, F_1 and F_2 are blending functions. The values of σ_k, σ_ω, β and γ are blended using equation (2.10) in which ϕ_1 and ϕ_2 are given in Table 2.1.

$$\phi = F_1\phi_1+(1-F_1)\phi_2 \tag{2.10}$$

Alternative turbulence models, such as $k-\varepsilon$ and $k-\omega$, were also tested in this study but they caused more wave damping over the length of the wave flume compared to $k-\omega\ SST$. Furthermore, application of LES obliges very fine grids in order to resolve $80\ \%$ of the turbulence resulting in longer simulation times. Therefore, RANS modelling with the $k-\omega\ SST$ model is selected.

However, for high steepness waves, even the original $k-\omega\ SST$ model causes significant wave damping. This damping is triggered by an increase in turbulent viscosity around the interface between water and air. This increase is induced by the large production of turbulent kinetic energy, k, in that zone. The production of k is linked to the velocity gradient which is large around the interface between water and air due to the large density ratio $(1000/1)$. Two important insights are made according to the original $k-\omega\ SST$ model implemented in OpenFOAM, equations (2.7) and (2.8):

1. The first one is already reported by Brown et al. (2014). None of the incompressible solvers implemented in OpenFOAM, including two-phase flow,

explicitly comprise the density. Only the turbulent kinematic viscosity ν_t is modelled rather than the dynamic viscosity $\mu_t = \rho\nu_t$. In a two-phase flow, the density varies around the interface between water and air which should therefore be included in the turbulence equations.

2. As mentioned in Van Maele and Merci (2006a), a buoyancy term is needed in order to take the varying density around the air-water interface into account. The buoyancy term is only included in the turbulent kinetic energy (TKE) equation based on the Standard Gradient Diffusion Hypothesis (SGDH) where the density ratio is neglected. This density ratio is $1000/1$ for water and air and could lead to instabilities in the solution method of this study. Moreover, Van Maele and Merci (2006a) reported that the influence of buoyancy on the ε-equation (cfr. ω-equation) is negligible if the SGDH is used. However, neglecting buoyancy in the TKE-equation is influencing the results significantly. The more advanced Generalized Gradient Diffusion Hypothesis (GGDH) leads to failing simulations during this research due to an instability in the TKE-equation.

Based on those two insights, a modified $k-\omega\ SST$ model is implemented in OpenFOAM® (2013) to prevent significant wave damping over the length of the wave flume. Firstly, the density ρ is explicitly implemented in both equations (2.11) and (2.12) of the $k-\omega\ SST$ turbulence model to take its variability around the air-water interface into account. Secondly, a buoyancy term G_b described by the SGDH, equation (2.13), is added to the TKE-equation (2.11). The final equations for this buoyancy-modified $k-\omega\ SST$ turbulence model are formulated as follow:

$$\frac{\partial \rho k}{\partial t} + \frac{\partial \rho u_j k}{\partial x_j} - \frac{\partial}{\partial x_j}\left[\rho\left(\nu + \sigma_k \nu_t\right)\frac{\partial k}{\partial x_j}\right] = \rho P_k + G_b - \rho\beta^* \omega k \tag{2.11}$$

$$\begin{aligned}\frac{\partial \rho \omega}{\partial t} + \frac{\partial \rho u_j \omega}{\partial x_j} - \frac{\partial}{\partial x_j}\left[\rho\left(\nu + \sigma_\omega \nu_t\right)\frac{\partial \omega}{\partial x_j}\right] \\ = \frac{\gamma}{\nu_t}\rho G - \rho\beta\omega^2 + 2\left(1 - F_1\right)\rho\frac{\sigma_{\omega 2}}{\omega}\frac{\partial k}{\partial x_j}\frac{\partial \omega}{\partial x_j}\end{aligned} \tag{2.12}$$

$$G_b = -\frac{\nu_t}{\sigma_t}\frac{\partial \rho}{\partial x_j} g_j \tag{2.13}$$

in which the buoyancy term G_b is treated implicitly, the scalar $\sigma_t = 0.85$ and vector $g = [0\ ;\ 0\ ;\ -9.81]\ m/s^2$. The value of σ_t decides how much buoyancy is modelled and is kept constant during all the simulations presented. It is beyond the scope of this research to find the optimal value of σ_t to return the most accurate results. The purpose of including a buoyancy term in this study is to suppress the turbulence level at the free water surface, i.e. in the zone where a vertical density gradient exists. Because of the implicit treatment of the buoyancy term G_b in the TKE-equation, the very large vertical density gradient near the free water

surface drives the turbulent viscosity ν_t to zero. This is demonstrated in Figure 2.5 and Figure 2.7 later in this paper. As a result, in case of propagating waves, the model switches to the laminar regime near the free water surface, preventing excessive wave damping. Please note that in the zone of e.g. breaking waves with a more horizontal density gradient, the original turbulence model will be recovered, as $G_b = 0$.

2.3.3 Computational domain

Because the geometry of the experimental wave flume is symmetrical around its length axis, only one half of the wave flume is modelled in the numerical model. As mentioned in Section 2.1, a pair of asymmetric vortices will develop but no vortex shedding is expected. Therefore, preliminary simulations are performed without the symmetry plane, by modelling the full domain. As a result, no differences in the wave run-up pattern around the monopile are observed. Moreover, Saghafian et al. (2003) reported small lift forces when the KC number is smaller than 6 for a Reynolds number of $11\ 240$. Furthermore, vortex shedding become prominent if $\mathrm{KC} > 7$. Consequently, only simulations using a symmetry plane are presented. Figure 2.2 shows a plan view of the computational domain together with the boundary conditions types which are listed in the next Section 2.3.4. As mentioned before, the bottom of the numerical domain is flat. The height of the numerical wave flume is $0.80\ m$ in the Z-direction. The initial condition consists of a water depth of $0.50\ m$ for which the volume fraction α equal to 1 and on top $0.30\ m$ air for which α is equal to 0.

It is important to stress that the length of the numerical flume ($L = 20\ m$) is reduced compared to the length of the experimental flume ($L = 30\ m$). Moreover, the pile was not placed in the centre of the experimental wave flume (in longitudinal direction) whereas in the numerical setup, the pile is placed centrally in the computational domain. The length of the numerical wave flume is chosen to allow a few wave lengths inside the flume to assess the quality of propagating water waves using the buoyancy-modified $k-\omega\ SST$ turbulence model.

After discretisation, the largest size of a cell in the vertical Z-direction Δz is $0.04\ m$ $(H/3)$ for the coarsest mesh. Thereafter, the mesh is locally refined in all directions in a zone where the free water surface will be located, resulting in $\Delta z = 0.02\ m$ $(H/6)$. Next, the zone close to the monopile is refined, but only in the vertical direction, leading to $\Delta z = 0.01\ m$ $(H/12)$. The sizes of each cell in X- and Y-direction are based on a maximum aspect ratio (i.e. ratio of largest dimension of a cell over the smallest dimension) of about 2.5. The final grid is presented in Figure 2.3, which is the coarsest grid for all the simulations performed (case 1) and consists of $397\ 484$ cells. Additionally, two more simulations are performed: all cells of case 1 are refined in all directions resulting in case 2 and all cells of case 2 are refined again leading to case 3. During such a refinement, one cell is split up in eight equal cells. A summary of the three cases is given in Table 2.2. The consecutives lines for each case in column two and three give the cell size for the coarsest part, the zone in which the free water surface will be located and the zone around the monopile respectively.

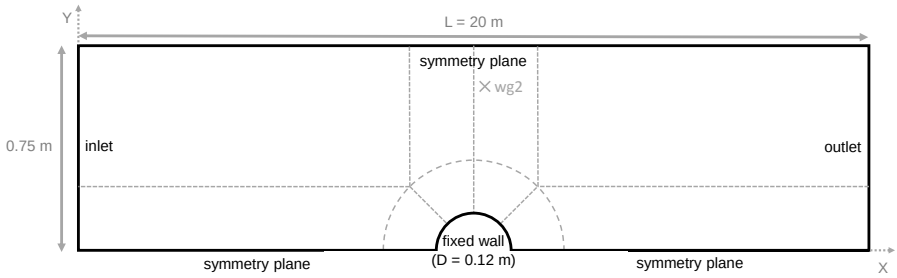

Figure 2.2: Definition sketch of the geometry of the computational domain in plan view (XY-direction). The dashed lines inside the geometry indicate the internal grid structure whereas the black words characterise the boundary condition type. wg2 ($x = 10.08\ m$, $y = 0.43\ m$) is a wave gauge used for checking the incoming wave field.

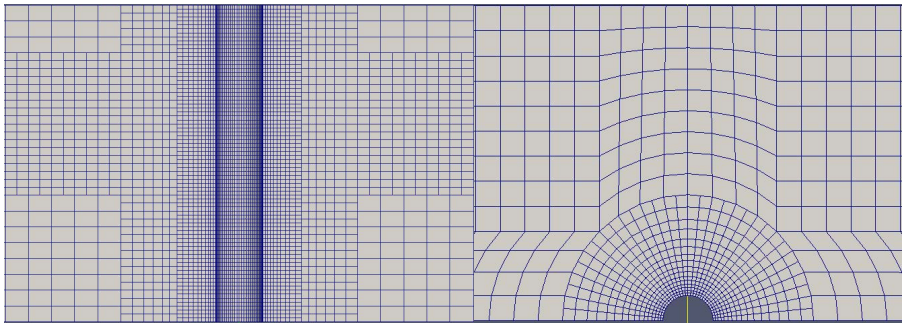

(a) **(b)**

Figure 2.3: (a) Detail of the longitudinal cross section parallel to the XZ-plane through the centre of the monopile. (b) Detailed plan view (XY-direction) around the monopile.

Table 2.2: Grid characteristics of the three different cases used. For each case, the first line indicates the overall discretisation. The second line shows the additional refinement in a zone where the free water surface will be located. Finally, the third line shows the final discretisation around the monopile.

case	maxΔx and maxΔy	maxΔz	cells
1	$0.10\ m$	$0.04\ m\ (H/3)$	397 484
	$0.05\ m$	$0.02\ m\ (H/6)$	
	$0.05\ m$	$0.01\ m\ (H/12)$	
2	$0.05\ m$	$0.02\ m\ (H/6)$	3 179 872
	$0.025\ m$	$0.01\ m\ (H/12)$	
	$0.025\ m$	$0.005\ m\ (H/24)$	
3	$0.025\ m$	$0.01\ m\ (H/12)$	25 418 496
	$0.0125\ m$	$0.005\ m\ (H/24)$	
	$0.0125\ m$	$0.0025\ m\ (H/48)$	

2.3.4 Boundary conditions

The types of boundary conditions in a horizontal plane are given in Figure 2.2: inlet on the left, outlet on the right, symmetry plane for the side wall and fixed wall for the monopile. The top of the computational domain is represented by an atmospheric condition while the bottom is a fixed wall.

Two solid walls are modelled, the bottom and the monopile's surface. On both walls, wall functions are activated for k and ω according to the $k-\omega\ SST$ turbulence model. A continuous wall function based on Spalding's law (Spalding, 1961) switching between low- and high-Reynolds numbers is implemented for the turbulent viscosity. By using this particular scalable wall function, the dimensionless wall distance y^+ should be between 1 and 300. On the walls, a Dirichlet boundary condition is set for the velocity ($0\ m/s$ in the three directions) while the pressure and volume fraction are set to a Neumann condition. The atmospheric conditions at the top of the numerical domain are set to a mixed Dirichlet-Neumann boundary condition for the velocity, pressure and volume fraction. The side wall of the wave flume is implemented as a symmetry plane and not as a physical wall to avoid the use of wall functions. This approximation is justified because the ratio of the flume width to the pile diameter (W/D) is 12.5, which is larger than 6 to avoid side-effects of that wall (Whitehouse, 1998).

At the inlet and outlet, special boundary conditions are needed to generate and absorb waves. Therefore, IHFOAM (Higuera et al., 2013a,b) is deployed as an external toolbox for those boundary conditions. At the inlet, wave generation together with active wave absorption is activated whereas only wave absorption is implemented at the outlet. The implemented wave absorption in IHFOAM is developed by assuming shallow water conditions. However, the waves studied in the present work are close to deep water waves. As mentioned in Higuera et al. (2013a), the absorption function works relatively well outside its range of applicability. Moreover, the reflection coefficient is not below $10\ \%$ in experimental laboratories as reported by Cruz (2008). Therefore, it is difficult to compare results when the reflection coefficient is not equal between experimental and numerical setups. The difference between experimental and numerical wave reflection has to be taken into account during the discussion of the results.

During the regular wave tests in the laboratory, wave heights between $0.01\ m$ and $0.26\ m$ were generated, with a wave period between $0.40\ s$ and $2.78\ s$ resulting in a minimum and maximum wave steepness s of 0.03 and 0.07 respectively. Two regular wave trains with a wave steepness of 0.04 and 0.07 are selected to perform numerical simulations. The wave parameters consist of a fixed wave height H equal to $0.12\ m$ and a wave period T equal to $1.60\ s$ and $1.05\ s$ for wave train 1 and 2 respectively. The water depth d is fixed to $0.50\ m$. According to Le Méhauté (1969), a 5th order Stokes theory is sufficiently accurate for all the test cases presented.

2.3.5 Solver settings

For all the simulations presented, the following solver settings are used: central discretisation for the pressure gradient and the diffusion terms; TVD (total variation diminishing) schemes with a van Leer limiter (van Leer, 1974) for the divergence operators; backward Euler time discretisation; a maximum Courant number of 0.75.

2.4 Results empty wave flume

Preliminary simulations are performed in an empty wave flume (i.e. without monopile) in order to assess the quality of the undisturbed propagating wave field over the length of the flume. Therefore, regular waves are generated at the inlet featuring the same wave height and period as the waves used for the study of wave run-up around a monopile.

The two-dimensional (XZ-plane) computational domain is discretised according to the values presented in Table 2.2. Only the vertical refinement around the monopile is excluded for the empty wave flume simulations (third line for every case). The total number of cells is equal to $9\ 400$, $37\ 600$ and $150\ 400$ for case 1, case 2 and case 3 respectively. For each case, three simulations are performed using the original turbulence model, the buoyancy-modified turbulence model and a laminar model applying the same numerical settings. The laminar result is used as a reference solution because no turbulence is assumed during wave propagation. Moreover, the laminar result will show that numerical damping based on RANS turbulence modelling is dominating over possible damping due to the VoF method applied or integration of the RANS equations.

In the following two subsections, time series are provided at particular locations along the flume: $x = 1\ m$, $x = 3\ m$, $x = 5\ m$, $x = 10\ m$, $x = 15\ m$, $x = 17\ m$ and $x = 19\ m$. The vertical axis denotes the surface elevation η with respect to the bottom ($z = 0\ m$) and the horizontal axis denotes the time for three wave periods after the warming-up phase. Additionally, the turbulent viscosity ν_t is visualised for both the original and buoyancy-modified turbulence model. Only the results of case 2 (see Table 2.2) are presented since they are already grid independent.

2.4.1 Wave train 1

This first subsection presents the results of the empty wave flume using the first regular wave train ($H = 0.12\ m$, $T = 1.60\ s$, $d = 0.50\ m$). The wave steepness s is 0.04 and those waves are classified as rather low steepness waves. Figure 2.4 depicts surface elevations in the empty wave flume for a laminar solution, the original and buoyancy-modified turbulence model. All three simulations return the same time signal at the start of the flume ($x = 1\ m$). Moving towards the end of the flume, small discrepancies in the surface elevation are visible between the original turbulence model and both the laminar model and buoyancy-modified turbulence model. Only a phase shift is observed but the wave height remains constant. As a conclusion, Figure 2.4 clearly indicates that there is no significant wave damping over the length of the flume based on RANS turbulence modelling

for the case of low steepness waves.

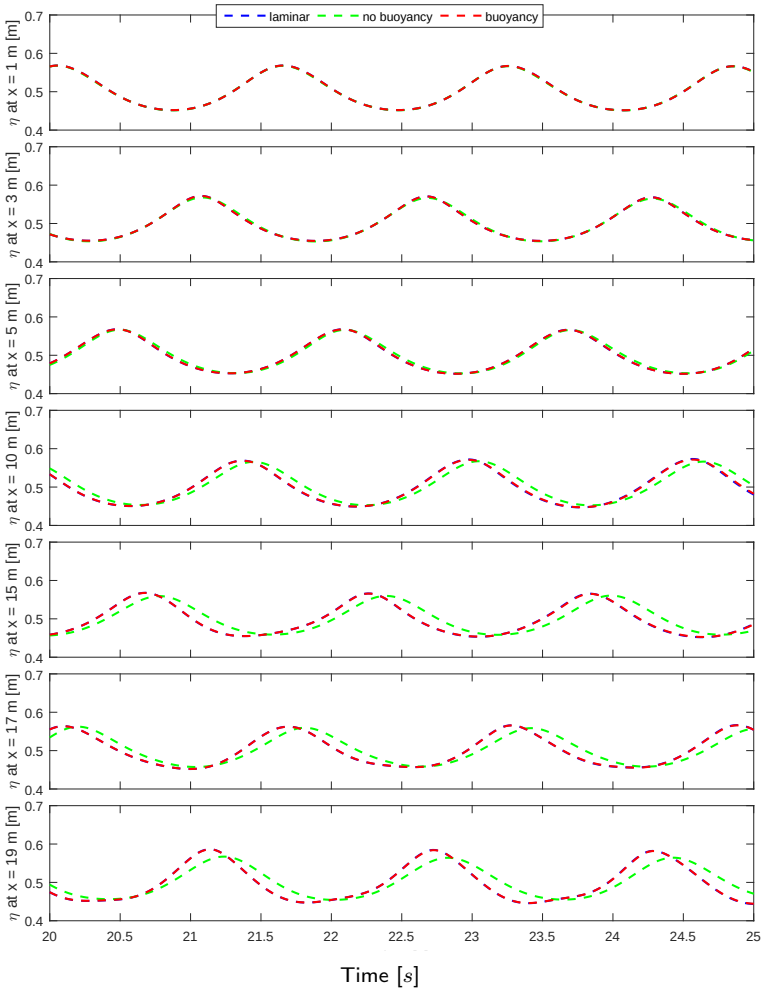

Figure 2.4: Time series of the surface elevation η with respect to the bottom ($z = 0\ m$) from the start ($x = 1\ m$) towards the end ($x = 19\ m$) of the empty wave flume (case 2) for a laminar solution and solutions without and with buoyancy using regular waves: $H = 0.12\ m$, $T = 1.60\ s$, $d = 0.50\ m$.

The turbulent viscosity ν_t for one wave length at the start of the flume is depicted in Figure 2.5 for both the original and buoyancy-modified turbulence model respectively. The white solid line visualises the location of the free water surface. It is clearly observed that the turbulent viscosity around the free water surface is a few orders of magnitudes larger for the original turbulence model compared to the buoyancy-modified one. However in the case of low steepness waves, this increased viscosity at the free water surface is not affecting the wave height along the length

of the wave flume (see Figure 2.4).

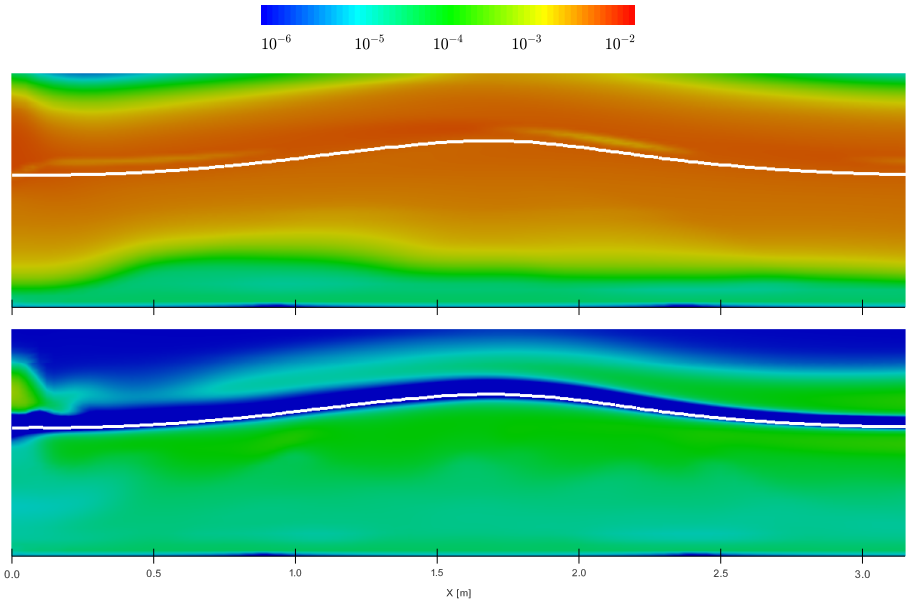

Figure 2.5: Contour plot of the turbulent kinematic viscosity ν_t $[m^2/s]$ for one wave length (low steepness waves) at the start of the wave flume ($x = 0\ m$) using a logarithmic scale ($t = 22\ s$): buoyancy term excluded (top panel) and buoyancy included in the TKE-equation (bottom panel). The white solid line indicates the free water surface.

2.4.2 Wave train 2

This second subsection gives the results of the empty wave flume for the second regular wave train ($H = 0.12\ m$, $T = 1.05\ s$, $d = 0.50\ m$). The wave steepness s is now equal to 0.07 and those waves are classified as high steepness waves. Figure 2.6 depicts surface elevations in the empty wave flume for a laminar solution, the original and buoyancy-modified turbulence model. Close to the wave generation boundary ($x = 1\ m$), the time signal is identical for all the simulations. However, along the length of the flume, a significant decrease of the wave height is observed in case buoyancy is excluded. This damping is not caused by the VoF method since the laminar solution does not show any wave damping. When the buoyancy term is activated, the amplitudes of the surface elevation are close to the laminar solution and do not show any decrease in wave height along the flume. As a conclusion, Figure 2.6 strongly proves that including a buoyancy term is necessary in order to simulate properly propagating high steepness water waves.

The turbulent viscosity ν_t for one wave length at the start of the flume is shown in Figure 2.7 for both the original and buoyancy-modified turbulence model respectively. It is clearly observed that the turbulent viscosity around the free

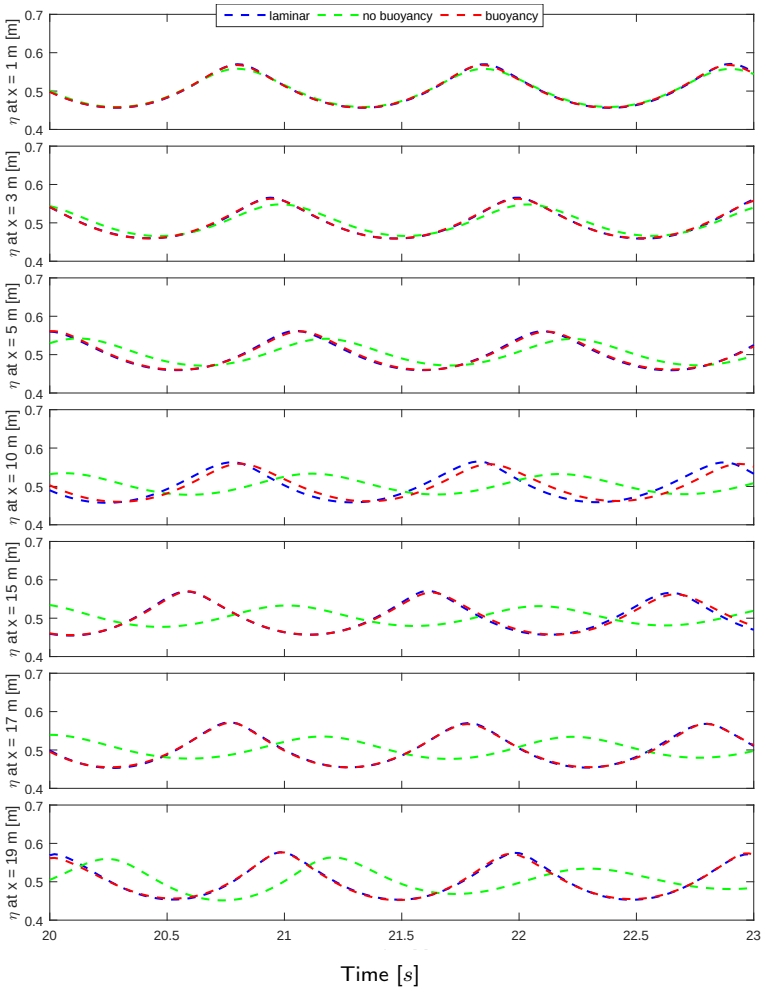

Figure 2.6: Time series of the surface elevation η with respect to the bottom ($z = 0\ m$) from the start ($x = 1\ m$) towards the end ($x = 19\ m$) of the empty wave flume (case 2) for a laminar solution and solutions without and with buoyancy using regular waves: $H = 0.12\ m$, $T = 1.05\ s$, $d = 0.50\ m$.

water surface (white solid line) is a few orders of magnitudes larger for the original turbulence model compared to the buoyancy-modified one. As a result for the high steepness waves, the increased viscosity at the free water surface has a significant influence on the wave height along the wave flume (see Figure 2.6). This increase in turbulent viscosity is the main reason for the observed wave damping. However, this wave damping is not observed in case the buoyancy term is included. As mentioned before, the buoyancy term drives the turbulent viscosity around the free water surface to zero and the model switches locally to the laminar regime,

preventing excessive wave damping.

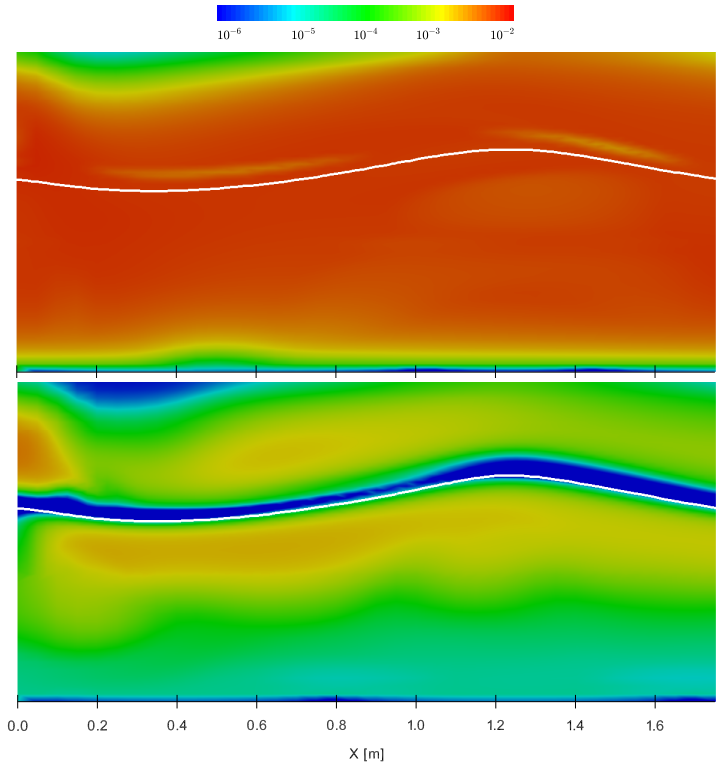

Figure 2.7: Contour plot of the turbulent kinematic viscosity ν_t $[m^2/s]$ for one wave length (high steepness waves) at the start of the wave flume ($x = 0\ m$) using a logarithmic scale ($t = 22\ s$): buoyancy term excluded (top panel) and buoyancy included in the TKE-equation (bottom panel). The white solid line indicates the free water surface.

2.5 Results wave run-up around a monopile

In this section, the numerical obtained wave run-up around a monopile is validated by using laboratory measurements from De Vos et al. (2007). Thereafter, a grid refinement study using the three cases as outlined in Table 2.2 is reported in order to verify the numerical results. Additionally, numerical results are tested against analytical formulations. Each numerical simulation ran for 20 seconds after the warming-up phase. For every simulation, the quality of the incoming wave field is checked against the experimental data at the location of wg2, see Figure 2.2. As a result, a very similar incoming wave field is observed between the numerical and experimental data.

In the following two subsections, time series of the wave run-up pattern around

a monopile are provided in which the vertical axis denotes the surface elevation η with respect to the bottom ($z = 0\ m$). In all the graphs, the horizontal axis denotes the time for three wave periods.

2.5.1 Wave train 1

This first subsection presents the results of wave run-up around a monopile using the first regular wave train ($H = 0.12\ m$, $T = 1.60\ s$, $d = 0.50\ m$). As reported in section 2.4.1, no significant wave damping over the length of the flume based on RANS turbulence modelling for the case of low steepness waves ($s = 0.04$) is expected. Therefore, the wave run-up pattern around a monopile is presented in the following two paragraphs for respectively excluding and including the buoyancy term.

2.5.1.1 Buoyancy term not included in the TKE-equation

The set of nine graphs displayed in Figure 2.8 shows the experimental and numerical wave run-up pattern around the monopile without including the buoyancy term in the TKE-equation. The maximum achieved y^+ on the monopile varies from 170 (case 1), 103 (case 2) down to 65 (case 3). Firstly, in general, the same trends in wave run-up are observed for the numerical and experimental data. However, the experimental signal at $112.5°$ is not reliable while the numerical model at that location returns plausible results. No reason is found or reported by De Vos et al. (2007) regarding this specific discrepancy. Moreover, Figure 2.8 clearly indicates that both the shape of the time signal and the local secondary peak in the surface elevation obtained with the numerical model are comparable to the experimental records. Secondly, the numerical solutions seem to be grid independent because the first two grids, case 1 and case 2, are presenting similar results. Interestingly, the numerical results of case 3, show larger discrepancies in the wave run-up pattern compared to case 1 and case 2. These differences are more significant in front of the monopile (angle wave gauge $< 90°$). It is also remarkable that the largest differences between cases 1 and 2 and case 3 are situated around the wave crest and not around the wave trough.

2.5.1.2 Buoyancy term included in the TKE-equation

In contrast to the previous paragraph, turbulence modelling is now applied by including the buoyancy term in the TKE-equation as formulated in section 2.3.2. The maximum value of y^+ on the monopile varies from 240 (case 1), 102 (case 2) down to 45 (case 3). Figure 2.9 presents the wave run-up pattern around the monopile for both the experimental and numerical model. In general, the numerical model captures the main effects of wave run-up relatively well. However, the time series indicate clearly that the peak values of the wave run-up are significantly larger in the numerical model compared to the experimental data. Although this difference, the shape, the secondary peak and the surface elevations around the trough are comparable to the experimental time series. Moreover, the solution seems to be grid independent because the three cases are presenting similar results.

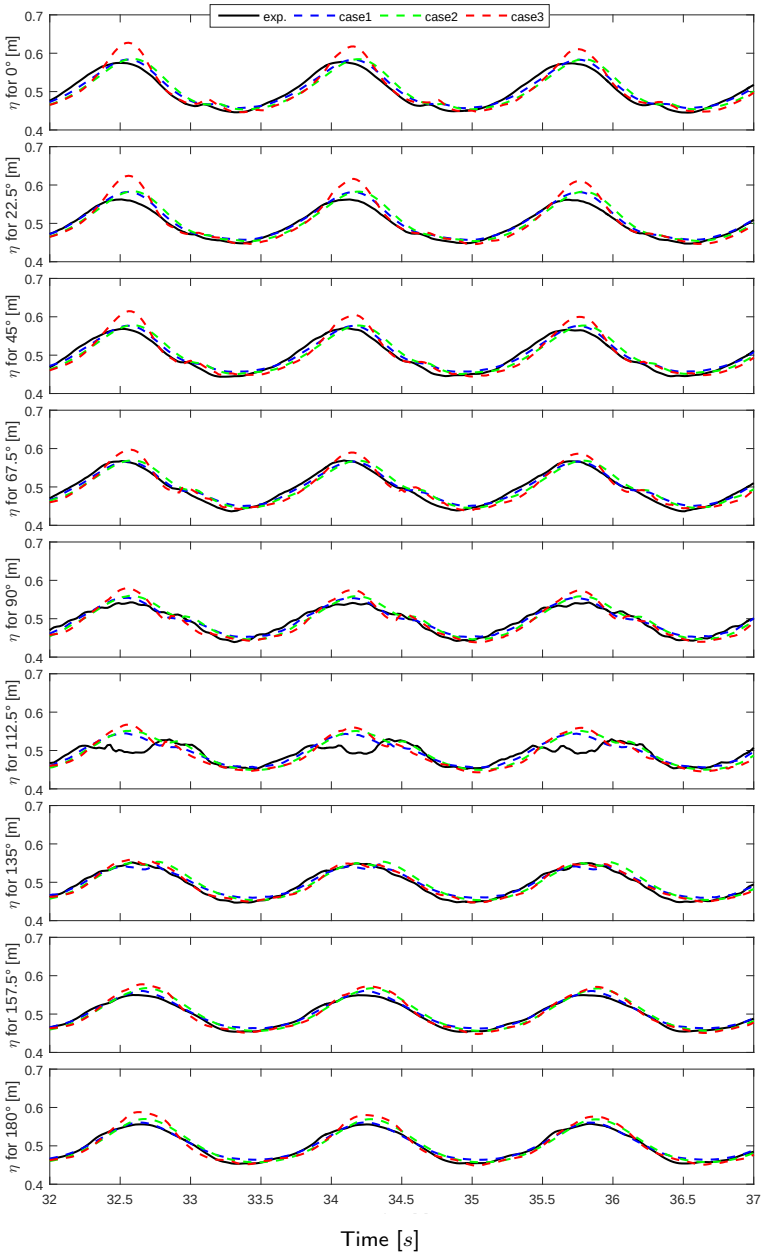

Figure 2.8: Time series of the wave run-up pattern around the monopile for the experimental data and cases 1, 2 and 3 for different angles of the gauge with respect to the incoming waves. The vertical axis expresses the position of the surface elevation η with respect to the bottom ($z = 0\ m$) for regular waves: $H = 0.12\ m$, $T = 1.60\ s$, $d = 0.50\ m$, in which the buoyancy term is not included in the TKE-equation.

This means that case 3 is not leading to deflected results as observed in the previous paragraph where buoyancy was not included in the TKE-equation.

2.5.2 Wave train 2

This second subsection gives the results of wave run-up around a monopile for the second regular wave train ($H = 0.12\ m$, $T = 1.05\ s$, $d = 0.50\ m$). As concluded in section 2.4.2, the buoyancy term is needed in the TKE-equation because excessive wave damping over the length of the flume is expected for the case of high steepness waves ($s = \ 0.07$). Because the incident wave heights are too small close to the monopile in case buoyancy is not activated, only numerical results including buoyancy are presented.

The set of nine graphs given in Figure 2.10 shows the experimental and numerical wave run-up around the monopile if the buoyancy term is included in the TKE-equation. y^+ on the monopile varies from maximal 300 (case 1), 130 (case 2) down to 70 (case 3). In general, the three numerical cases converge towards a grid independent solution and deliver a comparable output to the experimental results. For example, the local secondary peak in the surface elevation is observed in both numerical and experimental data. However, the peak values of the wave run-up in front of the monopile are sometimes overestimated by the numerical model. Furthermore, the experimental time signal at $90°$ is significantly different than the numerically obtained time signals. Several reason can be dedicated for this discrepancy as reported later on in section 2.6. Moreover, there are some contradictions between experimental and numerical records around the rear part of the monopile.

2.5.3 Grid refinement study

A grid refinement study using the three cases as outlined in Table 2.2 is performed. A summary is given in Table 2.3 for the low steepness waves (both original and buoyancy-modified turbulence model) and high steepness waves (buoyancy-modified turbulence model) respectively. The variable used for this analysis is the time-integral of the absolute value of the force on the monopile in X-direction over one wave period. This integration is performed when the first wave reaches the outlet boundary. This is needed because wave reflection is strongly dependent on the grid refinement of the mesh (cfr. reflection coefficients reported in section 2.6). The extrapolated values are computed with Richardson's extrapolation method: $F_{extra.} = F_{case\ 2} + (F_{case\ 3} - F_{case\ 2})/(1 - 2^{-\alpha})$ with $\alpha = \ln((F_{case\ 1} - F_{case\ 2})/(F_{case\ 2} - F_{case\ 3}))/\ln(2)$. $F_{extra.}$ can be regarded as the value calculated from the exact solution. As follows from Table 2.3, the solutions converge monotonically towards the exact solution.

2.5.4 Spatial resolution of wave run-up

In this subsection, high spatial resolutions of the wave run-up pattern around the monopile over one wave period obtained using the numerical model are presented together with the nine discrete experimental measurements and two analytical

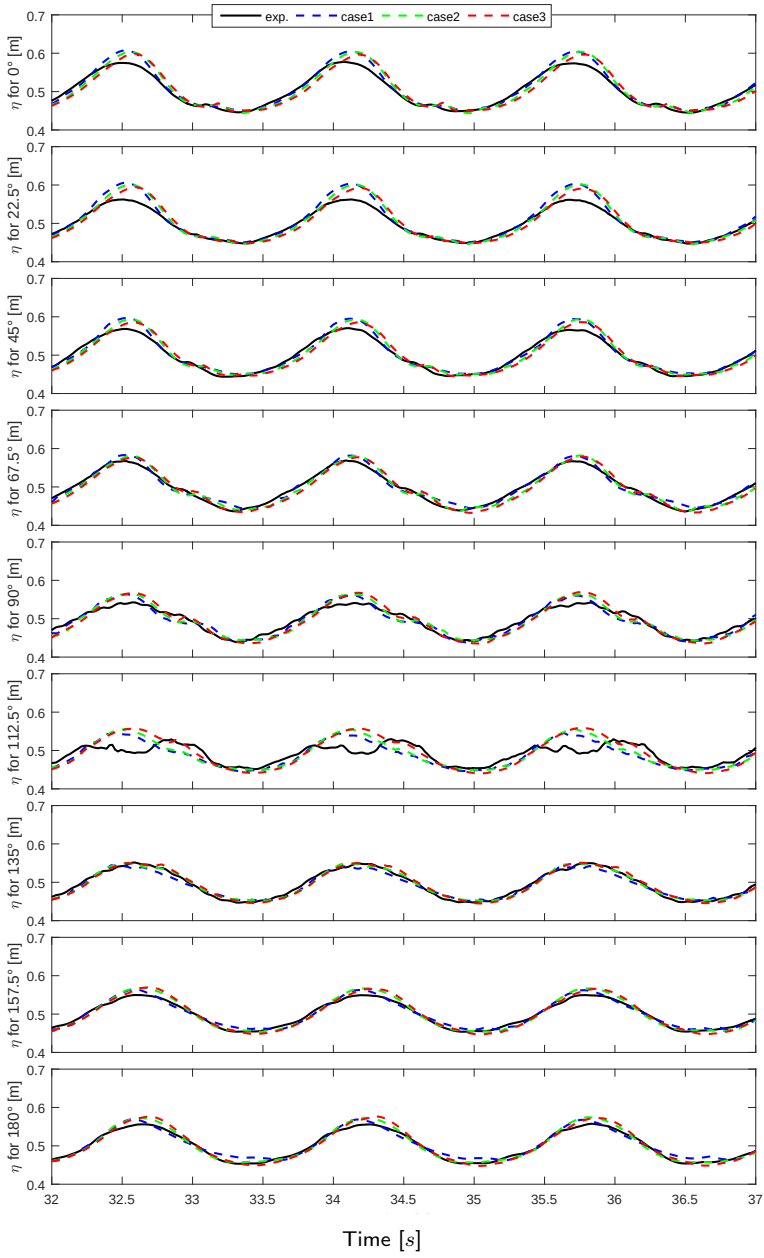

Figure 2.9: Time series of the wave run-up pattern around the monopile for the experimental data and cases 1, 2 and 3 for different angles of the gauge with respect to the incoming waves. The vertical axis expresses the position of the surface elevation η with respect to the bottom ($z = 0\ m$) for regular waves: $H = 0.12\ m$, $T = 1.60\ s$, $d = 0.50\ m$, in which the buoyancy term is included in the TKE-equation.

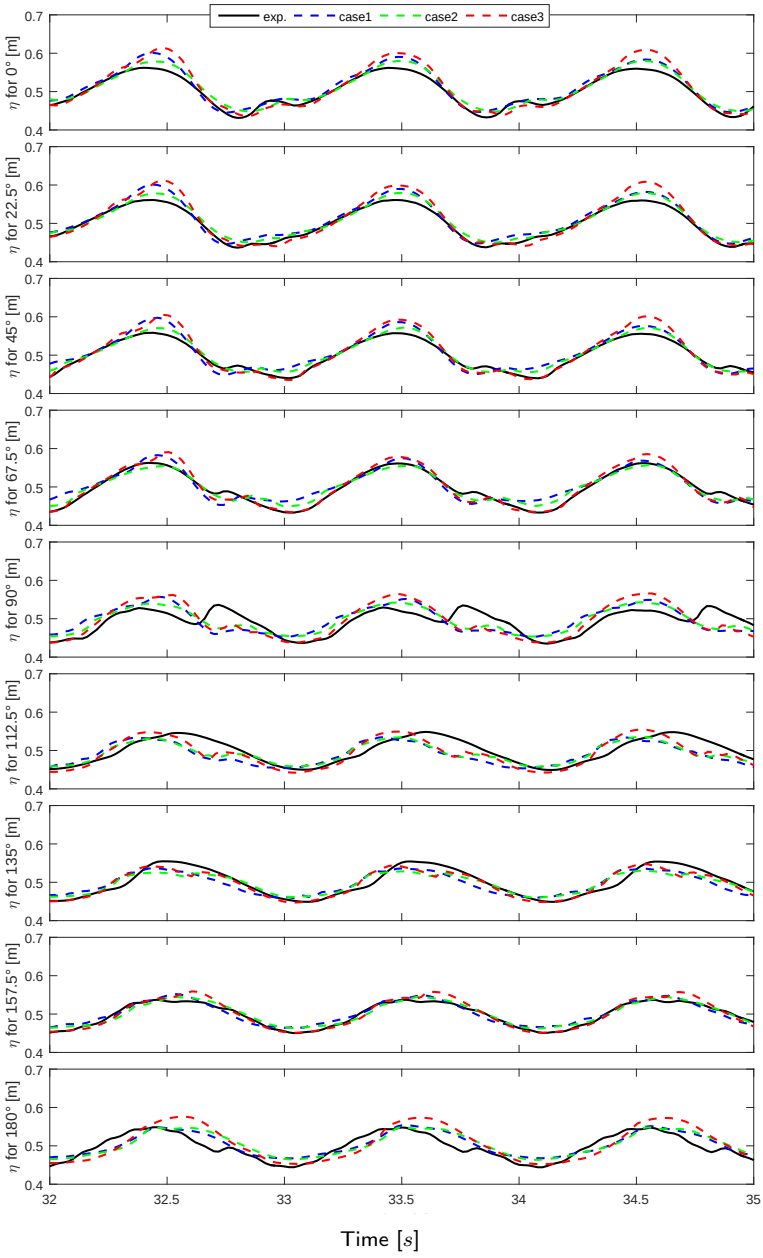

Figure 2.10: Time series of the wave run-up pattern around the monopile for the experimental data and cases 1, 2 and 3 for different angles of the gauge with respect to the incoming waves. The vertical axis expresses the position of the surface elevation η with respect to the bottom ($z = 0\ m$) for regular waves: $H = 0.12\ m$, $T = 1.05\ s$, $d = 0.50\ m$, in which the buoyancy term is included in the TKE equation.

Table 2.3: Grid refinement study for the low steepness waves using both the original and buoyancy-modified turbulence model and the high steepness waves using the buoyancy-modified turbulence model. N_z is the number of cells in vertical direction next to the cylinder. F is the time-integral of the absolute value of the force on the monopile in X-direction over one wave period when the first wave reaches the outlet boundary. $F_{extra.}$ is the exact solution.

Steepness		Low				High	
Buoyancy		No		Yes		Yes	
case	N_z	$F\ [Ns]$	error	$F\ [Ns]$	error	$F\ [Ns]$	error
1	80	4.921	3.59 %	4.917	5.07 %	4.016	9.94 %
2	160	5.048	1.10 %	5.108	1.38 %	4.448	0.25 %
3	320	5.087	0.34 %	5.160	0.38 %	4.459	0.01 %
$F_{extra.}$		5.104		5.179		4.459	

formulations. For the experimental dataset, only the maximum wave run-up at the wave gauge's locations over one wave period are shown.

The first analytical expression is reported by De Vos et al. (2007) and is used to calculate the maximum wave run-up around a monopile in case of regular waves:

$$R_u = \eta_{\max} + m\frac{U^2}{2g} \tag{2.14}$$

in which m is equal to 1, g is the gravitational constant ($9.81\ m/s^2$), $\eta_{\max}$ is the maximum surface elevation and U is the horizontal particle velocity at the wave crest. η_{max} and U are both based on the 2nd order Stokes wave theory. Secondly, Kazeminezhad and Etemad-Shahidi (2015) have recently re-analysed a few experimental datasets and came up with an alternative formulation for the maximum wave run-up level in case of regular waves:

$$\begin{aligned} R_u &= H\left(0.76\left(\frac{H}{d}\right)^{0.15}\left(\frac{H}{L_0}\right)^{-0.055}\right) && for\ \frac{H}{d} \leq 0.41 \\ R_u &= H\left(0.65\left(\frac{H}{L_0}\right)^{-0.055}\right) \\ &\quad + H\left(3.2\times10^{-3}\left(\frac{H}{d}-0.41\right)^{0.15}\left(\frac{H}{L_0}\right)^{-1.5}\right) && for\ \frac{H}{d} > 0.41 \end{aligned} \tag{2.15}$$

in which H is the wave height, d is the water depth and L_0 the deep water wave length.

The two formulations (2.14) and (2.15) lead respectively to a wave run-up level of $0.08\ m$ and $0.09\ m$ with respect to the still water level or an absolute value of $0.58\ m$ and 0.59 with respect to the bottom ($z = 0\ m$) for the first regular wave train ($H = 0.12\ m$, $T = 1.60\ s$, $d = 0.50\ m$). Figure 2.11 shows the wave run-up pattern around the monopile using the numerical model (case 2), the experimental obtained wave run-up (dots) and two analytical solutions (horizontal lines). In Figure 2.11a, the buoyancy term is not included whereas in Figure 2.11b that term is implemented in the TKE-equation. The output of the numerical model is represented by a series of grey lines, each characterising a specific point in time. The time step between two consecutive lines is $0.02\ s$. As Figure 2.11a suggests, the two analytical results are in line with the maximum surface elevation in front of the pile if the buoyancy term is excluded in the numerical model. Moreover, the numerical model shows a significant decrease in the peak value of the wave run-up around $135°$. Including buoyancy (Figure 2.11b) shows that the obtained wave run-up is in general higher but it is considerably higher in front of the monopile.

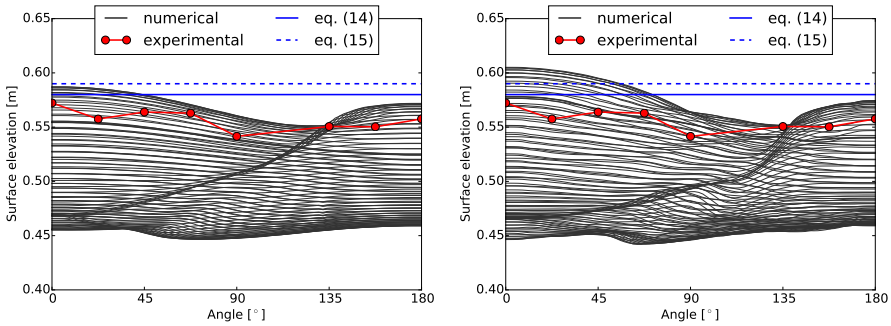

(a) **(b)**

Figure 2.11: Spatial variance of the wave run-up around the monopile for $y > 0$ over one wave period in function of the angle with respect to the incoming waves (wave train 1, case 2): (a) buoyancy term not included and (b) buoyancy term included in the TKE-equation.

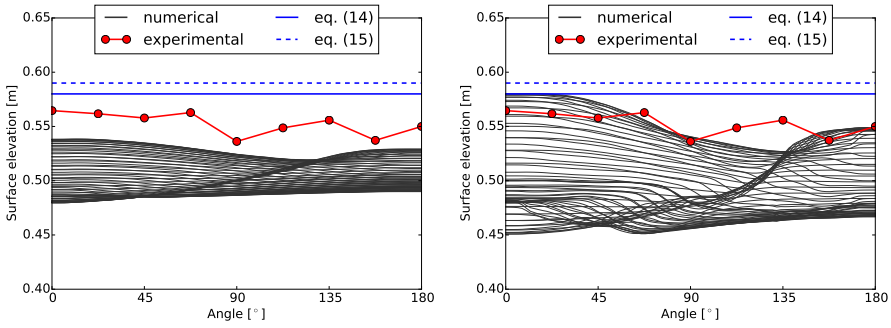

(a) **(b)**

Figure 2.12: Spatial variance of the wave run-up around the monopile for $y > 0$ over one wave period in function of the angle with respect to the incoming waves (wave train 2, case 2): (a) buoyancy term not included and (b) buoyancy term included in the TKE-equation.

In case of the second regular wave train ($H = 0.12\ m$, $T = 1.05\ s$, $d = 0.50\ m$), the run-up levels are $0.08\ m$ and $0.09\ m$ for equation (2.14) and (2.15) respectively. This results in absolute values with respect to the bottom ($z = 0\ m$) of $0.58\ m$ and $0.59\ m$ respectively. Figure 2.12 shows the wave run-up around the monopile for the numerical model (case 2), experimental tests (dots) and two analytical formulae (horizontal lines). Again, each grey line represents numerical data at a certain point in time every $0.02\ s$. Numerical results are obtained by excluding (Figure

2.12a) and including the buoyancy term in the TKE-equation (Figure 2.12b). If the buoyancy term is excluded (Figure 2.12a), wave run-up around the monopile is significant smaller than the experimental data and analytical solutions. This phenomenon is addressed to excessive wave damping over the length of the wave flume, as already discussed in Section 2.5.2. However, if the buoyancy term is modelled (Figure 2.12b), the two analytical solutions are in line with the maximum wave run-up in front of the pile. Again, the numerical model shows a significant decrease in the peak value of the wave run-up around $135°$.

2.6 Discussion

Two types of differences in the results are observed. The first one is the difference in numerical results by excluding or including the buoyancy term. For the case of low steepness waves, it is shown that the buoyancy term has only a small effect on the surface elevation over the length of the wave flume. However, there are some larger differences in wave run-up around the monopile between excluding or including the buoyancy term in the TKE-equation. For example, the surface elevations are larger in front of the monopile if buoyancy is taken into account. This observation is related to slightly less damping of the incident waves close to the monopile if buoyancy is modelled. For the case of high steepness waves, the buoyancy term is needed in order to avoid non-physical wave damping over the length of the flume.

The second type of differences is related to the deviations in surface elevations around the monopile between numerical and experimental data. Those deviations are largely assigned to the difference in reflection between the laboratory flume (with an absorbing beach) and the numerical wave flume (with a shallow water absorbing boundary condition). However, De Vos et al. (2007) did not report a value for the reflection coefficient of the absorbing beach in the experimental flume. In this study, the numerical reflection coefficient at the outlet is determined using four wave gauges (at positions $x_1 = 15.5\ m$; $x_2 = 15.808\ m$; $x_3 = 16.3\ m$; $x_4 = 16.5\ m$; all in the centre of the flume) (Lin and Huang, 2004). For the first wave train without modelling the buoyancy term, the obtained reflection coefficients are $6.4\ \%$, $5.9\ \%$ and $16\ \%$ for case 1, case 2 and case 3 respectively. In case buoyancy is activated for the first wave train, the reflection coefficients increase to $15\ \%$, $13\ \%$ and $11\ \%$ for case 1, case 2 and case 3 respectively. These latter values are higher, compared to those where buoyancy is neglected. By including buoyancy in the TKE-equation, less wave damping is observed along the flume, resulting in slightly higher waves reaching the outlet boundary. Because the absorbing correction velocity is directly related to the measured surface elevation at the outlet (Higuera et al., 2013a), the reflected waves are also larger. For the high steepness waves, the obtained reflection coefficients are $23\ \%$, $22\ \%$ and $26\ \%$ for case 1, case 2 and case 3 respectively (with buoyancy modelled). The reflection coefficients of this second wave train are significantly higher compared to the first wave train. These high steepness waves are even further away from the shallow water region compared to the low steepness waves, resulting in an inferior

performance of the shallow water absorbing boundary condition at the outlet.

In addition, there is also reflection at the inlet boundary of the computational domain from both the reflected waves from the monopile and the outlet. Therefore, active wave absorption (also based on shallow water theory) is activated at the inlet to prevent this re-reflection. Hence, the front part of the monopile is more susceptible for this type of reflected waves. However, no qualitative method is used to assess this re-reflection from the inlet boundary.

A minor source of deviations between numerical and experimental results is the measurement technique for the wave run-up level. However, De Vos et al. (2007) reported no details about the accuracy of the experimental wave run-up measurements. The experimental measurements may be influenced by the presence of the wave gauges (two cylindrical rods) near the pile, while in the numerical model the wave gauges are not modelled (wave run-up is measured at that same location however). This effect is considered marginal in contrast to the difference in reflection between experimental and numerical models.

Despite the observed inaccuracies, in general the numerical results are in good agreement with the experimentally obtained wave run-up levels. It may be expected that the inaccuracies related to the experimental measurements also contribute to the achieved level of agreement. In contrast to the experimental data, which are only available at nine discrete locations, the numerical model yields a much higher spatial resolution of the wave run-up levels around the monopile. As a result, the wave run-up phenomenon features are much easier to identify using the numerical toolbox.

2.7 Conclusions and future work

In this paper, we presented a buoyancy-modified $k-\omega\ SST$ turbulence model that prevents an excessive decrease in wave height over the length of the numerical wave flume based on RANS turbulence modelling. Therefore, a buoyancy term has been implemented in the TKE-equation in order to develop an overall stable wave propagation model without significant wave damping over the length of the flume. The influence of that buoyancy term was demonstrated by performing wave propagation simulations in an empty wave flume using OpenFOAM®. Subsequently, we validated this buoyancy-modified turbulence model by simulating wave run-up around a monopile subjected to regular waves. Therefore, two regular wave trains were generated, each with a different wave steepness. The obtained numerical results of the wave run-up pattern around the monopile show a fair agreement with experimental data and two analytical formulations. The outcome of this paper proves the successful capability of a buoyancy-modified turbulence model in order to simulate offshore and coastal engineering processes. Future work includes the validation of wave breaking processes using the buoyancy-modified $k-\omega\ SST$ turbulence model. The buoyancy term will not only result in a stable wave propagation model without significant wave damping over the length of the flume but it will also predict the turbulence level in the flow field more accurately at the locations where wave breaking occurs.

Chapter 3

Wave breaking simulations

This chapter is a continuation of the work on turbulence modelling in a numerical wave tank presented in the previous chapter, Chapter 2. Now, the focus is on wave breaking simulations under regular waves on a sloping beach. RANS turbulence modelling is performed by applying the original and the buoyancy-modified $k-\omega$ and $k-\omega\ SST$ models. The performance of the buoyancy-modified models is analysed by validating the numerically obtained results with the widely used benchmark data set of Ting and Kirby (1994). An in-depth analysis of the turbulent kinetic energy in the flow field during wave breaking events is reported in Appendix A. Note that all the figures are included in the last section at the end of this chapter, section 3.6.

Submitted for publication as:
Devolder, B., Troch, P., and Rauwoens, P. (2018). Performance of a buoyancy-modified $k-\omega$ and $k-\omega\ SST$ turbulence model for simulating wave breaking under regular waves using OpenFOAM®. *Coastal Engineering*, 138:49–65. doi:10.1016/j.coastaleng.2018.04.011.

Performance of a buoyancy-modified $k-\omega$ and $k-\omega\ SST$ turbulence model for simulating wave breaking under regular waves using OpenFOAM®

Brecht Devolder, Peter Troch, Pieter Rauwoens

Abstract

In this work, the performance of a buoyancy-modified turbulence model is shown for simulating wave breaking in a numerical wave flume. Reynolds-Averaged Navier-Stokes (RANS) modelling is performed by applying both a $k-\omega$ and a $k-\omega\ SST$ turbulence model using the Computational Fluid Dynamics (CFD) toolbox OpenFOAM. In previous work of the authors (Devolder et al., 2017), the observed significant decrease in wave height over the length of the numerical wave flume based on RANS turbulence modelling for the case of propagating waves has been avoided by developing a buoyancy-modified $k-\omega\ SST$ model in which (i) the density is explicitly included in the turbulence transport equations and (ii) a buoyancy term is added to the turbulent kinetic energy (TKE) equation. In this paper, two buoyancy-modified turbulence models are applied for the case of wave breaking simulations: $k-\omega$ and $k-\omega\ SST$. Numerical results of wave breaking under regular waves are validated with experimental data measured in a wave flume by Ting and Kirby (1994). The numerical results show a good agreement with the experimental measurements for the surface elevations, undertow profiles of the horizontal velocity and turbulent kinetic energy profiles. Moreover, the underlying motivations for the concept of a buoyancy-modified turbulence model are demonstrated by the numerical results and confirmed by the experimental observations. Firstly, the buoyancy term forces the solution of the flow field near the free water surface to a laminar solution in case of wave propagation. Secondly in the surf zone where waves break, the buoyancy term goes to zero and a fully turbulent solution of the flow field is calculated. Finally and most importantly, the buoyancy-modified turbulence models significantly reduce the common overestimation of TKE in the flow field.

Keywords: CFD; OpenFOAM/IHFOAM; Buoyancy-modified turbulence model; Wave breaking

3.1 Introduction

Wave breaking is seen as one of the last and most complex life events of a wave. When waves propagate from offshore towards the shoreline, shoaling occurs due to a decreasing water depth. In the surf zone, the wave steepness increases significantly and the waves break. Wave breaking is characterised by several parameters such as the wave height H, the wave length L and the bathymetry of the seabed. Therefore, Galvin (1968) reported four different breaker types: spilling, plunging, surging and collapsing. During wave breaking, turbulence generation is one of the governing processes. However, it is very challenging to quantify wave breaking turbulence based on field observations. Therefore, a large number of experimental flume tests have been performed in a repeatable and controlled environment studying both regular and irregular wave breaking, e.g. Ting and Kirby (1994), Boers (1996), Cox and Kobayashi (2000), Ting (2001) ,Ting (2002) ,Ting (2006), Ting (2008), Huang et al. (2010), Ting and Nelson (2011), Sumer et al. (2011), Ting (2013) and van der A et al. (2017). Those flume tests revealed that wave breaking is the primary source of turbulence generation and is responsible for the dissipation of wave energy. In particular, wave breaking events increase the turbulent intensity in the vicinity of the seabed, which plays an important role in near shore sediment transport. Next to experimental modelling, numerical simulations provide additional insights since a lot of difficulties for measuring wave breaking characteristics exist during field measurements or small-scale experimental tests. In particular, the disturbance effect of measurement devices on the hydrodynamic flow field and the influence of entrapped air on measuring surface elevations and velocity profiles are the main contributions to the overall error in the experimentally obtained results.

The focus of the present numerical study is solely put on wave breaking induced turbulence modelling using a Navier-Stokes solver and not on sediment transport. Numerical studies regarding sediment transport under breaking wave conditions have been reported in Jacobsen et al. (2014), Jacobsen and Fredsoe (2014), Fernandez-Mora et al. (2017) and Zhou et al. (2017) for example. Furthermore, long duration tests using irregular waves are not considered in this numerical validation study in order to minimise the computational effort. In this paper, Ting and Kirby (1994) is selected as the experimental validation dataset since a rigid seabed was used and regular waves were generated. The experimental dataset contains measurements of both surface elevations and undertow profiles for spilling and plunging breakers respectively. Several authors reported numerical results using that experimental dataset, such as Lin and Liu (1998), Bradford (2000), Mayer and Madsen (2000), Christensen (2006), Hieu et al. (2004), Jacobsen et al. (2012), Xie (2013), Alagan Chella et al. (2015, 2016) and Brown et al. (2016). All the numerical studies have one aspect in common: they all use a turbulence model in their Navier-Stokes solver. The need for using a turbulence model is motivated by e.g. Thornton (1979): wave breaking is a paramount source of turbulence generation. Over the past decades, a large number of turbulence models have been derived and modified in order to enhance the predictive skills of numerical methods for turbulent fluid flows. Simulating surf zone turbulence specifically requires attention to the choice of a turbulence model. For the first numerical studies

simulating wave breaking, Reynolds-Averaged Navier-Stokes (RANS) models and in particular $k-\varepsilon$ models were popular (Lin and Liu, 1998; Bradford, 2000). Lin and Liu (1998) developed a RANS model using an algebraic Reynolds stress $k-\varepsilon$ model in combination with a Volume of Fluid (VoF) method to capture the free water surface. Their model was able to simulate the turbulence levels and the mean flow field in the surf zone away from the breaking point very well, even though their simulation did not reach the quasi-steady state. However, the authors found that the turbulence levels near the breaking point were significantly overestimated compared to the experimental data. As a consequence, energy dissipation was responsible for the smaller observed breaking wave height. Bradford (2000) performed RANS simulations using the commercial software Flow-3D by applying different one- and two-equation turbulence models: k-model, $k-\varepsilon$ model, RNG model. The results obtained using the one-equation k-model were insufficiently accurate, while the performance of the RNG model was lower than the $k-\varepsilon$ model for predicting turbulence levels. In general, Bradford (2000) concluded that the turbulent kinetic energy (TKE) in the wave crest prior to breaking is overpredicted using a $k-\varepsilon$ model, resulting in an underprediction of the breaking wave height. Therefore, Bradford (2000) advises to use a $k-\omega$ model instead, as presented by Mayer and Madsen (2000). However, Mayer and Madsen (2000) modified the $k-\omega$ model in order to overcome the generation of TKE in the potential flow region (i.e. wave propagation zone outside the surf zone) and to avoid wave damping over the length of the flume. Therefore, they implemented an ad-hoc modification of the production of TKE using the vorticity of the mean flow rather than the local mean velocity gradient. As a result, this modification eliminated the excessive generation of TKE outside the surf zone when using a $k-\omega$ model and enhanced significantly the predictive skills of the numerical model for simulating breaking waves. Their research also triggered the discussion on the fundamental problems of applying RANS models for wave modelling. An alternative approach to RANS models are large eddy simulations (LES). In LES, the large scale turbulent structures are computed directly while the small scale (sub-grid scale) structures are modelled using a turbulence model. Pope (2000) formulated that at least $80\ \%$ of the turbulence needs to be resolved by the computational grid for LES. As a consequence, very fine grids are needed, increasing the computational time significantly. Hieu et al. (2004) presented two-dimensional (2D) LES calculations using a two-phase flow solver for simulating breaking waves and satisfactory results were obtained for a limited simulation time. In their model, not only the water phase but also the air phase was modelled. They noted that the effects of air entrainment on the wave energy dissipation were not negligible. Furthermore, they reported that surface tension might be necessary for better simulations of air bubbles entrained in the water. Thereafter, Christensen (2006) presented three-dimensional (3D) LES calculations for modelling both spilling and plunging breakers. In his model the air phase was not considered at all in order to take the air-water mixture into account in the surf zone. In general, a fair agreement was found between numerical and experimental surface elevations in the inner part of the surf zone. However, the exact breaking point was not captured accurately and the breaking wave height was overestimated by the LES model. Also the undertow profiles showed discrep-

ancies between experimental and numerical results. Christensen (2006) concluded that the differences between numerical and experimental results were mainly due to the coarse resolution of the 3D mesh. Note that not only Christensen (2006) but also Lin and Liu (1998), Bradford (2000) and Mayer and Madsen (2000) used a single-phase fluid solver. However, single-phase solvers are not able to reproduce the energy dissipation caused by entrained air, as reported in Jacobsen et al. (2014), Christensen (2006) and Hieu et al. (2004), resulting in an overprediction of TKE (Lin and Liu, 1998; Bradford, 2000; Mayer and Madsen, 2000; Christensen, 2006). More recently, Jacobsen et al. (2012) presented a wave generation toolbox for the two-phase flow solver implemented in OpenFOAM and performed validation tests for breaking waves using the modified $k-\omega$ model proposed by Mayer and Madsen (2000). The results presented are averaged over 50 wave periods after the warming-up phase of 80 wave periods in order to avoid the apparent lack of mass conservation. Furthermore, Jacobsen et al. (2012) demonstrated the importance of the aspect ratio on the numerical results. In general, the numerical results for the surface elevations and undertow profiles obtained with an aspect ratio equal to 1 were significantly better compared to an aspect ratio equal to 2. Xie (2013) used a two-phase flow solver with a $k-\varepsilon$ model but only a limited number of waves were simulated. In general, their results showed a good agreement with the experimental data. The numerically obtained breaking wave height was under estimated by the numerical model while good results were obtained for the TKE levels. As an alternative to the VoF method, Alagan Chella et al. (2015, 2016) applied a Level Set Method (LSM) to track the free water surface in combination with a $k-\omega$ model implemented in the two-phase flow solver REEF3D. At the interface between water and air, a turbulence damping scheme was applied to avoid unphysical turbulence production. Their model predicted shoaling wave heights very well, however discrepancies were observed for the surface elevations in the surf zone. In contrast to all other numerical studies, their model underpredicted the TKE levels in the surf zone. Presumably, this was caused by applying a turbulence damping scheme everywhere near the free water surface, not only in the wave propagation zone but also in the surf zone. Consequently, the wave breaking induced turbulence generation was severely restricted. Very recently, Brown et al. (2016) reported an overview of using various turbulence models in OpenFOAM to simulate both spilling and plunging breakers. Moreover, the authors addressed the necessity of including the density explicitly in the turbulence transport equations. After implementing the density explicitly in the turbulence transport equations, Brown et al. (2016) concluded that the overall best model is the nonlinear $k-\varepsilon$ model but the $k-\omega$ model showed improvements for all the results compared to a solution without turbulence model.

Based on a review of those previous studies, two knowledge gaps are defined. Firstly, it is clear that no standard turbulence model exists for simulating breaking waves. In this study, we propose to test a widely-known Reynolds-Averaged Navier-Stokes (RANS) turbulence model to evaluate its performance during wave breaking simulations using a two-phase Navier-Stokes solver. Regarding the $k-\varepsilon$ model, it is known that the transport equation for ε becomes singular near the wall when it is integrated through the viscous sublayer. This singularity is treated with damping

functions but they feature stability issues (Menter, 1993). A robust alternative formulation is the $k-\omega$ model of Wilcox (1998). It has the advantage of an accurate near wall treatment without employing damping functions. The numerical stability is improved due to straightforward Dirichlet boundary conditions near the wall. Consequently, those two advantages have a direct impact on choosing a $k-\omega$ model to simulate breaking waves on a sloping beach because the bottom will have an influence on the wave breaking process. However, it is reported by Menter (1992) that the results obtained with a $k-\omega$ model strongly depend on the freestream values of ω outside the boundary layer in case of free shear layers. Therefore, Menter (1993) developed a $k-\omega$ shear stress transport (SST) model in order to overcome the freestream dependency of $k-\omega$. In that model, blending functions are applied in order to activate the $k-\omega$ model in the inner region of the boundary layer and the $k-\varepsilon$ model in the outer and free shear region. In this paper, both the $k-\omega$ and $k-\omega$ SST models are applied for the numerical simulations presented. Secondly, the review of previous studies emphasises the need for enhanced prediction tools to simulate accurately the turbulence levels in the flow field of surf zone and in particular near the breaking point. Many researchers, such as Jacobsen et al. (2014), Fernandez-Mora et al. (2017), Zhou et al. (2017), Christensen (2006), Xie (2013) and Brown et al. (2016), reported that the TKE in flow field is numerically overpredicted, except for Alagan Chella et al. (2016) who observed underpredictions. Moreover, it is generally known that none of the traditional turbulence models (e.g. $k-\varepsilon$, $k-\omega$ and $k-\omega$ SST) are developed for two-phase flow simulations (such as wave breaking) but for an incompressible single phase flow. For example, the $k-\omega$ model is originally developed for aerodynamic and aerospace applications. Therefore, these traditional models have to be modified to account for the effect of density variations in the numerical wave flume. In general for a two-phase flow solver, the density should be included in the turbulence transport equations. For the $k-\omega$ model in particular, Jacobsen et al. (2012) also applied a revised production term for the TKE in order to enhance its prediction in the flow field. However, Mayer and Madsen (2000) did not advise this modification as generally valid and recommended fundamental analysis and developments.

In general for wave breaking simulations in a numerical wave flume, two zones are distinguished: the wave propagation zone (no turbulence model needed) and the surf zone (turbulence model needed). Consequently, the numerical wave flume needs to be split up and separate (coupled) simulations have to be performed. However in this paper, we propose a unified model that can handle both regions at the same time. Therefore, we not only include the density in the turbulence transport equations but we also account for the effect caused by density variations in a two-phase flow. The latter is realised by adding a buoyancy source term in the TKE-equation as introduced in Devolder et al. (2017a). Note that Lin and Liu (1998), Bradford (2000), Mayer and Madsen (2000) and Christensen (2006) all used a single-phase fluid solver and consequently, they did not need a buoyancy correction in the TKE-equation to account for density variations in the numerical wave flume. However, as stated before, single-phase fluid solvers overpredict TKE. For a two-phase fluid solver, the buoyancy term is not an ad-hoc modification but appears when the transport equation for the TKE is fundamentally derived from

the Favre-averaged (density weighted) low Mach number equations, as reported in Van Maele and Merci (2006a,b). The similarity in terms of a varying density between our research and the fire flows studied in Van Maele and Merci (2006a,b) was already clarified in our previous work Devolder et al. (2017a). Furthermore as reported in Devolder et al. (2017a), the RANS approach using a two-phase flow solver might cause a significant decrease in wave height over the length of the numerical wave flume for wave propagation simulations. Moreover, we pointed out the need for a buoyancy-modified turbulence model to simulate both low and high steepness propagating waves in non-breaking conditions. Therefore, a buoyancy term was implemented in the turbulent kinetic energy (TKE) equation of the $k-\omega\ SST$ model inducing a laminar result near the free water surface. This new implementation resulted in an overall stable wave propagation model without a significant decrease in wave height over the length of the flume.

In order to fill the knowledge gaps, the focus of this paper is put on the performance of our buoyancy-modified $k-\omega$ and $k-\omega\ SST$ models for wave breaking processes. The first question which will be addressed for the case of wave breaking simulations is whether the zone specifically requiring a turbulence model (i.e. the surf zone) is still well predicted with a buoyancy-modified turbulence model? In other words: is a fully turbulent flow field resolved at the locations where wave breaking is happening? Secondly by using a buoyancy-modified turbulence model, can we solve the issue of overpredicting the TKE in the two-phase flow field? Therefore in this paper, we present a study on the performance of buoyancy-modified turbulence models for simulating wave breaking under regular waves using the Computational Fluid Dynamics (CFD) toolbox OpenFOAM® (2013). Numerical simulations are performed and compared with the experimental dataset of Ting and Kirby (1994) for both spilling and plunging breakers on a plane slope $(1:35)$. RANS turbulence modelling is performed by applying both the original and buoyancy-modified $k-\omega$ and $k-\omega\ SST$ models.

The remainder of this paper is organised as follows. Firstly, in section 3.2, the governing equations for the numerical model are presented, followed by a description of the computational domain, the boundary conditions applied and the solver settings. Subsequently in section 3.3, the numerical model is used to perform wave breaking simulations and the numerical results are compared to experimental measurements while in section 3.4 the obtained numerical results are discussed in detail. Finally, the conclusions are drawn in section 3.5.

3.2 Numerical model

The numerical simulations presented are achieved using OpenFOAM® (2013), version 2.2.2. Firstly, the flow equations are introduced, followed by a description of turbulence modelling. Subsequently, the computational domain is presented together with the grid characteristics. The last two parts of this section are dedicated to explain the different boundary conditions and solver settings.

3.2.1 Flow equations

The numerical model uses the incompressible RANS equations to express the motion of a fluid consisting of a mass conservation equation (3.1) and a momentum conservation equation (3.2) written in Einstein summation notation as:

$$\frac{\partial u_i}{\partial x_i} = 0 \tag{3.1}$$

$$\frac{\partial \rho u_i}{\partial t} + \frac{\partial \rho u_j u_i}{\partial x_j} - \frac{\partial}{\partial x_j}\left[\mu_{eff}\frac{\partial u_i}{\partial x_j}\right] = -\frac{\partial p^*}{\partial x_i} + F_{b,i} + f_{\sigma,i} \tag{3.2}$$

in which t is the time, u_i $(i = x, y, z)$ are the Cartesian components of the fluid velocity, ρ is the fluid density, μ_{eff} is the effective dynamic viscosity, p^* is the pressure in excess of the hydrostatic. F_b is an external body force (including gravity) and f_σ is the surface tension tensor term which are respectively defined as:

$$F_{b,i} = -g_i x_i \frac{\partial \rho}{\partial x_i} \tag{3.3}$$

$$f_{\sigma,i} = \sigma\kappa\frac{\partial \alpha}{\partial x_i} \tag{3.4}$$

in which vector $\vec{g} = [0\ ;\ 0\ ;\ -9.81]\ m/s^2$, $\vec{x}$ is the Cartesian coordinate vector (x, y, z), σ is the surface tension coefficient, κ is the mean curvature of the interface and α is the volume fraction. Note that the mean values for the variables considered are written in terms of Favre-averaging (density weighted) due to the varying density.

The interface between water and air is obtained by the VoF method as documented in Berberović et al. (2009). This enhanced formulation using a compression term reduces the dissipative nature of the interface compared to the VoF method of Hirt and Nichols (1981). The method is based on a volume fraction α which is 0 for a completely dry cell and 1 for a completely wet cell and in between 0 and 1 for an interface cell containing both water and air. The volume fraction is solved by an advection equation (3.5):

$$\frac{\partial \alpha}{\partial t} + \frac{\partial u_i \alpha}{\partial x_i} + \frac{\partial u_{c,i}\alpha\,(1-\alpha)}{\partial x_i} = 0 \tag{3.5}$$

The last term on the left-hand side is an artificial compression term where $u_{c,i} = \min[c_\alpha|u_i|, \max(|u_i|)]$. In the present study, the default value of c_α equal to 1 is applied. If a larger value is used, the compression of the interface increases, leading to larger detrimental velocity gradients around that interface.

The density of the fluid ρ within a computational cell is calculated by a weighted value based on the volume fraction α. The effective dynamic viscosity μ_{eff} is obtained by the sum of a weighted value based on the volume faction α and an additional turbulent dynamic viscosity $\rho\nu_t$:

$$\rho = \alpha\rho_{water} + (1-\alpha)\rho_{air} \tag{3.6}$$

$$\mu_{eff} = \alpha\mu_{water} + (1-\alpha)\mu_{air} + \rho\nu_t \tag{3.7}$$

In a post processing step, the position of the free water surface is determined by a discrete integration of the volume fraction α over a vertical line (Z-direction) divided in n equal parts:

$$z_{water\ level} = \sum_{i=0}^{n-1} \alpha_i (z_{i+1} - z_i) \tag{3.8}$$

3.2.2 Turbulence modelling

Turbulent effects are incorporated in the RANS equations (3.1) and (3.2) by solving one or more additional transport equations to yield a value for the turbulent kinematic viscosity ν_t. Once the turbulent viscosity is known, the Reynolds stress tensor can be calculated in OpenFOAM® (2013) as:

$$\tau_{ij} = \frac{2}{3}k\delta_{ij} - \nu_t \left(\frac{\partial u_i}{\partial x_j} + \frac{\partial u_j}{\partial x_i} \right) \tag{3.9}$$

where k is the turbulent kinetic energy, δ_{ij} is the Kronecker delta and ν_t is the turbulent kinematic viscosity.

In the present study, a $k-\omega$ and a $k-\omega\ SST$ model are tested regarding their performance for wave breaking simulations. The results obtained with the original implemented versions of both turbulence models in OpenFOAM® (2013) and their buoyancy-modified versions are compared with the experimental dataset.

3.2.2.1 Incompressible $k-\omega$ model

The incompressible $k-\omega$ model for a single fluid is a two-equation model (Wilcox, 1998) and is formulated in OpenFOAM® (2013) as:

$$\frac{\partial k}{\partial t} + \frac{\partial u_j k}{\partial x_j} - \frac{\partial}{\partial x_j}\left[(\nu + \sigma_k \nu_t) \frac{\partial k}{\partial x_j} \right] = P_k - \beta^* \omega k \tag{3.10}$$

$$\frac{\partial \omega}{\partial t} + \frac{\partial u_j \omega}{\partial x_j} - \frac{\partial}{\partial x_j}\left[(\nu + \sigma_\omega \nu_t) \frac{\partial \omega}{\partial x_j} \right] = \gamma \frac{\omega}{k} P_k - \beta \omega^2 \tag{3.11}$$

$$
\begin{aligned}
P_k &= \nu_t \frac{\partial u_i}{\partial x_j}\left(\frac{\partial u_i}{\partial x_j} + \frac{\partial u_j}{\partial x_i}\right) \\
\nu_t &= \frac{k}{\omega}
\end{aligned}
\tag{3.12}
$$

where k is the turbulent kinetic energy, P_k is the production term of k, ν is the kinematic viscosity, ν_t is the turbulent kinematic viscosity, ω is the specific dissipation rate, $\sigma_k = \sigma_\omega = 0.5$, $\beta^* = 0.09$, $\beta = 0.072$ and $\gamma = 0.52$.

3.2.2.2 Incompressible $k-\omega$ SST model

The incompressible $k-\omega$ SST model for a single fluid is a two-equation model (Menter et al., 2003) and is formulated in OpenFOAM® (2013) as:

$$
\frac{\partial k}{\partial t} + \frac{\partial u_j k}{\partial x_j} - \frac{\partial}{\partial x_j}\left[\left(\nu + \sigma_k \nu_t\right)\frac{\partial k}{\partial x_j}\right] = P_k - \beta^* \omega k \tag{3.13}
$$

$$
\begin{aligned}
&\frac{\partial \omega}{\partial t} + \frac{\partial u_j \omega}{\partial x_j} - \frac{\partial}{\partial x_j}\left[\left(\nu + \sigma_\omega \nu_t\right)\frac{\partial \omega}{\partial x_j}\right] \\
&\qquad = \frac{\gamma}{\nu_t} G - \beta \omega^2 + 2\left(1 - F_1\right)\frac{\sigma_{\omega 2}}{\omega}\frac{\partial k}{\partial x_j}\frac{\partial \omega}{\partial x_j}
\end{aligned}
\tag{3.14}
$$

$$
\begin{aligned}
P_k &= \min(G,\ 10\beta^* k\omega) \\
G &= \nu_t \frac{\partial u_i}{\partial x_j}\left(\frac{\partial u_i}{\partial x_j} + \frac{\partial u_j}{\partial x_i}\right) \\
\nu_t &= \frac{a_1 k}{\max(a_1 \omega,\ SF_2)}
\end{aligned}
\tag{3.15}
$$

where k is the turbulent kinetic energy, P_k is the production term of k, ν is the kinematic viscosity, ν_t is the turbulent kinematic viscosity, ω is the specific dissipation rate, S is the mean rate of strain of the flow, $\beta^* = 0.09$ and $a_1 = 0.31$. F_1 and F_2 are blending functions. F_1 is designed to be one in the near wall region (activating $k-\omega$) and zero away from the wall (activating $k-\varepsilon$). The values of σ_k, σ_ω, β and γ are blended using equation (3.16) in which ϕ_1 and ϕ_2 are given in Table 3.1.

$$
\phi = F_1 \phi_1 + (1 - F_1)\phi_2 \tag{3.16}
$$

3.2.2.3 Buoyancy-modified $k-\omega$ and $k-\omega$ SST models

As reported in Devolder et al. (2017a), the original $k-\omega$ SST model causes significant wave damping for non-breaking propagating high steepness waves. This

Table 3.1: Default values for ϕ_1 and ϕ_2 used in equation (3.16) to calculate σ_k, σ_ω, β and γ for the $k-\omega$ SST turbulence model.

ϕ	σ_k	σ_ω	β	γ
ϕ_1	0.85034	0.5	0.075	0.5532
ϕ_2	1.0	0.85616	0.0828	0.4403

damping is triggered by an increase in turbulent viscosity around the interface between water and air. This increase is induced by the large production of turbulent kinetic energy (TKE), k, in that zone. The production of TKE is linked to the velocity gradient which is large around the interface between water and air due to spurious air velocities. Those spurious air velocities arise due to the pressure-density coupling resolved in the conditionally averaged momentum equation using segregated solution algorithms (Vukčević et al., 2017). Consequently, a natural imbalance exists between the pressure gradient and the large density gradient at the free water surface due to the large density ratio (1000/1). A recent paper addressing the spurious velocities is e.g. Vukčević et al. (2017). In this study however, both a buoyancy-modified $k-\omega$ and $k-\omega$ SST model are implemented in OpenFOAM by:

1. including the density ρ explicitly in the equations (3.10) (3.11) (3.13) (3.14);
2. adding a buoyancy term G_b in the TKE-equations (3.10) and (3.13). The term is not included in the equation for ω since not much influence is expected on the results (Devolder et al., 2017a).

The buoyancy-modified $k-\omega$ model is defined as:

$$\frac{\partial \rho k}{\partial t} + \frac{\partial \rho u_j k}{\partial x_j} - \frac{\partial}{\partial x_j}\left[\rho\left(\nu + \sigma_k \nu_t\right)\frac{\partial k}{\partial x_j}\right] = \rho P_k + G_b - \rho\beta^* \omega k \tag{3.17}$$

$$\frac{\partial \rho \omega}{\partial t} + \frac{\partial \rho u_j \omega}{\partial x_j} - \frac{\partial}{\partial x_j}\left[\rho\left(\nu + \sigma_\omega \nu_t\right)\frac{\partial \omega}{\partial x_j}\right] = \gamma\frac{\omega}{k}\rho P_k - \rho\beta\omega^2 \tag{3.18}$$

The buoyancy-modified $k-\omega$ SST model is defined as:

$$\frac{\partial \rho k}{\partial t} + \frac{\partial \rho u_j k}{\partial x_j} - \frac{\partial}{\partial x_j}\left[\rho\left(\nu + \sigma_k \nu_t\right)\frac{\partial k}{\partial x_j}\right] = \rho P_k + G_b - \rho\beta^* \omega k \tag{3.19}$$

$$\begin{aligned}\frac{\partial \rho \omega}{\partial t} + \frac{\partial \rho u_j \omega}{\partial x_j} - \frac{\partial}{\partial x_j}\left[\rho\left(\nu + \sigma_\omega \nu_t\right)\frac{\partial \omega}{\partial x_j}\right] \\ = \frac{\gamma}{\nu_t}\rho G - \rho\beta\omega^2 + 2\left(1 - F_1\right)\rho\frac{\sigma_{\omega 2}}{\omega}\frac{\partial k}{\partial x_j}\frac{\partial \omega}{\partial x_j}\end{aligned} \tag{3.20}$$

The buoyancy term G_b is defined as:

$$G_b = -\frac{\nu_t}{\sigma_t}\frac{\partial \rho}{\partial x_j} g_j \tag{3.21}$$

in which the scalar $\sigma_t = 0.85$ (Devolder et al., 2017a). The buoyancy term G_b is treated implicitly in the TKE-equation because ν_t is equal to k/ω, see equations (3.12) and (3.15).

The purpose of including a buoyancy term in this study is twofold. The first objective is to suppress the turbulence level at the free water surface, i.e. in the zone where the governing direction of the density gradient is vertical (predominantly horizontal free water surface). More specific, this is the zone near the interface where non-breaking waves are propagating. Because of the implicit treatment of the buoyancy term G_b in the TKE-equation, the very large vertical density gradient near the free water surface drives the turbulent viscosity ν_t to zero. As a result, in case of propagating waves, the model switches to a laminar regime near the free water surface, preventing excessive wave damping. This has already been demonstrated in Devolder et al. (2017a). The second objective is to obtain a fully turbulent solution of the flow field in the surf zone, i.e. in the zone where the density gradient consists of an important horizontal component. At the breaking point, this condition is obtained when shoaling waves are reaching their limiting wave height. In the limit of a vertical wave front, G_b is equal to 0 and consequently the original turbulence model formulation (including the density but without buoyancy modification) is regained.

3.2.3 Computational domain

For this study a two-dimensional simulation in a vertical plane (2DV) is performed. Although wave breaking is a three-dimensional process, a 2DV model is able to simulate the governing wave breaking characteristics with a reasonable accuracy as shown by several other 2DV numerical studies in literature (Lin and Liu, 1998; Bradford, 2000; Mayer and Madsen, 2000; Hieu et al., 2004; Jacobsen et al., 2012; Xie, 2013; Alagan Chella et al., 2015, 2016; Brown et al., 2016). In particular, Zhou et al. (2017) reported a comparison between 2DV and 3D results. They concluded that wave breaking starts form 2D horizontal rollers and subsequently evolves into full 3D hairpin-shaded turbulent structures causing cross-sectional variability in the flow field. As a result, discrepancies between 2DV and 3D models are mainly observed in the inner surf zone (Zhou et al., 2017). Figure 3.1 shows the computational domain together with the boundary condition types which are listed in the next section 3.2.4. The waves are generated at the inlet in a water depth of $0.40\ m$ and propagate first over a horizontal bed ($1.3\ m$ long) and subsequently over a uniform slope of $1:35$ in order to replicate the experimental tests.

After uniform discretisation, the largest size of a cell in both the horizontal X-direction (Δx) and vertical Z-direction (Δz) is $0.01\ m$. Subsequently, the mesh is locally refined in horizontal and vertical direction in a zone where the free water surface will be located, resulting in $\Delta x = \Delta z = 0.005\ m$. In general, the aspect

ratio (i.e. ratio of largest dimension of a cell over the smallest dimension) is 1 as suggested by Jacobsen et al. (2012). However, additional layers with $\Delta x = 0.005\ m$ are added next to the bottom boundary in order to resolve the boundary layer properly, locally increasing the aspect ratio up to 8. These cell sizes are sufficiently small based on the mesh refinement study of Brown et al. (2016). The final grid consists of $329\ 946$ cells and $360\ 594$ cells for the spilling and plunging breakers respectively.

3.2.4 Boundary conditions

The types of boundary conditions for this 2DV simulation are given in Figure 3.1: bottom, atmosphere on the top, inlet on the left and outlet on the right. The bottom is modelled as a smooth solid wall on which wall functions are activated for k and ω. A continuous wall function based on Spalding's law (Spalding, 1961) switching between low- and high-Reynolds numbers is implemented for the turbulent viscosity ν_t. By using this scalable wall function, the dimensionless wall distance y^+ should be between 1 and 300. The initial values for k and ω in the computational domain are set to $1 \times 10^{-6}\ m^2/s^2$ and $1.0\ s^{-1}$ respectively. Furthermore on the bottom, a Dirichlet boundary condition is set for the velocity ($0\ m/s$ in the two directions) while the pressure and volume fraction are set to a Neumann condition. The atmospheric conditions at the top of the numerical domain are set to a mixed Dirichlet-Neumann boundary condition for the velocity, pressure and volume fraction. At the inlet, a special boundary condition is needed to generate the incoming and absorb the reflected waves. IHFOAM (Higuera et al., 2013a,b) is deployed as an external toolbox for that boundary condition. Both wave generation and active wave absorption are activated at the inlet. Wave reflection is not observed at the outlet because no water will reach that boundary. Therefore, a fixed wall boundary condition is implemented at the outlet boundary, similar to the bottom boundary.

In case of spilling breakers, a wave height $H = 0.125\ m$ is generated with a wave period $T = 2\ s$ resulting in a breaker parameter $\xi_0 = m/(H_0/L_0)^{1/2} = 0.20$ based on deep water conditions for H and L, and m is the bottom slope ($1:35$) (Ting and Kirby, 1994). In case of plunging breakers, the wave height $H = 0.127\ m$ and the wave period $T = 5\ s$ resulting in a breaker parameter $\xi_0 = m/(H_0/L_0)^{1/2} = 0.60$ (Ting and Kirby, 1994). For both cases, the water depth d at the wave generating boundary is fixed to $0.40\ m$. Stream function theory is used for the generation of both spilling and plunging breakers in the numerical wave flume, and the Stokes velocity is set to zero (i.e. no mass transported in a closed wave flume).

3.2.5 Solver settings

For all the simulations presented, the following solver settings are used: central discretisation for the pressure gradient and the diffusion terms; TVD (total variation diminishing) schemes with a van Leer limiter (van Leer, 1974) for the divergence operators; backward Euler time discretisation; a maximum Courant number equal to 0.20 (spilling breakers) and 0.10 (plunging breakers) (Brown et al., 2016).

Table 3.2: y^+ values on the bottom of the numerical wave flume for both spilling and plunging breakers using the six different turbulence models.

y^+	original		density only		buoyancy-modified	
	$k-\omega$	$k-\omega\ SST$	$k-\omega$	$k-\omega\ SST$	$k-\omega$	$k-\omega\ SST$
spilling	36	41	34	31	34	41
plunging	30	45	61	41	48	36

3.3 Results

In the following two subsections, the numerically obtained surface elevations, undertow profiles and TKE profiles are presented and compared to experimental measurements from Ting and Kirby (1994) for both spilling and plunging breakers respectively. Each numerical simulation ran for 50 wave periods to obtain a sufficiently long dataset after the warming-up phase. All the results presented in this section are phase averaged using the last 20 waves of the 50 waves simulated.

Five simulations are performed using no turbulence model, the original $k-\omega$ and $k-\omega\ SST$ models and the buoyancy-modified $k-\omega$ and $k-\omega\ SST$ models. Additionally, numerical results of the surface elevations using the $k-\omega$ and $k-\omega\ SST$ models in which only the density is included are also provided. Those results are obtained by switching off the buoyancy term: $G_b = 0$ in equations (3.17) and (3.19). The result without turbulence model is included to address the need of turbulence modelling for the case of breaking waves. The maximum achieved y^+ values on the bottom of the numerical wave flume are summarised in Table 3.2 for both spilling and plunging breakers using the six different turbulence models. Those y^+ values are within the application range reported in section 3.2.4.

3.3.1 Spilling breakers

In this subsection, both the experimental (Ting and Kirby, 1994) and numerical results are reported for the case of spilling breakers. Firstly, surface elevations are presented followed by velocities and TKE along several vertical profiles. Lastly, the turbulent behaviour of the flow using different RANS turbulence models is shown.

3.3.1.1 Surface elevations

The graphs displayed in Figure 3.2 include the surface elevations along the wave flume for the seven simulations. In each graph, the vertical axis denotes the phase averaged surface elevation η with respect to the bottom before the slope ($z = 0\ m$). On the horizontal axis, $x = -2\ m$ corresponds to the inlet boundary while $x = -0.7\ m$ indicates the start of the slope. The solid blue lines represent the numerical results for the maximum, average and minimum phase averaged surface elevations. The blue shaded bands indicate one standard deviation on both sides of the maximum and minimum surface elevations which represent about $68\ \%$ of all the values in case of a normal distribution. The root mean square error (RMSE), denoted by E, is calculated with respect to the experimental data (indicated by red

dots in Figure 3.2) for the maximum ($E_{\max}$), average (E_{av}) and minimum ($E_{\min}$) surface elevations respectively. Note that RMSE values are not dimensionless and therefore they are only used to compare in a qualitative way the performance of the various turbulence models. The vertical dashed black lines indicate the position where the vertical profiles are extracted, see section 3.3.1.2.

In general, Figure 3.2 addresses the need of using a turbulence model for simulating wave breaking processes. It is clearly observed that the solution without turbulence model gives significantly deviating results for the surface elevations compared to the experimental data. In particular, the numerically obtained breaking point is far away from the experimental one, as is the case for both the average and minimum surface elevations. In general, the results where a turbulence model is used, except for the original $k-\omega$ model and the $k-\omega$ model with only the density included, are in a good agreement with the experimental data both for the location of the breaking point and the surface elevations. This is shown by the smaller RMSE values for the maximum, average and minimum surface elevations using the buoyancy-modified $k-\omega$ model and all the $k-\omega$ SST models, compared to RMSE values for the solution without turbulence model, the original $k-\omega$ model and the $k-\omega$ model with only the density included. In contrast to the solution without applying a turbulence model, turbulence modelling enhances the capability of the numerical model to obtain repeatable waves over consecutive wave periods characterised with low standard deviations (see blue shaded bands in Figure 3.2). Remarkably, discrepancies between numerical and experimental results are only observed for the maximum surface elevations and not for the average and minimum ones.

Furthermore, a major difference in the performance between the original $k-\omega$ and $k-\omega$ SST model is observed. It is clearly shown in Figure 3.2 that significant wave damping is observed over the length of the flume in case of the original $k-\omega$ model while this is not simulated by the original $k-\omega$ SST model. This is explained by the limiter inside the production term of TKE: P_k, see equation (3.15). The motivation to use a limiter was to avoid excessive generation of turbulent viscosity in the vicinity of stagnation points around an airfoil (Menter, 1993). As a result in the present study, the production of TKE is limited and hence reducing the turbulent viscosity, avoiding wave damping. Although the original $k-\omega$ SST model slightly underpredicts the maximum surface elevation at the breaking point, the surface elevations after wave breaking are in a good agreement with the experimental data. If the density is included explicitly in the $k-\omega$ model, wave damping is still observed but not as strong as the original $k-\omega$ model. Surprisingly, Brown et al. (2016) did not observe wave damping for the spilling breakers using a $k-\omega$ model in which only the density is included. As expected, a major improvement in surface elevations is observed for the buoyancy-modified $k-\omega$ model. Now, the surface elevations are very similar to the experimental data and they all have small standard deviations. Regarding the $k-\omega$ SST model including only the density and the buoyancy-modified $k-\omega$ SST model, the maximum surface elevations are slightly better predicted at the breaking point compared to the original $k-\omega$ SST model. However, smaller and less smooth maximum surface elevations are observed after the waves broke. The small differences in the maximum surface elevations

obtained by the three $k-\omega$ SST models are also explained by the limiter inside the production term of TKE. As a result, the buoyancy-modified $k-\omega$ model has the best performance in terms of surface elevations for the case of spilling breakers. Moreover, it is also shown that the inclusion of the buoyancy term is essential for a $k-\omega$ model in order to avoid wave damping.

3.3.1.2 Undertow profiles

Figure 3.3 presents both measured and simulated undertow profiles at locations $x = -1.265\ m$, $x = 5.945\ m$, $x = 6.665\ m$, $x = 7.275\ m$, $x = 7.885\ m$, $x = 8.495\ m$, $x = 9.110\ m$ and $x = 9.725\ m$ (see vertical dashed lines in Figure 3.2). Along those vertical profiles, the calculated time averaged horizontal velocity $\overline{u}$ and time averaged turbulent kinetic energy (TKE) $\overline{k}$ are analysed. Note that in this work, only the mean value for TKE, $\overline{k}$, is studied. Jacobsen (2011) presented an analysis of the mean turbulence from the resolved flow field to the total TKE and observed that the modelled TKE by a RANS turbulence model was of larger importance. A similar analysis was performed in this study and a similar conclusion is obtained. Consequently, only the mean value for TKE, $\overline{k}$, modelled by a RANS turbulence model is presented in the remainder of this study. Numerical results are shown in solid blue lines whereas the discrete experimental data are indicated by red dots. On top of each curve, the RMSE E is reported with respect to the experimental results. Numerical results using no turbulence model and the original $k-\omega$ model are excluded because the surface elevations shown in Figure 3.2a and Figure 3.2b are inaccurate.

In general, all three simulations presented in Figure 3.3 predict a good qualitative behaviour of the undertow: i.e. negative values for $\overline{u}$ over the largest part of the water column and $\overline{u}$ becomes positive near the free water surface. Furthermore, the transition from positive to negative is captured correctly for all the profiles compared to the experimental data. However, near the bottom, deviations become visible among the turbulence models for the profiles located at $x \geq 7.275\ m$. A comparison of the original $k-\omega$ SST model and its buoyancy-modified version reveals that a better agreement with experimental data is obtained for the original model. In case of a buoyancy-modified $k-\omega$ SST model, larger values for $\overline{u}$ near the bottom are observed after wave breaking ($x \geq 7.275$ m). Based on the RMSE values, the buoyancy-modified $k-\omega$ model gives the best comparison with the experimental measurements, in particular for $x \geq 7.275$ m.

A common issue when applying RANS turbulence modelling is the overprediction of TKE inside the flow domain (see section 3.1). This is confirmed by the profiles presenting $\overline{k}$ for the original $k-\omega$ SST model (see Figure 3.3). For each profile, large deviations are visually observed and a significant RMSE is calculated between numerical and experimental data compared to the buoyancy-modified models. For the first three sampling locations however, no experimental data is available because no turbulence was expected (Brown et al., 2016). This is confirmed by the results using the buoyancy-modified $k-\omega$ SST model showing very small values of $\overline{k}$ along the water column. Remarkably, the buoyancy-modified $k-\omega$ model returns only small values for $\overline{k}$ at the first sampling location ($x = -1.265\ m$). If

the buoyancy term is implemented in the TKE-equation, the numerically predicted $\overline{k}$ approaches the experimental determined values for $x \geq 7.275\ m$. In particular for the buoyancy-modified $k-\omega\ SST$ model, excellent predictions are obtained similar to the experimental measurements. Strangely, the better predictions for $\overline{k}$ do not result in better profiles for $\overline{u}$, on the contrary.

3.3.1.3 Turbulent behaviour

In order to identify the behaviour of the different RANS turbulence models around the breaking point, contour plots of the turbulent kinematic viscosity ν_t at different time phases are depicted in Figure 3.4 using a logarithmic scale. In case no buoyancy term is implemented in the TKE-equation, the turbulent kinematic viscosity in every computational cell is several orders of magnitudes larger than the kinematic viscosity of water ($10^{-6}\ m^2/s$). However, if the density is explicitly included in the turbulence transport equations and a buoyancy term is added to the TKE-equation, two observations are made. Firstly, prior to wave breaking, i.e. wave propagation, the turbulent kinematic viscosity around the free water surface goes to zero. Secondly, around the breaking point, the turbulent kinematic viscosity around the free water surface is several orders of magnitudes larger than the kinematic viscosity of water. This means that there is a strong turbulent flow field at the free water surface where wave breaking occurs. A comparison between the buoyancy-modified $k-\omega$ and $k-\omega\ SST$ model shows some significant differences. For example, ν_t in the water column is predicted larger for the buoyancy-modified $k-\omega$ model compared to the buoyancy-modified $k-\omega\ SST$ model. This is again explained by the limiter inside the production term of TKE for the $k-\omega\ SST$ model.

Furthermore, Figure 3.4 depicts contour plots of the magnitude of the Reynolds stress tensor (equation (3.9)) using a linear scale for cells with a volume fraction α between 0.5 and 1 (i.e. cells below the free water surface). The magnitude of the Reynolds stress tensor is a good indicator to show where turbulence is present in the flow field. In general, a different spatial variation of the magnitude of the Reynolds stress tensor in the flow field is predicted by the three turbulence models. However for each model, turbulence is generated in the crest when the waves are breaking. The largest magnitudes are observed for the original $k-\omega\ SST$ model while the buoyancy-modified $k-\omega$ model predicts slightly larger magnitudes compared to the buoyancy-modified $k-\omega\ SST$ model. Moreover, turbulence is only observed in the upper part of the water column and spreads out slowly downwards. Interestingly, a large amount of entrapped air just below the free water surface is only observed for the buoyancy-modified $k-\omega\ SST$ model. Clearly, the smaller values of $\overline{k}$ have their effect on the more vivid (less damping) breaking process simulated involving bursts, splashes and more entrapped air.

3.3.2 Plunging breakers

In this subsection, tests are performed in case of plunging breakers. Similar graphs are reported as shown in section 3.3.1 for the case of spilling breakers. Again, surface elevations along the wave flume, time averaged horizontal velocities and

TKE along several vertical profiles and the turbulent behaviour of the flow using different RANS turbulence models are presented.

3.3.2.1 Surface elevations

Surface elevations along the wave flume are depicted in Figure 3.5 for the different numerical simulations performed. Remarkably, at first sight, the solution without turbulence model provides the best fit with the experimental data: the breaking point is correctly predicted and the breaking wave height is overestimated at the same level as the turbulent solutions. However, this solution should be avoided for two reasons. Firstly, there is a large standard deviation along the complete length of the wave flume, putting a burden on the wave-by-wave repeatability of the result. Secondly, as was the case for the spilling breakers, the average and minimum surface elevations are clearly underpredicted. In general, better results are obtained if a RANS turbulence model is applied. For example, the standard deviation decreases significantly over the length of the flume, except for the buoyancy-modified $k-\omega\ SST$ model after the waves broke. However, the breaking wave height is still overpredicted and also the numerically obtained breaking point is before the experimental observation. Similar to spilling breakers, deviations between numerical and experimental results are only observed for the maximum surface elevations and not for the average and minimum ones. These observations are not valid for the original $k-\omega$ model which shows again wave damping over the length of the flume. In contrast to the observations made for spilling breakers, the $k-\omega$ model including only the density is not showing significant wave damping. Probably, the lower wave steepness of the plunging breakers in the part with constant water depth ($H/L = 0.0128$) is not triggering wave damping as observed for the spilling breakers (steepness $H/L = 0.0388$) (cfr. wave propagation simulations for non-breaking waves in Devolder et al. (2017a)). In general, the buoyancy-modified $k-\omega$ model has again the best performance for the surface elevations in case of plunging breakers despite its slightly larger RMSE value for the maximum surface elevations $E_{\max}$ compared to the other models.

3.3.2.2 Undertow profiles

Figure 3.6 shows both the measured and simulated vertical profiles (i.e. time averaged horizontal velocity $\overline{u}$ and time averaged turbulent kinetic energy (TKE) $\overline{k}$) at locations $x = 7.295\ m$, $x = 7.795\ m$, $x = 8.345\ m$, $x = 8.795\ m$, $x = 9.295\ m$, $x = 9.795\ m$ and $x = 10.395\ m$ (see vertical dashed lines in Figure 3.5). Again, the numerical results using no turbulence model and the original $k-\omega$ model are excluded because the predicted surface elevations included in Figure 3.5a and Figure 3.5b are inaccurate.

Along the different profiles, the sign of $\overline{u}$ is predicted correctly by all three turbulent simulations. Again, the largest deviations between experimental and numerical results are found in the vicinity of the bottom, especially for $x \geq 8.345\ m$. In particular for the buoyancy-modified $k-\omega\ SST$ model, significantly overestimated values for $\overline{u}$ are calculated. This is also observed for the spilling breakers

reported in section 3.3.1.2. As a result, the performance of the buoyancy-modified $k-\omega$ model for $\overline{u}$ is substantially better compared to the other turbulence models based on the RMSE values.

Also for plunging breakers, an overprediction of TKE inside the flow domain is observed in case the original $k-\omega\ SST$ model is applied. This is revealed by the overpredicted values of $\overline{k}$ along the different vertical profiles. The RMSE values decrease significantly in case a buoyancy-modified turbulence model is used. In particular, the performance of the buoyancy-modified $k-\omega\ SST$ model is better than the buoyancy-modified $k-\omega$ model regarding the values of $\overline{k}$ along the different profiles. Interestingly, this better behaviour is more pronounced at the first four sampling locations shown in Figure 3.6 (see $x \leq 8.795\ m$). Again, better predictions for $\overline{k}$ are not reflected in the velocity field.

3.3.2.3 Turbulent behaviour

The behaviour of the different RANS turbulence models under plunging breakers is examined by Figure 3.7 in which contour plots of the turbulent kinematic viscosity ν_t are visualised using a logarithmic scale at different time phases around the breaking point. Similar observations are made as reported in section 3.1.3 for the spilling breakers. A buoyancy term is needed in order to force the turbulent kinematic viscosity around the free water surface to zero in case of wave propagation. If the wave breaks, the turbulent kinematic viscosity around the free water surface is several orders of magnitudes larger than the kinematic viscosity of water ($10^{-6}\ m^2/s$), indicating a strong turbulent flow field. Moreover, it is again observed that ν_t in the water column is predicted larger for the buoyancy-modified $k-\omega$ model compared to the buoyancy-modified $k-\omega\ SST$ model.
Subsequently, the Reynolds stress tensor is calculated by equation (3.9) and its magnitude is visualised in Figure 3.7 by contour plots using a linear scale for cells with a volume fraction α between 0.5 and 1. Similar to spilling breakers, the spatial variation of the magnitude of the Reynolds stress tensor in the flow field differs between the three turbulence models. Each buoyancy-modified turbulence model indicates that turbulence is generated by the impact of the overturning volume of water on the free water surface resulting in splash. This is also observed for the original $k-\omega\ SST$ model, but turbulence is already present before wave breaking. Again, the original $k-\omega\ SST$ model predicts the largest magnitudes followed by the buoyancy-modified $k-\omega$ model and the buoyancy-modified $k-\omega\ SST$ model. More importantly, turbulence is observed in a large part of the water column, even near the bottom. In case of plunging breakers, significantly more air is entrapped and for the buoyancy-modified $k-\omega\ SST$ model even observed near the bottom of the numerical wave flume.

3.4 Discussion

In general, the numerical results are in a very good agreement with the experimental data and with similar numerical studies for both spilling and plunging breakers, not only for the surface elevations along the wave flume but also for the undertow

profiles. Most importantly, enhanced predictions are obtained for the TKE in the flow field compared to other numerical studies. Furthermore, the behaviour of the flow field in the present numerical study is correctly predicted in the way reported by Ting and Kirby (1994):

- The turbulence levels are much higher in case of plunging breakers compared to spilling breakers;
- The variations of $\overline{u}$ and $\overline{k}$ in the vertical profiles are smaller for plunging breakers compared to spilling breakers;
- TKE in the surf zone decreases towards the bottom.

The most important observation lies in the influence of the buoyancy modification. The results show indeed that the improved turbulence models behave as expected. Observations of the turbulent kinematic viscosity are in line with the initial assumptions of the performance of the buoyancy term implemented in the TKE-equation:

- The buoyancy term G_b avoids wave damping in the wave propagation zone by inducing a laminar solution of the flow field near the free water surface (see Devolder et al. (2017a));
- The buoyancy term G_b goes to zero in the wave breaking zone and the original turbulence model (including the density) is regained near the free water surface;
- Furthermore, the buoyancy term G_b is not the direct cause of better predictions for TKE. However, it is observed that better predictions are obtained, in particular for TKE, with the buoyancy-modified turbulence models. In fact, the buoyancy term will only limit the build-up of TKE around the free water surface in the wave propagation zone (since a laminar solution is induced around the free water surface). This results in a lower and thus better prediction of TKE in the surf zone.
- Moreover, the influence of G_b on the results of TKE is much smaller for the $k-\omega\ SST$ model than for the $k-\omega$ model due to the limiter in the production term P_k of TKE for the $k-\omega\ SST$ model. That limiter is in general reducing the build-up of TKE independent of the inclusion of the buoyancy term.

Despite the improvements, the solution is still not perfect and small discrepancies are observed between the numerically obtained surface elevations and the experimental measurements. Firstly as mentioned in section 3.1, a lot of measurement difficulties exist in small-scale experimental tests. Secondly, numerical models involves discretisation and interpolation errors. Thirdly, post processing of the numerically obtained data also contributes to the interpolation error (e.g. evaluation of the surface elevations). For both spilling and plunging breakers, larger differences of the maximum surface elevations along the wave flume have been

noticed compared to the average and minimum ones. This may be related to air entrainment in the upper parts of the water column caused by the wave breaking process. It is also observed that more air is entrapped, even down to the bottom region, for the plunging breakers (see Figure 3.4 and Figure 3.7). The amount of entrapped air has a direct influence on the determination of the surface elevations due to a discrete integration of the volume fraction. Possibly, this explains why larger differences for the maximum surface elevations are observed compared to the experimental data for the plunging breakers. Moreover, a number of discrepancies between experimental and numerical data are observed for the undertow profiles for $\overline{u}$ and vertical profiles for $\overline{k}$. This is possibly correlated to a slightly different breaking point shifting the correspondent profile towards a slightly different location. Furthermore, it is expected that the inaccuracies related to the experimental measurements also contribute to the achieved level of agreement.

Lastly, the turbulence models themselves are not designed for the highly transient two-phase flow during wave breaking. Redesigning the turbulence models would require more validation data (TKE, but also Reynolds stresses, dissipation rate, etc.), which is scarce. Nevertheless, the discrepancies found are in line with other reported numerical results and we explicitly refer to the recent paper by Brown et al. (2016). In general, the results of our study using the buoyancy-modified turbulence models and the results using the same models reported by Brown et al. are fairly similar. More specifically regarding the surface elevations, the results are almost identical. For example, the breaking point is similar for the two numerical studies. Recall that Brown et al. (2016) also included the density in the turbulence transport equations, but did not introduce the buoyancy term. We notice that by comparing our results using the buoyancy term with Brown's results without (figures 5, 6, 8 and 9 in Brown et al. (2016)), a major improvement is found for the time averaged horizontal velocities $\overline{u}$ and time averaged turbulent kinetic energy $\overline{k}$. An accurate prediction of the latter is necessary to correctly calculate the turbulent viscosity. In particular, the turbulent viscosity will be of extreme importance once a movable bed is considered involving sediment transport under the action of wave induced bed shear stresses.

3.5 Conclusions

In this paper, we evaluated the performance of both a buoyancy-modified $k-\omega$ and a $k-\omega$ SST model for simulating breaking waves using OpenFOAM. The obtained numerical results of the surface elevations, undertow profiles and TKE levels show a good agreement with the experimental data for both spilling and plunging breakers. Moreover, the benefits of modifying existing turbulence models for buoyancy effects have been revealed. Firstly, in the flow field prior to wave breaking (i.e. during wave propagation), low turbulence levels are observed and a laminar solution is desirable. We demonstrated that the buoyancy term forces the solution of the flow field near the free water surface to a laminar solution in case of wave propagation. This also avoids wave damping over the length of the flume due to RANS turbulence modelling. Secondly in the surf zone where waves

break, significant turbulence levels are noticed. For this zone, the buoyancy term goes to zero and a fully turbulent flow field is resolved by the numerical model. For all the simulations presented, we conclude that the results predicted by the buoyancy-modified turbulence models agree the best with the experimental measurements. In particular, the buoyancy-modified turbulence models significantly reduce the common overestimation of TKE in the flow field. Furthermore, we also conclude that the best performance for simulating breaking waves is obtained with the buoyancy-modified $k-\omega$ model compared to the other models tested in this paper. Moreover, we demonstrated that the inclusion of the buoyancy term is essential for a $k-\omega$ model.

The outcome of this study jointly with Devolder et al. (2017a), proves the successful capability of buoyancy-modified turbulence models to simulate offshore and coastal engineering processes. The buoyancy-modified turbulence models not only result in a stable wave propagation model without wave damping but also their predicted turbulence levels inside the flow field are in a better agreement with the experimental measurements in the surf zone.

3.6 Figures

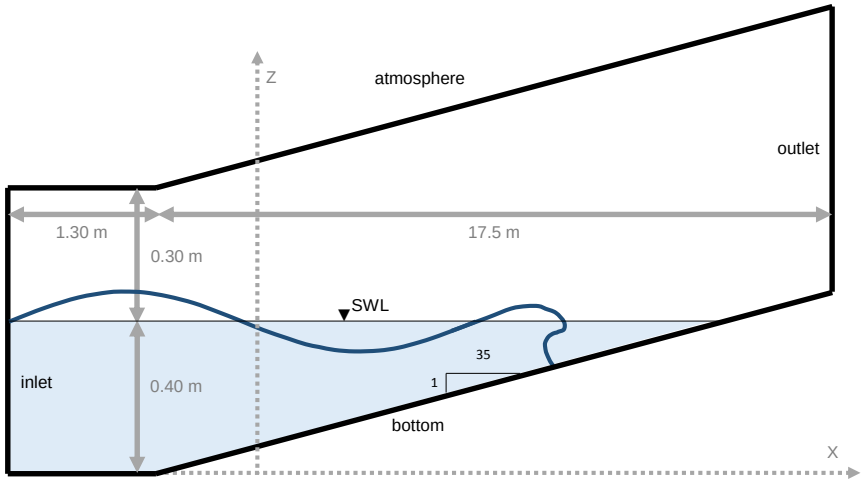

Figure 3.1: Definition sketch of the 2DV computational domain (in the XZ-plane). The thin horizontal line indicates the still water level (SWL), with water depth $d = 0.40\ m$ at the inlet, whereas the black words characterise the boundary condition type. The grey arrows denote the key distances (at distorted scale).

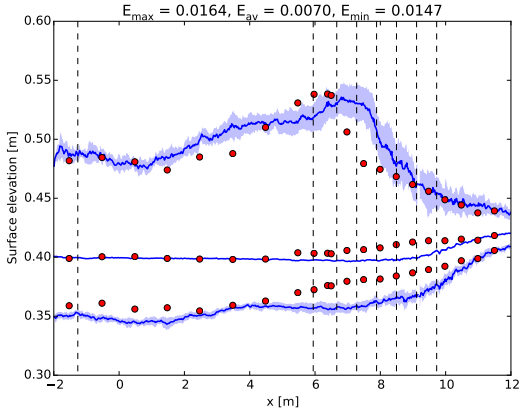

(a) no turbulence model

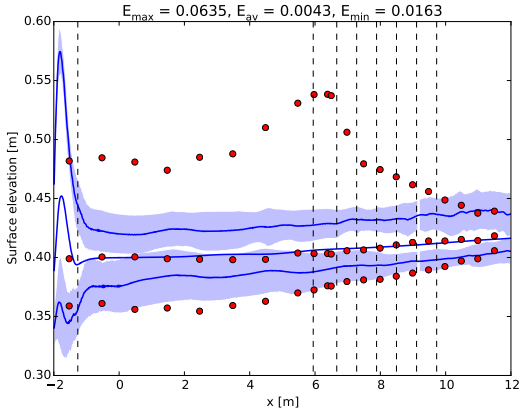

(b) original $k - \omega$

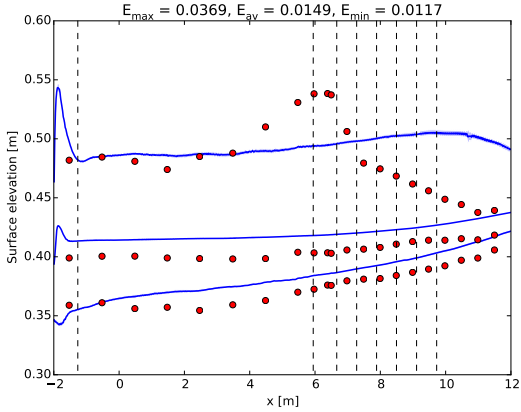

(c) $k - \omega$ including only the density

Figure 3.2: Continued on next page.

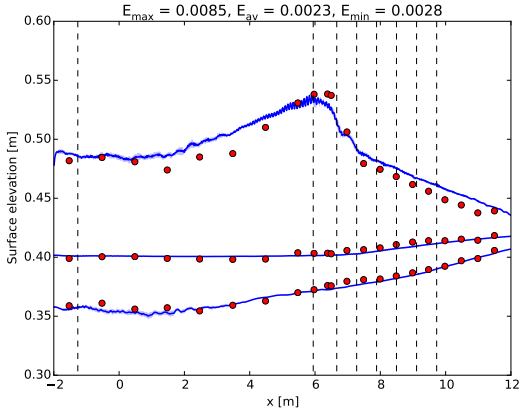

(d) buoyancy-modified $k-\omega$

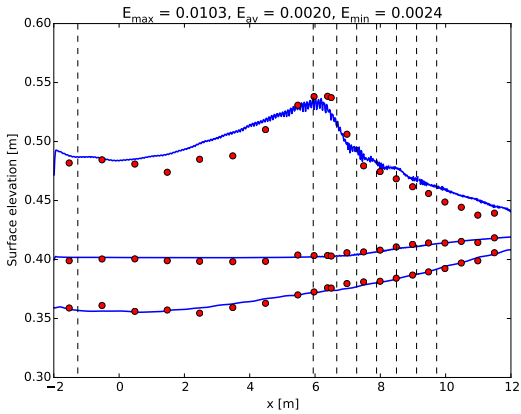

(e) original $k-\omega$ SST

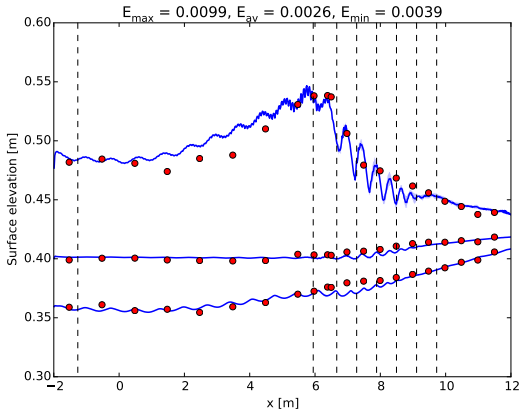

(f) $k-\omega$ SST including only the density

Figure 3.2: Continued on next page.

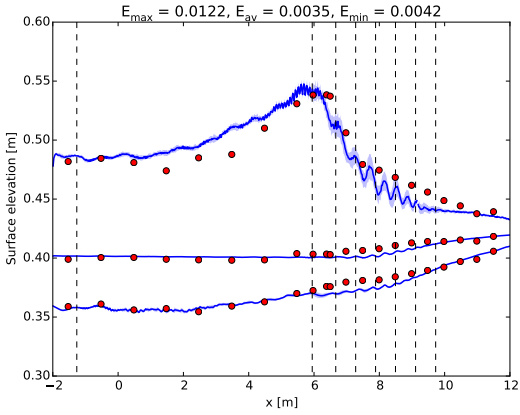

(g) buoyancy-modified $k-\omega$ SST

Figure 3.2: Numerically obtained surface elevations averaged over 20 wave periods along the wave flume for the case of spilling breakers using (a) no turbulence model (b) the original $k-\omega$ (c) $k-\omega$ including only the density (d) the buoyancy-modified $k-\omega$ (e) the original $k-\omega$ SST (f) $k-\omega$ SST including only the density (g) the buoyancy-modified $k-\omega$ SST model. The solid blue lines depict the maximum, average and minimum phase averaged surface elevations. On both sides of the maximum and minimum surface elevations, one standard deviation is visualised by a blue shaded band. RMSE values, E $[m]$, are calculated for the maximum, average and minimum surface elevations with respect to the experimental data (Ting and Kirby, 1994), represented by the red dots. The vertical dashed black lines indicate the position where the undertow profiles are extracted, see section 3.3.1.2.

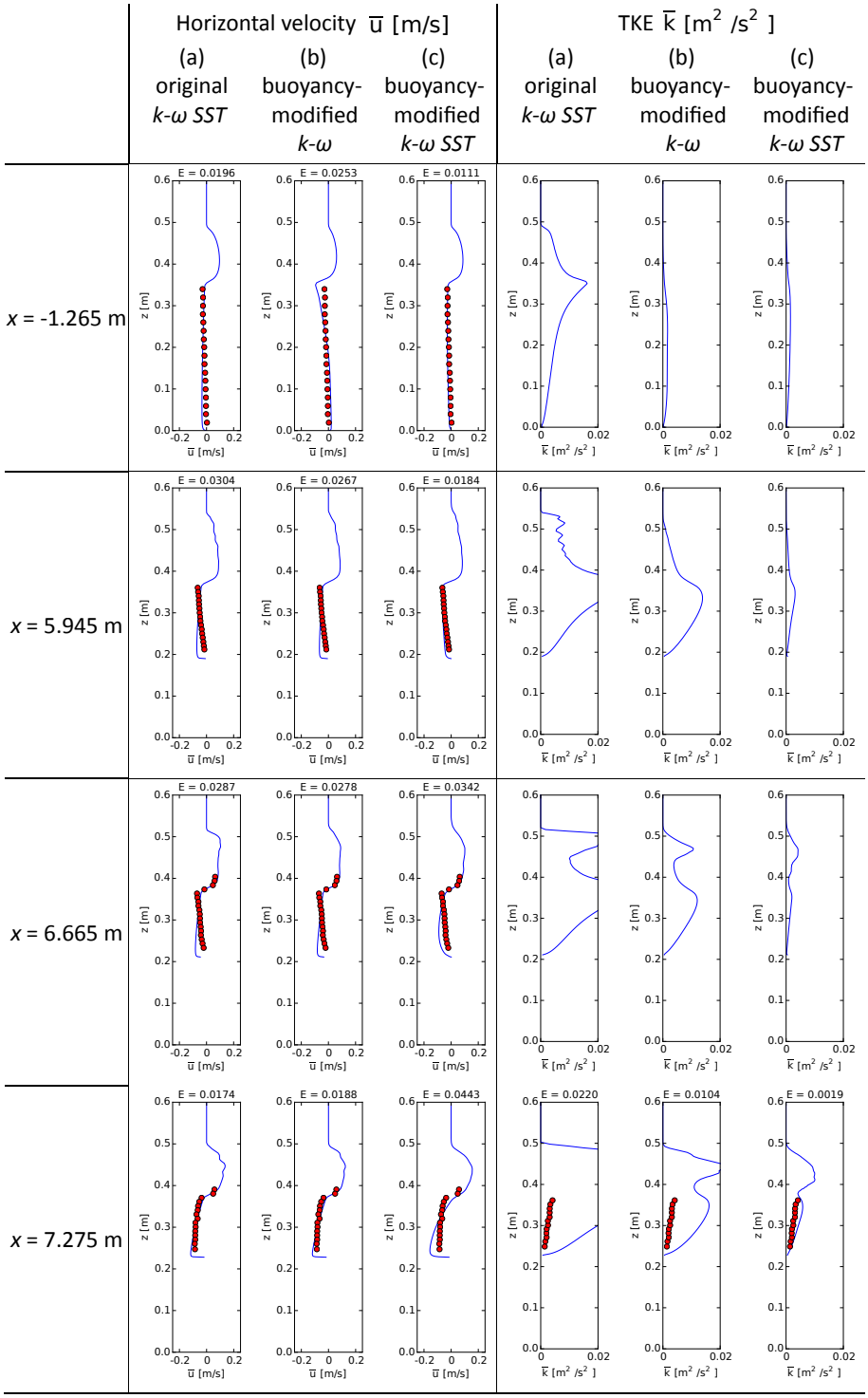

Figure 3.3: Continued on next page.

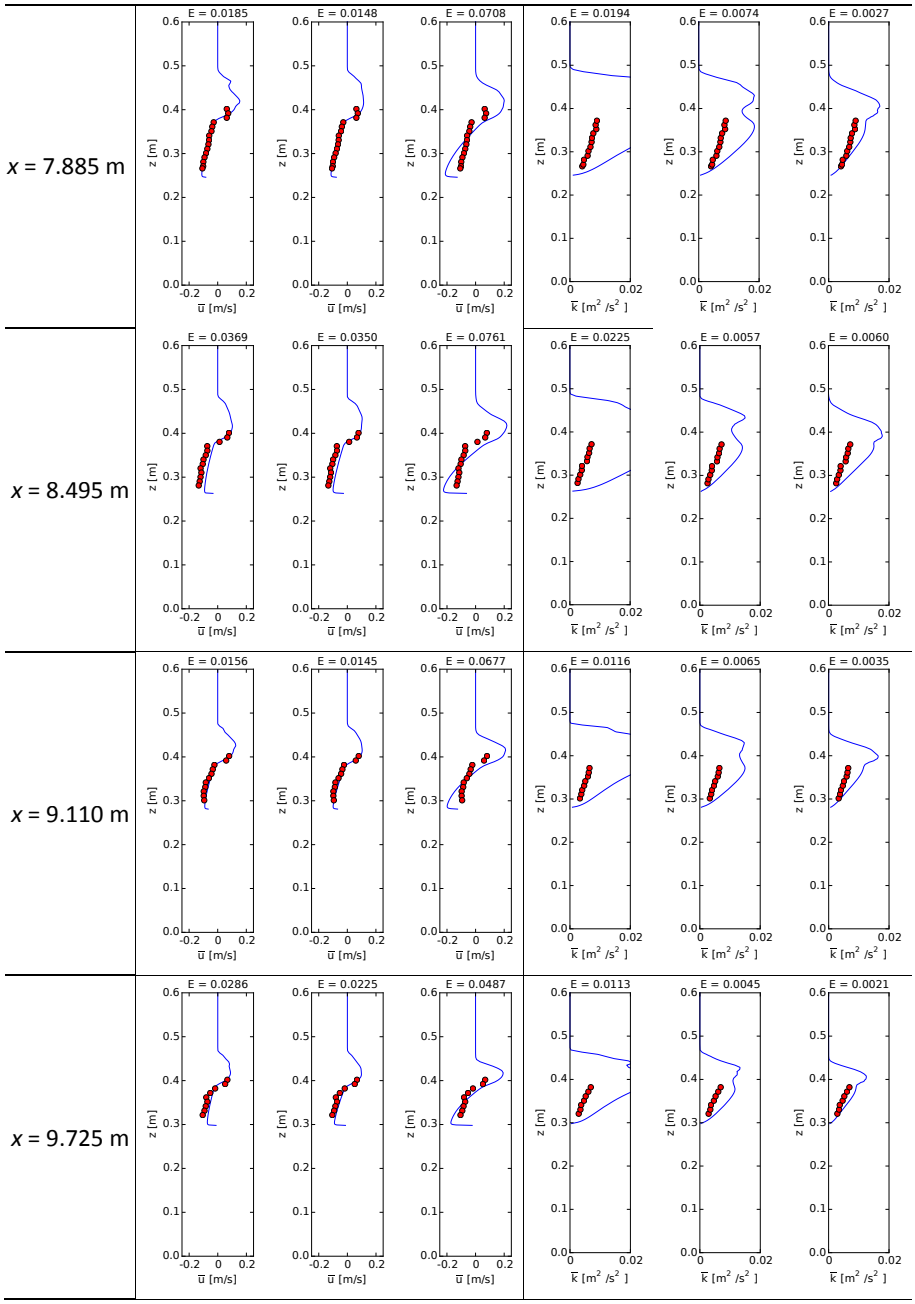

Figure 3.3: Numerically obtained undertows for the time averaged horizontal velocity $\overline{u}$ and time averaged TKE $\overline{k}$ (blue lines) averaged over 20 wave periods using the (a) buoyancy-modified $k-\omega$ (b) original $k-\omega$ SST (c) buoyancy-modified $k-\omega$ SST model. The red dots represent the experimental data (Ting and Kirby, 1994) for the case of spilling breakers. On top of each curve, RMSE values are denoted by E ($[m/s]$ for $\overline{u}$ and $[m^2/s^2]$ for $\overline{k}$).

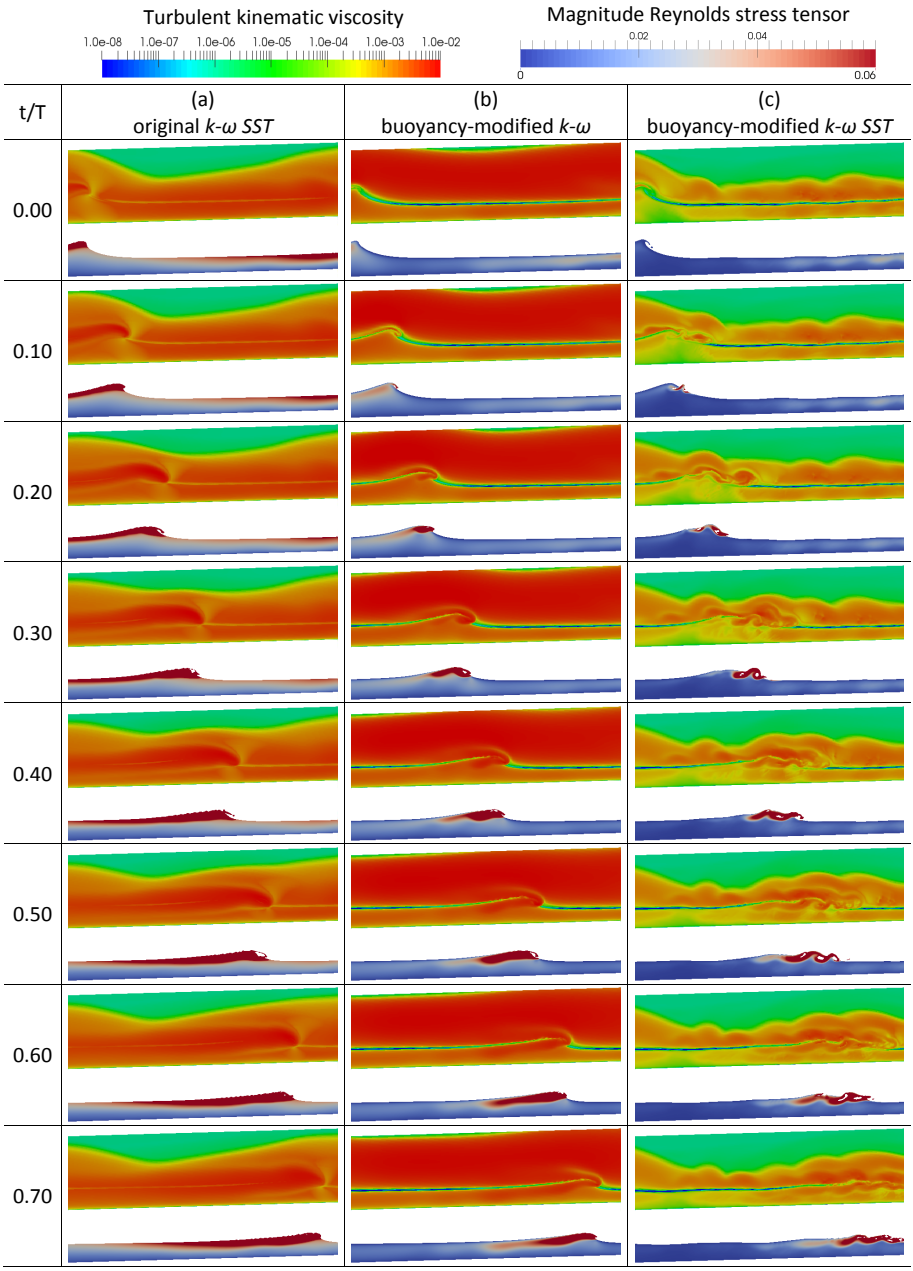

Figure 3.4: Numerically obtained snapshots around the breaking point of the turbulent kinematic viscosity ν_t $[m^2/s]$ and the magnitude of the Reynolds stress tensor (equation (3.9)) at different time phases for the case of spilling breakers using the (a) original $k-\omega$ SST (b) buoyancy-modified $k-\omega$ (c) buoyancy-modified $k-\omega$ SST model.

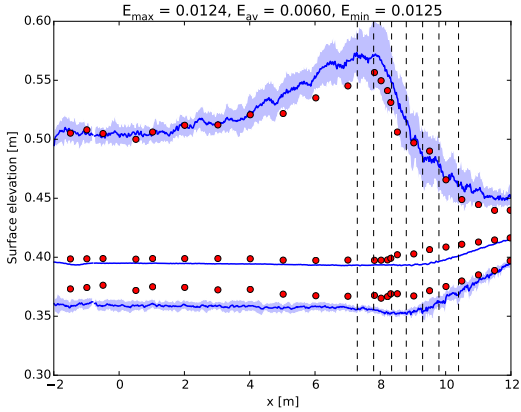

(a) no turbulence model

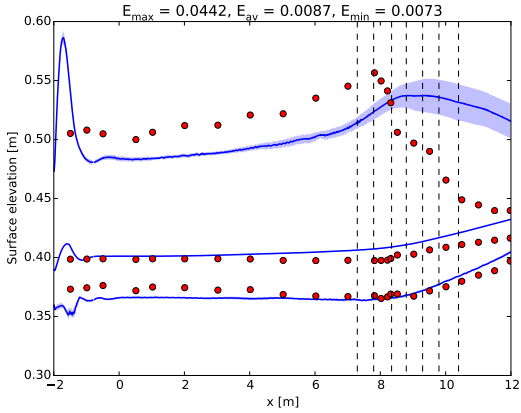

(b) original $k - \omega$

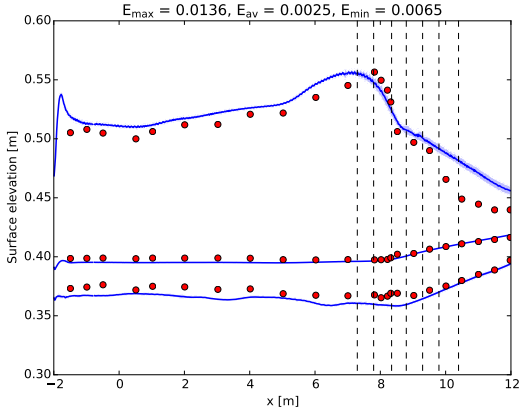

(c) $k - \omega$ including only the density

Figure 3.5: Continued on next page.

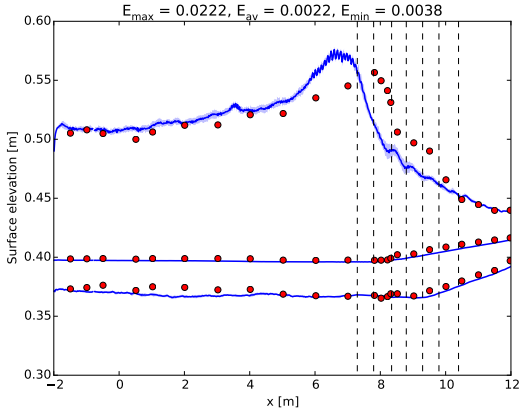

(d) buoyancy-modified $k-\omega$

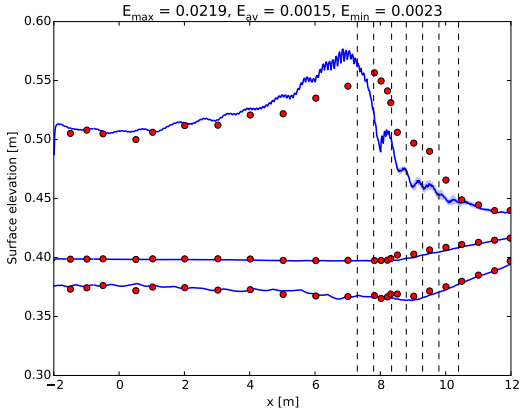

(e) original $k-\omega$ SST

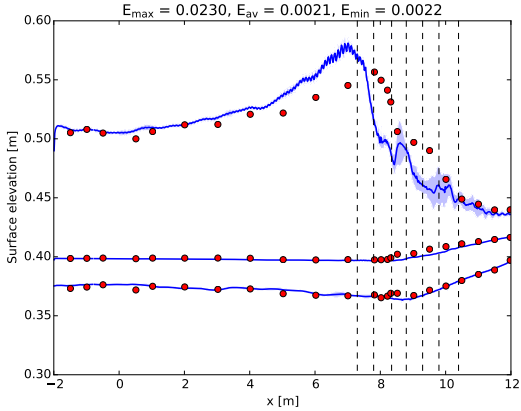

(f) $k-\omega$ SST including only the density

Figure 3.5: Continued on next page.

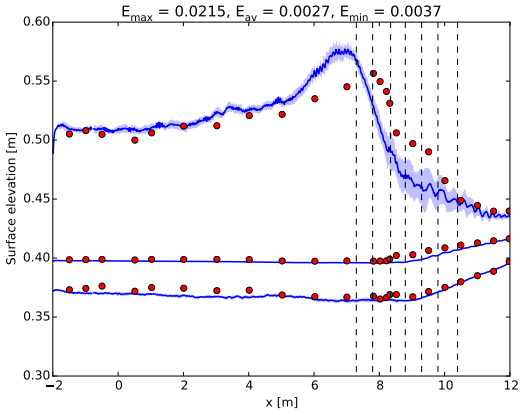

(g) buoyancy-modified $k-\omega$ SST

Figure 3.5: Numerically obtained surface elevations averaged over 20 wave periods along the wave flume for the case of plunging breakers using (a) no turbulence model (b) the original $k-\omega$ (c) $k-\omega$ including only the density (d) the buoyancy-modified $k-\omega$ (e) the original $k-\omega$ SST (f) $k-\omega$ SST including only the density (g) the buoyancy-modified $k-\omega$ SST model. The solid blue lines depict the maximum, average and minimum phase averaged surface elevations. On both sides of the maximum and minimum surface elevations, one standard deviation is visualised by a blue shaded band. RMSE values, E $[m]$, are calculated for the maximum, average and minimum surface elevations with respect to the experimental data (Ting and Kirby, 1994), represented by the red dots. The vertical dashed black lines indicate the position where the undertow profiles are extracted, see section 3.3.2.2.

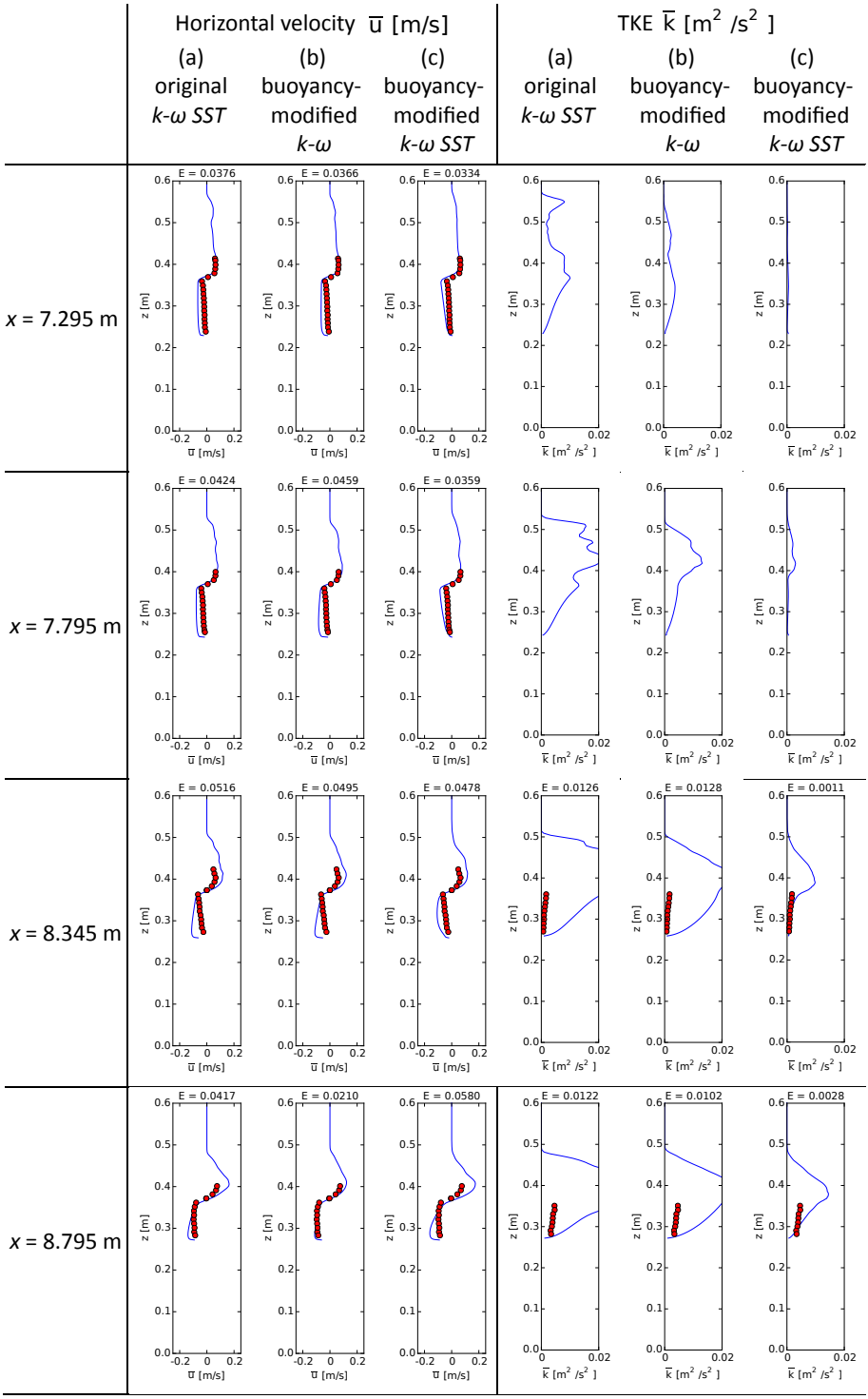

Figure 3.6: Continued on next page.

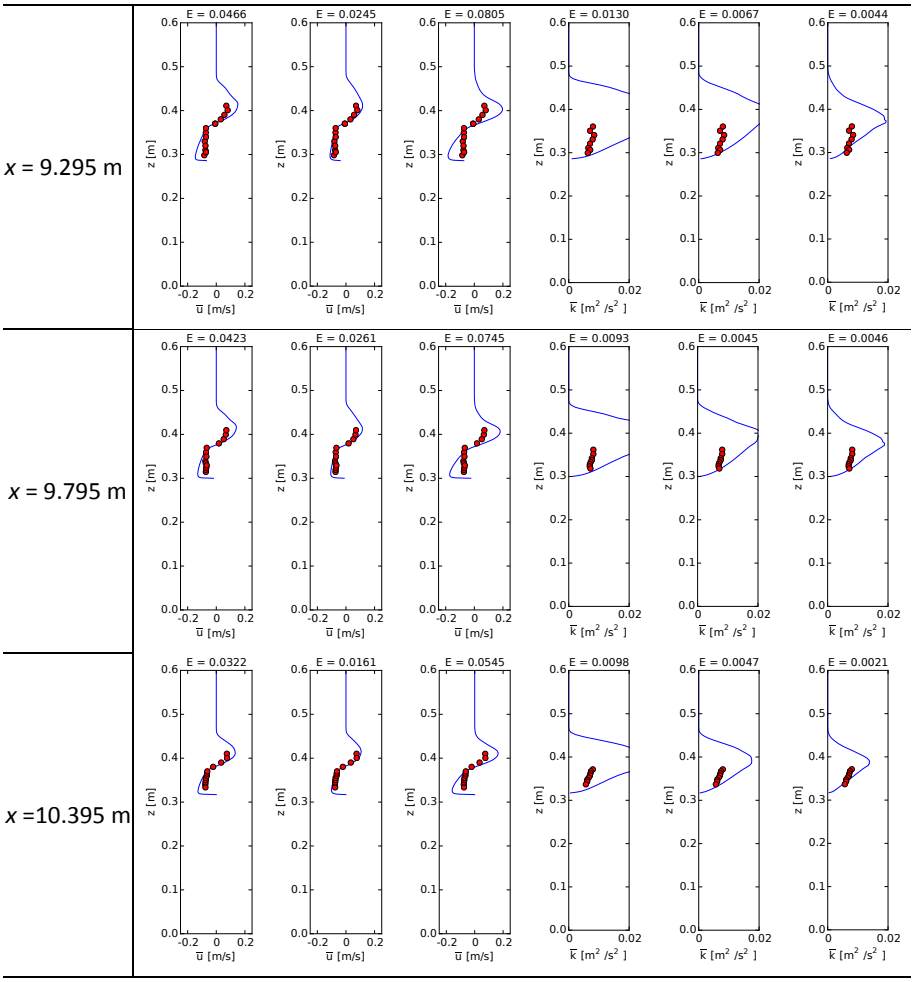

Figure 3.6: Numerically obtained undertows for the time averaged horizontal velocity $\overline{u}$ and time averaged TKE $\overline{k}$ (blue lines) averaged over 20 wave periods using the (a) buoyancy-modified $k-\omega$ (b) original $k-\omega$ SST (c) buoyancy-modified $k-\omega$ SST model. The red dots represent the experimental data (Ting and Kirby, 1994) for the case of plunging breakers. On top of each curve, RMSE values are denoted by E ($[m/s]$ for $\overline{u}$ and $[m^2/s^2]$ for $\overline{k}$).

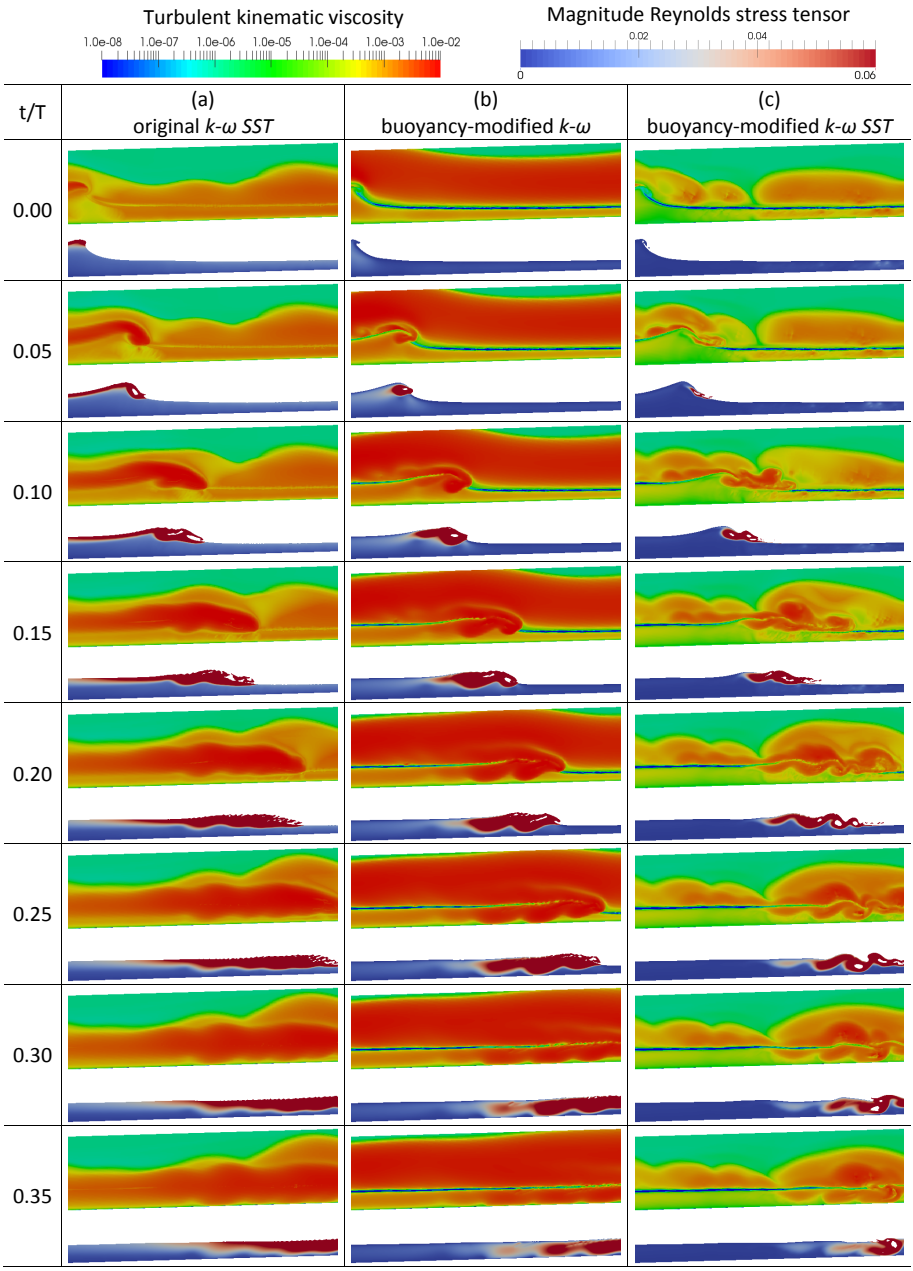

Figure 3.7: Numerically obtained snapshots around the breaking point of the turbulent kinematic viscosity ν_t $[m^2/s]$ and the magnitude of the Reynolds stress tensor (equation (3.9)) at different time phases for the case of plunging breakers using the (a) original $k-\omega$ SST (b) buoyancy-modified $k-\omega$ (c) buoyancy-modified $k-\omega$ SST model.

Part II

Fluid-structure interaction simulations using a numerical wave tank implemented in OpenFOAM

Chapter 4

Accelerated coupling algorithm for simulating a heaving floating body

In this first chapter of the second part of the thesis, a two-phase fluid solver with dynamic mesh handling is coupled with a motion solver to perform fluid-structure interaction simulations in a numerical wave tank. Fundamental research is performed to stabilise the fluid–motion coupling and an accelerated coupling algorithm is derived to efficiently simulate heaving floating bodies with a minimised computational cost.

Submitted for publication as:
Devolder, B., Troch, P., and Rauwoens, P. (2018). Accelerated numerical simulations of a heaving floating body by coupling a motion solver with a two-phase fluid solver. under review for *Computers & Mathematics with Applications*.

Accelerated numerical simulations of a heaving floating body by coupling a motion solver with a two-phase fluid solver

Brecht Devolder, Peter Troch, Pieter Rauwoens

Abstract
This paper presents a study on the coupling between a fluid solver and a motion solver to perform fluid-structure interaction (FSI) simulations of floating bodies such as point absorber wave energy converters heaving under wave loading. The two-phase fluid solver with dynamic mesh handling, *interDyMFoam*, is a part of the Computational Fluid Dynamics (CFD) toolbox OpenFOAM. The incompressible Navier-Stokes (NS) equations are solved together with a conservation equation for the Volume of Fluid (VoF). The motion solver is computing the kinematic body motion induced by the fluid flow. A coupling algorithm is needed between the fluid solver and the motion solver to obtain a converged solution between the hydrodynamic flow field around and the kinematic motion of the body during each time step in the transient simulation. For body geometries with a significant added mass effect, simple coupling algorithms show slow convergence or even instabilities. In this paper, we identify the mechanism for the numerical instability and we derive an accelerated coupling algorithm (based on a Jacobian) to enhance the convergence speed between the fluid and motion solver. Secondly, we illustrate the coupling algorithm by presenting a free decay test of a heaving wave energy converter. Thirdly and most challenging, a water impact test of a free falling wedge with a significant added mass effect is successfully simulated. For both test cases, the numerical results obtained by using the accelerated coupling algorithm are in a very good agreement with the experimental measurements.

Keywords: CFD; Fluid-structure interaction; Two-phase flow, Rigid body heave motion; Accelerated coupling algorithm

4.1 Introduction

Nowadays, floating bodies are observed everywhere in seas and oceans such as vessels, navigation buoys, berths, floating offshore wind turbines, etc. In particular, we focus on floating devices for marine renewable energy production. For example, wave energy converters (WECs) are used to capture wave energy from ocean waves and convert it into electrical power. In this study, WECs of the floating point absorber (FPA) type are selected of which an example is schematically visualised in Figure 4.1. The WEC is moored to the seabed and heaving under wave loading. A power take-off (PTO) system is required to convert the heave motion into electricity. In order to quantify and optimise the WEC's power output, the hydrodynamic flow field around and the kinematic motion of a WEC need to be resolved. Therefore, fluid-structure interaction (FSI) simulations are performed inside a numerical wave tank (NWT) using a partitioned approach, i.e. flow and motion equations are solved separately and a coupling algorithm is applied. The FSI simulations presented are carried out within the Computational Fluid Dynamics (CFD) toolbox OpenFOAM. CFD is able to include viscous, turbulent and non-linear effects which are absent in simplified radiation-diffraction models such as potential flow solvers based on boundary element methods (Davidson et al., 2015b; Wolgamot and Fitzgerald, 2015). Those effects are not only important during survivability conditions, such as extreme waves (Ransley et al., 2017a), but also when control strategies are applied to maximise the power output by driving the WEC's motion into resonance (Davidson et al., 2018).

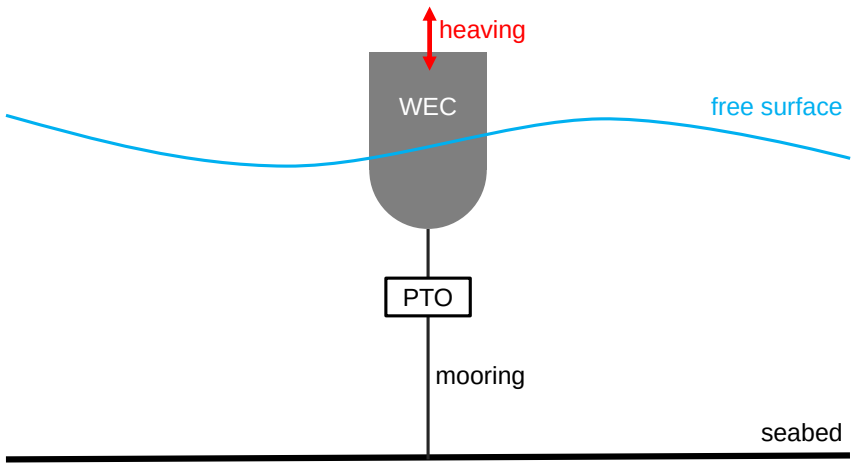

Figure 4.1: Definition sketch of a floating point absorber wave energy converter. The motion of the WEC is restricted to heave only. The WEC is moored to the seabed and a power take-off (PTO) system is required for electricity production.

FSI studies have been extensively reported in literature for a wide range of applications, see Degroote (2013) and references therein. In this paper, we limit our review to a few fundamental studies and specific applications of floating bodies. An important question for FSI simulations is 'How to integrate free motions of solids in fluids?'. This fundamental question was studied and answered by Söding (2001). It was reported that for bodies in a fluid of substantial density, such as water, the force acting on it strongly depends on its acceleration. This dependency originates from the inertia of the water particles surrounding the body, which are also accelerated when the body accelerates, as their motion is determined by the motion of the body through the boundary condition on the wetted surface of that body. The mass of the surrounding fluid (i.e. water) moving along with an accelerating or decelerating body is also called the added mass. For a floating body installed in a sea or ocean, the added mass is not only depending on the geometry but also on the incoming wave conditions (Babarit and Delhommeau, 2015). Due to added mass effects, explicit fluid–motion coupling (also known as loosely or weakly coupled techniques) is only conditionally stable. The stability is significantly enhanced by using implicit (or strongly coupled) techniques but multiple sub iterations are needed during every time step to obtain convergence between the fluid and motion solver, increasing the computational time significantly (Leroyer and Visonneau, 2005). Vierendeels et al. (2005) performed simulations of a rigid body moving in one degree of freedom in an incompressible fluid (single phase) with a density significantly larger than the density of the body. They demonstrated that both a standard explicit coupling scheme and an implicit procedure with explicit coupling in the sub iterations show stability issues. They suggested a procedure with implicit coupling in the sub iterations by using numerically computed derivatives (i.e. a Jacobian). For some applications, the assumption of a rigid body is not valid (e.g. inflatable storm surge barriers) and deformation of the fluid-structure interface is calculated by a structural solver. Degroote (2013) presented a complete overview on partitioned simulation techniques using two black-box solvers (fluid and structural solver) for strongly coupled FSI problems. Different partitioned simulation techniques were formulated, reviewed and compared to each other in terms of implementation and performance (e.g. number of sub iterations during every time step). They reported that the Gauss-Seidel iteration scheme was accelerated by using dynamic Aitken's relaxation (Küttler and Wall, 2008). Even larger accelerations were found by using more advanced state-of-the-art coupling algorithms such as IQN-ILS and IBQN-LS. More recently, Dunbar et al. (2015), Chow and Ng (2016), Kamath et al. (2017) and Gatin et al. (2017) presented FSI simulations using a coupled two-phase fluid solver with a rigid body motion solver. Dunbar et al. (2015) developed a strongly coupled model using sub iterations and dynamic Aitken's relaxation to take the added mass effect into account. They also reported a verification and validation study of a two dimensional (2D) heaving cylinder indicating promising results. In addition, Chow and Ng (2016) showed a reduction in simulation times varying between $70\ \%$ up to $80\ \%$ for using Aitken's relaxation compared to fixed relaxation. They also observed that Aitken's relaxation converged much faster during the first $10-20$ sub iterations compared to fixed relaxation. Their motion solver was based on a second order Adams-Bashforth-Moulton explicit-implicit scheme. Kamath

et al. (2017) studied the water impact and entry of a free falling wedge using the CFD toolbox REEF3D. They found a good agreement between numerical and experimental results for the vertical position and velocity of the wedge. The motion of the wedge was represented by the level set method in order to avoid mesh motion or overset meshes. Gatin et al. (2017) implemented a fifth-order Cash-Karp embedded Runge-Kutta scheme with error control and adaptive time-step size. The motion solver was called after every solution of the pressure equation in order to enhance the convergence of the coupled fluid–motion solver. In every sub iteration, the change of the body's velocity was directly incorporated in the pressure equation by means of a source term but the mesh was only moved once per time step. Their method resulted in an acceleration of a factor two and more for the CPU time to perform seakeeping simulations of a container ship.

For the application of floating bodies, two facts must be considered. Firstly, water impact tests and wave-induced body motions cause a temporal variation of the added mass. Secondly, if the added mass is larger than the physical mass, the fluid–motion coupling features stability issues. Based on a review of those previous studies, different algorithms exist to stabilise partitioned FSI simulations. Most of them are derived for coupling two black-box solvers which are inaccessible, i.e. a fluid solver and a structural solver. In our case of a rigid body, the structural solver is simplified to a motion solver which is merely an integration of Newton's second law. In this manuscript, we show that a stability issue in the coupling between the fluid solver and the motion solver can be resolved on the condition that a good estimate for the added mass is obtained, as suggested in Söding (2001). We compute the added mass using an accelerated coupling algorithm based on Vierendeels et al. (2005), i.e. implicit coupling in the sub iterations by calculating a Jacobian.

This paper presents a study on the coupling between a fluid solver and a motion solver for simulating a floating body in a NWT. We are using the two-phase fluid solver with dynamic mesh handling, *interDyMFoam*, which is a part of the CFD toolbox OpenFOAM. Only the dominant motion of a WEC is considered, the heave motion, which allows a reduction from a six to a one degree of freedom motion. We derive an accelerated coupling algorithm for cases with a significant added mass effect to stabilise the fluid–motion coupling. Both stabilisation and acceleration are achieved by applying implicit coupling in the sub iterations and by calculating a Jacobian. The performance of the coupled fluid–motion solver is validated by using two test cases involving floating bodies: a free decay test of a WEC and a water impact test of a free falling wedge with a significant added mass effect.

The remainder of this paper is organised as follows. Firstly in section 4.2, the governing equations for both the fluid and motion solver are presented. In section 4.3, the accelerated coupling algorithm between a fluid and motion solver is derived. Subsequently in section 4.4, the coupled fluid–motion solver is applied to perform FSI simulations of a free decay test of a heaving WEC and a water impact test of a free falling wedge. Finally, the conclusions are drawn in section 4.5.

4.2 Numerical model

In this section, the numerical methods used to study FSI problems in OpenFOAM® (2015a), version 3.0.1 are summarised. Both, the governing equations for the fluid and motion solver are formulated respectively followed by the kinematic condition at the fluid-structure interface.

4.2.1 Fluid solver

The two-phase fluid solver uses the three dimensional (3D) incompressible Reynolds-Averaged Navier-Stokes (RANS) equations to express the motion of the two fluids (i.e. water and air). The RANS equations consist of a mass conservation equation (4.1) and a momentum conservation equation (4.2) written in Einstein summation notation as:

$$\frac{\partial u_i}{\partial x_i} = 0 \tag{4.1}$$

$$\frac{\partial \rho u_i}{\partial t} + \frac{\partial \rho u_j u_i}{\partial x_j} - \frac{\partial}{\partial x_j}\left[\mu_{eff}\frac{\partial u_i}{\partial x_j}\right] = -\frac{\partial p^*}{\partial x_i} + F_{b,i} + f_{\sigma,i} \tag{4.2}$$

in which t is the time, u_i $(i = x, y, z)$ are the Cartesian components of the fluid velocity, ρ is the fluid density, μ_{eff} is the effective dynamic viscosity, p^* is the pressure in excess of the hydrostatic, F_b is an external body force (including gravity) which is defined as:

$$F_{b,i} = -g_i x_i \frac{\partial \rho}{\partial x_i} \tag{4.3}$$

in which the gravitational acceleration vector $\vec{g} = [0\ ;\ 0\ ;\ -9.81]\ m/s^2$ and $\vec{x}$ is the Cartesian coordinate vector (x, y, z). f_σ is the surface tension tensor term which is neglected in the present study. Note that the mean values for the variables considered are written in terms of Favre-averaging (density weighted) due to the varying density in the NWT.

The interface between water and air is obtained by the Volume of Fluid (VoF) method using a compression term as documented in Berberović et al. (2009). The method is based on a volume fraction α which is 0 for a completely dry cell and 1 for a completely wet cell and in between 0 and 1 for an interface cell containing both water and air. The volume fraction is solved by an advection equation (4.4):

$$\frac{\partial \alpha}{\partial t} + \frac{\partial u_i \alpha}{\partial x_i} + \frac{\partial u_{c,i}\alpha\,(1-\alpha)}{\partial x_i} = 0 \tag{4.4}$$

The last term on the left-hand side is an artificial compression term where $u_{c,i} = \min[c_\alpha |u_i|, \max(|u_i|)]$. In the present study, the default value of c_α equal to 1 is applied.

The density of the fluid ρ within a computational cell is calculated by a weighted value based on the volume fraction α. The effective dynamic viscosity μ_{eff} is obtained by the sum of a weighted value based on the volume faction α and an additional turbulent dynamic viscosity $\rho\nu_t$:

$$\rho = \alpha\rho_{water} + (1-\alpha)\rho_{air} \tag{4.5}$$

$$\mu_{eff} = \alpha\mu_{water} + (1-\alpha)\mu_{air} + \rho\nu_t \tag{4.6}$$

If a laminar solution is sufficiently accurate, the turbulent kinematic viscosity ν_t is equal to zero. In the other case, turbulent effects are incorporated in the RANS equations (4.1) and (4.2) by solving one or more additional transport equations to yield a value for the turbulent kinematic viscosity ν_t. In the present study, a buoyancy-modified $k-\omega\ SST$ model is applied which has been developed in previous works of the authors (Devolder et al., 2017a, 2018b). A buoyancy-modified turbulence model not only results in a stable wave propagation model without wave damping (Devolder et al., 2017a) but it also predict the turbulence level inside the flow field more accurately in the surf zone where waves break (Devolder et al., 2018b). The buoyancy-modified $k-\omega\ SST$ model is defined as:

$$\frac{\partial\rho k}{\partial t} + \frac{\partial\rho u_j k}{\partial x_j} - \frac{\partial}{\partial x_j}\left[\rho\left(\nu + \sigma_k\nu_t\right)\frac{\partial k}{\partial x_j}\right] = \rho P_k + G_b - \rho\beta^*\omega k \tag{4.7}$$

$$\begin{aligned}\frac{\partial\rho\omega}{\partial t} + \frac{\partial\rho u_j\omega}{\partial x_j} - \frac{\partial}{\partial x_j}\left[\rho\left(\nu + \sigma_\omega\nu_t\right)\frac{\partial\omega}{\partial x_j}\right] \\ = \frac{\gamma}{\nu_t}\rho G - \rho\beta\omega^2 + 2\left(1-F_1\right)\rho\frac{\sigma_{\omega 2}}{\omega}\frac{\partial k}{\partial x_j}\frac{\partial\omega}{\partial x_j}\end{aligned} \tag{4.8}$$

$$\begin{aligned}P_k &= \min(G,\ 10\beta^* k\omega) \\ G &= \nu_t\frac{\partial u_i}{\partial x_j}\left(\frac{\partial u_i}{\partial x_j} + \frac{\partial u_j}{\partial x_i}\right) \\ \nu_t &= \frac{a_1 k}{\max(a_1\omega,\ SF_2)}\end{aligned} \tag{4.9}$$

where k is the turbulent kinetic energy, P_k is the production term of k, ν is the kinematic viscosity, ν_t is the turbulent kinematic viscosity, ω is the specific dissipation rate, S is the mean rate of strain of the flow, $\beta^* = 0.09$ and $a_1 = 0.31$. F_1 and F_2 are blending functions. F_1 is designed to be one in the near wall region (activating $k-\omega$) and zero away from the wall (activating $k-\varepsilon$) (Menter et al., 2003). The values of σ_k, σ_ω, β and γ are blended using equation (4.10) in which ϕ_1 and ϕ_2 are given in Table 4.1.

$$\phi = F_1\phi_1 + \left(1-F_1\right)\phi_2 \tag{4.10}$$

Table 4.1: Default values for ϕ_1 and ϕ_2 used in equation (4.10) to calculate σ_k, σ_ω, β and γ for the $k-\omega$ SST turbulence model.

ϕ	σ_k	σ_ω	β	γ
ϕ_1	0.85034	0.5	0.075	0.5532
ϕ_2	1.0	0.85616	0.0828	0.4403

The buoyancy term G_b is treated implicitly and the scalar $\sigma_t = 0.85$ (Devolder et al., 2017a):

$$G_b = -\frac{\nu_t}{\sigma_t}\frac{\partial \rho}{\partial x_j} g_j \tag{4.11}$$

4.2.2 Motion solver

In this study, the motion solver is restricted to one degree of freedom, only the heave motion is allowed (Z-direction). The motion solver calculates the vertical position of the body by applying Newton's second law at the current time $n+1$:

$$F^{n+1} = ma^{n+1} \tag{4.12}$$

in which F^{n+1} is the overall vertical force (including gravity) obtained with the fluid solver by integrating the pressure and shear forces acting the body's surface and a^{n+1} is the vertical acceleration of the body. Once the acceleration a^{n+1} is known, the vertical velocity v^{n+1} and the vertical position z^{n+1} during the same time $n+1$ are calculated by an integration scheme:

$$v^{n+1} = v^n + (1-\theta)a^n \Delta T + \theta a^{n+1}\Delta T \tag{4.13}$$

$$z^{n+1} = z^n + (1-\theta)v^n \Delta T + \theta v^{n+1}\Delta T \tag{4.14}$$

in which n is the previous time, $n+1$ is the current time, ΔT is the time step and θ is a blending parameter. For $\theta = 0$, the forward Euler method arises which is explicit in time. In case $\theta = 1$, the backward Euler method pops up which is fully implicit in time. Both methods are only first order accurate leading to additional numerical damping. In order to improve the accuracy of the body's motion, a second order accurate Crank-Nicolson scheme is applied for the FSI studies presented by using $\theta = 0.5$. An additional asset of the Crank-Nicolson scheme is that it preserves the total amount of energy, i.e. the sum of kinetic and potential energy.

The new position of the body z^{n+1} serves as a boundary condition for the mesh motion operation which is organised that only the highest and lowest row of cells is distorted (compressed or expanded). An example is demonstrated in Figure 4.8 and Figure 4.18 later in this paper. This methodology is implemented

to prevent undesirable mesh deformation (i.e. high non-orthogonality and skewness of the grid cells) around the air-water interface, reducing the discretisation error for the applied finite volume method. This also results in accurate simulations of a floating body using the coupled fluid–motion solver based on the VoF method. The drawback of our approach is that high aspect ratios are obtained for the distorted cells. However since those cells are not inside the zones of interest, it will not affect the accuracy of the simulations.

4.2.3 Kinematic condition

In order to have convergence between the fluid and motion solver, the following kinematic condition needs to be fulfilled at the interface between the fluid and the body:

$$u_z = v \tag{4.15}$$

in which u_z and v are the vertical fluid velocity and the vertical body's velocity respectively. As such, this velocity is used in the moving wall boundary condition at the body's interface. Note that the fluid velocities u_x and u_y are equal to $0\ m/s$ at the fluid-structure interface because only heave motion of the body is allowed.

4.3 Accelerated coupling algorithm

This section presents the accelerated coupling algorithm between a two-phase fluid solver (section 4.2.1) and a one degree of freedom (heave) motion solver (section 4.2.2). For the sake of clarity, the complexity of the fluid solver is gradually increased. Firstly, the motion solver is tested against a mock-up fluid solver which is an analytical expression describing the fluid dynamics. Secondly, an acceleration in convergence between the CFD fluid solver and the motion solver is developed to speed up the simulations in terms of CPU time.

4.3.1 Mock-up fluid solver

The coupling between a fluid and a motion solver in rigid body simulations is done by interchanging the total force acting on the body calculated by the fluid solver. For a CFD fluid solver, the force (vector notation) is calculated as the discrete sum of the pressure forces, viscous forces and the downward weight of the body:

$$\vec{F}^{n+1} = \sum_{j}^{body} (p_j \vec{n_j} A_j) + \sum_{j}^{body} (\vec{\vec{\tau}}_j \vec{n_j} A_j) - m\vec{g} \tag{4.16}$$

p_j is the pressure acting on each boundary face around the body, $\vec{\vec{\tau}}_j$ is the shear stress tensor acting on each boundary face around the body, $\vec{n_j}$ is a unit vector normal to the area A_j of boundary face j and m is the dry mass of the body.

In this subsection, the CFD fluid solver is simplified to a mock-up fluid solver: an analytical expression which calculates the total vertical force F^{n+1} on the body. The main advantage of the mock-up fluid solver is to avoid the time consuming CFD fluid solver when acquiring quick insights in the coupling algorithm. The floating body is represented by a two dimensional rectangular body in a vertical plane (2DV) which is $4\ m$ wide, $1\ m$ high and has a mass m equal to $2000\ kg/m$ (see Figure 4.2). z^{eq} is the fixed Z-coordinate of the equilibrium position of the body's Centre of Mass (CoM). In order to bring the body out of equilibrium, the position of the CoM during the initial condition is $z^n < z^{eq}$, see Figure 4.2. As a result, the water exerts an upward force on the body and the body starts to oscillate until all the forces on the body are again in equilibrium.

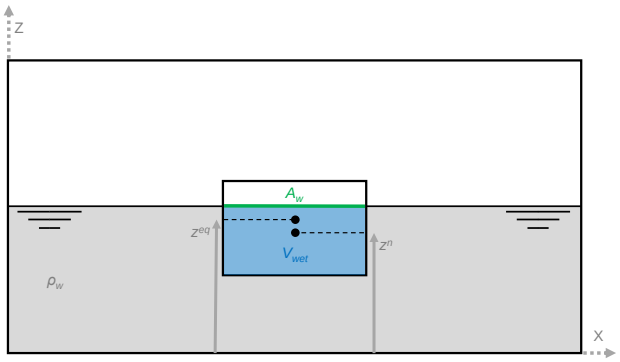

Figure 4.2: A definition sketch showing the geometry of the floating 2D rectangular body (XZ-direction, $4\ m$ wide by $1\ m$ high) with mass m equal to $2000\ kg/m$.

4.3.1.1 Hydrostatic force

The initial mock-up fluid solver takes only the upward hydrostatic force and the body's weight into account. The total vertical force on the 2D rectangular body is calculated as:

$$\begin{aligned} F^{n+1} &= \rho_w V_{wet} g - mg \\ &= -\rho_w A_{wet} g \left(z^n - z^{eq}\right) \end{aligned} \tag{4.17}$$

in which ρ_w is the density of water ($1000\ kg/m^3$), V_{wet} is the underwater volume of the body, A_{wet} is the horizontal water plane area and $z^n - z^{eq}$ is the distance between the CoM at the previous time n and the CoM in equilibrium (see Figure 4.2). Note that equation (4.17) is explicit: we use the body's position from the previous time, z^n, to calculate the force during the current time, F^{n+1}. Newton's second law, equation (4.12), is applied to derive the body's acceleration during the

current time $n+1$ by using the mock-up fluid solver (equation (4.17)):

$$\begin{aligned} a^{n+1} &= \frac{F^{n+1}}{m} \\ &= \frac{-\rho_w A_{wet} g}{m} \left(z^n - z^{eq}\right) \\ &= -\frac{k}{m} \left(z^n - z^{eq}\right) \end{aligned} \tag{4.18}$$

in which k is the restoring spring coefficient due to buoyancy and equal to $39\ 240\ kg/s^2$ for the 2D rectangular body. The mock-up fluid solver (equation (4.18)) is coupled to the motion solver (equations (4.13) and (4.14) with $\theta = 0.5$ and a fixed time step $\Delta T = 0.005\ s$). An initial displacement of $-0.25\ m$ is given to the body in order to bring it out of equilibrium ($z^0 = 4.75\ m$ and $z^{eq} = 5.0\ m$). Equations (4.18), (4.13) and (4.14) are solved consecutively and only once during every time step due to the explicit nature of the fluid–motion coupling. The resulting vertical acceleration, equation (4.18), as a function of time is shown in Figure 4.3. The progress of the acceleration matches the expectations, starting at a maximum value and reducing monotonically without any issues regarding stability or convergence.

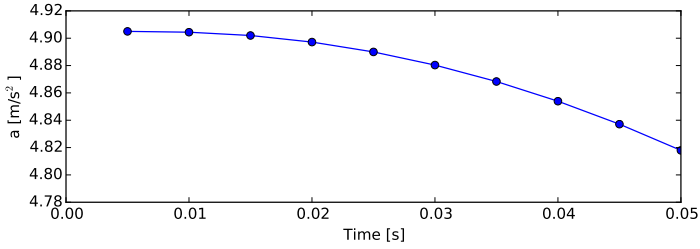

Figure 4.3: Vertical acceleration of the floating 2D rectangular body as a function of time for a fixed time step of $0.005\ s$.

4.3.1.2 Added mass effect

In a second step, the added mass effect is also considered in the explicit mock-up fluid solver:

$$m a^{n+1} = -m_a a^n - k\left(z^n - z^{eq}\right) \tag{4.19}$$

in which m_a is the added mass and a^n is the acceleration at the previous time n. This is a better approximation to the physics because all the fluid dynamics

are incorporated, except for the viscous forces (damping forces). Subsequently, equation (4.19) is rewritten to:

$$a^{n+1} = -\frac{m_a}{m}a^n - \frac{k}{m}\left(z^n - z^{eq}\right) \tag{4.20}$$

The extended mock-up fluid solver (equation (4.20)) is again coupled to the motion solver (equations (4.13) and (4.14) with $\theta = 0.5$ and a fixed time step $\Delta T = 0.005\ s$) and solved once during every time step. Three different numerical simulations are performed with $m_a/m = 0.5,\ 1.0$ and 1.5. Figure 4.4 shows the numerical results for the acceleration, equation (4.20), as a function of time. In case $m_a < m$, the oscillation in acceleration damps out. For $m_a = m$, the oscillation remains constant. For $m_a > m$, the oscillation increases and the simulation fails.

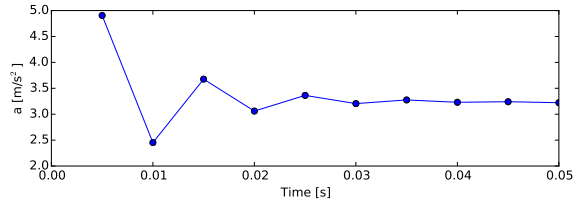

(a)

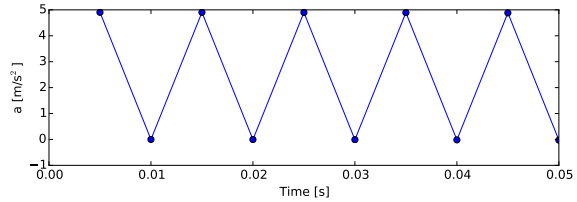

(b)

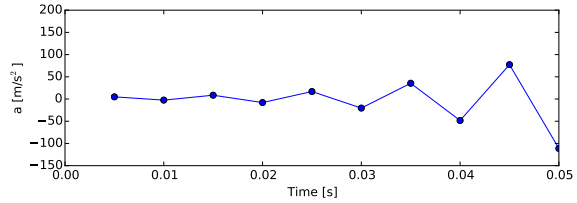

(c)

Figure 4.4: Vertical acceleration of the floating 2D rectangular body as a function of time for $m_a/m = 0.5$ (a), 1.0 (b) and 1.5 (c).

To stabilise the acceleration, equation (4.20) must be solved implicitly by using

multiple sub iterations during every time step:

$$\tilde{a}_{i+1}^{n+1} = -\frac{m_a}{m} a_i^{n+1} - \frac{k}{m}\left(z_i^{n+1} - z^{eq}\right) \tag{4.21}$$

in which $\tilde{a}_{i+1}^{n+1}$ is the intermediate value of the acceleration at the current sub iteration $i+1$ of time $n+1$, a_i^{n+1} and z_i^{n+1} are respectively the acceleration and position of the CoM from the previous sub iteration i during the same time $n+1$. Note that equation (4.21) is using explicit coupling in the sub iterations: all the variables in the right hand side are obtained during the previous sub iteration i. Additionally, relaxation of acceleration is required for a stable solution:

$$a_{i+1}^{n+1} = \alpha \tilde{a}_{i+1}^{n+1} + (1-\alpha) a_i^{n+1} \tag{4.22}$$

in which α is the relaxation factor. In order to know the stability region of the coupling scheme, a linear stability analysis is performed for the equations (4.21) and (4.22):

$$\begin{aligned} a_{i+1}^{n+1} &= \alpha \tilde{a}_{i+1}^{n+1} + (1-\alpha) a_i^{n+1} \\ &= -\alpha \frac{k}{m}\left(z_i^{n+1} - z^{eq}\right) - \alpha \frac{m_a}{m} a_i^{n+1} + (1-\alpha)\, a_i^{n+1} \\ &= -\alpha \frac{k}{m}\left(z_i^{n+1} - z^{eq}\right) + \left(1 - \alpha - \alpha \frac{m_a}{m}\right) a_i^{n+1} \\ &= -\alpha \frac{k}{m}\left(z_i^{n+1} - z^{eq}\right) + G a_i^{n+1} \end{aligned} \tag{4.23}$$

in which G is defined as the amplification factor. In order to have a stable solution, the absolute value of G must be smaller than one:

$$\begin{aligned} |G| &\leq 1 \\ G^2 &\leq 1 \\ \left(1 - \alpha - \alpha \frac{m_a}{m}\right)^2 &\leq 1 \end{aligned} \tag{4.24}$$

which results in a stability criterion for α and an optimal value, $\alpha_{optimal}$, for which G is equal to 0:

$$\alpha \leq \frac{2}{1 + m_a/m} \tag{4.25}$$

$$\alpha_{optimal} = \frac{1}{1 + m_a/m} = \frac{m}{m + m_a} \tag{4.26}$$

The stability region $|G| \leq 1$ as a function of the added mass coefficient m_a/m and α is depicted in Figure 4.5 as an unshaded area whereas the unstable region is shaded in grey. The contour lines indicate the value of the amplification factor $|G|$. The closer the relaxation factor is to its optimal value, the closer the amplification factor to zero and the lesser sub iterations are needed between the fluid and motion solver to converge. More importantly, a low number of sub iterations speeds up the simulation significantly in terms of CPU time.

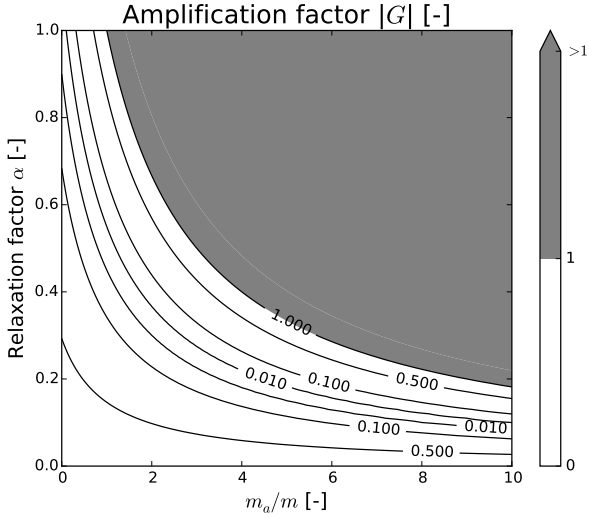

Figure 4.5: Contour plot of the amplification factor $|G|$ for the equations (4.21) and (4.22) as a function of the added mass coefficient m_a/m and the relaxation factor α. The grey shaded area is unstable whereas the decreasing values of the amplification factor are leading to faster simulation times.

The mock-up fluid solver (equation (4.22) with $m_a = 3m$) is coupled to the motion solver (equations (4.13) and (4.14) with $\theta = 0.5$ and a fixed time step $\Delta T = 0.005\ s$) and now 20 sub iterations per time step are performed. Figure 4.6 depicts the acceleration, equation (4.22), as a function of the number of sub iterations. In Figure 4.6, the red line represents the coupling scheme using a relaxation factor equal to 0.25, which is exact $\alpha_{optimal} = m/(m + m_a)$ (equation (4.26)). Only one iteration is needed to reach convergence in the acceleration. In case the relaxation factor is 0.45 (green line in Figure 4.6), convergence is reached with oscillations. With a relaxation factor of 0.05 (blue line in Figure 4.6), convergence is reached monotonically. The converged value of the acceleration during every time step is the same for the three different relaxation factors but the convergence speed is different. In order to obtain efficient simulations with a minimal number of sub iterations for cases with a significant added mass effect ($m_a > m$), the relaxation factor must not deviate too much from its optimal value (see equation (4.26)).

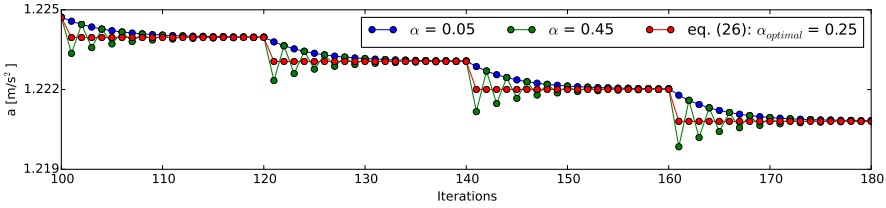

Figure 4.6: Vertical acceleration of the floating 2D rectangular body as a function of the number of sub iterations for different values of α and eq. (4.26). During each time step, 20 iterations are performed ($m_a/m = 3.0$).

4.3.2 CFD fluid solver

In the previous section 4.3.1, we have demonstrated a significant acceleration in convergence between a mock-up fluid solver and a motion solver. In case the value of the added mass is known, the optimal value for the relaxation factor is calculated by equation (4.26). In this section, we go one step further from the mock-up fluid solver to a CFD fluid solver where the value of the added mass is unknown.

4.3.2.1 Estimation of the added mass

In order to achieve an acceleration in convergence between a CFD fluid solver and a motion solver, we apply the method reported in Vierendeels et al. (2005): calculating a Jacobian. Therefore, Newton's second law in its fully implicit state, equation (4.27), is linearized to equation (4.28), resulting in equation (4.29).

$$F_{i+1}^{n+1} = m a_{i+1}^{n+1} \tag{4.27}$$

$$F_i^{n+1} + \left(\frac{dF}{da}\right)_i^{n+1} \left(a_{i+1}^{n+1} - a_i^{n+1}\right) \approx m a_{i+1}^{n+1} \tag{4.28}$$

$$a_{i+1}^{n+1} \approx \frac{F_i^{n+1} - \left(\frac{dF}{da}\right)_i^{n+1} a_i^{n+1}}{m - \left(\frac{dF}{da}\right)_i^{n+1}} \tag{4.29}$$

Note that equation (4.27) is using implicit coupling in the sub iterations: the variables on both left and right hand side are considered on the same sub iteration $i+1$. The total derivative $\left(\frac{dF}{da}\right)_i^{n+1}$ is estimated by the difference quotient:

$$\left(\frac{dF}{da}\right)_i^{n+1} \approx \frac{F_i^{n+1} - F_1^{n+1}}{a_i^{n+1} - a_1^{n+1}} \tag{4.30}$$

In order to know the physical meaning of $\left(\frac{dF}{da}\right)_i^{n+1}$, a mass-spring-damper system is assumed and the total force F_i^{n+1} is decomposed in an added mass force, a hydrodynamic damping force, a hydrostatic restoring force (i.e. buoyancy) and the sum of all other external forces:

$$F_i^{n+1} = -m_a a_i^{n+1} - b v_i^{n+1} - k(z_i^{n+1} - z^{eq}) + \sum_k F_{ext,k} \tag{4.31}$$

in which m_a is the added mass, b is the hydrodynamic damping coefficient and k is the restoring spring coefficient (see also section 4.3.1.1). z^{eq} is a fixed value representing the equilibrium position of floating body. $F_{ext,k}$ is an external force independent of the kinematic motion of the body, such as the exiting wave force or a PTO force for the case of WECs. By substituting equations (4.13) and (4.14) with $\theta = 0.5$ in equation (4.31), $\left(\frac{dF}{da}\right)_i^{n+1}$ is equal to:

$$\begin{aligned}\left(\frac{dF}{da}\right)_i^{n+1} &= \left(\frac{\partial F}{\partial a}\right)_i^{n+1}\frac{da}{da} + \left(\frac{\partial F}{\partial v}\right)_i^{n+1}\frac{dv}{da} + \left(\frac{\partial F}{\partial z}\right)_i^{n+1}\frac{dz}{da} \\ &= -m_a - b\frac{dv}{da} - k\frac{dz}{da} \\ &= -m_a - \frac{1}{2}b\Delta T - \frac{1}{4}k(\Delta T)^2\end{aligned} \tag{4.32}$$

Söding (2001) reported that a significant part of the force depends on the acceleration for fluids of substantial density such as water. If this assumption is valid, m_a is the dominating component and $b\frac{dv}{da}$ or $\frac{1}{2}b\Delta T$ and $k\frac{dz}{da}$ or $\frac{1}{4}k(\Delta T)^2$ are small values in equation (4.32). The assumption is checked later in this paper for the applications presented (see section 4.4). Consequently, $\left(\frac{dF}{da}\right)_i^{n+1}$ is approximated by:

$$\left(\frac{dF}{da}\right)_i^{n+1} \approx -m_a \tag{4.33}$$

This demonstrates a strong relation between $\left(\frac{dF}{da}\right)_i^{n+1}$ and the added mass m_a:

$$m_a \approx -\left(\frac{dF}{da}\right)_i^{n+1} \approx -\frac{F_i^{n+1} - F_1^{n+1}}{a_i^{n+1} - a_1^{n+1}} \tag{4.34}$$

In order to estimate the added mass by calculating a Jacobian, we need at least three sub iterations during every time step:

- a_1^{n+1}: the acceleration during the first sub iteration ($i = 0$);
- F_1^{n+1}: the force resulting from the hydrodynamic flow field during the first sub iteration ($i = 0$);

– F_i^{n+1}: the force resulting from the hydrodynamic flow field during the second or higher sub iteration ($i > 1$). Note that due to the numerical implementation, the force F_i^{n+1} is only called in sub iteration $i+1$ by the motion solver (see the flowchart in Figure 4.7 later in this paper).

4.3.2.2 Numerical implementation

The numerical implementation of the accelerated coupling algorithm is shown in Figure 4.7. At the start of a FSI simulation, all the variables are initialised, such as the pressure, velocity, etc. For each time step, there are $i+1$ sub iterations needed to reach convergence between the fluid and motion solver. Acceleration in convergence is obtained by computing $\left(\frac{dF}{da}\right)_i^{n+1}$ to estimate the added mass m_a for which we need at least three sub iterations (see the previous section 4.3.2.1):

1. During the first sub iteration ($i = 0$), the body's position is calculated based on the final acceleration during the previous time step a^n increased with a small constant value δ (Vierendeels et al., 2005):

$$a_{i+1}^{n+1} = a^n + \delta \tag{4.35}$$

   The value of δ is a few orders of magnitude lower (2 or 3) than the maximum acceleration and is therefore application dependent and user defined. As reported by Vierendeels et al. (2005), the hydrodynamic flow field and the kinematic motion during every time step are not sensitive to the value of δ.

2. In the second sub iteration ($i = 1$), relaxation of acceleration is performed:

$$\begin{aligned} a_{i+1}^{n+1} &= \alpha^n \tilde{a}_{i+1}^{n+1} + (1-\alpha^n) a_i^{n+1} \\ &= \alpha^n \frac{F_i^{n+1}}{m} + (1-\alpha^n) a_i^{n+1} \end{aligned} \tag{4.36}$$

   in which a_i^{n+1} is the acceleration from the first sub iteration and is equal to $a^n + \delta$. During the first time step, the relaxation factor α^n is user defined. In all the other time steps, the relaxation factor is updated based on the estimated value of m_a (equation (4.34)) during the previous time step:

$$\alpha^n = \frac{m}{m + (m_a)^n} \approx \frac{m}{m - \left(\frac{dF}{da}\right)^n} \tag{4.37}$$

   By following this methodology during the second sub iteration, we only need two sub iterations to have a convergence between the fluid and motion solver for two scenario's: (i) if the added mass is significantly smaller than the mass or (ii) if the added mass is not varying significantly between two consecutive time steps.

3. In all the following sub iterations ($i > 1$), $\left(\frac{dF}{da}\right)_i^{n+1}$ and a_{i+1}^{n+1} are calculated by equations (4.30) and (4.29) respectively. To avoid overshoots in the coupling algorithm, the estimated value of the added mass is bounded between 0 and $10m$. This assumption is valid since the added mass of a floating body cannot be negative nor exceed the value of $10m$ for practical applications in unrestricted water.

Once the acceleration is calculated in a specific sub iteration, the vertical velocity and position of the body are computed by equations (4.13) and (4.14) respectively. Subsequently, the body is moved, the mesh motion is performed and the flow equations (4.1), (4.2), (4.4), (4.7) and (4.8) are solved to obtain the hydrodynamics flow field. This iterative procedure stops until convergence between the fluid and motion solver (i.e. Newton's second law, equation (4.27)) is achieved within a certain time step. During every sub iteration ($i > 1$), the normalised residual r_i^{n+1} is calculated as:

$$r_i^{n+1} = \frac{\left|F_i^{n+1} - ma_i^{n+1}\right|}{F_{\max}} \tag{4.38}$$

in which $F_{\max}$ is a representative value for the maximum force during a simulation. The convergence criterion is formulated such that the normalised residual must be lower than a threshold, 0.001 for example (Vierendeels et al., 2005; Chow and Ng, 2016).

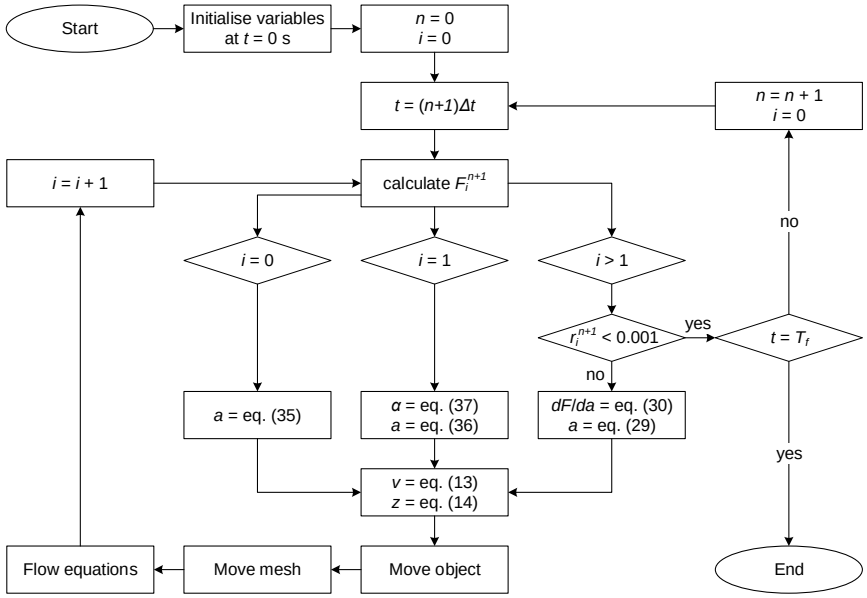

Figure 4.7: Flowchart of the coupled fluid–motion solver using an accelerated coupling algorithm. n is the time and i indicates the sub iteration.

4.4 Applications

In this section two test cases are presented using the accelerated coupling algorithm for the fluid–motion solver elaborated in section 4.3.2. For all simulations the following settings are used in the fluid solver: second order linear discretisation for the gradient and the Laplacian; first/second order bounded Van Leer scheme for the divergence operators; second order, bounded, implicit time discretisation. For every time step, maximum 50 sub iterations are performed depending on the residual calculated with equation (4.38).

4.4.1 Free decay test of a WEC

For the first application, a 3D WEC is modelled and a free decay test is performed. Numerical results are compared with experimental data which are described in previous work of the authors (Devolder et al., 2016). The same numerical method is used as reported in Devolder et al. (2016) but instead of applying a fixed relation factor for the acceleration, the accelerated coupling algorithm is used. In this study, a maximum Courant number of 0.3 and a vertical grid size Δz equal to $0.02\ m$ are used (see verification study in Devolder et al. (2016) for a fixed time step).

4.4.1.1 Computational domain

The numerical wave flume is represented by a structured grid consisting of only hexahedral cells ($139\ 058$ cells). An overview of the numerical domain around the WEC during a free decay test is depicted in Figure 4.8. In panels (a) & (b), the initial condition is shown, where blue is water, red is air and green represents $50\ \%$ water and $50\ \%$ air. In panel (c), the maximum displacement of the mesh points during the numerical simulation is visualized ($t = 0.55\ s$).

4.4.1.2 Boundary conditions

Two symmetry planes are used to reduce the amount of grid cells, see Devolder et al. (2016). The bottom and side wall of the numerical wave flume are modelled as a solid wall: a Dirichlet boundary condition is set for the velocity ($0\ m/s$ in the two directions) while the pressure and volume fraction are set to a Neumann condition. At the outlet, wave absorption is implemented using the IHFOAM toolbox (Higuera et al., 2013a,b). On all the boundary faces of the WEC, the velocity vector is set to a moving wall condition (see equation (4.15)) and the pressure and volume fraction are set to a Neumann condition. The atmospheric conditions at the top of the numerical domain are set to a mixed Dirichlet-Neumann boundary condition for the velocity, pressure and volume fraction. Finally, the value for δ in equation (4.35) is equal to $1.0\ m/s^2$.

Turbulent effects are not expected since no water impact events will happen nor separation of the flow behind the WEC will occur (low Keulegan-Carpenter number). Therefore in the first instance, only laminar solutions are generated. As shown later on, the main features of the WEC's motion and radiated wave field are already captured by using a laminar solution only.

4.4.1.3 Results

Firstly, Figure 4.9 presents the vertical position of the WEC during a free decay test with an initial displacement $z^0 = -0.124\ m$ relative to its equilibrium position. The continuous blue line represents the numerical result while the dashed red line shows the experimental data. The dashed-dotted black line depicts the analytical envelope (Devolder et al., 2016). In general, Figure 4.9 shows that the numerical result is in a very good agreement with the experimental decaying motion. After $13\ s$, some small discrepancies in the phase of the signal are observed between CFD and the experiment. This is caused by the different absorption methodology used in the numerical and experimental wave flume (Devolder et al., 2016).

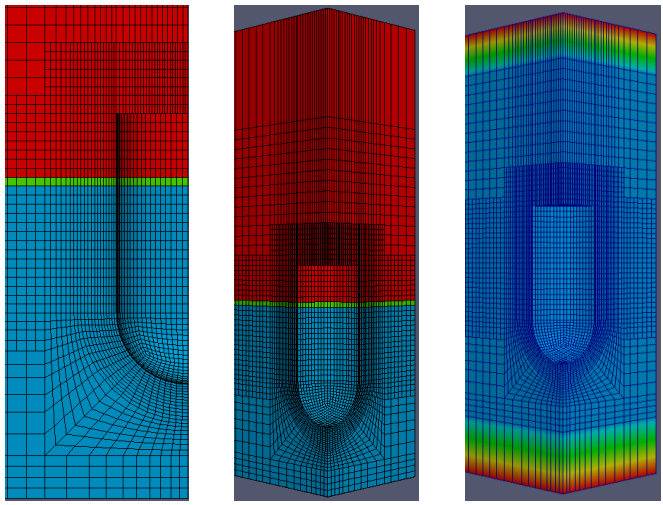

Figure 4.8: (a) 2D view, initial condition (blue = water, red = air). (b) 3D cut out, initial condition (blue = water, red = air). (c) 3D view of the maximum displacement of the mesh points during the simulation, $t = 0.55\ s$ (blue = $0.231\ m$, red = $0\ m$).

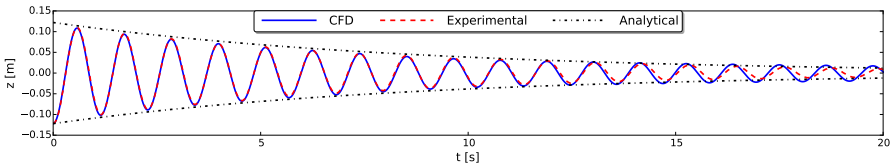

Figure 4.9: Vertical position of the WEC during a free decay test with respect to its equilibrium position ($z^{eq} = 0\ m$) obtained with CFD (continuous blue line) compared to the experimental decaying motion (dashed red line) and the analytical envelope (dashed-dotted black line).

Secondly, the radiated wave field generated by the decaying motion of the WEC in calm water is captured by five wave gauges as indicated in the plan view of the wave flume in Figure 4.10. The first gauge is installed closest to the absorbing boundary and its result is represented by the surface elevation η_1. The numerically obtained surface elevations are based on the volume fraction α in each computational cell. In a post processing step, the position of the free water surface is determined by a discrete integration of the volume fraction α over a vertical line

(Z-direction) divided in n equal parts:

$$z_{water\ level} = \sum_{i=0}^{n-1} \alpha_i \left(z_{i+1} - z_i\right) \tag{4.39}$$

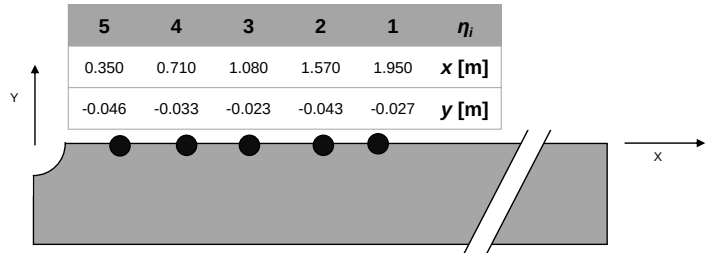

Figure 4.10: Plan view of the five wave gauges inside the numerical wave flume. The WEC's centre ($x = 0\ m$; $y = 0\ m$) is located at the upper left corner and the absorbing wave boundary condition is located at the right side of the domain ($x = 4.95\ m$).

Figure 4.11 shows the numerical and experimental results of the surface elevations. During the first 10 seconds, the amplitude as well as the phase of the radiated wave field is modelled very similar to the experimental data. Thereafter, some deviations between both results are observed. Again this observation is partially caused by the different absorption methodology used in the numerical and experimental wave flume (Devolder et al., 2016).

As mentioned in section 4.3.2.1, the accelerated coupling algorithm assumes a dominant contribution of the added mass in equation (4.32). The methodology described in Devolder et al. (2016) gives values for $k = 745\ kg/s^2$, $b = 6.19\ kg/s$ and $m_a = 3.74\ kg$ by using the time series of the WEC's decaying motion (Figure 4.9). Figure 4.12 shows the order of magnitude of each term in equation (4.32) as a function of ΔT on a log-log scale. It is demonstrated that the added mass (horizontal black line) is dominating for ΔT smaller than $0.13\ s$, which is always the case for this CFD simulation using a VoF method with a maximum Courant number of 0.3.

Figure 4.13 depicts both the added mass coefficient m_a/m based on equation (4.34) and the relaxation factor α as a function of time. It is observed that the value of the added mass coefficient is always smaller than one. Strictly speaking, the accelerated coupling algorithm is not needed to stabilise the fluid–motion coupling for this test case. However, an efficient simulation is still achieved since the number of sub iterations during every time step is mostly two or maximum three, as demonstrated in Figure 4.14. This indicates the feasibility of the accelerated coupling algorithm for floating bodies with a small added mass effect.

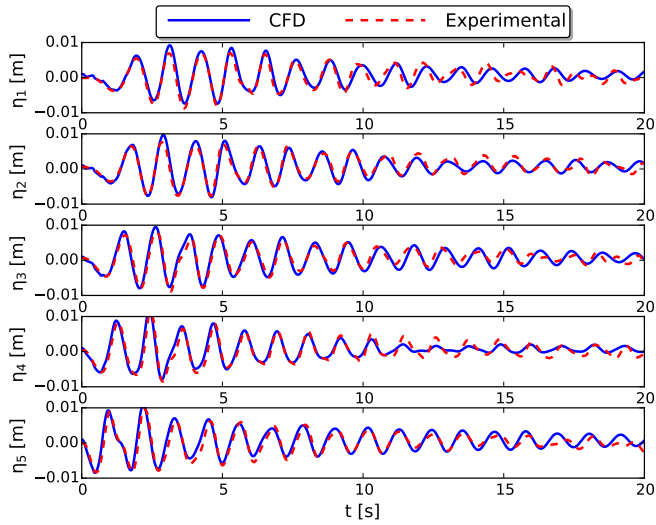

Figure 4.11: The radiated wave field between the WEC including a linear damper and the wave paddle represented by the surface elevation η_i as a function of time t.

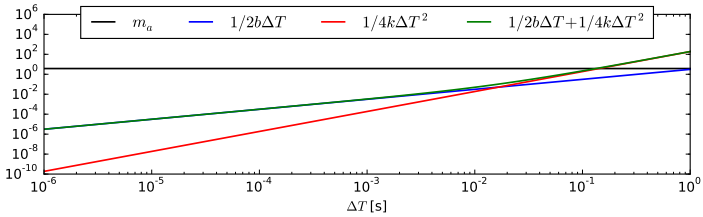

Figure 4.12: Order of magnitudes of the terms in equation (4.32) as a function of ΔT for the free decay test of a WEC ($k = 745\ kg/s^2$, $b = 6.19\ kg/s$ and $m_a = 3.74\ kg$).

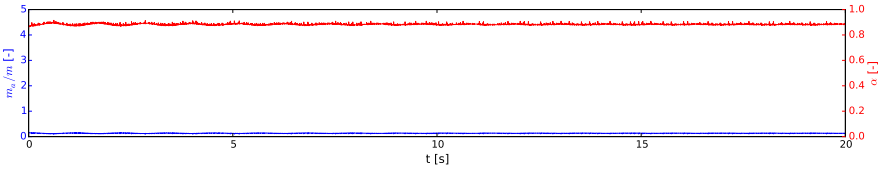

Figure 4.13: Added mass coefficient m_a/m (in blue) and relaxation parameter α (in red) as a function of time during the free decay test of a WEC.

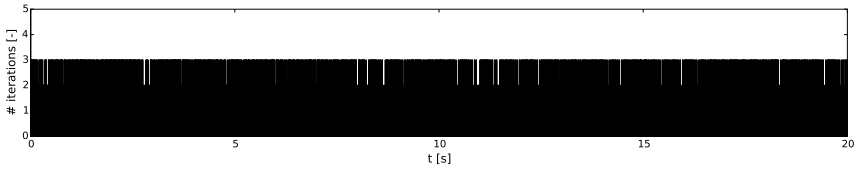

Figure 4.14: The number of sub iterations for every time step during the free decay test of a WEC.

4.4.2 Free falling wedge

The second and most challenging test case comprises a numerical verification and validation study of a free falling wedge with a significant added mass effect. Experimental data are available in Yettou et al. (2006). A definition sketch of the wedge's geometry is depicted in Figure 4.15. The wedge, with a mass of $78.33\ kg/m$, is dropped $1.0\ m$ above the water level. During the impact of the wedge with the water surface, turbulent effects are expected and a buoyancy-modified $k-\omega\ SST$ model is applied.

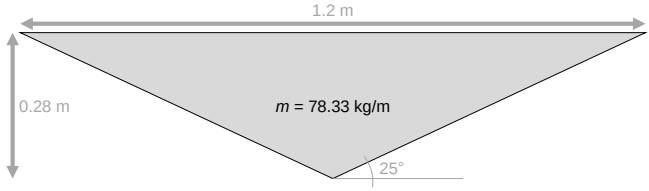

Figure 4.15: Cross section of the wedge's geometry used during the experiments performed by Yettou et al. (2006).

4.4.2.1 Computational domain

Figure 4.16 shows the computational domain of the 2DV simulation together with the boundary conditions types which are listed in the next paragraph 4.4.2.2. In order to speed up the simulations, a symmetry plane is used through the centre axis of the wedge simulating only half of the $30\ m$ long domain. The total height of the domain is $3.59\ m$ in the Z-direction and the water depth is equal to $1.0\ m$ (Yettou et al., 2006). The initial state of the wedge is shown in Figure 4.16 where the drop height above the water level is equal to $1.0\ m$.

After discretisation, the maximum size of a cell in both the horizontal X-direction Δx and vertical Z-direction Δz is equal to $0.04\ m$ for the coarsest grid (grid 1, $18\ 000$ cells). This results in an aspect ratio (i.e. the ratio of the cell size in horizontal to the vertical direction) equal to 1. The cells around the wedge

are skewed as visualised in Figure 4.17. Additionally, two more simulations are performed reducing Δx and the maximum of Δz to $0.02\ m$ and $0.01\ m$ respectively, resulting in $72\ 000$ cells (medium grid) and $285\ 000$ cells (fine grid). A summary of the three meshes is provided in Table 4.2.

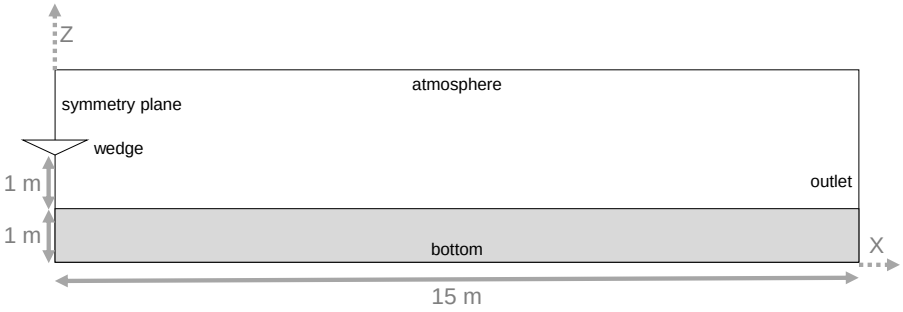

Figure 4.16: A definition sketch showing the cross-section (XZ-direction) of the computational domain. The black words characterise the boundary condition type while the grey distances indicate the key sizes.

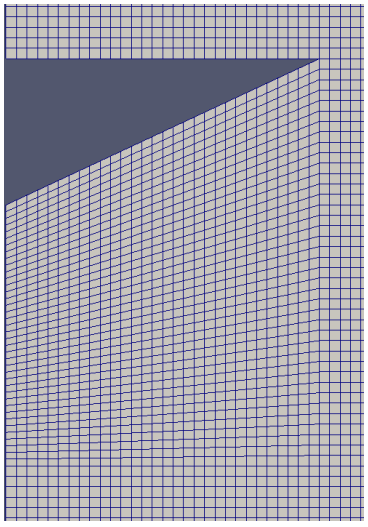

Figure 4.17: A detail of the grid around the wedge.

4.4.2.2 Boundary conditions

The types of boundary conditions in a vertical plane are given in Figure 4.16: symmetry plane on the left, outlet on the right, bottom, atmosphere and wedge.

Table 4.2: Mesh characteristics of the three different grids used.

grid	Δx and $\max(\Delta z)$	cells
coarse	$0.04\ m$	$18\ 000$
medium	$0.02\ m$	$72\ 000$
fine	$0.01\ m$	$285\ 000$

The bottom is modelled as a solid wall on which wall functions are activated for k and ω. A continuous wall function based on Spalding's law (Spalding, 1961) switching between low- and high-Reynolds numbers is implemented for the turbulent viscosity ν_t. The initial values for k and ω in the computational domain are set to $1 \times 10^{-10}\ m^2/s^2$ and $1.0\ s^{-1}$ respectively. Furthermore on the bottom, a Dirichlet boundary condition is set for the velocity ($0\ m/s$ in the two directions) while the pressure and volume fraction are set to a Neumann condition. The outlet is implemented as a fully reflective wall by using identical boundary conditions as the bottom boundary. On all the boundary faces of the wedge, similar conditions are used as the bottom boundary except for the velocity vector which is set to a moving wall condition (see equation (4.15)). The atmospheric conditions at the top of the numerical domain are set to a mixed Dirichlet-Neumann boundary condition for the velocity, pressure and volume fraction. Finally, the value for δ in equation (4.35) is equal to $1.0\ m/s^2$.

4.4.2.3 Results

In this section, the numerical results of the free falling wedge are verified and validated by using experimental data obtained by Yettou et al. (2006). Both, a mesh convergence study and temporal sensitivity study are performed followed by a discussion on the accelerated coupling algorithm. All the numerical simulations presented ran for 5 seconds. During the first $0.4\ s$, only air is present in the computational domain and consequently a single-phase flow simulation is performed. After $0.4\ s$, water is added to the domain and the two-phase flow simulation is started. This methodology is visualised in Figure 4.18 and is needed to add the correct amount of water in the domain. Due to the large drop height, the cells in the lowest row have a height Δz equal to $1.7\ m$ while the water depth during the experiment was only $1.0\ m$. Based on a preliminary simulation, Δz for the cells in the lowest row become smaller than $1.0\ m$ for $t \geq 0.4$ s.

4.4.2.3a Mesh convergence study For the mesh convergence study in this first subsection, three numerical simulations are presented using the grids mentioned in Table 4.2. A maximum Courant number of 0.3 is applied as discussed in the next subsection 4.4.2.3b. Figure 4.19, Figure 4.20 and Figure 4.21 depict respectively the vertical position, velocity and acceleration of the wedge as a function of time. The experimental data is shown using a dashed black line for the vertical position and velocity only. The numerical results are visualised by a blue, green and red line for the coarse, medium and fine grid respectively. In general, only very small differences are visually observed between the three numerical sim-

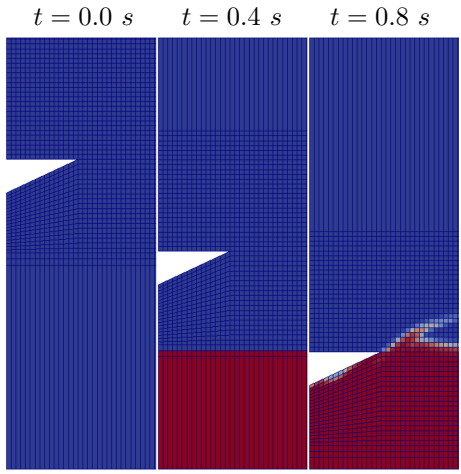

Figure 4.18: Mesh motion for the free falling wedge simulation, air is shown in blue and water is shown in red. At $t = 0\ s$, only air is present while for $t \geq 0.4\ s$, also water is included in the computational domain.

ulations. The three numerical simulations are in a very good agreement with the experimental data for the vertical position and the velocity. For the vertical velocity, discrepancies between numerical and experimental results are visible between $t = 1.4\ s$ and $t = 2\ s$. This is presumably caused by small friction forces due to the sliding mechanism in the experimental model which are neglected in the numerical setup. In Figure 4.20, the abrupt change in velocity is due to the impact of the wedge on the water surface. It is observed that the impact is modelled in a very good agreement with the experimental measurements for the velocity of the wedge. Figure 4.21 only presents numerical simulations for the vertical acceleration of the wedge as a function of time. At $t = 0.40\ s$, a spike is observed in the wedge's acceleration. This is an artefact due to the addition of water in the computational domain as explained before and visualised in Figure 4.18 but has no further impact on the results. In general, no significant differences are observed among the three numerical simulations, except for the peak values of the acceleration at the moment of impact (see detailed view in Figure 4.22). The mesh convergence study is provided in Table 4.3 based on the peak value of the acceleration during the impact of the wedge on the water surface (see Figure 4.22 around $t = 0.53\ s$). The extrapolated values are computed with Richardson's extrapolation method: $a_{extra.} = a_{medium} + (a_{fine} - a_{medium})/(1 - 2^{-\alpha})$ with $\alpha = \ln((a_{coarse} - a_{medium})/(a_{medium} - a_{fine}))/\ln(2)$. $a_{extra.}$ can be regarded as the value calculated from the exact solution. As follows from Table 4.3, the solutions converge monotonically towards the exact solution and the medium grid returns an acceptable solution with an error of $3\ \%$.

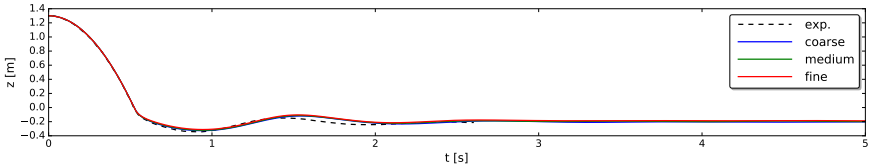

Figure 4.19: Vertical position of the wedge as a function of time obtained numerically for three meshes (see Table 4.2) with a maximum Courant number of 0.3 (blue, green and red lines) and compared to experimental data (Yettou et al., 2006) (dashed black line).

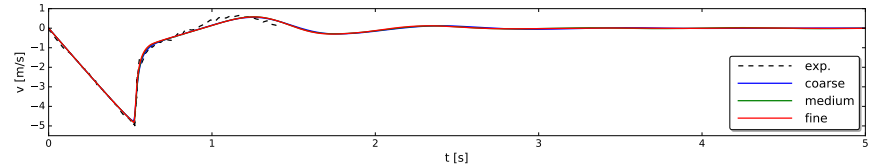

Figure 4.20: Vertical velocity of the wedge as a function of time obtained numerically for three meshes (see Table 4.2) with a maximum Courant number of 0.3 (blue, green and red lines) and compared to experimental data (Yettou et al., 2006) (dashed black line).

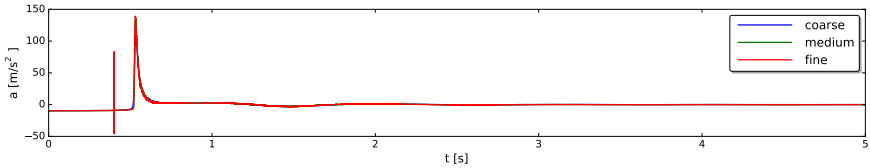

Figure 4.21: Vertical acceleration of the wedge as a function of time obtained numerically for three meshes (see Table 4.2) with a maximum Courant number of 0.3 (blue, green and red lines).

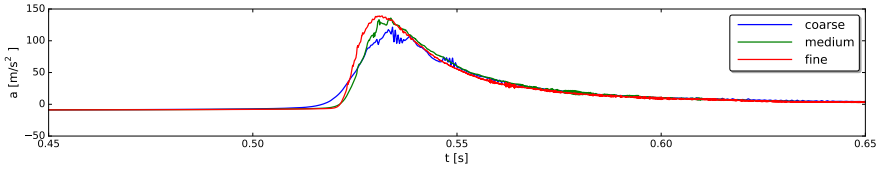

Figure 4.22: Vertical acceleration of the wedge during the impact between $t = 0.45\ s$ and $t = 0.65\ s$ obtained numerically for three meshes (see Table 4.2) with a maximum Courant number of 0.3 (blue, green and red lines).

Table 4.3: Grid refinement study for the acceleration of the wedge. N_z is the number of cells in vertical direction. a is the maximum value of the acceleration during the water impact. $a_{extra.}$ is the exact solution.

grid	N_z	$a\ [m^2/s]$	error
coarse	46	121.464	13.26 %
medium	94	135.814	3.01 %
fine	188	139.074	0.68 %
$a_{extra.}$		140.032	

4.4.2.3b Temporal sensitivity study In this second subsection, three numerical simulations are presented using a maximum Courant number of 0.5, 0.3 and 0.1 respectively. Only the medium grid is considered since an error of 3 % for the peak value of the acceleration during the water impact is found (see Table 4.2). Figure 4.23, Figure 4.24 and Figure 4.25 visualise again time series of respectively the vertical position, velocity and acceleration of the wedge. The experimental data is shown using a dashed black line while the numerical results are depicted in blue, green and red for a maximum Courant number of 0.5, 0.3 and 0.1 respectively. The same observations are made as reported in the previous subsection 4.4.2.3a: the three numerical simulations are very similar and are in a very good agreement with the experimental data for the vertical position and velocity of the wedge. Also for the acceleration, no differences are visually observed between the three numerical simulations provided in Figure 4.25. Moreover as shown in Figure 4.26, the peak value of the acceleration during the impact is not sensitive to the maximum Courant number. Based on our experience of using the VoF method for FSI simulations, we recommend a maximum Courant number of 0.3.

4.4.2.3c Acceleration of the coupling scheme The achieved acceleration for the fluid–motion coupling is discussed using the medium grid with a maximum Courant number of 0.3. Firstly as mentioned in section 4.3.2.1, the accelerated coupling algorithm requires a dominant contribution of the added mass in equation (4.32). Values for k, b and m_a are computed by using the time series of the wedge's motion. Only approximated values are calculated since they depend on the displaced volume of water which varies over time for the case of a wedge geometry:

- For k, the value at the moment of water entry is considered: $k = 4019\ kg/s^2/m$;
- For b, the methodology described in Devolder et al. (2016) leads approximately to: $b = 400\ kg/s/m$;
- For m_a, a minimum value is the most severe condition and the methodology described in Devolder et al. (2016) gives approximately: $m_a = 72\ kg/m$.

Figure 4.27 indicates that the added mass (black line) is dominating for ΔT smaller than $0.18\ s$, which is again always the case for this simulation.

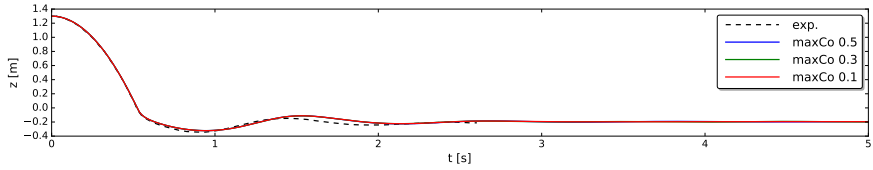

Figure 4.23: Vertical position of the wedge as a function of time obtained numerically for the medium grid (see Table 4.2) with a maximum Courant number of 0.5, 0.3 and 0.1 (blue, green and red lines) and compared to experimental data (Yettou et al., 2006) (dashed black line).

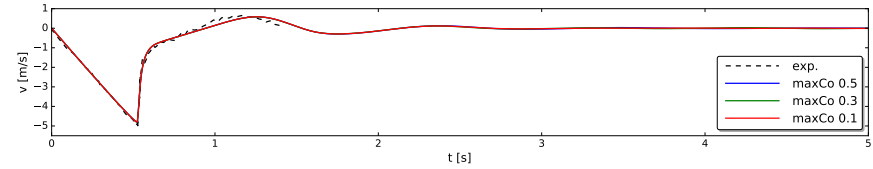

Figure 4.24: Vertical velocity of the wedge as a function of time obtained numerically for the medium grid (see Table 4.2) with a maximum Courant number of 0.5, 0.3 and 0.1 (blue, green and red lines) and compared to experimental data (Yettou et al., 2006) (dashed black line).

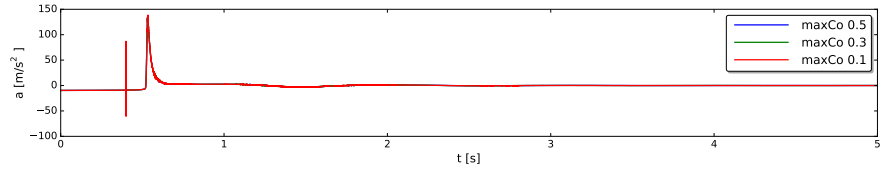

Figure 4.25: Vertical acceleration of the wedge as a function of time obtained numerically for the medium grid (see Table 4.2) with a maximum Courant number of 0.5, 0.3 and 0.1 (blue, green and red lines).

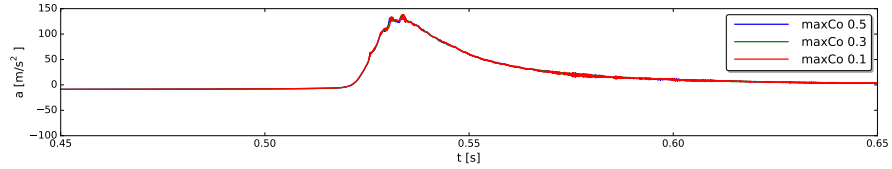

Figure 4.26: Vertical acceleration of the wedge during the impact between $t = 0.45\ s$ and $t = 0.65\ s$ obtained numerically for the medium grid (see Table 4.2) with a maximum Courant number of 0.5, 0.3 and 0.1 (blue, green and red lines).

Figure 4.28 presents both the added mass coefficient m_a/m estimated by equation (4.34) and the relaxation factor α as a function of time. Figure 4.29 depicts the number of sub iterations for every time step. Between $0\ s$ and $0.5\ s$, the wedge is freely falling towards the water surface and is surrounded by air only. Due to the low density of air, the added mass is very small and only two sub iterations during every time step are needed to reach convergence between the fluid and motion solver. Around $0.5\ s$, the wedge is impacting on the water surface and the added mass coefficient increases up to four times the mass of the wedge. As a result of our accelerated coupling algorithm, the relaxation factor lowers to reduce the number of sub iterations. Based on Figure 4.29, only a large number of sub iterations is simulated at the moment when the wedge is touching the water surface. Thereafter, the motion of the wedge is decaying and the added mass is changing over time and therefore only two, occasionally three, sub iterations are needed to obtain convergence between the fluid and motion solver.

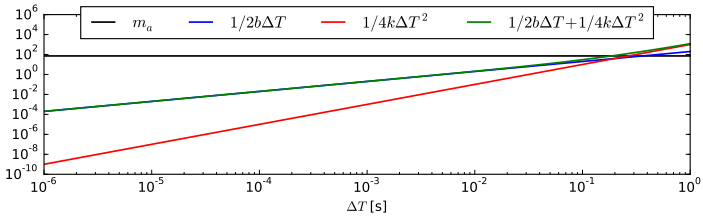

Figure 4.27: Order of magnitudes of the terms in equation (4.32) as a function of ΔT for the 2D free falling wedge ($k = 4019\ kg/s^2/m$, $b = 400\ kg/s/m$ and $m_a = 72\ kg/m$).

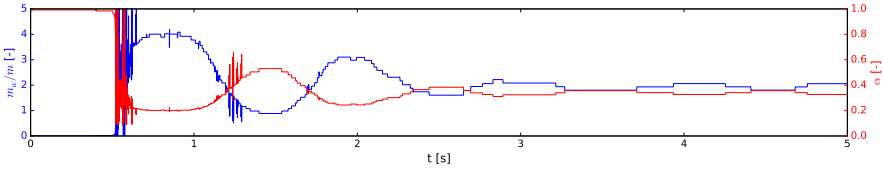

Figure 4.28: Added mass coefficient m_a/m (in blue) and relaxation parameter α (in red) as a function of time using the medium grid (see Table 4.2) with a maximum Courant number of 0.3.

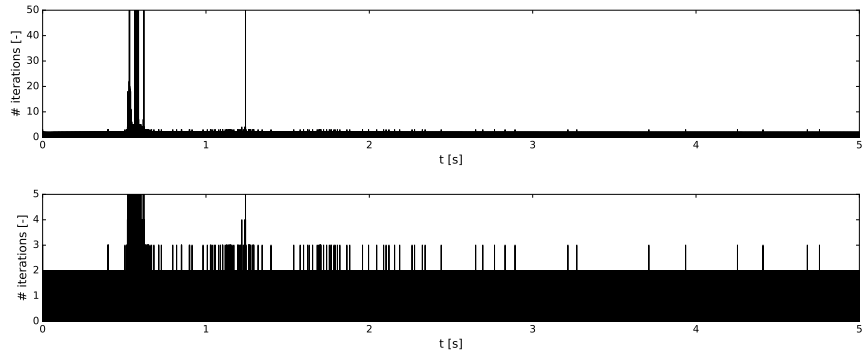

Figure 4.29: The number of sub iterations for every time step using the medium grid (see Table 4.2) with a maximum Courant number of 0.3. Top graph: maximum 50 sub iterations on the vertical axis. Bottom graph: detail of the top graph where only 5 sub iterations are shown on the vertical axis.

4.5 Conclusions

In this paper, we presented an accelerated coupling algorithm between a two-phase fluid solver and a motion solver to perform FSI simulations of a floating body. The coupling algorithm is applying multiple sub iterations during every time step in the transient simulation to reach convergence between the fluid and motion solver. The convergence speed is enhanced by using our accelerated coupling algorithm by calculating a Jacobian, based on the available solutions of previous sub iterations for the acceleration of the floating body and the force acting on it. This method results in efficient simulations for body geometries with a significant added mass effect. The coupled fluid–motion solver is applied to two different floating bodies: a free decay test of a WEC (small added mass effect) and a free falling wedge impacting the water surface (significant added mass effect). For both test cases, numerical results are validated by using experimental data. Firstly, the WEC's heave motion and radiated wave field during the free decay test are very similar to the experimental measurements. Secondly for the free falling wedge, a good agreement between numerical and experimental data is found for the wedge's vertical position and velocity. We demonstrated the successful capability of the coupled fluid–motion solver using an accelerated coupling algorithm in order to efficiently simulate heaving floating bodies with a significant reduced computational cost.

Chapter 5

Numerical simulations of a point absorber wave energy converter

In this chapter, fluid-structure interaction simulations of a single floating point absorber wave energy converter (WEC) are presented. Both free decay and regular wave tests are performed and validated with experimentally obtained data measured in the large wave flume of the department of civil engineering at Ghent University. Subsequently, the numerical simulations of a single floating point absorber WEC are extended from operational conditions to survivability conditions. A proof of concept study is presented for the design of a WEC unit under survivability conditions in order to quantify the WEC's motion and the forces acting on the WEC by simulating breaking waves impacting on the WEC in a numerical wave tank.

Sections 5.1 to 5.5 of this chapter are originally published as:
Devolder, B., Rauwoens, P., and Troch, P. (2016). Numerical simulation of a single Floating Point Absorber Wave Energy Converter using OpenFOAM®. In *Progress in Renewable Energies Offshore*, pp. 197–205. CRC Press. doi:10.1201/9781315229256-25.

Section 5.6 of this chapter is submitted for publication as:
Devolder, B., Troch, P., and Rauwoens, P. (2018). Survivability Simulation of a Wave Energy Converter in a Numerical Wave Tank, abstract accepted for the 13th OpenFOAM workshop.

Numerical simulation of a single Floating Point Absorber Wave Energy Converter using OpenFOAM®

Brecht Devolder, Pieter Rauwoens, Peter Troch
Brecht Devolder, Peter Troch, Pieter Rauwoens

Abstract
This paper uses the CFD toolbox OpenFOAM to perform numerical simulations of a single floating point absorber (FPA) Wave Energy Converter (WEC) unit inside a numerical wave flume. The Navier-Stokes fluid solver is coupled with a motion solver to simulate wave-induced rigid body motions restricted to the heave direction only. Laboratory experiments are undertaken to validate the numerical model for a free decay test and specific regular wave trains. A general methodology is reported for modelling a WEC inside a numerical wave flume taking small deviations in geometry and friction into account. Several CFD simulations are presented with varying time step and grid resolution. The obtained heave motion of the WEC during a free decay test shows a good agreement with the experimental data. In addition, the radiated wave field due to the WEC's motion is captured very accurately by the CFD solver. Even more accurate results are obtained by implementing a linear damper to take the friction in the experimental model in consideration. Subsequently, a WEC is subjected to two specific regular wave trains and both its heave motion and the perturbed wave field are in very good agreement compared to the experimental data. Finally, the numerical simulations are extended from operational conditions to survivability conditions by simulating breaking waves impacting on the WEC. OpenFOAM proofs a suitable and accurate CFD toolbox to study wave-structure interaction of a floating body.

Keywords: Wave energy; Floating point absorber; Single unit; Coupled CFD–motion solver; Verification and experimental validation; Survivability simulation

5.1 Introduction

Wave energy from ocean waves is captured by Wave Energy Converters (WECs) and converted into electrical power. In this study, WECs of the floating point absorber (FPA) type are selected. Their geometry is represented by a cylindrical buoy with a spherical end. The focus of this study is limited to a single WEC. However, this is a starting point for wave farm modelling in which the interaction between multiple closely spaced WECs will be analysed.

Prior to the analysis of farm effects, the flow field around a single WEC unit has to be understood in detail. Therefore, a Computational Fluid Dynamics (CFD) toolbox, OpenFOAM® (2015b), is used to solve the three dimensional flow field around and the motion of the WEC in a numerical wave flume. CFD is able to include viscous, turbulent and non-linear effects which may be absent in simplified radiation-diffraction models such as potential flow solvers based on boundary element methods.

The main focus of the paper is put on the numerical simulation of a free decay test of a heaving WEC. The WEC is initially placed out of equilibrium and released, leading to a damped oscillatory motion until all the forces acting on that WEC are in equilibrium. Moreover, the motion of the WEC generates radiated waves with decreasing wave heights away from the WEC. Simulations are performed in order to compare solely the radiated wave field and the motion of the heaving WEC with experimental data measured in a wave flume. The purpose of the simulations is to assess the ability and accuracy of the coupled CFD–motion solver to simulate wave propagation of the radiated wave field. A few authors already reported free decay tests. Stratigaki (2014) performed an experimental free decay test in a wave flume. Davidson et al. (2015b) simulated multiple free decay tests with OpenFOAM indicating nonlinearities. Stansby et al. (2015) reported a free decay test of a heaving WEC using STAR CCM+ and compared this with experimental data.

The second part of the paper is dedicated to present CFD simulations of a single WEC unit subjected to two specific regular wave trains. Only the heave motion of the WEC is considered and together with the perturbed wave field validated against laboratory results. The capability of OpenFOAM to study wave-body interactions is already reported by Davidson et al. (2015a). Wolgamot and Fitzgerald (2015) provided an excellent description and comparison of the different numerical models for wave energy devices. Moreover, they mentioned that good agreements have been obtained between CFD and experimental results.

5.2 Experimental setup

An experimental model is installed in the large wave flume of the Department of Civil Engineering at Ghent University ($30\ m \times 1\ m \times 1.2\ m$). An overview of the setup is shown in Figure 5.1a. The WEC is installed $4.95\ m$ away from the wave paddle in an uniform water depth of $0.70\ m$. During the free decay tests, only active wave absorption is activated at the wave paddle to absorb the radiated

waves. Furthermore, five wave gauges sampling at $40\ Hz$ are installed in between the wave paddle and the WEC. Behind the WEC, a mild-slope foreshore is installed followed by a beach to absorb the radiated waves.

The WEC's geometry is sketched in Figure 5.1b. This WEC is characterised by a mass m of $20.605\ kg$, a total height h_{WEC} of $0.60\ m$, a diameter D of $0.315\ m$ and a draft d_{WEC} of $0.3232\ m$. A steel shaft of $4\ cm$ by $4\ cm$ with a gravity metal base is installed through the WEC to simulate the heave motion only. Therefore, a square shaft bearing of $4.45\ cm$ by $4.45\ cm$ is present inside the WEC. Friction between the steel shaft and the WEC is limited by using PTFE-bearings at the top and at the bottom.

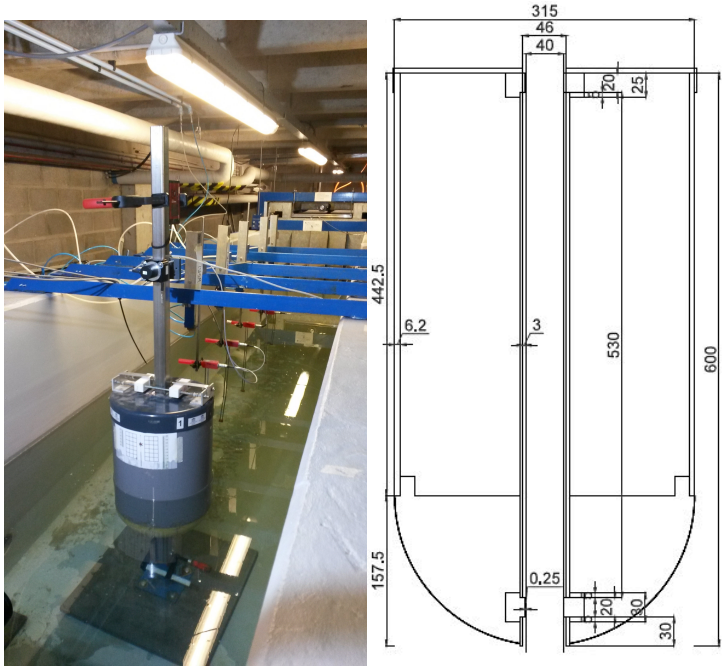

(a) **(b)**

Figure 5.1: (a) Overview of the experimental setup: WEC, steel shaft, five wave gauges and the wave paddle of the wave flume. (b) Design drawing of the WEC (dimensions in mm). Cross section showing the two PTFE-bearings at the top and bottom. The steel shaft passes through a shaft bearing along the entire length of the WEC. Adopted from Stratigaki (2014).

During all the free decay tests reported, the WEC is placed out of equilibrium by pushing it $12.4\ cm$ down ($q_0 = -0.124\ m$). A GoPro HERO4 video camera is used to capture the motion of the WEC with 60 frames per second. A marker is installed on the WEC to extract that motion from the recordings in terms of a displacement with respect to the WEC's equilibrium position. However, each frame

of the video file is corrected to remove the lens distortion (fish-eye effect). This post processing step results in a motion of the marker in one undistorted vertical plane. By following this approach, very accurate results are generated from the video files recorded.

5.3 Numerical framework

Numerical modelling is performed to study the behaviour of a single WEC unit in a numerical wave flume. The two-phase flow solver with dynamic mesh handling, *interDyMFoam*, is available in OpenFOAM to investigate the flow field around and the response of a floating body.

Simulations of the two-phase flow field are performed by using the incompressible Navier-Stokes equations. Turbulent effects are not expected since the flow of the simulations presented is always characterised by a low Keulegan-Carpenter number. In that case, no separation of the flow behind the WEC will occur according to Sumer and Fredsøe (1997). Therefore in the first instance, only laminar solutions are generated. However, turbulence may become important during some simulations and this will be included in further research. As shown later on, the main features of the WEC's motion and perturbed wave field are already captured by using a laminar solution only. Boundary conditions for wave generation and absorption are adopted from the IHFOAM toolbox (Higuera et al., 2013a,b). For all simulations the following settings are used: second order linear discretisation for the gradient and the Laplacian; first/second order bounded Van Leer scheme for the divergence operators; second order, bounded, implicit time discretisation.

The CFD-fluid solver is coupled with a motion solver in order to simulate rigid body motions. Only the governing motion of the WEC's behaviour is considered, the heave motion. This assumption allows a reduction from a six to a one degree of freedom motion. A second order accurate Crank-Nicolson integration scheme is used to derive the new position of the WEC from its acceleration. The acceleration itself is based on Newton's second law: $F = ma$ in which the force F is the sum of the pressure, shear and gravity forces acting on all the boundary faces of the WEC. Four implicit iterations are performed during every time step in order have a converged solution between the fluid and motion solver (Devolder et al., 2015).

5.3.1 Computational domain

All the simulations presented are performed in a numerical wave flume which represents the physical wave flume as good as possible. However, some simplifications are made in order to obtain economical simulation times. Firstly, a vertical symmetry plane through the centre of the WEC is implemented over the length over the wave flume. This is justified because the WEC is installed in the middle of the flume and no asymmetric effects are expected (low Keulegan-Carpenter numbers). This simplification is valid for both the free decay test and the two regular wave trains. Secondly, another vertical symmetry plane through the centre of the WEC is modelled over the width of the wave flume. This second symmetry plane is only

used during free decay simulations. This assumption is motivated as follows. On the physical wave paddle, wave generation is not activated during a free decay test. Only active wave absorption is used. On the other side of the WEC, an absorbing beach is installed in the wave flume, which behaves similar as the active wave absorption at the paddle. Because modelling the absorbing beach with CFD is too complicated, a second symmetry plane is implemented in the numerical model. This means that the absorbing beach is modelled as a wave absorption boundary. The dimensions of the numerical wave flume including two symmetry planes are $4.95\ m \times 0.5\ m \times 1.8\ m$.

Each boundary of the computational domain needs specific boundary conditions. At the outlet, wave absorption is implemented using the IHFOAM toolbox. The side wall of the flume is set to a no-slip condition and behaves as a fully reflective structure. On all the boundary faces of the WEC, the velocity vector is set to a moving wall condition.

The numerical wave flume is represented by a structured grid consisting of only hexahedral cells. An overview of the numerical domain around the WEC during a free decay test is depicted in Figure 5.2. In panels (a) & (b), the initial condition is shown, where blue is water, red is air and green represents $50\ \%$ water and $50\ \%$ air. While in panel (c), the maximum displacement of the mesh points during a simulation is visualized ($t = 0.55\ s$). Only the lowest and highest row of cells are distorted. This is implemented to prevent undesirable mesh deformation around the interface between water and air.

5.3.2 Free surface

The free surface between water and air is obtained by the Volume of Fluid (VoF) method (Hirt and Nichols, 1981). The method is based on a volume fraction α which is 0 for a completely dry cell and 1 for a completely wet cell and in between 0 and 1 for an interface cell containing both water and air. In a post processing step, the position of the free water surface (sampled at $50\ Hz$) is determined by a discrete integration of the volume fraction α over a vertical line (Z-direction) divided in n equal parts:

$$z_{water\ level} = \sum_{i=0}^{n-1} \alpha_i (z_{i+1} - z_i) \tag{5.1}$$

5.3.3 Rigid body motion

During a free decay test, the WEC is placed out of equilibrium, released and a damped oscillatory motion is started. Moreover, this motion can be described mathematically by hydrodynamic parameters such as the damping ratio ζ_d, natural angular frequency ω_n and damped angular frequency ω_d. These parameters depend on the WEC's mass m (including added mass m_a) and shape. In order to compare experimental and numerical results, an identical WEC geometry is needed. Because of the complexity of meshing the shaft bearing inside the WEC, another

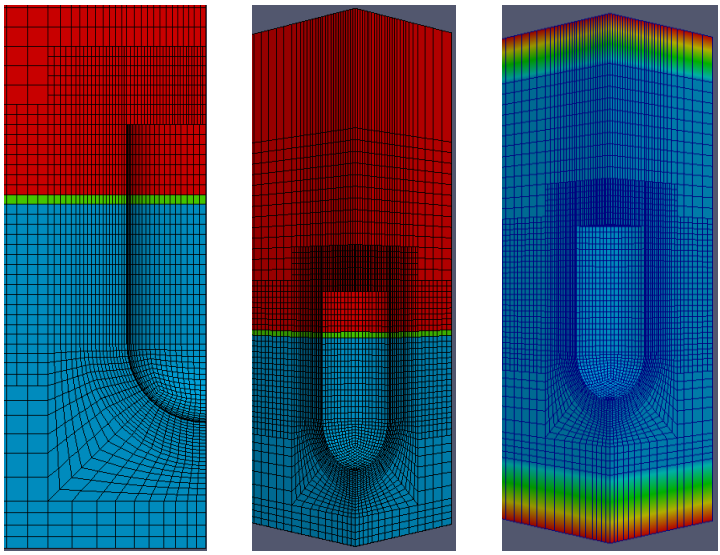

Figure 5.2: (a) 2D view, initial condition (blue = water, red = air). (b) 3D view, initial condition (blue = water, red = air). (c) 3D view of the maximum displacement of the mesh points during the simulation, $t = 0.55\ s$ (blue = $0.231\ m$, red = $0\ m$).

methodology is formulated to obtain a grid around the WEC without that vertical shaft (see Figure 5.2). The shaft inside the physical WEC reduces the water-plane area A_w. Interestingly, this water-plane area is an important parameter to determine the natural frequency ω_n of the WEC. Moreover, the natural frequency is also dependent on the mass m and added mass m_a of the WEC. Therefore a WEC without vertical shaft but with a modified mass m_{num} is implemented in OpenFOAM. This is done to obtain the same natural frequency as the physical WEC, assuming that the damping ratio ζ_d and added mass m_a are identical in both experimental and numerical models, see equation (5.2). The modified-mass method can be derived starting from the expression in equation (5.2). Subsequently, the damped frequency ω_d in both numerical and experimental models are rewritten by using equations (5.3) and (5.4). Finally, this procedure returns equation (5.5) which calculates the modified mass m_{num} needed in the numerical model to satisfy equation (5.2).

$$\omega_{d,num} = \omega_{d,exp} \tag{5.2}$$

$$\omega_d = \omega_n \sqrt{1 - \zeta_d^2} \tag{5.3}$$

$$\omega_n = \sqrt{\frac{\rho g A_w}{m + m_a}} \tag{5.4}$$

$$m_{num} = m_{exp}\left[\left(1 + \frac{m_a}{m_{\exp}}\right)\frac{A_{w,num}}{A_{w,exp}} - \frac{m_a}{m_{exp}}\right] \tag{5.5}$$

The only way to obtain the damping ratio ζ_d and added mass m_a for the physical WEC including the shaft bearing is by performing a free decay test in an experimental laboratory. A frequency analysis of the WEC's experimental decaying motion returns its damped natural frequency ω_d, $5.53\ rad/s$ and its damped natural period T_d, $1.136\ s$. The damping ratio is determined based on methodology mentioned in Stratigaki (2014), $\zeta_d = 0.0224$. When these two parameters are known, the added mass m_a of the WEC during the experiment can be calculated by using equations (5.3) and (5.4): $3.74\ kg$. Finally equation (5.5) gives the modified mass of the WEC equal to $21.24\ kg$.

5.4 Results & Discussion

This section presents the results of both the experimental and numerical models. First the motion of the WEC is given in function of the time during a free decay test and compared to experimental data. Different numerical simulations are presented to show the influence of the time step and grid density. The WEC's mass implemented in CFD is determined based on the methodology explained in the previous subsection 5.3.3. Subsequently, the radiated wave field during the same free decay test is analysed and compared to the experimental result. Finally, numerical and experimental results of both the heave motion of and the perturbed wave field near the WEC subjected to two specific regular wave trains are presented and discussed.

5.4.1 Motion of the WEC during a free decay test

The motion of the WEC is simulated using different fixed time steps Δt: $0.005\ s$, $0.0025\ s$ and $0.001\ s$. Moreover, the influence of the grid spacing is analysed by using two cell heights Δz around the interface between water and air of $0.02\ m$ ($139\ 058$ cells) and $0.01\ m$ ($1\ 088\ 660$ cells) respectively.

Figure 5.3 presents the vertical position of the WEC during a free decay test with an initial displacement $q_0 = -0.124\ m$ relative to its equilibrium position ($\Delta t = 0.001\ s$, $\Delta z = 0.02\ m$). The continuous blue line represents the numerical result while the dashed red line shows the experimental data. The dashed-dotted black line depicts the analytical envelope (see Stratigaki (2014)). In general, the figure proves that this numerical result is extremely close to the experimental decaying motion. After $13\ s$, some small discrepancies in the phase of the signal are observed between CFD and the experiment. This is addressed to the different absorption methodology in numerical and experimental model. Moreover, small deviations in

the amplitude of the WEC's motion are visible after $13\ s$ which are discussed in the next paragraphs.

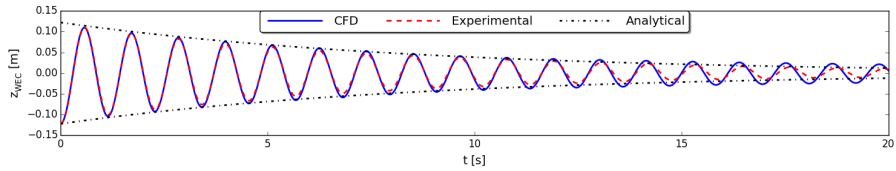

Figure 5.3: Vertical position of the WEC during a free decay test with respect to its equilibrium position ($z_{WEC} = 0\ m$) obtained with CFD (continuous blue line, $\Delta t = 0.001\ s$, $\Delta z = 0.02\ m$) compared to the experimental decaying motion (dashed red line) and the analytical envelope (dashed-dotted black line).

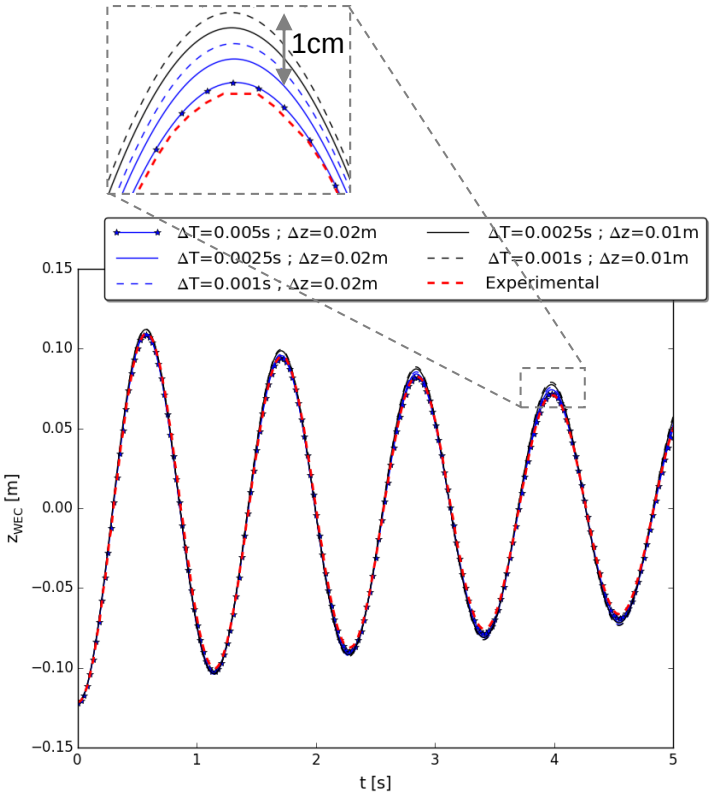

Figure 5.4: Vertical position of the WEC for various simulations during a free decay test with respect to its equilibrium position ($z_{WEC} = 0\ m$) compared to experimental data (dashed red line).

In order to compare different time steps and grid resolutions, a narrower time window is needed to observe the differences in the motion of the WEC. Therefore,

only the first five seconds are shown in Figure 5.4. In general, the differences between all the numerical simulations are very small. However, when the data is zoomed towards a peak in the position of the WEC ($3.85\ s$ – $4.10\ s$), differences up to almost $1\ cm$ are observed between the lowest and highest peak. More importantly, the different simulations are converging towards a grid- and time-independent solution. The peak becomes higher when the time step decreases or the vertical grid size becomes smaller. This means that additional numerical damping is introduced when the time step is larger or when the grid is too coarse. Interestingly, the result of the largest time step and coarsest mesh is the closest to the experimental data. This phenomenon is dedicated to friction in the experimental model which is absent in the CFD model. A vertical shaft is installed through a shaft bearing. This means that there is a motion of a viscous fluid, water, in the underwater space between the steel shaft and the shaft bearing. This flow can be simplified as a Couette flow between two parallel plates of which one is moving relative to the other. However, this Couette flow is not modelled numerically because the WEC's shaft bearing is absent in the computational mesh. For example, a smaller damping ratio is observed with CFD ($\zeta_d = 0.0215$, $\Delta t = 0.001\ s$, $\Delta z = 0.02\ m$) compared to the experiment ($\zeta_d = 0.0224$). However, the influence of that friction is almost negligible if the amplitudes of motion are large enough. Nevertheless, an attempt to model the Couette flow is reported in the next paragraph.

In order to model the Couette flow between the steel shaft and the shaft bearing, the damping characteristics are adapted. This Couette flow causes a viscous force on the WEC acting parallel to its motion. This force is dependent on the viscosity of water, the space between the plates and the velocity. However, a simplified model is assumed by only including the velocity v explicitly using a linear damper ($F = -cv$) in which c is the damping coefficient. As expressed in equation (5.6), the damping ratio ζ_d in both numerical and experimental model is calculated and equal to the ratio of the damping coefficient b_d and the critical damping coefficient b_c. The target damping coefficient $b_{d,target}$ is calculated by equation (5.6) using the experimental damping ratio (0.0224) and the modified mass of the WEC ($21.24\ kg$). Subsequently, the numerical damping coefficient $b_{d,num}$ is determined following the same equation (5.6) but now using the numerical damping ratio (0.0215). This numerical damping ratio is obtained from a CFD simulation without linear damper. Finally, the difference between both damping coefficients is used as the damping coefficient c equal to $0.2487\ kg/s$ of the linear damper to account for the Couette flow, see equation (5.7).

$$\zeta_d = \frac{b_d}{b_c} = \frac{b_d}{2\omega_n(m + m_a)} \tag{5.6}$$

$$c = \Delta b_d = b_{d,target} - b_{d,num} \tag{5.7}$$

The numerical results, including a linear damper, are shown in Figure 5.5. Only simulations using a linear damper (LD in Figure 5.5) for $\Delta t = 0.0025\ s$ and $0.001\ s$

with $\Delta z = 0.02\ m$ are shown. In general, the differences between the numerical simulations seem very small. However, if the data is zoomed in between $t = 3.85\ s$ and $4.10\ s$, differences become visible around the peak: the linear damper reduces the peak value of the WEC's heave motion. As indicated by Figure 5.5, the case with $\Delta t = 0.001\ s$, $\Delta z = 0.02\ m$ and including a linear damper (dashed black line) is very close to the experimental data (dashed red line). This proves that a linear damper is able to simulate the Couette flow between the steel shaft and the WEC's shaft bearing accurately.

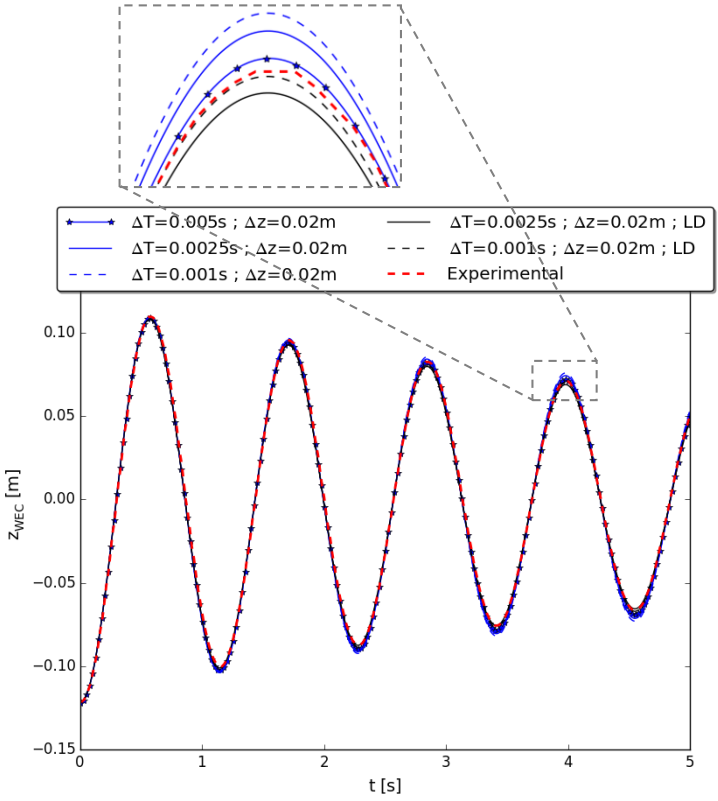

Figure 5.5: Vertical position of the WEC for various simulations during a free decay test with respect to its equilibrium position ($z_{WEC} = 0\ m$) compared to experimental data (dashed red line).

Figure 5.6 presents a simulation ($\Delta t = 0.001\ s$, $\Delta z = 0.02\ m$) for a larger time window together with the experimental data and the analytical envelope. Comparing Figure 5.3 and Figure 5.6 reveals that using a linear damper returns even more accurate results. For example, after $13\ s$, the amplitude of the numerical data is closer to the experimental one. However, the difference in phase of both signals is still observed after $13\ s$ due to the different absorption strategies used in the numerical and experimental model.

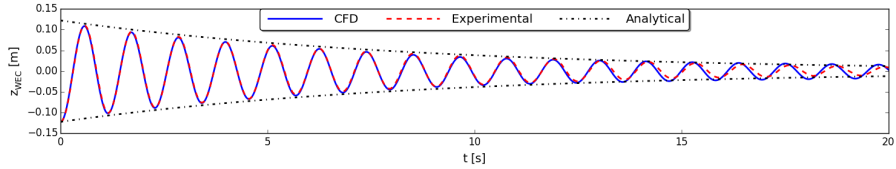

Figure 5.6: Vertical position of the WEC including a linear damper during a free decay test with respect to its equilibrium position ($z_{WEC} = 0\ m$) obtained with CFD (continuous blue line, $\Delta t = 0.001\ s$, $\Delta z = 0.02\ m$) compared to the experimental decaying motion (dashed red line) and the analytical envelope (dashed-dotted black line).

5.4.2 Radiated wave field near the WEC during a free decay test

Not only the motion of the WEC is recorded during the experimental free decay tests but also the radiated wave field is captured by five wave gauges. The same positions of the physical wave gauges are used inside the numerical model to extract free surface elevations using equation (5.1). The positions of those wave gauges inside the numerical wave flume are sketched in Figure 5.7. The wave gauges are installed in between the absorbing wave boundary (right) and the WEC (upper left corner). The first gauge is installed closest to the right boundary and its result is represented by the surface elevation η_1. The fifth gauge η_5 is then closest to the WEC.

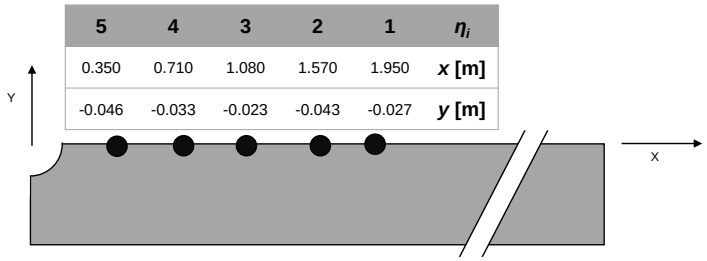

Figure 5.7: Plan view of the five wave gauges inside the numerical wave flume. The WEC's centre ($x = 0\ m$; $y = 0\ m$) is located at the upper left corner of the computational domain. The absorbing wave boundary condition is located at the right side of the domain ($x = 4.95\ m$).

Figure 5.8 shows the numerical ($\Delta t = 0.001\ s$, $\Delta z = 0.02\ m$) and experimental results of those five wave gauges. Again, a linear damper is implemented to take the Couette flow into account because the numerical WEC's motion was the closest to the experimental data. Moreover, it is this motion which is responsible for the

generation of those radiated waves. However, the radiated wave field is not influenced significantly by using a linear damper. The maximum observed amplitude of these radiated waves is smaller than $1\ cm$. Although these small-amplitude waves, both results are very similar. In the first 10 seconds of the signals, the amplitude as well as the phase of the radiated wave field is modelled close to the experimental results. Thereafter, some deviations between both results are observed.

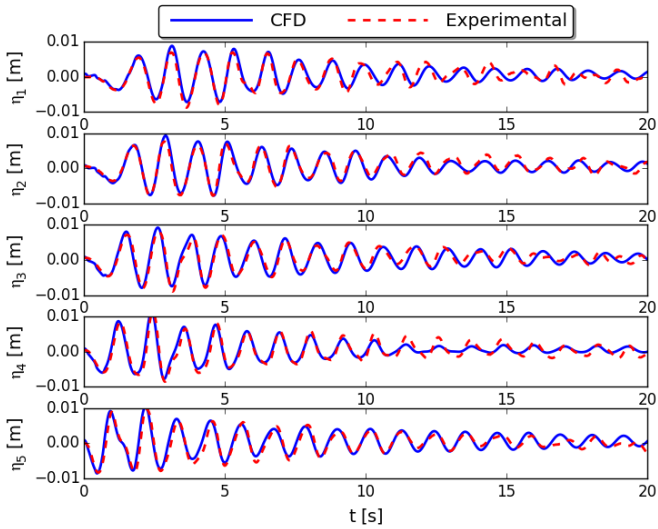

Figure 5.8: The radiated wave field between the WEC including a linear damper and the wave paddle represented by the surface elevation η_i in function of time t ($\Delta t = 0.001\ s$, $\Delta z = 0.02\ m$).

5.4.3 Motion of the WEC subjected to regular wave trains

This section focusses on simulations of a heaving WEC inside a wave flume subjected to regular waves. Again, a water depth of $0.70\ m$ is maintained while now two regular wave trains are generated at the inlet. They are characterised by a wave height H equal to $0.04\ m$ and a wave period T of $1.60\ s$ and $1.14\ s$ respectively. Three additional wave gauges (η_6, η_7 and η_8) are installed to capture the surface elevations in the wake behind the WEC.

Because longer time series are simulated, the time step is set automatically according to a maximum Courant number of 0.3 (fastest simulation speed for a certain level of accuracy). Moreover, only one symmetry plane is implemented due to the different behaviour of the inlet (wave generation & absorption) and outlet (only absorption). The dimensions of the numerical wave flume including one symmetry plane are $9.90\ m \times 0.5\ m \times 1.6\ m$ ($\Delta z = 0.01\ m$; $251\ 344$ cells).

Figure 5.9 visualises both the numerical and experimental result for the first wave train ($H = 0.04\ m$; $T = 1.60\ s$). The numerical model captures the WEC's

motion very close to the experimental data. Moreover, the amplitude of the WEC's motion is about $0.02\ m$ which is the same as the amplitude of the waves ($50\ \%$ of the wave height). This is because the first wave train has a wave period of $1.60\ s$ which is significantly higher than the natural period of the WEC, $1.136\ s$. This means that the WEC follows the motion of these relatively long waves without any amplification of its motion.

Figure 5.11 shows the perturbed wave field near the WEC for both the numerical and experimental model. In general, the results are similar to each other. However, small discrepancies are visible which may be addressed to slightly different positions of the wave gauges in both models. For all the wave gauges, the same wave height is observed in general. This means that the WEC is not disturbing the flow significantly.

Figure 5.10 gives both the numerical and experimental results for the second wave train ($H = 0.04\ m$; $T = 1.14\ s$). Again, both results are similar to each other. However, the amplitude of the WEC's motion is significantly larger than the amplitude of the waves, $0.10\ m$ versus $0.02\ m$. This is because the second wave train has a wave period close to the natural period of the WEC, $1.136\ s$. In such a case, resonance occurs and the viscous force contribution is important to dampen the WEC's motion.

Figure 5.12 shows the perturbed wave field near the WEC for both the numerical and experimental model which are again similar to each other. In contrast to the first wave train, the wave height varies significantly near the WEC. In this case, the WEC disturbs the flow significantly. In front of the WEC (η_1 to η_5), an extremely perturbed wave field is observed consisting of incident waves, reflected waves and large radiated waves. Behind the WEC (η_6 to η_8), a wake is present in which the wave height is reduced from $4\ cm$ to about $2\ cm$.

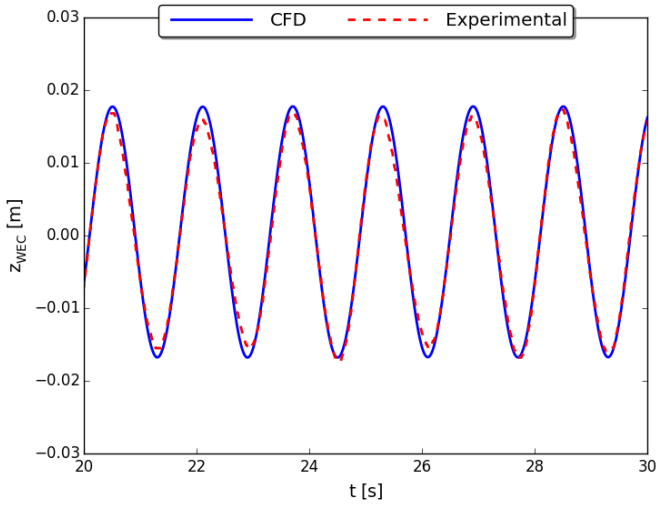

Figure 5.9: Vertical position of the WEC subjected to regular waves ($H = 0.04\ m$; $T = 1.60\ s$) with respect to its equilibrium position ($z_{WEC} = 0\ m$).

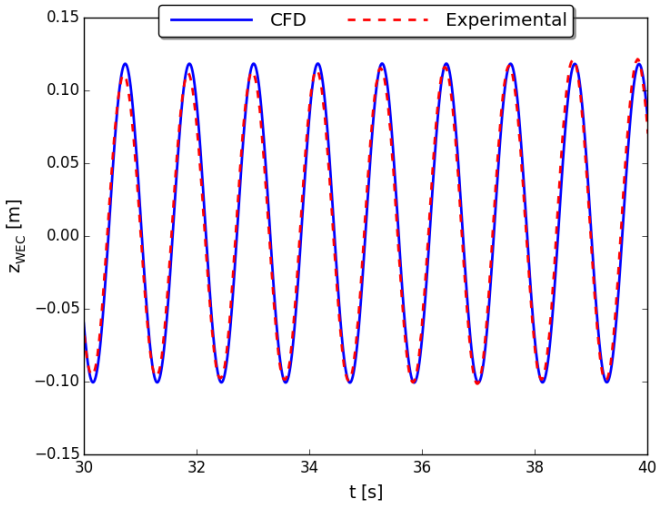

Figure 5.10: Vertical position of the WEC subjected to regular waves ($H = 0.04\ m$; $T = 1.14\ s$) with respect to its equilibrium position ($z_{WEC} = 0\ m$).

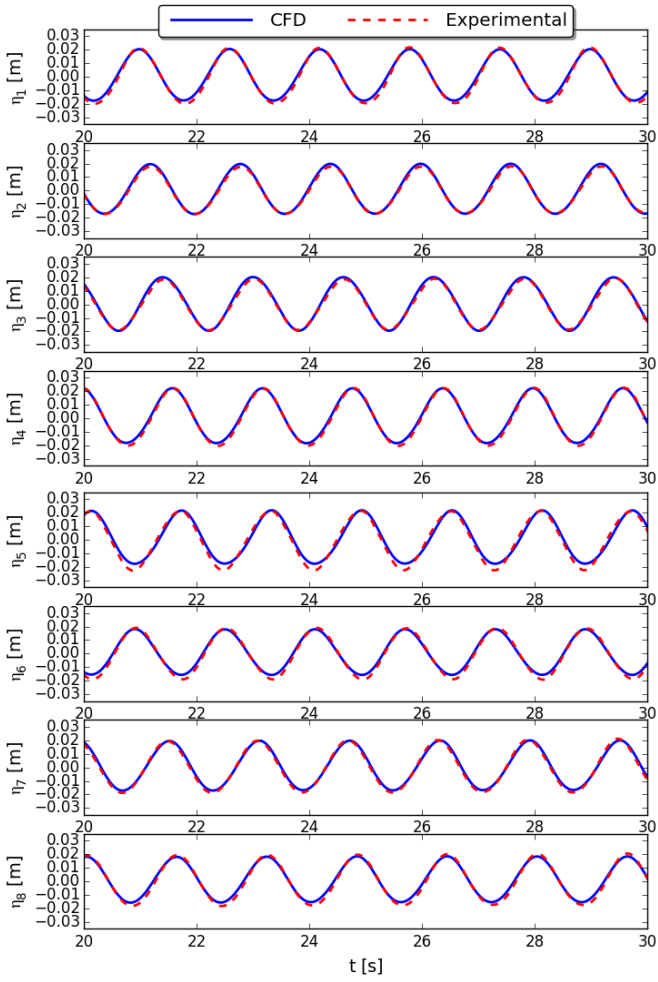

Figure 5.11: Perturbed wave field near the WEC subjected to regular waves ($H = 0.04\ m$; $T = 1.60\ s$) represented by the surface elevation η_i in function of time t ($\Delta t = 0.001\ s$, $\Delta z = 0.02\ m$).

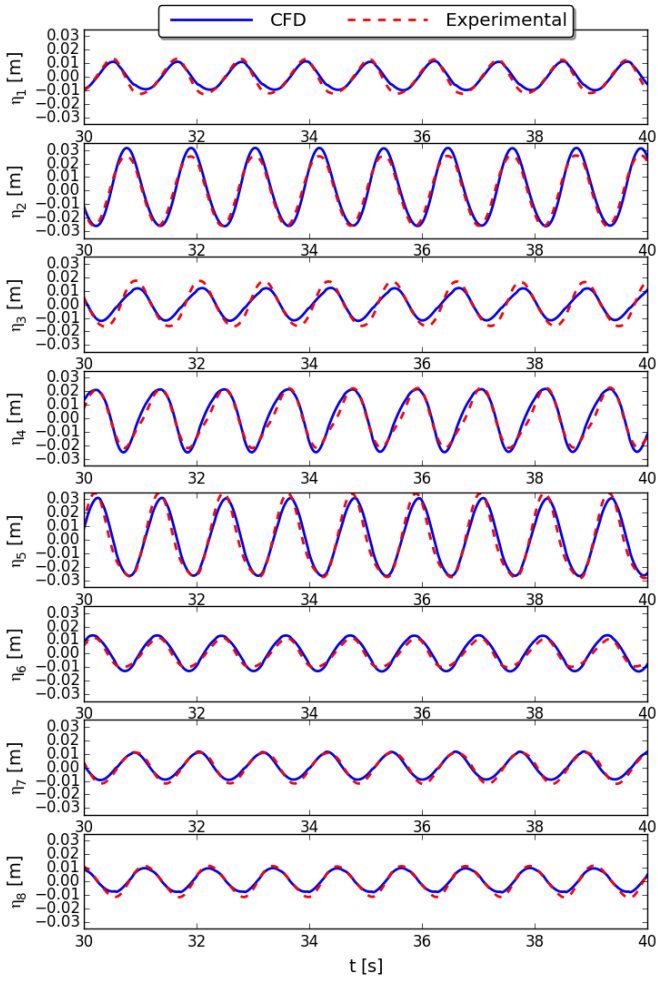

Figure 5.12: Perturbed wave field near the WEC subjected to regular waves ($H = 0.04\ m$; $T = 1.14\ s$) represented by the surface elevation η_i in function of time t ($\Delta t = 0.001\ s$, $\Delta z = 0.02\ m$).

5.4.4 Discussion

In the previous sections, numerical results are presented together with experimental data. In general, an excellent agreement is found between both results. However, some limitations are faced and should be kept in mind when analysing the results:

- the accuracy of the recorded motion of the WEC with a camera and its post processing;
- the difference in absorption methodology between the experimental and numerical wave flume;
- the accuracy of the wave gauges, especially when measuring very small wave heights;
- the accuracy of the VoF method to resolve small-amplitude waves with the mesh sizes used;
- the Couette flow in between shaft and shaft bearing of the WEC and the simplification made in the numerical model by using a linear damper;
- the friction between the two PTFE-bearings when the WEC is subjected to a regular wave train due to the horizontal wave-induced force.

5.5 Research topics under investigation

The behaviour of a single WEC unit subjected to regular waves inside a wave flume has to be analysed to the finest details. Firstly, the sensitivity of the linear damper on the results should be tackled. For example, regular waves cause a net horizontal force acting on the WEC inducing an additional vertical damping force. Secondly, turbulent effects may become important for some simulations. Therefore a well-suited RANS turbulence model (e.g. $k-\omega\ SST$ model) should be applied in order to simulate large displacements of the WEC together with accurate wave propagation of the incident, diffracted and radiated wave field.

Subsequently, wave farm modelling will be performed using multiple WECs. First, largely-spaced WEC units will be simulated. Thereafter, simulations of closely-spaced WEC units will be performed maintaining a good mesh quality around the air-water interface.

The topics listed above will be investigated in the near future.

5.6 Survivability simulation of a point absorber wave energy converter

Wave energy from ocean waves is captured by wave energy converters (WECs) and converted into electrical power. WECs of the floating point absorber (FPA) type are selected which are heaving under wave loading. In this study, the numerical simulations of a WEC under operational wave conditions (Devolder et al., 2016)

are extended to a survivability simulation of a WEC under extreme design load conditions. Therefore, the WEC is subjected to breaking waves in a numerical wave tank (NWT).

5.6.1 Numerical framework

CFD-modelling is performed to study the behaviour of a floating WEC unit inside a NWT implemented in OpenFOAM. The two-phase flow field is resolved by the incompressible RANS equations together with a conservation equation for the volume of fluid (VoF) method. RANS turbulence modelling is applied by using a buoyancy-modified $k-\omega\ SST$ model developed by the authors (Devolder et al., 2017a, 2018b). Wave generation and absorption at the boundaries of the NWT are adopted from the IHFOAM toolbox. The CFD-fluid solver is coupled to a motion solver in order to simulate rigid body motions. Only the governing motion of the WEC's behaviour is considered, the heave motion, allowing a reduction from a six to a one degree of freedom motion solver. The mesh motion is organised that only the highest and lowest row of cells is distorted (compressed or expanded) to prevent undesirable mesh deformations around the air-water interface. A coupling algorithm between the fluid and the motion solver is needed to obtain a converged solution between the hydrodynamic flow field around the WEC and the WEC's kinematic motion during every time step in the transient simulation. The coupling algorithm is using implicit coupling in the sub iterations by calculating a Jacobian, based on the available solutions of previous sub iterations for the acceleration of the floating body and the force acting on it, in order to minimise the number of sub iterations and consequently the CPU time (Devolder et al., 2018a).

5.6.2 Results & Discussion

This section presents two numerical results obtained in the NWT. Firstly, as a preliminary simulation, a two-dimensional (2D) NWT is considered without a floating WEC unit, i.e. an empty NWT. For a survivability simulation, breaking waves on the WEC are required. In order to trigger steepness-induced wave breaking in a constant water depth $d = 1.70\ m$, irregular waves are generated at the inlet by using three wave components and the method of wave focussing is applied. The surface elevations at the inlet ($x = 0\ m$) are calculated by superposition assuming linear wave theory:

$$\eta(x,t) = \sum_{i=1}^{3} \frac{H_i}{2} \cos\left(\frac{2\pi}{L_i}x - \frac{2\pi}{T_i}t + \phi_i\right) \tag{5.8}$$

in which H_i is the wave height, T_i the wave period, L_i the linear wave length and ϕ_i the phase of wave component i. Breaking waves are achieved by bringing the three wave components in phase at $x_f = 5\ m$ for $t_f = 10\ s$ by calculating ϕ_i of each wave component i as: $\frac{2\pi}{L_i}x_f - \frac{2\pi}{T_i}t_f + \phi_i = 0$ (linear wave theory). The numerical values for each wave component are as follows:

- $H_1 = 0.15\ m$; $T_1 = 1.00\ s \longrightarrow L_1 = 1.56\ m \longrightarrow \phi_1 = 42.71$;
- $H_2 = 0.10\ m$; $T_2 = 1.10\ s \longrightarrow L_2 = 1.89\ m \longrightarrow \phi_2 = 40.49$;
- $H_3 = 0.05\ m$; $T_3 = 1.20\ s \longrightarrow L_3 = 2.25\ m \longrightarrow \phi_3 = 38.38$;

Note that the wave periods are around the natural period of the WEC equal to $1.136\ s$, causing resonance of the WEC's heave motion. The three wave components are non-linear and therefore linear wave theory is not applicable and a non-linear fluid solver is required. Furthermore, waves generated with different wave periods generate new wave components which do not satisfy the linear dispersion relation. This is indicated in Figure 5.13 by the surface elevations over the length of the NWT at $x = 1\ m$, $x = 2\ m$, $x = 3\ m$, $x = 4\ m$, $x = 5\ m$ and $x = 6\ m$ for both the linear wave theory (dashed blue lines), equation (5.8), and the CFD result (solid red lines) during the first 30 seconds of the simulation. Due to the large wave steepness, wave breaking is induced between $x = 2\ m$ and $x = 3\ m$. This observation stresses the need for a CFD NWT to perform survivability simulations of a WEC subjected to breaking waves.

For the second simulation, a WEC is installed in a three-dimensional (3D) NWT and the same irregular waves are generated. The WEC's centre is located at $x = 3\ m$, inside the wave breaking zone as found during the preliminary simulation using an empty NWT. A longitudinal symmetry plane is implemented to reduce the size of the computational domain. The NWT is $8\ m$ long, $1.6\ m$ high and $0.7875\ m$ wide. The computational domain has a vertical resolution of $1\ cm$ and a horizontal resolution of maximum $2\ cm$ around the free water surface. A detail of a longitudinal cross section around the WEC is visualised in Figure 5.14. The aspect ratio of the cells behind the WEC towards the outlet boundary on the right increases gradually which will cause numerical wave damping. This is however beneficial in order to avoid wave reflection from the absorbing outlet boundary. A maximum Courant number of 0.3 is used to limit the time step.

Figure 5.15 and Figure 5.16 visualise time series for the vertical position of the WEC z and the horizontal surge force acting on the WEC F_x respectively. Between $t = 5\ s$ and $t = 10\ s$ for example, the amplitude of the WEC's heave motion is gradually increasing due to resonance effects and the viscous damping force is important to predict correctly the WEC's heave motion. In Figure 5.16, the peaks observed in the time signal of the surge force on the WEC indicate the breaking wave impacts on the WEC. These forces obtained during a survivability simulation are important to quantify the design loading conditions on a WEC.

Figure 5.17 depicts the number of sub iterations to achieve a converged fluid–motion coupling during every time step. Mostly two and occasionally three or more sub iterations are needed which indicates the successful application of the accelerated coupling algorithm for a survivability simulation of a WEC unit.

Finally, a snapshot of a breaking wave impacting on the WEC is visualised in Figure 5.18 at $t = 6.20\ s$. The wave starts to break in front of the WEC and the overturning volume of water is impacting on the WEC. Those highly non-linear and fully turbulent flows for breaking wave impact simulations are only possible by using a CFD NWT.

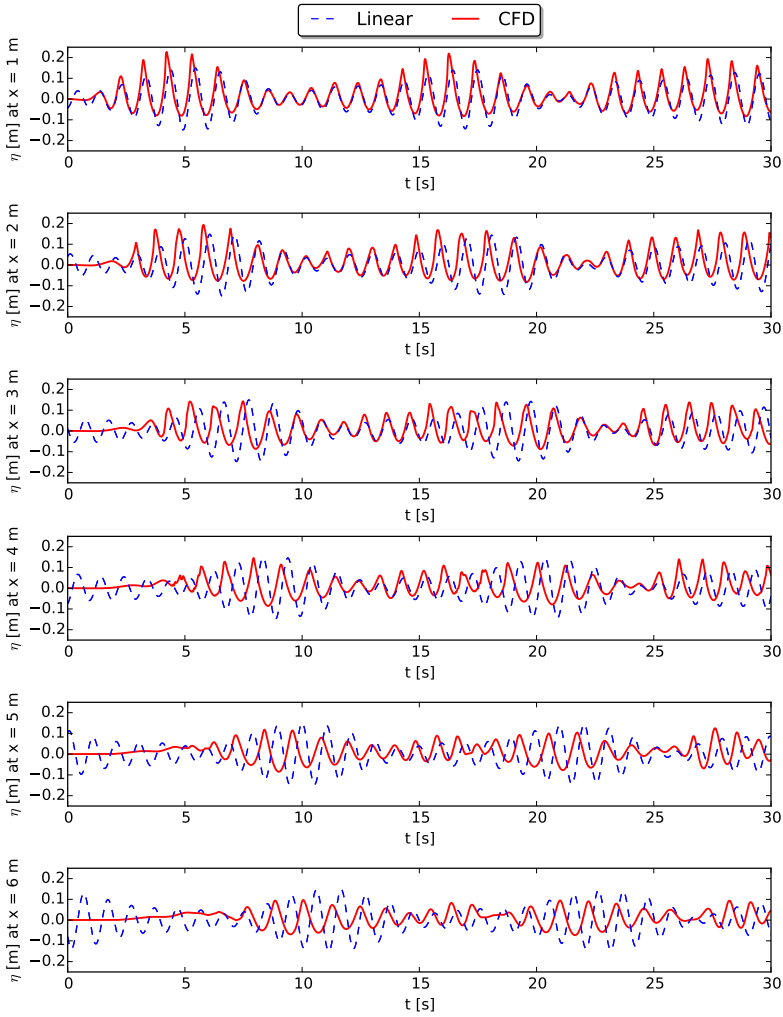

Figure 5.13: Surface elevations obtained with linear wave theory (equation (5.8), blue dashed lines) and in the empty CFD NWT (red solid lines).

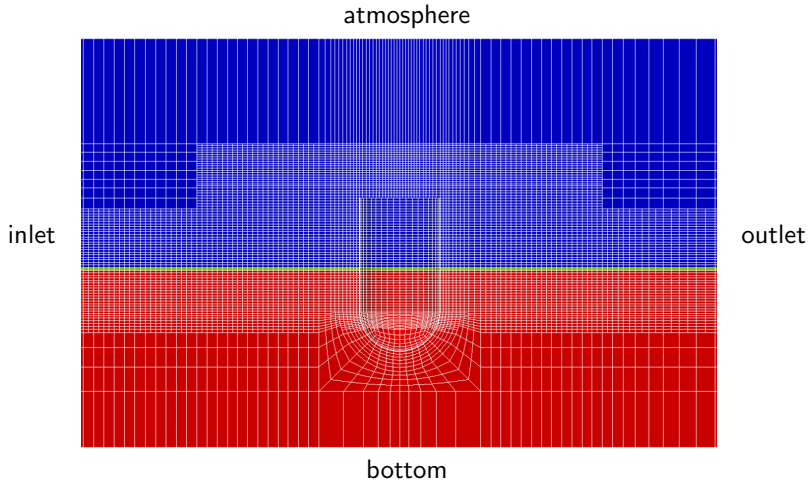

Figure 5.14: Cross section (XZ-plane) of the 3D computational domain in which a WEC is installed showing the initial condition for the volume fraction α at $t = 0\ s$ ($\alpha = 1$: water shown in red, $\alpha = 0$: air shown in blue).

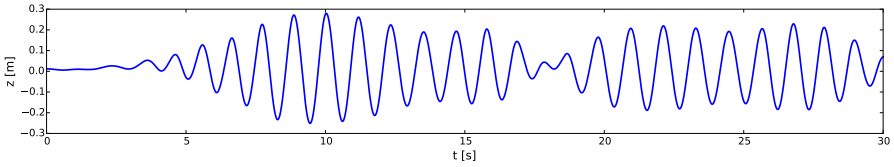

Figure 5.15: Vertical position z of the WEC subjected to breaking waves.

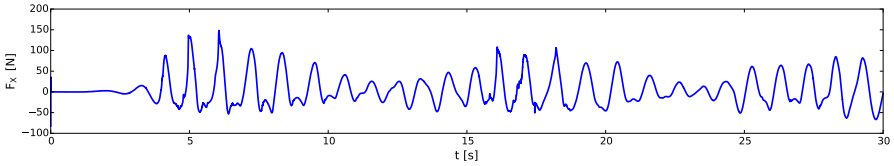

Figure 5.16: Horizontal surge force F_x acting on the WEC subjected to breaking waves.

5.7 Conclusions

Sections 5.1 to 5.5 presents several cases of a numerical simulation of a heaving WEC inside a numerical wave flume. These numerical results are validated against experimental data for both a free decay test and two specific regular wave trains. Regarding the free decay test, a very good agreement is obtained between numerical and experimental results. Both the vertical position of the WEC and the

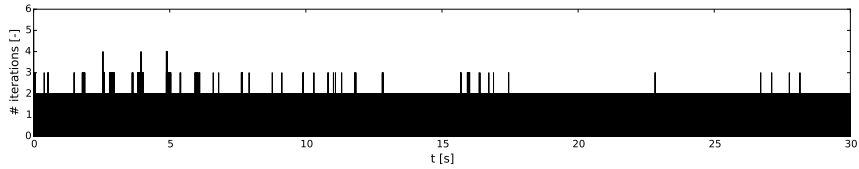

Figure 5.17: The number of sub iterations for every time step to have a converged fluid–motion coupling for the WEC subjected to breaking waves.

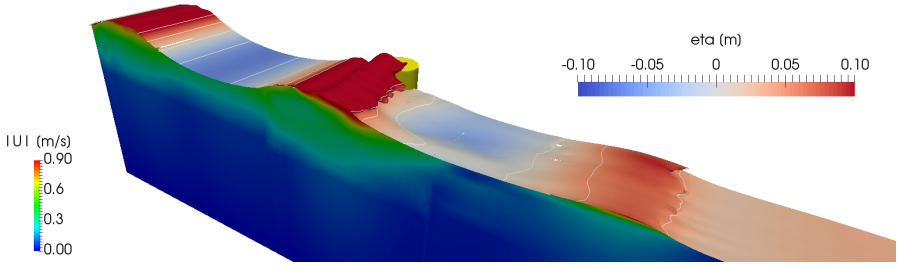

Figure 5.18: A snapshot at $t = 6.20\ s$ of a breaking wave impacting on the WEC in the NWT. Contour lines of the surface elevation $[m]$ are depicted on the isosurface for the volume fraction $\alpha = 0.50$. The vertical plane visualises the velocity magnitude $[m/s]$.

radiated wave field show an excellent agreement. Furthermore, simulations of a WEC subjected to two specific regular wave trains return promising results for its motion and perturbed wave field. The paper shows that the combination of OpenFOAM and IHFOAM is a robust and suitable toolbox to research fluid-structure interaction. Moreover, OpenFOAM/IHFOAM seems capable to study the interaction between multiple WECs because the radiated wave field is captured very accurately.

Based on the proof of concept study reported in section 5.6, we conclude that a CFD NWT is necessary to resolve non-linear wave–wave interactions during wave propagation and to simulate wave breaking events on a WEC for testing survivability conditions. Furthermore, it has been demonstrated that our coupling algorithm for the fluid–motion solver remains stable under extreme wave conditions and large displacements of the WEC by using few sub iterations during every time step. Future research is required to validate the numerical model for extreme wave conditions by using experimental measurements. In addition, a coupling between an accurate wave-structure interaction solver (e.g. OpenFOAM as a non-linear viscous NWT) and a fast wave-propagation solver (e.g. OceanWave3D as a non-linear potential flow NWT) will increase the efficiency of the numerical simulations by reducing the time-consuming 3D CFD domain.

Chapter 6

Numerical simulations of a wave energy converter array

The last chapter dealing with fluid-structure interaction simulations focusses on the implementation of multiple closely-spaced wave energy converters in an array configuration installed in a numerical wave tank. The numerically obtained results are validated with the largest database of wave energy converter arrays available: the WECwakes data set (Hydralab IV project, HyIV-DHI-08, 2013).

This chapter is originally published as:
Devolder, B., Stratigaki, V., Troch, P., and Rauwoens, P. (2018). CFD Simulations of Floating Point Absorber Wave Energy Converter Arrays Subjected to Regular Waves. *Energies*, 11(3):641. doi:10.3390/en11030641.

CFD Simulations of Floating Point Absorber Wave Energy Converter Arrays Subjected to Regular Waves

Brecht Devolder, Vasiliki Stratigaki, Peter Troch, Pieter Rauwoens

Abstract
In this paper we use the Computational Fluid Dynamics (CFD) toolbox OpenFOAM to perform numerical simulations of multiple floating point absorber Wave Energy Converters (WECs) arranged in a geometrical array configuration inside a numerical wave tank (NWT). The two-phase Navier-Stokes fluid solver is coupled with a motion solver to simulate the hydrodynamic flow field around the WECs and the wave-induced rigid body heave motion of each WEC within the array. In this study, the numerical simulations of a single WEC unit are extended to multiple WECs and the complexity of modelling individual floating objects close to each other in an array layout is tackled. The NWT is validated for fluid-structure interaction (FSI) simulations by using experimental measurements for an array of two, five and up to nine heaving WECs subjected to regular waves. The validation is achieved by using mathematical models to include frictional forces observed during the experimental tests. For all the simulations presented, a good agreement is found between the numerical and the experimental results for the WECs' heave motions, the surge forces on the WECs and the perturbed wave field around the WECs. As a result, our coupled CFD–motion solver proves to be a suitable and accurate toolbox for the study of fluid-structure interaction problems of WEC arrays.

Keywords: CFD; OpenFOAM®/IHFOAM; Wave energy; Array modelling; Validation study

6.1 Introduction

Wave energy from ocean waves is captured by Wave Energy Converters (WECs) and converted into electrical power. In this study, WECs of the floating point absorber (FPA) type are selected. In order to extract a considerable amount of wave power at a location in a cost-effective way, a number of WECs are arranged in arrays or farms using a particular geometrical configuration. Firstly, interactions between the individual WECs (near-field effects) affect the overall power production of the array. One should avoid, for instance, that one WEC is positioned in the wake region, with lower wave heights, of another WEC within the array. Secondly, the wave height reduction behind one or more WEC arrays (far-field effects) affects other users in the sea, the environment or even the coastline. In this study, fluid-structure interaction (FSI) simulations are performed inside a numerical wave tank (NWT) to study the near-field effects. The FSI simulations presented are carried out within the Computational Fluid Dynamics (CFD) toolbox OpenFOAM which solves the hydrodynamic flow field around the WECs and the kinematic motion of each individual WEC unit within the array. CFD is able to include viscous, turbulent and non-linear effects which are absent in simplified radiation-diffraction models such as potential flow solvers based on the boundary element method (BEM). These effects are not only important during survivability conditions, such as extreme waves with wave breaking events (Ransley et al., 2017a), but also when control strategies are applied to maximise the power output by driving the WEC's motion into resonance (Davidson et al., 2018).

Numerical modelling of WECs has been reported extensively in the literature and an excellent description and comparison of the different models is provided in Wolgamot and Fitzgerald (2015). A good agreement between CFD and experimental results has been reported in Wolgamot and Fitzgerald (2015), demonstrating the feasibility of CFD simulations for wave energy applications. CFD simulations of a single WEC unit have been reported in previous work of the authors (Devolder et al., 2016) but also in Davidson et al. (2015a), Stansby et al. (2015) and Ransley et al. (2017b,a). The application of OpenFOAM is outlined in Davidson et al. (2015a) as a NWT for testing WECs by presenting a free decay test, a forced motion of the WEC and an irregular wave test. In Stansby et al. (2015), a CFD NWT is used to enhance the capture width of a particular WEC: the three float line absorber M4. They stressed that mechanical resistance in the experiments might influence the experimentally obtained heave motions. This also explains the differences observed between the numerical results and the experimental measurements. Thorough validation of the numerical results for a single WEC unit using experimental data is performed by Ransley et al. (2017b). They modelled the Wavestar point absorber WEC in a CFD NWT and performed diffraction tests (i.e. the WEC is fixed at a specific draft), a freely floating WEC subjected to operational conditions and a test with extreme wave conditions. In general, good results are obtained for the pressure on the WEC and the WEC's response to incident waves. The extreme wave case simulation remained stable and is further investigated in Ransley et al. (2017a). The authors subjected both a fixed truncated circular cylinder and a floating WEC to extreme waves. A good comparison is found between

numerical and experimental data for the pressure and run-up on the cylinder surface as well as for the floating WEC's motion and the mooring load. In Devolder et al. (2016), the numerically obtained viscous flow field around the WECs and the response of a single WEC unit have been verified and validated with experimental data for free decay and regular wave tests. A good agreement between experimental and numerical data was found for the WEC's heave motion and the wave field around the WEC. More importantly, attention is required for correctly including frictional forces observed during the experiments in a CFD model. These simulations were the starting point prior to model multiple WECs installed in an array configuration inside a CFD NWT. Numerical simulations of WEC arrays using simplified radiation-diffraction models have been published in Babarit et al. (2013), McNatt et al. (2015), Wolgamot et al. (2016) and Troch and Stratigaki (2016) for example. However, CFD simulations of a WEC array are scarce and have only been reported by a few researchers, e.g. Agamloh et al. (2008) and Mccallum (2017). In Agamloh et al. (2008), only a brief introduction regarding an array of two WECs subjected to regular waves is reported. It is also mentioned that more simulations are needed in order to fully quantify the interactions between multiple WECs. More recently, Mccallum (2017) performed free decay tests of a single WEC unit and an array of two and five WECs in a CFD NWT and compared the numerical results with experimental data from the WECwakes project (Stratigaki et al., 2014, 2015). However, CFD simulations modelling the WECs' response to an incident wave field are lacking. In Mccallum (2017), it is reported that the sliding mechanism used for the experiments (see later in Figure 6.1a) is responsible for additional frictional forces acting on the WEC. To address this, Mccallum (2017) recommended the use of a linear damper in the numerical simulations in first instance.

In this work we present numerical results of WEC arrays subjected to non-breaking regular waves representing operational conditions. Validation of these numerical results with experimental data is required prior to survivability simulations of WEC arrays under extreme wave loading with breaking wave events. The ability of our coupled fluid–motion solver to simulate multiple independently moving WECs arranged in different array configurations subjected to regular waves has been demonstrated in Devolder et al. (2017b) and Devolder et al. (2017c). In this paper, we extend the comparison study between the numerical results obtained with our coupled fluid–motion solver and the experimental data obtained during the WECwakes project (Stratigaki et al., 2014, 2015) for an array of two, five and up to nine WECs. The geometry of an individual heaving FPA type WEC is depicted in Figure 6.1. Figure 6.1 also shows the supporting axis which serves as a sliding mechanism to allow solely heave motion of the WEC. A power take-off system is installed on the WEC by mimicking a coulomb damper using friction brakes (composed of two PTFE blocks and four springs) between the floating WEC and the supporting axis. The WECwakes tests focussed on recording WEC responses, forces on WECs and wave field modifications around single WEC units and WEC arrays of 2 up to 25 WECs. The experiments performed in the wave basin at DHI (Denamrk) within the EU FP7 Hydralab IV program are until today the largest experimental setup of this kind worldwide. WECwakes resulted in a comprehensive database which is publicly available for researchers trough the Hydralab rules. Not

only the WECs' heave motions but also the surge forces acting on the WECs and the perturbed wave field around the different WEC arrays obtained in a CFD NWT are validated in this paper using the WECwakes dataset.

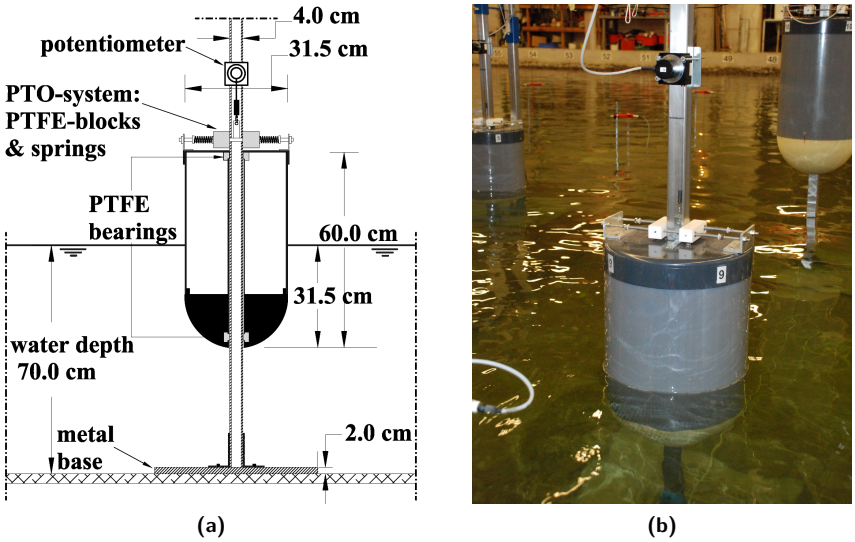

Figure 6.1: (a) Definition sketch of the cross section of a single WEC unit; (b) photograph of a single WEC unit within an array installed in the DHI wave basin during the WECwakes project. Adopted from Stratigaki et al. (2014).

The remainder of this paper is organised as follows. Firstly, in section 6.2, the governing equations for the numerical model are presented, followed by a description of the computational domain, the boundary conditions applied and the solver settings. Subsequently in section 6.3, the numerical model is used to perform several simulations while in section 6.4 the obtained results are discussed in detail. Finally, the conclusions are drawn in section 6.5.

6.2 Numerical model

In this section, the numerical model used for simulating WEC arrays inside a CFD NWT is summarised. Subsequently, the computational domain is presented together with the grid characteristics. The last two parts of this section are dedicated to explain the different boundary conditions and solver settings.

6.2.1 Coupled fluid–motion solver

The coupled fluid–motion solver is implemented in OpenFOAM®, version 3.0.1 (2015a). The governing equations for the fluid and motion solver together with the FSI coupling algorithm are formulated in following three subsections.

6.2.1.1 Fluid solver

The two-phase fluid solver uses the three dimensional (3D) incompressible Reynolds-Averaged Navier-Stokes (RANS) equations to express the motion of the two fluids (i.e. water and air). The RANS equations consist of a mass conservation equation (6.1) and a momentum conservation equation (6.2) written in Einstein summation notation as:

$$\frac{\partial u_i}{\partial x_i} = 0 \tag{6.1}$$

$$\frac{\partial \rho u_i}{\partial t} + \frac{\partial \rho u_j u_i}{\partial x_j} - \frac{\partial}{\partial x_j}\left[\mu_{eff}\frac{\partial u_i}{\partial x_j}\right] = -\frac{\partial p^*}{\partial x_i} + F_{b,i} + f_{\sigma,i} \tag{6.2}$$

in which t is the time, u_i $(i = x, y, z)$ are the Cartesian components of the fluid velocity, ρ is the fluid density, μ_{eff} is the effective dynamic viscosity, p^* is the pressure in excess of the hydrostatic. F_b is an external body force (including gravity) which is defined as:

$$F_{b,i} = -g_i x_i \frac{\partial \rho}{\partial x_i} \tag{6.3}$$

in which the gravitational acceleration vector $\vec{g} = [0\ ;\ 0\ ;\ -9.81]\ m/s^2$, $\vec{x}$ is the Cartesian coordinate vector $(x,\ y,\ z)$, f_σ is the surface tension tensor term which is neglected in the present study. Note that the mean values for the variables considered are written in terms of Favre-averaging (density weighted) due to the varying density in the NWT.

The interface between water and air is obtained by the Volume of Fluid (VoF) method using a compression term as documented in Berberović et al. (2009). The method is based on a volume fraction α which is 0 for a completely dry cell and 1 for a completely wet cell and in between 0 and 1 for an interface cell containing both water and air. The volume fraction is solved by an advection equation (6.4):

$$\frac{\partial \alpha}{\partial t} + \frac{\partial u_i \alpha}{\partial x_i} + \frac{\partial u_{c,i}\alpha\,(1-\alpha)}{\partial x_i} = 0 \tag{6.4}$$

where $u_{c,i} = \min[c_\alpha |u_i|, \max(|u_i|)]$. In the present study, the default value of c_α equal to 1 is applied.

In a post-processing step, the position of the free water surface is determined by a discrete integration of the volume fraction α over a vertical line (Z-direction) divided in n equal parts:

$$z_{water\ level} = \sum_{i=0}^{n-1} \alpha_i (z_{i+1} - z_i) \tag{6.5}$$

The density of the fluid ρ within a computational cell is calculated by a weighted value based on the volume fraction α. The effective dynamic viscosity μ_{eff} is obtained by the sum of a weighted value based on the volume faction α and an additional turbulent dynamic viscosity $\rho\nu_t$:

$$\rho = \alpha\rho_{water} + (1-\alpha)\rho_{air} \tag{6.6}$$

$$\mu_{eff} = \alpha\mu_{water} + (1-\alpha)\mu_{air} + \rho\nu_t \tag{6.7}$$

For the waves studied in this work, the Reynolds (Re) number and the Keulegan-Carpenter (KC) number are equal to 6.19×10^4 and 0.79 respectively. According to Sumer and Fredsøe (1997), no clear turbulent behaviour is expected around the WECs for those Re and KC values. Therefore, in the first instance, only laminar solutions are calculated by setting ν_t equal to 0. As shown later on, the main features of the WECs' heave motions, the surge forces on the WECs and the perturbed wave field are already captured by assuming laminar flow conditions. However, in case turbulence plays a major role (e.g. flow separation due to a non-streamlined WEC geometry or during wave breaking events), we refer to our previous works (Devolder et al., 2017a, 2018b) on how to properly deal with RANS turbulence modelling for a two-phase fluid solver by using a buoyancy-modified $k-\omega$ or $k-\omega\ SST$ turbulence model. A buoyancy-modified turbulence model not only results in a stable wave propagation model without wave damping (Devolder et al., 2017a) but it also predicts the turbulence level inside the flow field more accurately in the surf zone where waves break (Devolder et al., 2018b).

6.2.1.2 Motion solver

The kinematic motion of a rigid body is calculated by a motion solver. During the WECwakes project, the motion of the WECs was restricted to heave only. This allows a reduction from a six to a one degree of freedom motion solver. The motion solver calculates the vertical position z of the body by applying Newton's second law at the current time $n+1$:

$$F^{n+1} = ma^{n+1} \tag{6.8}$$

in which F^{n+1} is the overall vertical force (including gravity) obtained with the fluid solver by integrating the pressure and shear forces acting on the body's surface and a^{n+1} is the vertical acceleration of the body. Once the acceleration a^{n+1} is known, the vertical velocity v^{n+1} and the vertical position z^{n+1} during the same time $n+1$ are calculated by a second order accurate Crank-Nicolson integration scheme:

$$v^{n+1} = v^n + \frac{1}{2}(a^n + a^{n+1})\Delta T \tag{6.9}$$

$$z^{n+1} = z^n + \frac{1}{2}(v^n + v^{n+1})\Delta T \tag{6.10}$$

in which n is the previous time, $n+1$ is the current time and ΔT is the time step. The new position of the body serves as a boundary condition for the mesh motion operation (see later in section 6.2.2).

In order to have a converged solution between the hydrodynamic flow field around and the kinematic motion of a WEC, the following kinematic condition needs to be fulfilled at the interface between the fluid and the WEC:

$$u_z = v \tag{6.11}$$

in which u_z and v are the vertical fluid velocity and the vertical WEC's velocity respectively. Note that the fluid velocities u_x and u_y are equal to $0\ m/s$ at the fluid-WEC interface because only heave motion of the WEC is allowed.

6.2.1.3 Coupling algorithm

The coupling between a fluid and a motion solver in rigid body simulations is done by interchanging the total force acting on the body. In the present study, the fluid solver returns the vertical force acting on the WEC which is calculated as the discrete sum of the pressure forces, viscous forces, the downward weight of the body and all the external forces acting on the WEC:

$$\vec{F}^{n+1} = \sum_{j}^{body}(p_j \vec{n_j} A_j) + \sum_{j}^{body}(\vec{\vec{\tau}}_j \vec{n_j} A_j) - m\vec{g} + \sum_{k}(\vec{F}_{ext,k}) \tag{6.12}$$

in which p_j and $\vec{\vec{\tau}}_j$ are respectively the pressure and the shear stress tensor acting on each boundary face around the WEC, $\vec{n_j}$ is a unit vector normal to the area A_j of boundary face j and m is the dry mass of the WEC. F_{ext} is any external force acting on the WEC such as the power take-off (PTO) system force or the frictional force caused by the sliding mechanism used in the experimental setup (see Figure 6.1 and further in section 6.3).

In order to satisfy equation (6.8), the coupling algorithm is applying multiple sub iterations during every time step in the transient simulation. The convergence speed between the fluid and motion solver is enhanced by using an accelerated coupling algorithm derived in previous work of the authors (Devolder et al., 2018a), reducing the computational cost in terms of CPU time. For floating bodies with a small added mass effect, such as the WECs considered in this research, a fixed amount of three sub iterations is sufficient to reach convergence of equation (6.8) during every time step, see Devolder et al. (2018a).

6.2.2 Computational domain

All the numerical simulations are performed in a NWT which represents the experimental wave basin as well as possible. Details regarding the experimental wave

basin at DHI have been included in previous work (Devolder et al., 2017c). A plan view of the NWT setup is depicted in Figure 6.2 showing the WECs' and wave gauges' (WG) positions as used during the WECwakes experiments. In summary, the NWT is represented by a structured grid consisting of only hexahedral cells. In order to limit the number of grid cells in the computational domain, a longitudinal symmetry plane is used along the X-axis. As an example, a longitudinal cross section along the X-axis of the numerical domain for the 5-WEC array is shown in Figure 6.3. Local mesh refinements are performed in the zones of interest: around the free water surface and around the individual WECs. The vertical grid resolution Δz is $1\ cm$ ($\approx H/7$ in which $H = 0.074\ m$ is the wave height, see later in section 6.3) in the zones of interest, which is sufficiently according to Devolder et al. (2016) and Devolder et al. (2017c). The horizontal cell sizes Δx and Δy are equal to $2\ cm$ ($\approx L/119$ in which $L = 2.38\ m$ is the wave length, see Stratigaki (2014)) and increase towards the boundaries of the NWT in order to limit the number of cells and thus also the required computing time. The only exception is that Δx is kept constant towards the inlet boundary in order to properly simulate wave propagation towards the WEC array. Note that properly resolving the boundary layer around the WEC units would require a very fine mesh resolution, resulting in cells with a large aspect ratio. It is known that those type of cells are to be avoided for a VoF-type fluid solver, as they will adversely affect the accuracy of the free surface position. Furthermore, for the simulations presented in this work, pressure forces acting on the WEC will dominate over viscous effects with respect to the wave-induced WEC's heave motions.

In order to simulate multiple independently moving WECs in an array configuration, arbitrary mesh interfaces (AMIs) are implemented in order to create sliding meshes (see dashed vertical lines in Figure 6.4 for the case of two WECs). These AMIs define a zone of cells around each WEC. In each zone, only the lowest and highest row of cells (see blue shaded boxes in Figure 6.4) are expanded or compressed according to the motion of the WEC located in that zone. This methodology is implemented to prevent undesirable mesh deformations around the interface between water and air (i.e. high non-orthogonality and skewness of the computational cells). As a disadvantage, high aspect ratios are obtained for the distorted cells. However since those cells are not inside the zones of interest, it does not affect the accuracy of the simulations. All the variables solved with the fluid solver, such as velocity, pressure and volume fraction, are interpolated over the AMIs.

6.2.3 Boundary conditions

The bottom and side wall of the NWT are modelled as a solid wall: a Dirichlet boundary condition is set for the velocity ($0\ m/s$ in the three directions) while the pressure and volume fraction are set to a Neumann condition. At the inlet and outlet, wave generation and absorption are implemented using the IHFOAM toolbox (Higuera et al., 2013a,b). On all the boundary faces of each WEC, the velocity vector is set to a moving wall condition (see equation (6.11)) and the pressure and volume fraction are set to a Neumann condition. The atmospheric

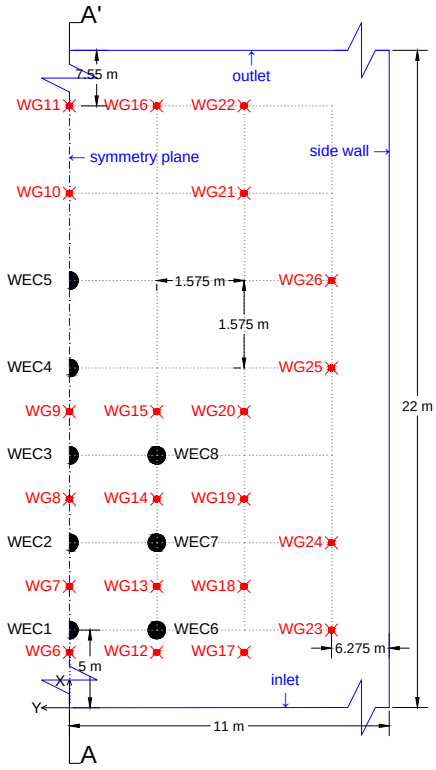

Figure 6.2: Plan view (XY-plane) of the NWT using one symmetry plane on the left side and including all the WECs considered for the simulations presented. The red marks indicate the position of all the available wave gauges (WG) installed in the DHI wave basin.

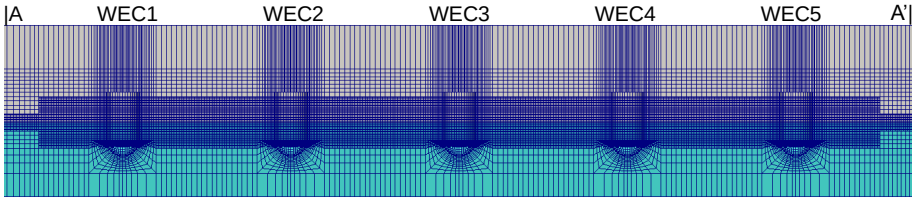

Figure 6.3: Cross section A–A' (XZ-plane, see Figure 6.2) of the computational domain for the 5-WEC array (WEC1 on the left and WEC5 on the right) (blue = water, grey = air).

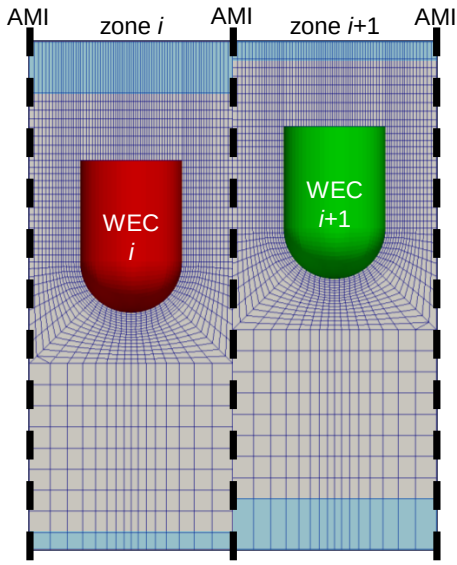

Figure 6.4: A cross section (XZ-plane) of two independently moving WECs. Only the highest and lowest row of cells (blue shaded boxes) in a zone are distorted (expanded or compressed) according to the heave motion of the WEC located in that zone. In between the zones, AMIs are implemented to create sliding meshes (dashed lines).

conditions at the top of the numerical domain are set to a mixed Dirichlet-Neumann boundary condition for the velocity, pressure and volume fraction.

6.2.4 Solver settings

For all the simulations presented, the following solver settings are used: central discretisation for the pressure gradient and the diffusion terms; TVD (total variation diminishing) schemes with a van Leer limiter (van Leer, 1974) for the divergence operators; second order implicit time discretisation; a maximum Courant number equal to 0.3 as recommended in Devolder et al. (2018a) for FSI simulations using a VoF method.

6.3 Results

In this section, we present numerical simulations of three different WEC array configurations subjected to regular waves. An overview of the employed benchmark data, both numerical and experimental results, is summarised in Table 6.1. In this study, the underlined tests and results are presented and validated using the experimental WECwakes dataset. The other results, i.e. the free decay tests, have been reported in previous works (Devolder et al., 2017b,c). For the 2-WEC and

5-WEC array, a simulation with fixed WECs is also performed in which the WECs are not moving. Subsequently, more challenging simulations are presented in which the heave motion is allowed for a 2-WEC, 5-WEC and 9-WEC array in response to an incident regular wave train. For each test, the waves have a height H equal to $0.074\ m$, a wave period T of $1.26\ s$ and are generated in a water depth d of $0.70\ m$. At the inlet of the numerical wave tank, waves are generated using a second order Stokes theory and active wave absorption is turned on. Each numerical simulation ran for 50 seconds to obtain a sufficiently long dataset after the warming-up phase but only the last 10 seconds are shown. The numerical results are validated by using experimental data for the WECs' heave motions, the surge forces on the WECs and the surface elevations in the wave tank. The relative error between the numerical result (*num*) and the experimental result (*exp*), in percent, is defined as:

$$error = \frac{|(\phi_{\max}^{num} - \phi_{\min}^{num}) - (\phi_{\max}^{exp} - \phi_{\min}^{exp})|}{\phi_{\max}^{exp} - \phi_{\min}^{exp}} \times 100\ \% \tag{6.13}$$

in which ϕ is representing the heave motion, surge force or surface elevation. The maximum and minimum values for ϕ observed in the time signals are averaged between $t = 40\ s$ and $t = 50\ s$. The numerically computed values for the error, equation (6.13), are presented in Table 6.2.

Table 6.1: Overview of the employed benchmark data (numerical and experimental results). The arrows show the direction of the incoming waves.
([1]Devolder et al. (2017b), [2]Devolder et al. (2017c))

Layout	**Available type of tests**	**Available results**
2 -WEC array	Free decay (no PTO)[1]	WECs' heave motion
→	Free decay (PTO)[2]	Surge force on WECs
→ ④ ⑤	Fixed WECs	Surface elevations
→	Heaving WECs	
5-WEC array	Free decay (no PTO)[1]	
→	Fixed WECs	
→ ① ② ③ ④ ⑤	Heaving WECs	
→		
9-WEC array	Heaving WECs	
→ ⑪ ⑫ ⑬		
→ ① ② ③		
→ ⑥ ⑦ ⑧		

Table 6.2: The relative error between the numerical and experimental result (equation (6.13)) for all the simulations presented.

	2-WEC array		5-WEC array		9-WEC array
Result	fixed	heaving	fixed	heaving	heaving
z_{WEC1}	/	/	/	37 %	2 %
z_{WEC2}	/	/	/	18 %	1 %
z_{WEC3}	/	/	/	13 %	7 %
z_{WEC4}	/	27 %	/	44 %	/
z_{WEC5}	/	13 %	/	5 %	/
z_{WEC6}	/	/	/	/	64 %
z_{WEC7}	/	/	/	/	16 %
z_{WEC8}	/	/	/	/	29 %
$F_{X,WEC1}$	/	/	5 %	9 %	18 %
$F_{X,WEC2}$	/	/	5 %	7 %	5 %
$F_{X,WEC3}$	/	/	7 %	2 %	6 %
$F_{X,WEC4}$	7 %	/	10 %	9 %	/
$F_{X,WEC5}$	5 %	/	8 %	3 %	/
WG6	/	/	3 %	6 %	21 %
WG7	/	/	4 %	16 %	30 %
WG8	/	/	17 %	15 %	11 %
WG9	4 %	8 %	2 %	6 %	13 %
WG10	7 %	8 %	6 %	6 %	/
WG11	23 %	11 %	14 %	9 %	/
WG12	/	/	8 %	5 %	10 %
WG13	/	/	3 %	5 %	5 %
WG14	/	/	2 %	3 %	11 %
WG15	/	/	0 %	20 %	12 %
WG17	/	/	/	/	8 %
WG18	/	/	/	/	1 %
WG19	/	/	/	/	20 %
WG20	/	/	/	/	10 %

6.3.1 2-WEC array

In this first subsection, two WECs in line are modelled in the NWT (WEC4 and WEC5 in Figure 6.2). The distance between the WECs' centre is equal to five times their diameter ($D_{WEC} = 0.315\ m$), see Figure 6.2. Firstly, the WECs are kept fixed in their equilibrium position and no motion is allowed. Secondly, the WECs are allowed to heave in response to the incident waves.

6.3.1.1 Fixed 2-WEC array

If the WECs are kept fixed, the incident wave field is perturbed by wave reflection and wave diffraction. The purpose of this particular test is to check the reproduction of the perturbed wave field in a numerical model without considering the wave

field modification by the WECs' heave motion (i.e. radiated wave field around each WEC).

Figure 6.5 presents the wave-induced surge (horizontal) forces acting on WEC4 and WEC5 as a function of time. The red line indicates the experimental data while the blue line depicts the numerically obtained force by the CFD fluid solver. Note that the noise in the time signals of the experimental force measurements has been filtered out using a bandpass filter. An outstanding agreement is observed between the numerical and experimental data which is also confirmed in Table 6.2 by relative errors equal to $7\ \%$ and $5\ \%$ for WEC4 and WEC5 respectively. This achievement is a necessary requirement for the simulations with heaving WECs later in this study because the wave-induced force acting on a floating body determines its kinematic motion.

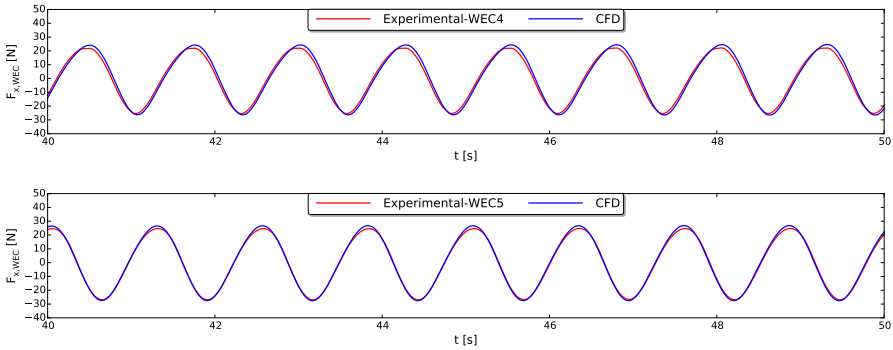

Figure 6.5: Wave-induced surge force $F_{X,WEC}$ on WEC4 (top) and WEC5 (bottom), both fixed, obtained with CFD (blue line) compared to the experimental measurements (red line) after filtering out the noise.

The perturbed wave field due to reflection and diffraction is visualised in Figure 6.6 by the surface elevations at three locations in the NWT: WG9, WG10 and WG11 (see Figure 6.2). Again, the red lines indicate the experimental measurements and the blue lines are the processed time series of the surface elevations in the NWT (equation (6.5)). For WG9, before the 2-WEC array, and WG10, behind the 2-WEC array, an identical signal is observed between numerical and experimental data (see Table 6.2 for the relative errors). However, for WG11 further behind the 2-WEC array, small discrepancies between numerical and experimental data are visible in the maximum and minimum surface elevation (relative error of $23\ \%$) but the wave phase is similar. It is also observed that the wave height is the same for the three wave gauges in the NWT and equal to $0.067\ m$ which is slightly smaller than the incident wave height equal to $0.074\ m$. It is very remarkable that this is not the case for the experimental records, which show an increased wave height for WG11. We expect however that due to the slender geometry of the WECs, wave diffraction is not significant and no wave field modification is present at the position of WG10 and WG11 behind WEC5. This is indicated by Figure 3.20a in Stratigaki (2014)

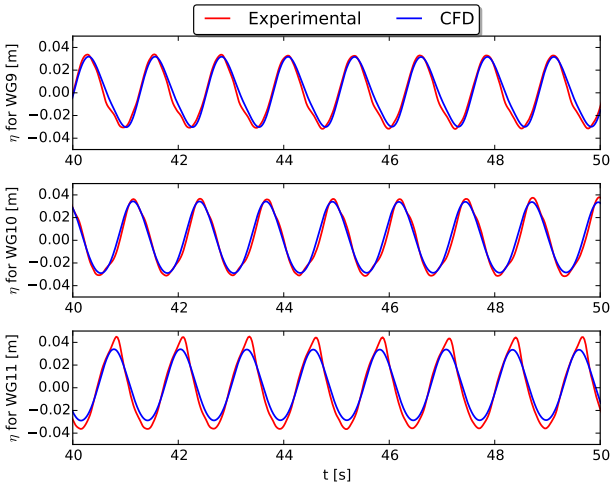

Figure 6.6: Perturbed wave field using several wave gauges (see Figure 6.2) around the 2-WEC array with fixed WECs during a regular wave test ($H = 0.074\ m$, $T = 1.26\ s$, $d = 0.70\ m$) obtained with CFD (blue line) compared to the experimental data (red line).

which presents a cross section of the incident and diffracted wave fields' amplitude for a fixed single WEC unit obtained with the BEM solver WAMIT (2016).

6.3.1.2 Heaving 2-WEC array

In this section, the two WECs are allowed to heave in response to the incident regular waves. The incident wave field is not only perturbed by diffracted and reflected waves but also by radiated waves generated by the heave motion of the WECs. For heaving WECs, the perturbed wave field is thus a combination of incoming, diffracted, reflected and radiated waves. The radiated wave field has been validated separately in previous work (Devolder et al., 2017c) by simulating a free decay test of these WECs. It was concluded that the correspondence between numerically and experimentally obtained surface elevations is good despite the small wave amplitudes of the radiated wave field. However, internal friction caused by the sliding mechanism between the WEC and the vertical supporting axis through internal contact points during the experiments (see Figure 6.1a) requires attention to correctly include it in a CFD model for validation studies. Therefore the following two measures are undertaken to simulate the studied heaving WECs subjected to regular waves. Firstly, the WEC's mass is modified and a linear damper is needed to account for the internal friction due to the sliding mechanism used in the experiments (cfr. viscous flow of water between the shaft and shaft bearing, see Figure 6.1a). The method is described in Devolder et al. (2016) and is based on tuning the WEC's heave motion to the experimental measurement for a free decay test. The linear damper is formulated by an additional frictional force on the

WEC:

$$F_{LD} = -cv(t) \tag{6.14}$$

in which c is the damping coefficient equal to $4.86\ kg/s$, as calculated in Devolder et al. (2017c) by validating a free decay test using WEC5 and $v(t)$ is the WEC's vertical velocity. Secondly, the incident waves push the experimental WECs against their sliding mechanism (cfr. a coulomb damper (Devolder et al., 2017c)), resulting in an additional frictional force:

$$F_{bearings,X} = -\mu \left| F_{surge}(t) \right| sign(v(t)) \tag{6.15}$$

in which the coefficient of friction $\mu = 0.17$ and F_{surge} is the horizontal force in the X-direction acting on the WEC.

For this test case, a PTO system is activated on both WECs to extract energy out of the incident wave field (see Figure 6.1a). The PTO system used in the experiments is modelled as a second coulomb damper (Devolder et al., 2017c):

$$F_{PTO} = -\mu F_{spring} sign(v(t)) = -\mu 4 dx k_{spring} sign(v(t)) \tag{6.16}$$

in which the spring compression increment $dx = 30.5\ mm$ and the spring stiffness coefficient $k_{spring} = 0.14\ N/mm$.

Figure 6.7 shows the time series of the WECs' heave motions for both numerical and experimental data and in general a good correspondence is observed. The shape and the phase of both time signals are similar while the differences in heave amplitudes are limited. For the experimental signals, the maximum heave amplitude of WEC4 ($0.050\ m$) is only slightly larger than that of WEC5 ($0.045\ m$) while the numerically obtained results show larger differences: $0.065\ m$ and $0.050\ m$ for WEC4 and WEC5 respectively.

The time series of the surface elevations are presented in Figure 6.8. Differences between numerical and experimental signals are observed for the minimum and mainly for the maximum surface elevations. The largest relative error is again observed for WG11, which was also the case for the fixed WECs simulation presented in Figure 6.6 (see Table 6.2). Figure 6.9 depicts a snapshot of the perturbed wave field at $t = 50\ s$ inside the NWT. Waves are generated and absorbed at the right and left boundary respectively. The observed reduced wave height behind the 2-WEC array near the outlet boundary is due to the increasing aspect ratio of the grid cells as reported in section 6.2.2. This increasing aspect ratio is responsible for numerical wave damping. This is however beneficial in order to avoid wave reflection from the absorbing outlet boundary. Only in a limited area around the 2-WEC array, a significantly perturbed wave field is observed in the NWT. The wave gauges used in Figure 6.8 are however outside that zone which explains the identical wave height in the NWT at those three locations. Due to the perturbed wave field near the WECs, each WEC is slightly influencing the numerically predicted heave motion of the other WEC which shows the interaction between the

two WECs. This is also illustrated in Figure 6.7 by observing a different amplitude of the numerically obtained heave motions for both WECs.

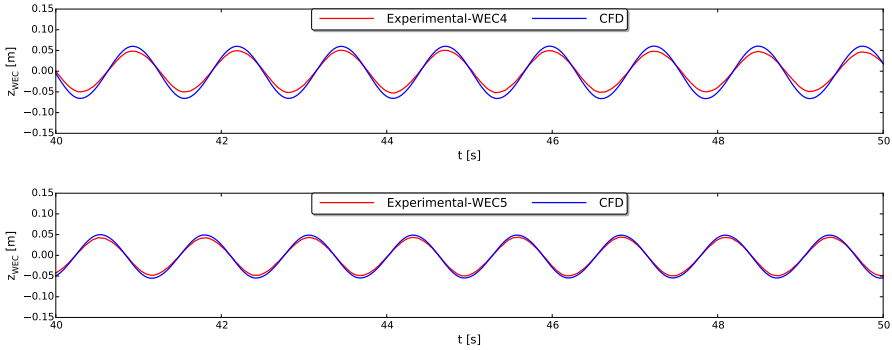

Figure 6.7: Vertical position of WEC4 (top) and WEC5 (bottom) obtained with CFD (blue line) compared to the experimental heave motions (red line).

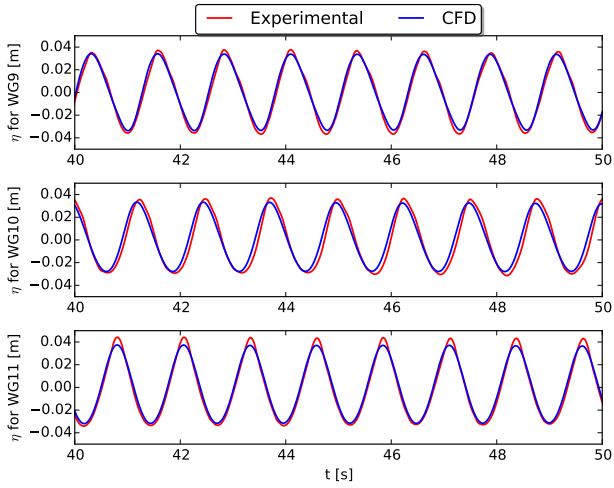

Figure 6.8: Perturbed wave field using WG9, WG10 and WG11 (see Figure 6.2) around the heaving 2-WEC array during a regular wave test ($H = 0.074\ m$, $T = 1.26\ s$, $d = 0.70\ m$) obtained with CFD (blue line) compared to the experimental data (red line).

6.3.2 5-WEC array

In this subsection, three more WECs are added to the NWT resulting in an array of five WECs installed in a line: WEC1 to WEC5 (see Figures 6.2 and 6.3). Again, numerical and experimental results are presented using both fixed and heaving WECs subjected to regular waves.

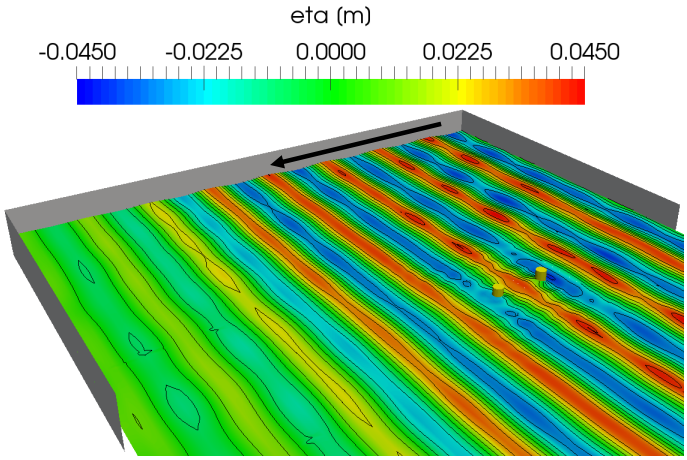

Figure 6.9: A three dimensional snapshot of the perturbed wave field around the heaving 2-WEC array obtained with CFD at $t = 50\ s$. The arrow indicates the direction of the incoming waves.

6.3.2.1 Fixed 5-WEC array

Figure 6.10 depicts the wave-induced surge force on the five fixed WECs as a function of time for both numerical (blue lines) and experimental data (red lines). Again, the numerically obtained surge forces are in a very good agreement with the experimental data and show relative errors of maximum $10\ \%$ in Table 6.2. The time signals also reveal that the maximum and minimum surge force on the WECs is independent of the WEC's position in the array and wave basin. This is also confirmed by comparing Figure 6.5 (2-WEC array) and Figure 6.10 (5-WEC array) showing identical loading cycles on the fixed WECs.

The perturbed wave field due to the presence of fixed WECs is visualised by using time series for the surface elevations in Figure 6.11 at different locations in the NWT (see Figure 6.2). The numerical results are in a very good agreement with the experimental measurements, except for WG8 and WG11 (see also the larger relative errors in Table 6.2 compared to the other WGs). Similar to the observation for the fixed 2-WEC array (section 6.3.1.1), a larger amplitude of the experimentally obtained surface elevations for WG11 is observed compared to the numerical results. For this test case, wave gauges were also installed in between the WECs, see Figure 6.2. For WG6 to WG9, Figure 6.11 indicates a small perturbed wave field due to reflection and diffraction: WG6: $H = 0.086\ m$ (reflection only), WG7: $H = 0.070\ m$, WG8: $H = 0.062\ m$ and WG9: $H = 0.059\ m$. Next to the array (WG12, WG13, WG14 and WG15), no disturbance is observed in the time signal of the surface elevations because those wave gauges are located outside the zone of a significantly perturbed wave field.

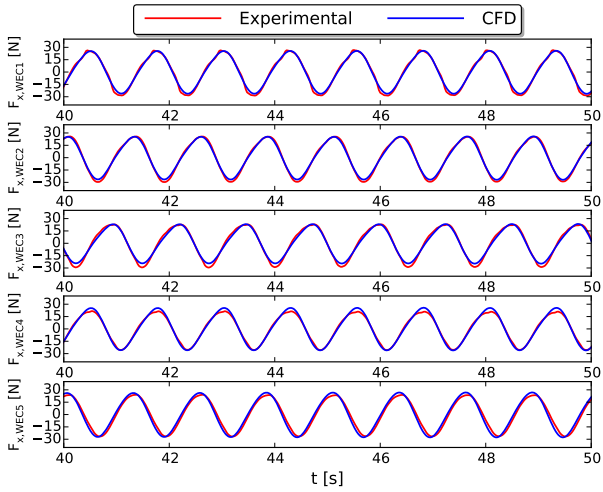

Figure 6.10: Wave-induced surge force $F_{X,WEC}$ on WEC1 (top) to WEC5 (bottom), all fixed, obtained with CFD (blue line) compared to the experimental measurements (red line) after filtering out the noise.

6.3.2.2 Heaving 5-WEC array

If the WECs are allowed to heave, three frictional forces (F_{LD}, $F_{bearings,X}$ and F_{PTO}) are applied on each WEC with identical parameters as for the 2-WEC array described in section 6.3.1.2. The heave motions of the five WECs as a function of time are given in Figure 6.12 for both experimental and numerical data. The time series reveal that, in general, both results are comparable. However, significant differences in heave amplitudes are observed for WEC1 and WEC4 with relative errors larger than $35\ \%$ (see Table 6.2). Remarkably for WEC2, the numerically predicted heave motion shows a small phase difference with the experimental data. Those discrepancies are discussed in the next section 6.4.

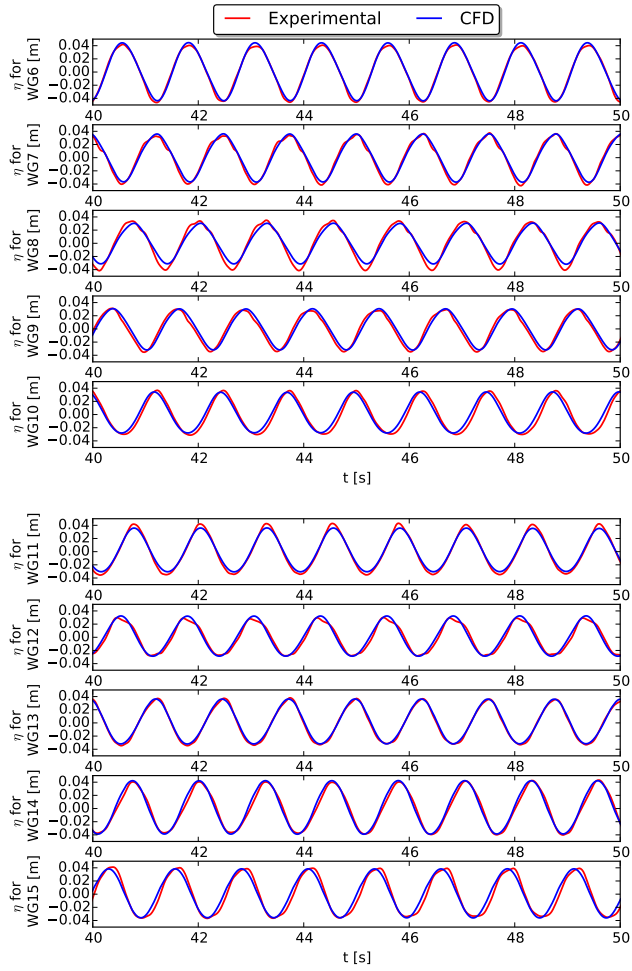

Figure 6.11: Perturbed wave field using WG6 to WG15 (see Figure 6.2) around the 5-WEC array with fixed WECs during a regular wave test ($H = 0.074\ m$, $T = 1.26\ s$, $d = 0.70\ m$) obtained with CFD (blue line) compared to the experimental data (red line).

Figure 6.13 depicts the wave-induced surge force acting on the WECs for both experimental and numerical data. In contrast to the discrepancies observed for the WECs' heave motions, a better agreement between numerical and experimental data is demonstrated for the surge forces on the WECs. However, for WEC1, the peaks and troughs in the experimental signal are deviating from the numerical result. This is due to large spikes observed in the experimental recorded time series before noise filtering is applied.

A good agreement is also found when comparing numerical and experimental data for the perturbed wave field around the 5-WEC array (Figure 6.14). However,

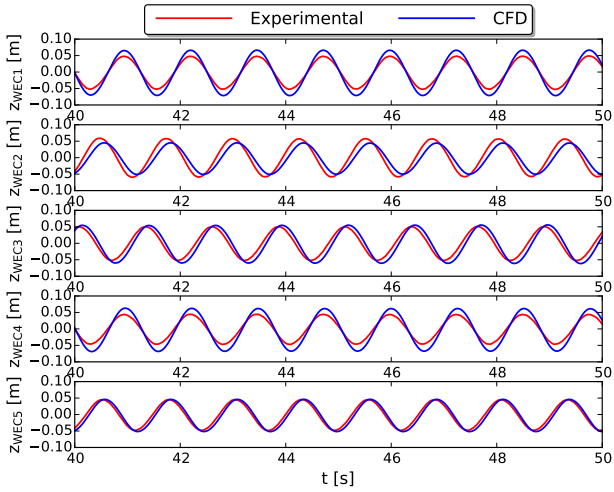

Figure 6.12: Vertical position of WEC1 (top) to WEC5 (bottom) obtained with CFD (blue line) compared to the experimental heave motions (red line).

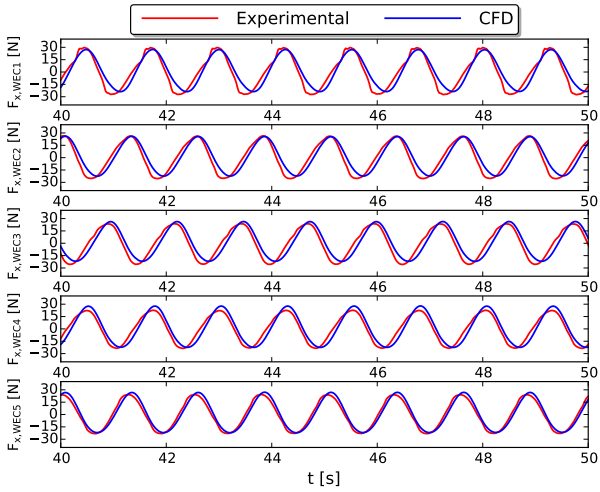

Figure 6.13: Wave-induced surge force $F_{X,WEC}$ on WEC1 (top) to WEC5 (bottom), all heaving, obtained with CFD (blue line) compared to the experimental measurements after filtering the noise (red line).

some discrepancies are observed regarding the time series of the surface elevations in the wave basin, in particular for the maximum and minimum surface elevations. Figure 6.15 depicts a snapshot of the perturbed wave field at $t = 50\ s$. Similar

to Figure 6.9, waves are generated and absorbed at the right and left boundary respectively. Again, the reduced wave height behind the 5-WEC array near the outlet boundary is due to the increasing aspect ratio of the grid cells leading to numerical wave damping. In a local zone near the array, a significantly perturbed wave field is predicted by the numerical model. Due to a perturbed wave field near the array, the numerically predicted heave motions for the individual WECs are not uniform (see the blue lines in Figure 6.12). Furthermore, an important reduction in wave height is observed right behind the array.

6.3.3 9-WEC array

The last test presented in this paper uses an array consisting of nine WECs arranged in a 3×3 layout. By using the symmetry plane shown in Figure 6.2, only six WECs are modelled: WEC1 to WEC3 and WEC6 to WEC8. Again, the same frictional forces are applied as previously defined in section 6.3.1.2 (F_{PTO}, $F_{bearings,X}$ and F_{LD}). In addition for WEC6, WEC7 and WEC8, an extra coulomb damper is implemented in order to take into account the frictional force of the bearings on the supporting axis (see Figure 6.1) in the Y-direction into account (cfr. equation 6.15):

$$F_{bearings,Y} = -\mu \left| F_{sway}(t) \right| sign(v(t)) \tag{6.17}$$

where $F_{sway}(t)$ is the horizontal force in the Y-direction acting on the WEC.

The heave motions for the six WECs are depicted in Figure 6.16. For WEC6 to WEC8, also the experimental signals for WEC11 to WEC13 (see Table 6.1) are shown in red. Those two time series are very similar and indicate a symmetrical behaviour for the experimentally obtained heave motions. For WEC1 to WEC3, installed on the symmetry plane, an identical result is observed between the experimental and the numerical model (low relative errors in Table 6.2). However for the outer WECs (WEC6 to WEC8), larger amplitudes are observed for the numerical result compared to the experimental data resulting in significant relative errors equal to $64\ \%$, $16\ \%$ and $29\ \%$ respectively. Probably, larger frictional forces were acting on WEC6 to WEC8 during the experiments.

The wave-induced surge force acting on WEC1 to WEC3, installed on the symmetry plane, are presented in Figure 6.17 for both the experimental and the numerical model. A good comparison is found between the results but again for WEC1, the peaks and troughs in the experimental signal are deviating from the numerical result due to large spikes observed in the experimental measurements before applying a bandpass filter.

The experimentally and numerically obtained perturbed wave field around the WECs are visualised in Figure 6.18 using several wave gauges (see Figure 6.2). Only the wave gauges positioned close to the 9-WEC array are presented. For the wave gauges which are not on the symmetry plane, two experimental results are shown. Only for WG18, WG19 and WG20, a slightly asymmetrical wave field is observed inside the experimental wave basin. In general, except for WG7, a good agreement is obtained between both models taking into account the remarks reported in the

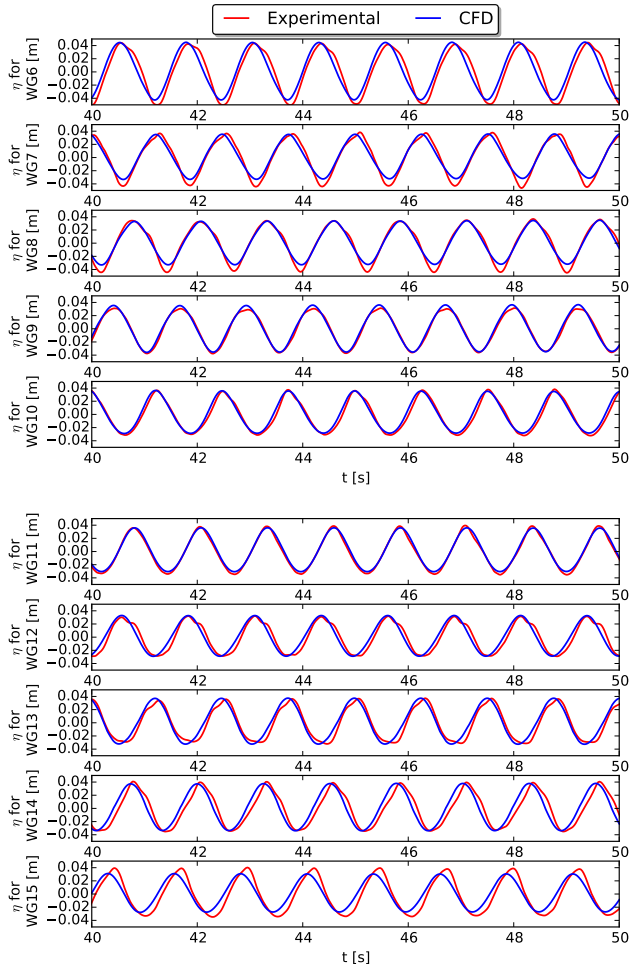

Figure 6.14: Perturbed wave field using several wave gauges (see Figure 6.2) around the heaving 5-WEC array during a regular wave test ($H = 0.074\ m$, $T = 1.26\ s$, $d = 0.70\ m$) obtained with CFD (blue line) compared to the experimental data (red line).

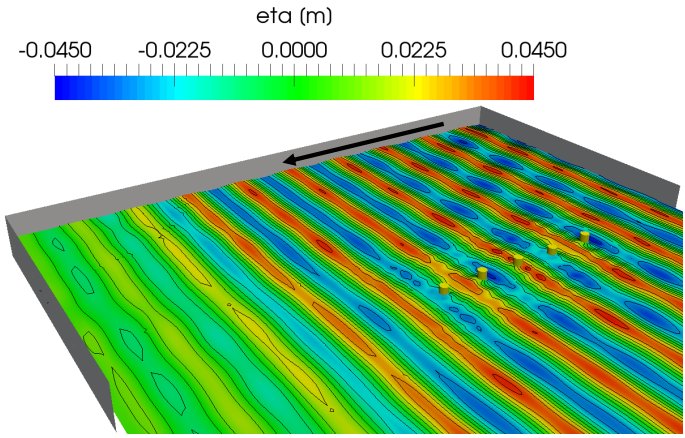

Figure 6.15: A three dimensional snapshot of the perturbed wave field around the 5-WEC array obtained with CFD at $t = 50\ s$. The arrow indicates the direction of the incoming waves.

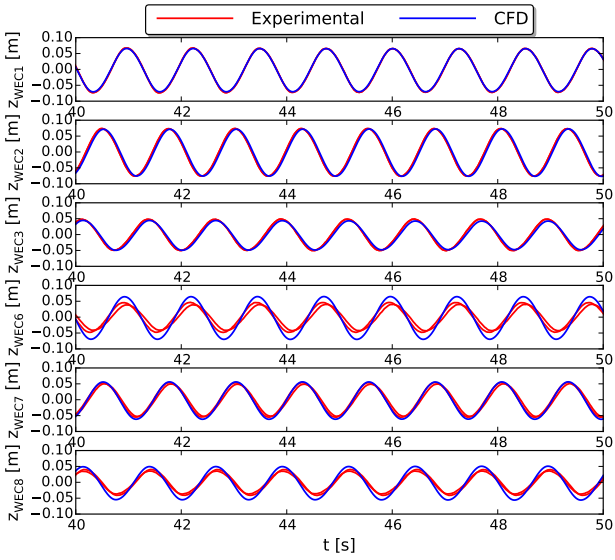

Figure 6.16: Vertical position of WEC1-2-3-6-7-8 obtained with CFD (blue line) compared to the experimental heave motions (red line).

previous sections 6.3.1.2 and 6.3.2.2. In particular for WG18, WG19 and WG20, the numerical result lies in-between the two experimental lines with a small phase shift. Figure 6.19 depicts a snapshot of the perturbed wave field at $t = 50\ s$. In

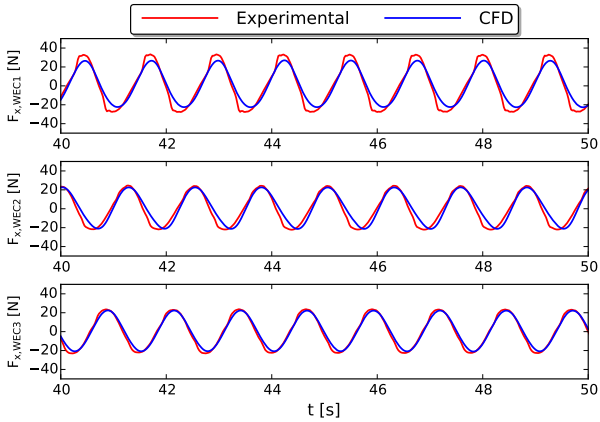

Figure 6.17: Wave-induced surge force $F_{X,WEC}$ acting on WEC1 (top) to WEC3 (bottom), all heaving, obtained with CFD (blue line) compared to the experimental measurements after filtering the noise (red line).

a large area around the 9WEC array, a significantly perturbed wave field by the heaving WECs is clearly visible. Due to the larger width of the array, compared to the 2-WEC and 5-WEC array (in a line), a clear reduction in wave height is visible behind the array, which is also observed in Figure 6.18 for WG9.

6.4 Discussion

In the previous section 6.3, two types of differences between the numerical and experimental results are observed. The first type of differences is seen in the heave motions of the WECs. In this work, we tried to capture as much physics as possible in the numerical model to reproduce the experimental tests. The WEC's PTO system and the sliding mechanism (see Figure 6.1) are included by mathematical models to take into account their influence on the WECs' kinematic motion. During the WECwakes experiments, the PTO system was mimicking a coulomb damper and is thus initially implemented in the numerical model as a coulomb damper only. The sliding mechanism was incorporated by both a linear damper (viscous flow of water between the shaft and shaft bearing) and a coulomb damper (caused by the wave induced horizontal force). However in our previous work (Devolder et al., 2017c), we found that the PTO system is not only behaving as a coulomb damper but also partially as an additional linear damper. Furthermore in reality, friction behaves uncontrolled. For example during the WECwakes project, it is noticed that the friction characteristics change due to fouling of the supporting axes for the sliding mechanism. Therefore before each testing day, the supporting axes were cleaned in order to minimise that particular model effect. This highlights partially the unknown physical behaviour of frictional forces in the experimental model. Furthermore, the frictional forces caused by the sliding mechanism might

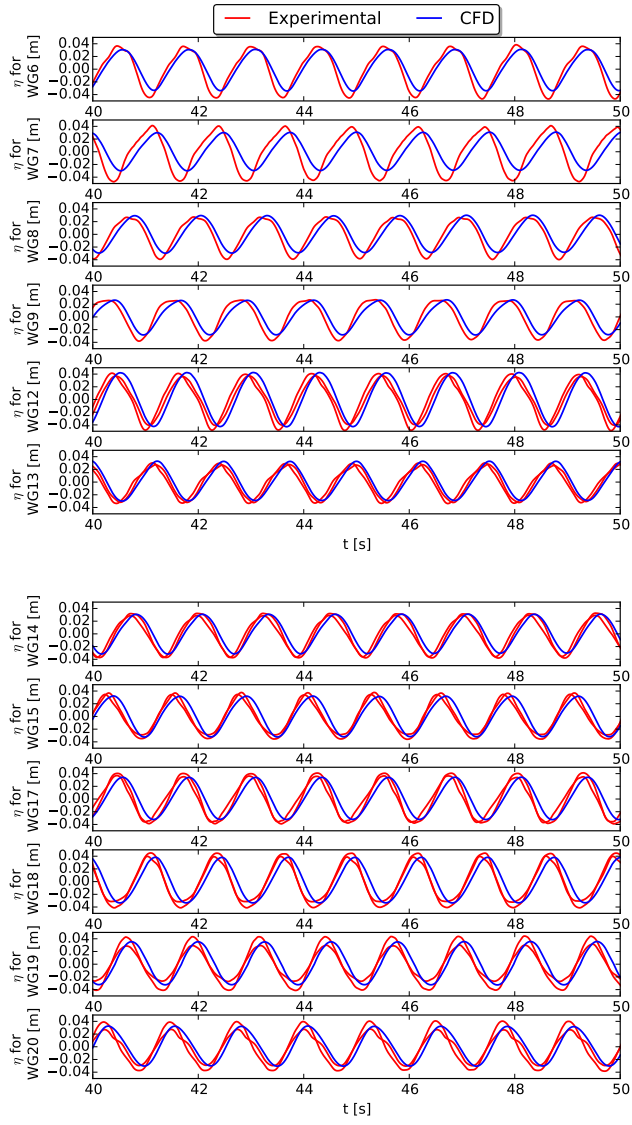

Figure 6.18: Perturbed wave field using several wave gauges (see Figure 6.2) around the heaving 9-WEC array during a regular wave test ($H = 0.074\ m$, $T = 1.26\ s$, $d = 0.70\ m$) obtained with CFD (blue line) compared to the experimental data (red line).

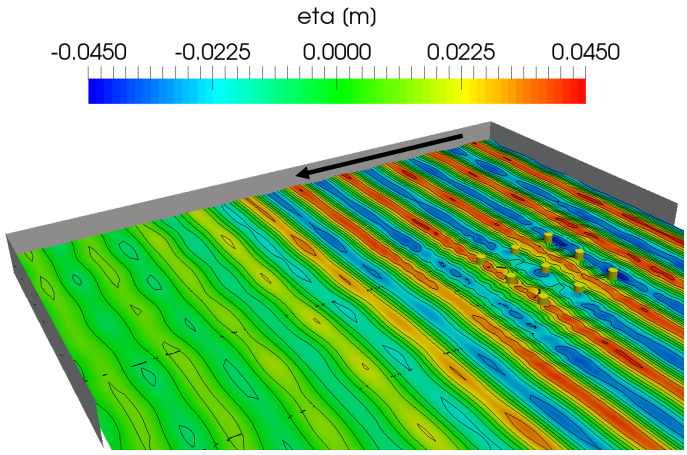

Figure 6.19: A three dimensional snapshot of the perturbed wave field around the heaving 9-WEC array obtained with CFD at $t = 50\ s$. The arrow indicates the direction of the incoming waves.

vary over the different WECs within the array. This is probably the most important explanation for the large variation in relative errors obtained for the heave motions over the different WECs, as indicated in Table 6.2. Note that in this study, identical parameters are used to model the frictional forces on all the WECs based on tuning the numerically obtained heave motion to the experimental measurement during a free decay test using WEC5. In order to perform a validation study of fluid-structure interaction simulations of floating heaving WECs, we recommend to start with validating a free decay test for each individual WEC within the array by using experimental data. This allows to estimate frictional forces due to a possible sliding mechanism by computing the hydrodynamic parameters of the device (e.g. the damped natural frequency and the hydrodynamic damping coefficient).

The second type of differences is found in the surface elevations of the perturbed wave field. Those deviations are largely assigned to the difference in reflection between the experimental wave basin (with an absorbing beach) and the numerical wave tank (with a shallow water absorbing boundary condition). Additionally, differences between experimental and numerical data are possibly caused by model effects in the experimental setup and numerical errors in simulations presented. For example, small errors in the calibration of the wave gauges contribute to the overall error observed in the experimentally obtained surface elevations. Interestingly, the surface elevations around the WECs, are showing smaller relative errors compared to the heave motions (see Table 6.2). Presumable, they are less influenced by the frictional forces acting on the WECs due to the sliding mechanism used for the experiments.

In general, a very good comparison is found for the horizontal wave-induced surge forces acting on the WECs, as indicated by the relative errors always smaller than $10\ \%$, except one, in Table 6.2. We expect that the surge force is not

influenced by the sliding mechanism and consequently does not depend on the frictional forces modelled by the coulomb damper and the linear damper in the numerical model. In order to run simulations with more degrees of freedom (e.g. surge motion), a good prediction of the surge force is required for example.

Despite the observed inaccuracies, in general, the numerical results are in good agreement with the experimentally obtained measurements. In contrast to the experimental data, which are only available at discrete locations, the numerical model yields a much higher spatial resolution of the perturbed wave field inside and around the WEC (array). During the validation of the numerically obtained surface elevations using the experimental measurements, a significantly perturbed wave field is not always observed at those specific locations. Snapshots of the surface elevations inside the numerical wave tank indicate that a significantly perturbed wave field is only observed very close to the WECs where no experimental wave gauges were installed. As a result, the WEC array effects are much easier to identify using the validated numerical wave tank.

6.5 Conclusions

Numerical simulations of two, five and nine heaving FPA WECs installed in a geometrical array configuration inside a numerical wave tank using CFD have been presented. The simulation results show the capability of state of the art numerical models, including stable coupled fluid–motion solvers, to accurately predict the independent motion of closely-spaced WECs in response to an incoming wave field. As such we are able, as a worldwide pioneering result, to simulate an array of nine independently moving WECs in a numerical wave tank using CFD. The numerically obtained results are validated using the WECwakes dataset. A good agreement is demonstrated for the WEC's heave motion, the wave-induced surge force acting on the WECs and surface elevations of the perturbed wave field at the measured locations. While results are perfect for the WECs on the symmetry plane of the numerical wave tank, deviations are noticed for the outer WECs, which we attribute to inaccuracies in the estimation of the frictional forces caused by the sliding mechanism of those particular WECs. In general, the numerical results have shown that our coupled fluid–motion solver is a robust and suitable toolbox to study fluid-structure interaction of WEC arrays, making it a complementary tool to experimental model tests. This research opens up the possibilities for numerical simulations of any kind of floating structure installed in any sea state using a numerical wave tank.

Chapter 7

Conclusions

7.1 Summary of the key findings

In this thesis, numerical simulations of coastal and offshore processes have been presented using a non-linear viscous numerical wave tank (NWT) implemented in the open source CFD toolbox OpenFOAM. The NWT uses a two-phase fluid solver based on the Navier-Stokes equations and a volume of fluid (VoF) method to track the interface between water and air. Boundary conditions for wave generation and absorption are adopted from the IHFOAM toolbox. In the first part of the thesis, Reynolds-averaged Navier-Stokes (RANS) turbulence modelling applied to a two-phase fluid solver has been investigated and enhanced for the simulation of wave propagation and wave breaking. The second part of the thesis has been focussing on accelerated fluid-structure interaction (FSI) simulations of floating bodies in the framework of wave energy converter (WEC) arrays.

The application of traditional RANS turbulence models for wave modelling in a NWT using a two-phase fluid solver are responsible for a large production of turbulent kinetic energy (TKE) around the air-water interface. This increases the turbulent viscosity at the free water surface significantly, resulting in excessive wave damping along the length of the computational domain. In this thesis, two buoyancy-modified RANS turbulence models, $k-\omega$ and $k-\omega\ SST$, have been applied to perform simulations of waves in a NWT. The modification is based on including explicitly the density in the turbulence transport equations and by adding implicitly a buoyancy source term to the TKE-equation. The influence of the buoyancy source term in the $k-\omega\ SST$ model has been demonstrated by simulating propagating regular waves. As a result, the buoyancy-modified $k-\omega\ SST$ model switches to the laminar regime near the free water surface, preventing excessive wave damping for non-breaking high-steepness waves. Furthermore, simulations of wave run-up around a monopile under regular waves have shown similar results for the surface elevations around the monopile as experimentally obtained in a physical wave flume. In case of wave breaking simulations, two zones have been defined in the NWT: a wave propagation zone and a wave breaking zone. A unified model that handles both regions at the same time is presented by using the buoyancy-

modified turbulence models. The performance of both a buoyancy-modified $k-\omega$ and a $k-\omega$ SST model for simulating breaking waves is evaluated for spilling and plunging breakers respectively. Firstly, in the flow field prior to wave breaking (i.e. during wave propagation), low turbulence levels are observed and a laminar solution is desirable. Again, it has been demonstrated that the buoyancy term forces the solution of the flow field near the free water surface to a laminar solution and wave damping is prevented. Secondly in the surf zone where waves break, significant turbulence levels are noticed. For this zone, the buoyancy term goes to zero and a fully turbulent flow field is resolved by the numerical model. For all the simulations presented, it has been concluded that the results predicted by the buoyancy-modified turbulence models agree the best with the experimental measurements for the surface elevations, undertow profiles and TKE levels compared to traditional turbulence models. In particular, the buoyancy-modified turbulence models significantly reduce the common overestimation of TKE in the two-phase flow field.

Fluid-structure interaction simulations of floating bodies in a NWT have shown stability issues between the fluid solver and the motion solver. In this thesis, the numerical instability is identified and related to the added mass effect. A stable fluid–motion coupling is obtained by using multiple sub iterations during every time step and by applying relaxation of acceleration of the floating body. As a result, a converged solution between the hydrodynamic flow field around and the kinematic motion of the floating body is achieved during every time step of the transient simulation. In order to lower the CPU time, the convergence speed of the fluid–motion coupling is increased by using an accelerated coupling algorithm. Therefore, implicit coupling during the sub iterations is assumed and the added mass is estimated by calculating a Jacobian, based on the available solutions of previous sub iterations for the acceleration of the floating body and the force acting on it. The coupled fluid–motion solver is firstly applied to perform FSI simulations of two benchmark test cases: a free decay test of a single WEC unit (small added mass effect) and a free falling wedge impacting on the water surface (significant added mass effect). In general, maximum three sub iterations per time step are needed to obtain a converged solution, except at the moment of water entry during the free falling wedge simulation. For both test cases, numerical results are validated by using experimental data. Firstly, the WEC's heave motion and radiated wave field during the free decay test are very similar to the experimental measurements. Secondly for the free falling wedge, a good agreement between numerical and experimental data is found for the wedge's vertical position and velocity. Subsequently, FSI simulations of the response of a single WEC unit to regular waves are performed inside a NWT. The numerical results are validated with experimental data for the WEC's heave motion and the surface elevations of the perturbed wave field obtained in the large wave flume of the department of civil engineering at Ghent University. A proof of concept study of a survivability simulation has demonstrated the need for a CFD NWT to resolve non-linear wave–wave interactions during wave propagation and to simulate wave breaking events on a WEC. Furthermore, it has been demonstrated that the accelerated coupling algorithm for the fluid–motion solver remains stable under extreme wave conditions

and large displacements of the WEC by using few sub iterations during every time step. The numerical simulations of a single WEC unit have been extended to simulations of a WEC array with independently heaving and closely-spaced WECs in response to an incoming wave field. In this thesis and as a worldwide pioneering result, numerical simulations have been performed for an array consisting of two, five and nine WECs inside a NWT using CFD. For all the simulations presented, numerical results are validated by using the WECwakes dataset. The pioneering WECwakes experimental tests focussed on recording WEC responses, forces on WECs and wave field modifications around WECs and WEC arrays of 2 up to 25 WECs, in the framework of the EU FP7 Hydralab IV program. A good agreement has been demonstrated between the numerical results and the experimental data for the WEC's heave motion, the wave-induced surge force acting on the WECs and the surface elevations of the perturbed wave field at the measured locations.

In general, the numerical results have shown that a CFD NWT is a robust and suitable toolbox to study WECs and WEC arrays. Furthermore, complex physical processes such as turbulent effects, wave breaking events and resonant non-linear WEC motions damped by viscous forces are accurately simulated in a CFD NWT. These processes are however not captured, or strongly simplified, by the widely used linear boundary element method (BEM) models based on potential flow theory. All this makes a CFD NWT a complementary tool to experimental model tests. In addition, this research opens up the possibilities for numerical simulations of any kind of floating structure(s) installed in any sea state using a CFD NWT.

7.2 Recommendations for future research

The work presented in this thesis contributes to the development of enhanced prediction tools for NWTs using CFD. This final section gives a number of recommendations for future research to further develop NWTs and to make NWTs an equivalent alternative complementary to physical wave flumes or wave basins:

1. Validation of the buoyancy-modified turbulence models for wave-current interaction simulations by using experimental measurements;
   Chapter 2 has been focussing on simulating propagating waves in a NWT and the flow field in the water phase consists only of wave-induced orbital velocities. By superimposing a steady current on propagating waves, the flow field will change and this will affect the velocity gradient and consequently the production of TKE in the flow field.

2. Accurate modelling of entrained air during wave breaking simulations using a two-phase fluid solver based on the VoF method to dissipate wave breaking induced turbulence;
   In Chapter 3, air entrainment has been observed for the wave breaking simulations using a VoF-type fluid solver. The VoF method however assumes that the two fluids are immiscible, making the method extremely suitable for segregated fluid flows such as propagating waves. On the contrary for wave breaking simulations, air bubbles are not resolved correctly by the VoF

method since they are dispersed in the water phase. A combination of buoyancy-modified RANS turbulence modelling with an accurate treatment of air bubbles in the surf zone might result in even better predictions for the turbulent quantities in the flow field and in particular for the dissipation of wave breaking induced turbulence by air bubbles.

3. Applying a realistic PTO system to control the motion of the WEC installed in a CFD NWT and to quantify realistic power production of WECs;
   The simulations of WECs and WEC arrays in Chapter 5 and Chapter 6 are using a coulomb damper to model a simplified PTO system. In practice and in order to maximise the WEC's energy absorption, sophisticated PTO models are used and they apply control strategies to drive the WEC's motion into resonance. To test these state of the art PTO models, a coupling with a CFD NWT is required to include both viscous and non-linear effects.

4. Increasing the degrees of freedom for the motion solver and implementing mooring lines in the CFD NWT, especially for survivability simulations;
   The coupled fluid–motion solver developed in Chapter 4 was restricted to a single degree of freedom motion solver. In practice, WECs operate in multiple degrees of freedom since they are connected to the seabed by mooring lines. These mooring lines are designed to withstand survivability conditions and require WEC testing in a CFD NWT including a multiple degrees of freedom motion solver coupled with a mooring line solver.

5. Extension of the experimental WEC dataset to extreme wave conditions, including breaking waves, and closely-spaced WECs to validate the coupled fluid–motion solver implemented in the CFD NWT;
   Experimental measurements obtained in a physical wave basin for WECs and WEC arrays are scarce. Until today, the WECwakes dataset is the largest publicly available database for single WECs and WEC arrays. However, the sea states tested are limited to operational conditions and the WEC-WEC distance is minimum five WEC diameters. In order to validate a CFD NWT thoroughly, experimental data for survivability simulations and very closely-spaced WECs in an array configuration are required.

6. Coupling between an accurate CFD NWT and a fast wave propagation solver to increase the efficiency in terms of CPU time for WEC array simulations over large domains.
   CFD NWTs suffer from long computation times, having a negative impact on their feasibility for practical applications. By quantifying the relative importance of viscous versus potential fluid flow and non-linear versus linear effects, the near-field zone can be demarcated. At the interface between potential and viscous or linear and non-linear fluid flow for example, a coupling between an accurate wave-structure interaction solver (e.g. OpenFOAM as a non-linear viscous NWT) and a fast wave-propagation solver (e.g. a linear or a non-linear potential flow NWT) might increase the efficiency of the numerical simulations by reducing the time-consuming 3D CFD NWT.

Appendix A

Turbulent kinetic energy levels under breaking waves

This appendix belongs to Chapter 3, dealing with wave breaking simulations in a numerical wave tank (NWT) using buoyancy-modified RANS turbulence models. The results presented for the turbulent kinetic energy (TKE) are the computed values of k by the turbulence model and they are validated with experimental data. Therefore, it is important to know how the experimentally obtained values for TKE are calculated. Ting and Kirby (1994) used velocity measurements to quantify TKE in the flow field:

$$k_{exp} = \frac{2}{3}(\widetilde{u'^2_{x,exp}} + \widetilde{u'^2_{z,exp}}) \tag{A.1}$$

in which $u'_{x,exp}$ and $u'_{z,exp}$ are the experimentally obtained turbulent fluctuations from the mean velocity (i.e. undertow and orbital wave motion) in both X- and Z-direction and the tilde is an operator to take a phase average.

In Chapter 3, unsteady RANS simulations are performed for the velocity field, i.e. the velocity components u_x and u_z are ensemble averaged quantities. In the ideal scenario, unsteady RANS simulations return the same results for e.g. the velocity field at a specific phase during every regular wave cycle and no fluctuations for the velocity field are expected. However, some variability in the velocity field for a specific phase is observed during every wave cycle. An example is shown in Figure A.1 for the spilling breakers using the profile of the horizontal velocity component at $x = 7.885\ m$ for phase 0 between $t = 60\ s$ and $t = 100\ s$ (20 wave periods, $T = 2\ s$). The red lines are the instantaneous profiles during every wave period at phase 0 (i.e. $t = 60\ s$, $t = 62\ s$, etc.) while the blue line represents the averaged profile for phase 0 using 20 wave periods. It is demonstrated that for the buoyancy-modified $k-\omega$ model the variation of the horizontal velocity component over different wave periods is much smaller compared to the $k-\omega\ SST$ model. This is also expected based on the surface elevations: a larger standard deviation for the $k-\omega\ SST$ model is observed compared to the $k-\omega$ model (see Figure

3.2 and Figure 3.5 in Chapter 3).

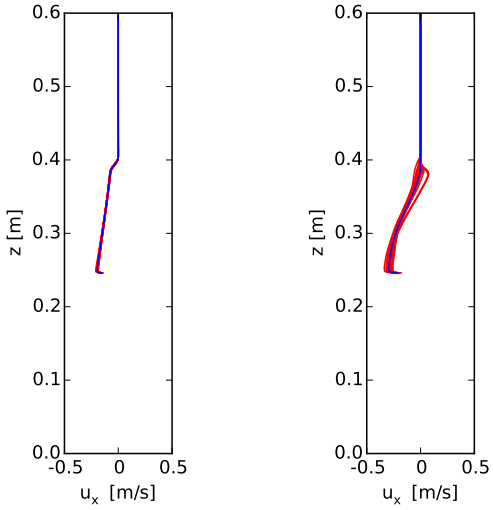

Figure A.1: Numerically obtained undertows for spilling breakers at $x = 7.885\ m$ showing instantaneous profiles of the horizontal velocity u_x for 20 wave periods at phase 0 (red lines) and the mean value (blue line) using a buoyancy-modified $k-\omega$ (left panel) and a buoyancy-modified $k-\omega$ SST model (right panel).

The questions is now, how large is the variability for u_x and u_z over different wave periods because this can be seen as a supplementary value for the TKE: k_{sup}. Such an analysis was reported in Jacobsen (2011). In order to estimate the supplementary TKE, the same analysis is performed. Therefore, the values for $u_x^{'}$ and $u_z^{'}$ are computed which are fluctuations from the ensemble averaged quantities u_x and u_z resolved by the Navier-Stokes equations (3.1) and (3.1). The contribution to the overall TKE is calculated analogue to Ting and Kirby (1994), equation (A.1):

$$k_{sup} = \frac{2}{3}(\widetilde{u_x^{'2}} + \widetilde{u_z^{'2}}) \tag{A.2}$$

In the Figures A.2 and A.3, the results for TKE are shown for both spilling and plunging breakers respectively at the different profiles using the buoyancy-modified $k-\omega$ and $k-\omega$ SST models. The solid blue lines indicate the average value over 20 wave periods computed by the RANS turbulence model $\overline{k}$. The dashed blue lines additionally include the turbulence based on the period average of the velocity field, also averaged over 20 wave periods, $\overline{k} + \overline{k_{sup}}$. It is shown that $\overline{k}$ is dominating over $\overline{k_{sup}}$, which was also concluded in Jacobsen (2011). Consequently, the fluctuating component of the velocity field over different wave periods is not considered in the analysis for TKE in Chapter 3.

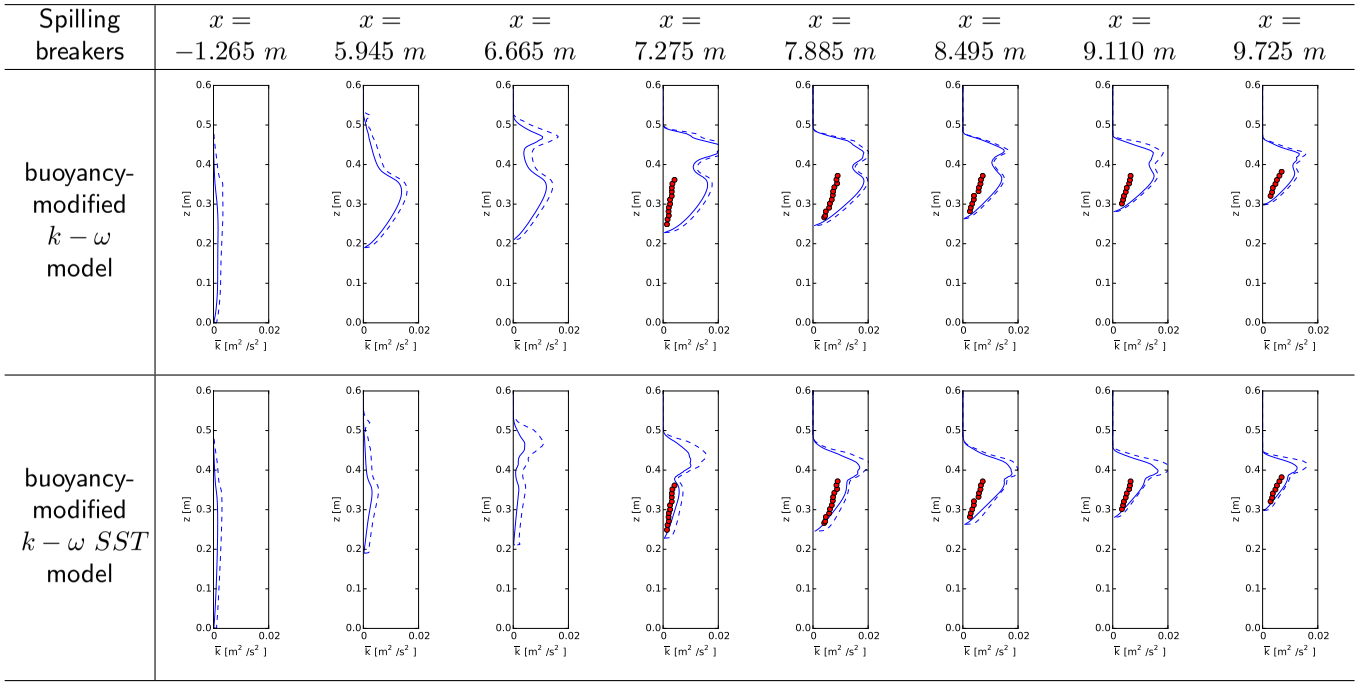

Figure A.2: Numerically obtained undertows for the time averaged TKE $\overline{k}$ (blue lines) averaged over 20 wave periods computed by the buoyancy-modified $k-\omega$ and buoyancy-modified $k-\omega\ SST$ model. The blue dashed lines depict $\overline{k}+\overline{k_{sup}}$ also averaged over 20 wave periods. The red dots represent the experimental data (Ting and Kirby, 1994) for the case of spilling breakers.

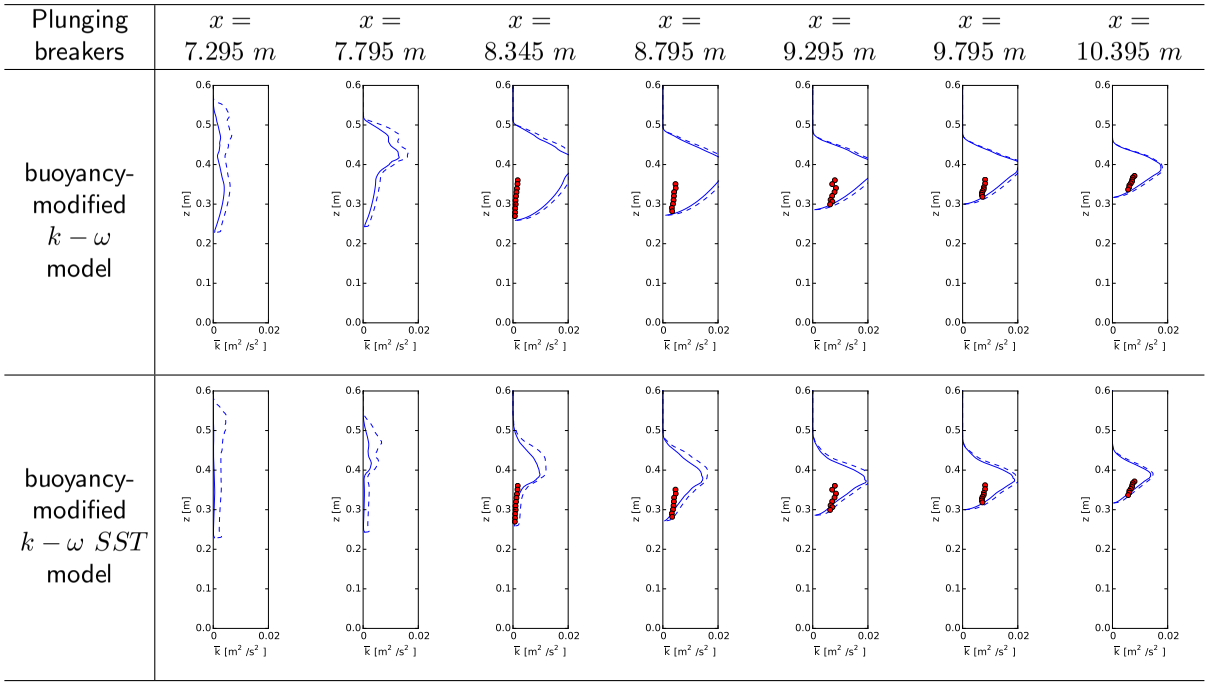

Figure A.3: Numerically obtained undertows for the time averaged TKE $\overline{k}$ (blue lines) averaged over 20 wave periods computed by the buoyancy-modified $k-\omega$ and buoyancy-modified $k-\omega\ SST$ model. The blue dashed lines depict $\overline{k}+\overline{k_{sup}}$ also averaged over 20 wave periods. The red dots represent the experimental data (Ting and Kirby, 1994) for the case of plunging breakers.

References

Abanades, J., Greaves, D., and Iglesias, G. (2015). Coastal defence using wave farms: The role of farm-to-coast distance. *Renewable Energy*, 75:572–582.

Agamloh, E. B., Wallace, A. K., and von Jouanne, A. (2008). Application of fluid-structure interaction simulation of an ocean wave energy extraction device. *Renewable Energy*, 33(4):748–757.

Alagan Chella, M., Bihs, H., Myrhaug, D., and Muskulus, M. (2015). Breaking characteristics and geometric properties of spilling breakers over slopes. *Coastal Engineering*, 95:4–19.

Alagan Chella, M., Bihs, H., Myrhaug, D., and Muskulus, M. (2016). Hydrodynamic characteristics and geometric properties of plunging and spilling breakers over impermeable slopes. *Ocean Modelling*, 103:53–72.

Alves, M. (2016). Frequency-Domain Models. In *Numerical Modelling of Wave Energy Converters*, pages 11–30. Elsevier.

Aqwa, A. (2018). Hydrodynamics Simulation and Diffraction Analysis.

Babarit, A. (2017). *Ocean wave energy conversion : resource, technologies and performance*. Elsevier.

Babarit, A. and Delhommeau, G. (2015). Theoretical and numerical aspects of the open source BEM solver NEMOH. In *Proceedings of the 11th European Wave and Tidal Energy Conference*.

Babarit, A., Folley, M., Charrayre, F., Peyrard, C., and Benoit, M. (2013). On the modelling of WECs in wave models using far field coefficients. *European Wave and Tidal Energy Conference, EWTEC*, pages 1–9.

Berberović, E., van Hinsberg, N. P., Jakirlić, S., Roisman, I. V., and Tropea, C. (2009). Drop impact onto a liquid layer of finite thickness: Dynamics of the cavity evolution. *Physical Review E*, 79(3):036306.

Bitner-Gregersen, E. and Gramstad, O. (2016). Rogue waves. Impact on ship and offshore structures. *DNV GL R&I Position Paper*, pages 1–60.

Boers, M. (1996). Simulation of a Surf Zone with a Barred Beach; Part 1: Wave Heights and Wave Breaking. Technical report, Delft University of Technology.

Bradford, S. F. (2000). Numerical Simulation of Surf Zone Dynamics. *Journal of Waterway, Port, Coastal, and Ocean Engineering*, 126(1):1–13.

Brown, S., Greaves, D., Magar, V., and Conley, D. (2016). Evaluation of turbulence closure models under spilling and plunging breakers in the surf zone. *Coastal Engineering*, 114:177–193.

Brown, S. A., Magar, V., Greaves, D. M., and Conley, D. C. (2014). An Evaluation of RANS Turbulence Closure Models for Spilling Breakers. *Coastal Engineering Proceedings*, 1(3879):5.

Budal, K. (1977). Theory for absorption of wave power by a system of interacting bodies. *Journal of Ship Research*.

Bullock, G., Crawford, A., Hewson, P., Walkden, M., and Bird, P. (2001). The influence of air and scale on wave impact pressures. *Coastal Engineering*, 42(4):291–312.

Chen, L. F., Zang, J., Hillis, a. J., Morgan, G. C. J., and Plummer, a. R. (2014). Numerical investigation of wave-structure interaction using OpenFOAM. *Ocean Engineering*, 88:91–109.

Child, B. (2016). Semi-analytical Array Models. In *Numerical Modelling of Wave Energy Converters*, pages 165–190. Elsevier.

Choi, J. and Yoon, S. B. (2009). Numerical simulations using momentum source wave-maker applied to RANS equation model. *Coastal Engineering*, 56(10):1043–1060.

Chow, J. H. and Ng, E. Y. K. (2016). Strongly coupled partitioned six degree-of-freedom rigid body motion solver with Aitken's dynamic under-relaxation. *International Journal of Naval Architecture and Ocean Engineering*, 8(4):320–329.

Christensen, E. D. (2006). Large eddy simulation of spilling and plunging breakers. *Coastal Engineering*, 53(5):463–485.

Christensen, E. D., Bredmose, H., and Hansen, E. A. (2005). Extreme wave forces and wave run-up on offshore wind-turbine foundations. In *Copenhagen Offshore Wind 2005*, pages 1–10.

Cox, D. T. and Kobayashi, N. (2000). Identification of intense, intermittent coherent motions under shoaling and breaking waves. *Journal of Geophysical Research: Oceans*, 105(C6):14223–14236.

Cruz, J. (2008). Ocean Wave Energy: Current Status and Future Perspectives.

Davidson, J., Cathelain, M., Guillemet, L., Le Huec, T., and Ringwood, J. (2015a). Implementation of an OpenFOAM Numerical Wave Tank for Wave Energy Experiments. In *Proceedings of the 11th European wave and tidal energy conference*, pages 09B1–1–1 – 09B1–1–10, Nantes, France. European Wave and Tidal Energy Conference.

Davidson, J., Giorgi, S., and Ringwood, J. V. (2015b). Linear parametric hydrodynamic models for ocean wave energy converters identified from numerical wave tank experiments. *Ocean Engineering*, 103:31–39.

Davidson, J., Windt, C., Giorgi, G., Genest, R., and Ringwood, J. V. (2018). Evaluation of energy maximising control systems for wave energy converters using OpenFOAM for wave energy converters using OpenFOAM. In Nobrega, M. and Jasak, H., editors, *OpenFOAM - Selected papers from the 11th Workshop*, number February. Springer International Publishing.

Day, A., Babarit, A., Fontaine, A., He, Y.-P., Kraskowski, M., Murai, M., Penesis, I., Salvatore, F., and Shin, H.-K. (2015). Hydrodynamic modelling of marine renewable energy devices: A state of the art review. *Ocean Engineering*, 108:46–69.

De Vos, L., Frigaard, P., and De Rouck, J. (2007). Wave run-up on cylindrical and cone shaped foundations for offshore wind turbines. *Coastal Engineering*, 54:17–29.

Degroote, J. (2013). Partitioned Simulation of Fluid-Structure Interaction. *Archives of Computational Methods in Engineering*, 20(3):185–238.

del Jesus, M., Lara, J. L., and Losada, I. J. (2012). Three-dimensional interaction of waves and porous coastal structures: Part I: Numerical model formulation. *Coastal Engineering*, 64:57–72.

Delhommeau, G. (1987). *Les problemes de diffraction-radiation et de resistance de vagues : etude theorique et resolution numerique par la methode des singularites*. PhD thesis, École Nationale Supérieure de Mécanique de Nante.

Devolder, B., Rauwoens, P., and Troch, P. (2016). Numerical simulation of a single Floating Point Absorber Wave Energy Converter using OpenFOAM®. In *Progress in Renewable Energies Offshore*, pages 197–205. CRC Press.

Devolder, B., Rauwoens, P., and Troch, P. (2017a). Application of a buoyancy-modified k-ω SST turbulence model to simulate wave run-up around a monopile subjected to regular waves using OpenFOAM®. *Coastal Engineering*, 125:81–94.

Devolder, B., Rauwoens, P., and Troch, P. (2017b). Numerical simulation of heaving Floating Point Absorber Wave Energy Converters using OpenFOAM. In *VII International Conference on Computational Methods in Marine Engineering*, pages 777–788, Nantes, France.

Devolder, B., Rauwoens, P., and Troch, P. (2017c). Towards the numerical simulation of 5 Floating Point Absorber Wave Energy Converters installed in a line array using OpenFOAM. In *12th European Wave and Tidal Energy Conference (EWTEC2017)*, pages 739–1 739–10, Cork, Ireland.

Devolder, B., Schmitt, P., Rauwoens, P., Elsaesser, B., and Troch, P. (2015). A Review of the Implicit Motion Solver Algorithm in OpenFOAM® to Simulate a Heaving Buoy. In *18th Numerical Towing Tank Symposium*, Cortona, Italy.

Devolder, B., Troch, P., and Rauwoens, P. (2018a). Accelerated numerical simulations of a heaving floating body by coupling a motion solver with a two-phase fluid solver. *under review for Computers & Mathematics with Applications*.

Devolder, B., Troch, P., and Rauwoens, P. (2018b). Performance of a buoyancy-modified k-ω and k-ω SST turbulence model for simulating wave breaking under regular waves using OpenFOAM®. *Coastal Engineering*, 138:49–65.

Dunbar, A. J., Craven, B. A., and Paterson, E. G. (2015). Development and validation of a tightly coupled CFD/6-DOF solver for simulating floating offshore wind turbine platforms. *Ocean Engineering*, 110:98–105.

El Safti, H., Bonakdar, L., and Oumeraci, H. (2014). A Hybrid 2D-3D CFD Model System for Offshore Pile Groups Subject to Wave Loading. In *Proceedings of the 33rd International Conference on Ocean, Offshore and Arctic Engineering (OMAE 2014)*, pages 1–11, San Fransisco, California, USA. ASME.

Elhanafi, A., Fleming, A., Leong, Z., and MacFarlane, G. (2017). Effect of RANS-based Turbulence Models on Nonlinear Wave Generation in a Two-Phase Numerical Wave Tank. *Progress in Computational Fluid Dynamics, an International Journal*, 17(3):141–158.

Evans, D. (1980). Some analytic results for two and three dimensional wave-energy absorbers. *Power from sea waves*.

Falnes, J. (1980). Radiation impedance matrix and optimum power absorption for interacting oscillators in surface waves. *Applied ocean research*.

Fernandez-Mora, A., Ribberink, J. S., van der Zanden, J., van der Werf, J. J., and Jacobsen, N. G. (2017). RANS-VOF modeling of hydrodynamics and sand transport under full-scale non-breaking and breaking waves. *Coastal Engineering Proceedings*, 1(35):29.

Fitzgerald, C. (2016). Nonlinear Potential Flow Models. In *Numerical Modelling of Wave Energy Converters*, pages 83–104. Elsevier.

FlanSea (2013). www.FlanSea.eu.

Foam-extend (2016). foam-extend (https://sourceforge.net/projects/foam-extend/).

Folley, M. (2016a). *Numerical modelling of wave energy converters : state-of-the-art techniques for single devices and arrays*. Academic Press.

Folley, M. (2016b). Spectral-Domain Models. In *Numerical Modelling of Wave Energy Converters*, pages 67–80. Elsevier.

Folley, M., Babarit, A., Child, B., Forehand, D., O'Boyle, L., Silverthorne, K., Spinneken, J., Stratigaki, V., and Troch, P. (2012). A Review of Numerical Modelling of Wave Energy Converter Arrays. In *Proceedings of the ASME 2012 31st International Conference on Ocean, Offshore and Arctic Engineering (OMAE 2012)*, page 535, Rio de Janeiro, Brazil. ASME.

Galvin, C. J. (1968). Breaker type classification on three laboratory beaches. *Journal of Geophysical Research*, 73(12):3651–3659.

Gatin, I., Vukčević, V., Jasak, H., and Rusche, H. (2017). Enhanced coupling of solid body motion and fluid flow in finite volume framework. *Ocean Engineering*, 143:295–304.

Hieu, P. D., Katsutoshi, T., and Ca, V. T. (2004). Numerical simulation of breaking waves using a two-phase flow model. *Applied Mathematical Modelling*, 28(11):983–1005.

Higuera, P., Lara, J. L., and Losada, I. J. (2013a). Realistic wave generation and active wave absorption for Navier-Stokes models. Application to OpenFOAM. *Coastal Engineering*, 71:102–118.

Higuera, P., Lara, J. L., and Losada, I. J. (2013b). Simulating coastal engineering processes with OpenFOAM. *Coastal Engineering*, 71:119–134.

Higuera, P., Losada, I. J., and Lara, J. L. (2015). Three-dimensional numerical wave generation with moving boundaries. *Coastal Engineering*, 101:35–47.

Hirt, C. and Nichols, B. (1981). Volume of Fluid (VoF) Method for the Dynamics of Free Boundaries. *Journal of Computational Physics*, 39(1):201–225.

Huang, Z.-C., Hwung, H.-H., Hsiao, S.-C., and Chang, K.-A. (2010). Laboratory observation of boundary layer flow under spilling breakers in surf zone using particle image velocimetry. *Coastal Engineering*, 57(3):343–357.

IPCC (2012). *Renewable Energy Sources and Climate Change Mitigation - Special Report of the Intergovernmental Panel on Climate Change*. Cambridge University Press, New York, USA.

IPCC (2014). Climate Change 2014: Synthesis Report. Contribution of Working Groups I, II and III to the Fifth Assessment Report of the Intergovernmental Panel on Climate Change [Core Writing Team, R.K. Pachauri and L.A. Meyer (eds.)]. Technical report, IPCC, Geneva, Switzerland.

Jacobsen, N. G. (2011). *A Full Hydro- and Morphodynamic Description of Breaker Bar Development*. PhD thesis, Technical University of Denmark.

Jacobsen, N. G. and Fredsoe, J. (2014). Formation and development of a breaker bar under regular waves. Part 2: Sediment transport and morphology. *Coastal Engineering*, 88:55–68.

Jacobsen, N. G., Fredsoe, J., and Jensen, J. H. (2014). Formation and development of a breaker bar under regular waves. Part 1: Model description and hydrodynamics. *Coastal Engineering*, 88:182–193.

Jacobsen, N. G., Fuhrman, D. R., and Fredsøe, J. (2012). A wave generation toolbox for the open-source CFD library: OpenFoam®. *International Journal for Numerical Methods in Fluids*, 70(9):1073–1088.

Jasak, H. and Tuković, Z. (2006). Automatic Mesh Motion for the Unstructured Finite Volume Method. *Transactions of FAMENA*, 30(2):1–20.

Kamath, A., Alagan Chella, M., Bihs, H., and Arntsen, Ø. A. (2015a). Evaluating wave forces on groups of three and nine cylinders using a 3D numerical wave tank. *Engineering Applications of Computational Fluid Mechanics*, 9(1):343–354.

Kamath, A., Bihs, H., and Arntsen, Ø. A. (2017). Study of Water Impact and Entry of a Free Falling Wedge Using Computational Fluid Dynamics Simulations. *Journal of Offshore Mechanics and Arctic Engineering*, 139(3):031802.

Kamath, A., Chella, M. A., Bihs, H., and Arntsen, Ø. A. (2015b). CFD investigations of wave interaction with a pair of large tandem cylinders. *Ocean Engineering*, 108:738–748.

Kazeminezhad, M. H. and Etemad-Shahidi, A. (2015). A new method for the prediction of wave runup on vertical piles. *Coastal Engineering*, 98:55–64.

Küttler, U. and Wall, W. A. (2008). Fixed-point fluid-structure interaction solvers with dynamic relaxation. *Computational Mechanics*, 43(1):61–72.

Lamont-Kane, P., Folley, M., and Whittaker, T. (2013). Investigating Uncertainties in Physical Testing of Wave Energy Converter Arrays. *Proceedings of 10th European Wave and Tidal Energy Conference (EWTEC)*.

Lara, J. L., Higuera, P., Guanche, R., and Losada, I. J. (2013). Wave Interaction With Piled Structures: Application With IH-FOAM. In *Proceedings of the ASME 2013 32nd International Conference on Ocean, Offshore and Arctic Engineering (OMAE 2013)*, Nantes, France. ASME.

Launder, B. and Spalding, D. (1974). The numerical computation of turbulent flows. *Computer Methods in Applied Mechanics and Engineering*, 3(2):269–289.

Le Méhauté, B. (1969). An Introduction to Hydrodynamics and Water Waves. *Oceanic Fronts in Coastal Processes*.

Leroyer, A. and Visonneau, M. (2005). Numerical methods for RANSE simulations of a self-propelled fish-like body. *Journal of Fluids and Structures*, 20(7 SPEC. ISS.):975–991.

Li, Y. and Yu, Y.-H. (2012). A synthesis of numerical methods for modeling wave energy converter-point absorbers. *Renewable and Sustainable Energy Reviews*, 16(6):4352–4364.

Lin, C. Y. and Huang, C. J. (2004). Decomposition of incident and reflected higher harmonic waves using four wave gauges. *Coastal Engineering*, 51(5-6):395–406.

Lin, P. and Liu, P. L. F. (1998). A numerical study of breaking waves in the surf zone. *Journal of Fluid Mechanics*, 359:239–264.

Lin, P. and Liu, P. L.-F. (1999). Internal Wave-Maker for Navier-Stokes Equations Models. *Journal of Waterway, Port, Coastal, and Ocean Engineering*, 125(4):207–215.

Mayer, S., Garapon, A., and Sørensen, L. S. (1998). A fractional step method for unsteady free-surface flow with applications to non-linear wave dynamics. *International Journal for Numerical Methods in Fluids*, 28(2):293–315.

Mayer, S. and Madsen, P. A. (2000). Simulation of Breaking Waves in the Surf Zone using a Navier-Stokes Solver. *Coastal Engineering*, pages 928–941.

Mccallum, P. D. (2017). *Numerical methods for modelling the viscous effects on the interactions between multiple wave energy converters*. PhD thesis, PhD manuscript, The University of Edinburgh.

McNatt, J. C., Venugopal, V., and Forehand, D. (2015). A novel method for deriving the diffraction transfer matrix and its application to multi-body interactions in water waves. *Ocean Engineering*, 94:173–185.

Mendoza, E., Silva, R., Zanuttigh, B., Angelelli, E., Andersen, T. L., Martinelli, L., Nørgaard, J. Q. H., and Ruol, P. (2014). Beach response to wave energy converter farms acting as coastal defence. *Coastal Engineering*, 87:97–111.

Menter, F. R. (1992). Influence of freestream values on k-ω turbulence model predictions. *AIAA Journal*, 30(6):1657–1659.

Menter, F. R. (1993). Zonal Two Equation k-ω Turbulence Models For Aerodynamic Flows. In *23rd Fluid Dynamics, Plasmadynamics, and Lasers Conference*, Reston, Virigina. American Institute of Aeronautics and Astronautics.

Menter, F. R., Ferreira, J., and Esch, T. (2003). The SST Turbulence Model with Improved Wall Treatment for Heat Transfer Predictions in Gas Turbines. *International Gas Turbine Congress 2003*, (1992):1–7.

Mingham, C., Qian, L., and Causon, D. (2016). Computational Fluid Dynamics (CFD) Models. In *Numerical Modelling of Wave Energy Converters*, pages 105–122. Elsevier.

Mori, N., Shimura, T., Nakajo, S., Tsujio, D., Yasuda, T., Mase, H., and Suh, K. D. (2014). Projection of future wave climate change and application to coastal structure design. In *From Sea to ShoreMeeting the Challenges of the Sea: (Coasts, Marine Structures and Breakwaters 2013)*, pages 204–213. ICE Publishing.

O'Boyle, L., Elsaesser, B., Whittaker, T., and Folley, M. (2011). Assessment of Wave Basin Homogeneity for Wave Energy Converter Array Studies. In *9th European Wave and Tidal Energy Conference (EWTEC2011)*.

O'Boyle, L., Elsäßer, B., and Whittaker, T. (2017). Experimental Measurement of Wave Field Variations around Wave Energy Converter Arrays. *Sustainability*, 9(1):70.

OlaFlow CFD (2018). olaFlow (https://sites.google.com/view/olaflowcfd).

OpenCFD (2018). OpenFOAM (https://www.openfoam.com/).

OpenFOAM® (2013). OpenFOAM-2.2.2.

OpenFOAM® (2015a). OpenFOAM-3.0.1.

OpenFOAM® (2015b). OpenFOAM-3.0.x.

OpenFOAM Foundation (2018). OpenFOAM (https://openfoam.org/).

Paulsen, B. T., Bredmose, H., and Bingham, H. B. (2014). An efficient domain decomposition strategy for wave loads on surface piercing circular cylinders. *Coastal Engineering*, 86:57–76.

Pecher, A. and Kofoed, J. P. (2017). *Handbook of Ocean Wave Energy*. Springer International Publishing.

Penalba, M., Giorgi, G., and Ringwood, J. V. (2017). Mathematical modelling of wave energy converters: A review of nonlinear approaches. *Renewable and Sustainable Energy Reviews*, 78:1188–1207.

Peng, Z., Wellens, P., and Raaijmakers, T. (2012). 3-D Numerical Modeling of Wave Run-Up on Monopiles. In *Proceedings of The 31st International Conference on Ocean, Offshore and Arctic Engineering (OMAE 2012)*, pages 1–9, Rio de Janeiro, Brazil. ASME.

Pope, S. B. (2000). *Turbulent flows*. Cambridge University Press.

Rahman, M. M., Karim, M. M., and Alim, M. A. (2008). Numerical investigation of unsteady flow past a circular cylinder using 2-D finite volume method. *Journal of Naval Architecture and Marine Engineering*, 4(1):27–42.

Ransley, E., Greaves, D., Raby, A., Simmonds, D., and Hann, M. (2017a). Survivability of wave energy converters using CFD. *Renewable Energy*, 109:235–247.

Ransley, E., Greaves, D., Raby, A., Simmonds, D., Jakobsen, M., and Kramer, M. (2017b). RANS-VOF modelling of the Wavestar point absorber. *Renewable Energy*, 109:49–65.

Ransley, E., Hann, M., Greaves, D., Raby, A., and Simmonds, D. (2013). Numerical and Physical Modelling of Extreme Wave Impacts on a Fixed Truncated Circular Cylinder. In *Proceedings of the 10th European wave and tidal energy conference (EWTEC)*.

Ricci, P. (2016). Time-Domain Models. In *Numerical Modelling of Wave Energy Converters*, pages 31–66. Elsevier.

Robertson et al., A. N. (2017). OC5 Project Phase II: Validation of Global Loads of the DeepCwind Floating Semisubmersible Wind Turbine. *Energy Procedia*, 137:38–57.

Saghafian, M., Stansby, P., Saidi, M., and Apsley, D. (2003). Simulation of turbulent flows around a circular cylinder using nonlinear eddy-viscosity modelling: steady and oscillatory ambient flows. *Journal of Fluids and Structures*, 17(8):1213–1236.

Salter, S. H. (1974). Wave power. *Nature*, 249(5459):720–724.

Schmitt, P. and Elsaesser, B. (2015a). A Review of Wave Makers for 3D Numerical Simulations. In *VI International Conference on Computational Methods in Marine Engineering (MARINE 2015)*, pages 1–10.

Schmitt, P. and Elsaesser, B. (2015b). On the use of OpenFOAM to model Oscillating wave surge converters. *Ocean Engineering*, 108:98–104.

Schmitt, P. and Elsäßer, B. (2017). The application of Froude scaling to model tests of Oscillating Wave Surge Converters. *Ocean Engineering*, 141:108–115.

Schmitt, P., Whittaker, T., Clabby, D., and Doherty, K. (2012). The opportunities and limitations of using CFD in the development of wave energy converters. In *Marine & Offshore Renewable Energy*, pages 89–97, London, UK.

Söding, H. (2001). How to integrate free motions of solids in fluids. In *4th Numerical Towing Tank Symposium, Hamburg*.

Spalding, D. B. (1961). A Single Formula for the 'Law of the Wall'. *Journal of Applied Mechanics*, 28(3):455.

Stansby, P., Gu, H., Moreno, E. C., and Stallard, T. (2015). Drag minimisation for high capture width with three float wave energy converter M4. In *Proceedings of the 11th European wave and tidal energy conference*, Nantes, France.

Stratigaki, V. (2014). *Experimental Study and Numerical Modelling of Intra-Array Interactions and Extra-Array Effects of Wave Energy Converter Arrays*. PhD thesis, Ghent University.

Stratigaki, V., Troch, P., Stallard, T., Forehand, D., Folley, M., Kofoed, J. P., Benoit, M., Babarit, A., Vantorre, M., and Kirkegaard, J. (2015). Sea-state modification and heaving float interaction factors from physical modelling of arrays of wave energy converters. *Journal of Renewable and Sustainable Energy*, 7(6):061705.

Stratigaki, V., Troch, P., Stallard, T., Forehand, D., Kofoed, J. P., Folley, M., Benoit, M., Babarit, A., and Kirkegaard, J. (2014). Wave basin experiments with large wave energy converter arrays to study interactions between the converters

and effects on other users in the sea and the coastal area. *Energies*, 7(2):701–734.

Sumer, B. and Fredsøe, J. (1997). *Hydrodynamics around cylindrical structures*. World Scientific.

Sumer, B. M., Sen, M. B., Karagali, I., Ceren, B., Fredsøe, J., Sottile, M., Zilioli, L., and Fuhrman, D. R. (2011). Flow and sediment transport induced by a plunging solitary wave. *Journal of Geophysical Research*, 116(C1):C01008.

Thornton, E. B. (1979). Energetics of breaking waves within the surf zone. *Journal of Geophysical Research*, 84(C8):4931.

Ting, F. C. (2001). Laboratory study of wave and turbulence velocities in a broad-banded irregular wave surf zone. *Coastal Engineering*, 43(3-4):183–208.

Ting, F. C. (2002). Laboratory study of wave and turbulence characteristics in narrow-band irregular breaking waves. *Coastal Engineering*, 46(4):291–313.

Ting, F. C. (2006). Large-scale turbulence under a solitary wave. *Coastal Engineering*, 53(5-6):441–462.

Ting, F. C. (2008). Large-scale turbulence under a solitary wave: Part 2. *Coastal Engineering*, 55(6):522–536.

Ting, F. C. (2013). Laboratory measurements of large-scale near-bed turbulent flow structures under plunging regular waves. *Coastal Engineering*, 77:120–139.

Ting, F. C. and Kirby, J. T. (1994). Observation of undertow and turbulence in a laboratory surf zone. *Coastal Engineering*, 24(1-2):51–80.

Ting, F. C. and Nelson, J. R. (2011). Laboratory measurements of large-scale near-bed turbulent flow structures under spilling regular waves. *Coastal Engineering*, 58(2):151–172.

Troch, P. and De Rouck, J. (1999). An active wave generating-absorbing boundary condition for VOF type numerical model. *Coastal Engineering*, 38(4):223–247.

Troch, P. and Stratigaki, V. (2016). Phase-Resolving Wave Propagation Array Models. In *Numerical Modelling of Wave Energy Converters*, pages 191–216. Elsevier.

UNFCCC (2015). Adoption of the Paris Agreement. Report No. FCCC/CP/2015/L.9/Rev.1. Technical report.

van der A, D. A., van der Zanden, J., O'Donoghue, T., Hurther, D., Cáceres, I., McLelland, S. J., and Ribberink, J. S. (2017). Large-scale laboratory study of breaking wave hydrodynamics over a fixed bar. *Journal of Geophysical Research: Oceans*, 122(4):3287–3310.

van Leer, B. (1974). Towards the ultimate conservative difference scheme. II. Monotonicity and conservation combined in a second-order scheme. *Journal of Computational Physics*, 14(4):361–370.

Van Maele, K. and Merci, B. (2006a). Application of two buoyancy-modified k-ϵ turbulence models to different types of buoyant plumes. *Fire Safety Journal*, 41(2):122–138.

Van Maele, K. and Merci, B. (2006b). Importance of buoyancy and chemistry modelling in steady RANS simulations of well-ventilated tunnel fires. *Turkish Journal of Engineering and Environmental Sciences*, 30(3):145–155.

Vanneste, D. and Troch, P. (2015). 2D numerical simulation of large-scale physical model tests of wave interaction with a rubble-mound breakwater. *Coastal Engineering*, 103:22–41.

Verbrugghe, T., Devolder, B., Kortenhaus, A., and Troch, P. (2017a). Feasibility study of applying SPH in a coupled simulation tool for wave energy converter arrays. In *12th European Wave and Tidal Energy Conference (EWTEC2017)*, pages 739–1 – 739–10.

Verbrugghe, T., Domínguez, J. M., Crespo, A. J., Altomare, C., Stratigaki, V., Troch, P., and Kortenhaus, A. (2018). Coupling methodology for smoothed particle hydrodynamics modelling of non-linear wave-structure interactions. *Coastal Engineering*, 138:184–198.

Verbrugghe, T., Stratigaki, V., Troch, P., Rabussier, R., and Kortenhaus, A. (2017b). A Comparison Study of a Generic Coupling Methodology for Modeling Wake Effects of Wave Energy Converter Arrays. *Energies*, 10(11):1697.

Versteeg, H. K. and Malalasekera, W. (2007). *An Introduction to Computational Fluid Dynamics*, volume M. Pearson Education.

Vierendeels, J., Dumont, K., Dick, E., and Verdonck, P. (2005). Analysis and Stabilization of Fluid-Structure Interaction Algorithm for Rigid-Body Motion. *AIAA Journal*, 43(12):2549–2557.

Vukčević, V., Jasak, H., and Gatin, I. (2017). Implementation of the Ghost Fluid Method for free surface flows in polyhedral Finite Volume framework. *Computers & Fluids*, 153:1–19.

Wamit (2016). Wamit User Manual.

Weller, H. G., Tabor, G., Jasak, H., and Fureby, C. (1998). A tensorial approach to computational continuum mechanics using object-oriented techniques. *Computers in Physics*, 12(6):620.

Whitehouse, R. (1998). *Scour at marine structures: A manual for practical applications*. Thomas Telford.

Wilcox, D. C. (1998). *Turbulence modeling for CFD*. DCW Industries, Inc., La Canada, California.

Wolgamot, H., Eatock Taylor, R., and Taylor, P. (2016). Effects of second-order hydrodynamics on the efficiency of a wave energy array. *International Journal of Marine Energy*, 15:85–99.

Wolgamot, H. A. and Fitzgerald, C. J. (2015). Nonlinear hydrodynamic and real fluid effects on wave energy converters. *Proceedings of the Institution of Mechanical Engineers, Part A: Journal of Power and Energy*, 229(7):772–794.

Xie, Z. (2013). Two-phase flow modelling of spilling and plunging breaking waves. *Applied Mathematical Modelling*, 37(6):3698–3713.

Yettou, E.-M., Desrochers, A., and Champoux, Y. (2006). Experimental study on the water impact of a symmetrical wedge. *Fluid Dynamics Research*, 38(1):47–66.

Zhou, Z., Hsu, T.-J., Cox, D., and Liu, X. (2017). Large-eddy simulation of wave-breaking induced turbulent coherent structures and suspended sediment transport on a barred beach. *Journal of Geophysical Research: Oceans*, 122(1):207–235.